

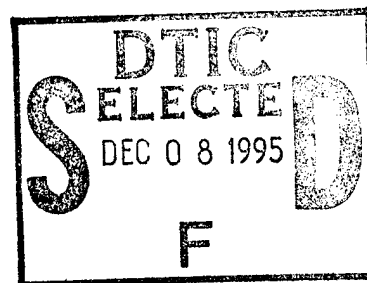
WL-TR-95-4012

RESEARCH ON ADVANCED NDE METHODS FOR  
AEROSPACE STRUCTURES

Brian Frock, Prasanna Karpur, Richard Martin  
Theodore Matikas, and Mark Ruddell



University of Dayton Research Institute  
300 College Park  
Dayton OH 45469-0128



November 1994

Final Report for Period 1 September 1989 - 31 August 1994

Approved for public release; distribution is unlimited.

"Original contains color plates: All DTIC reproductions will be in black and white."

19951206 033

MATERIALS DIRECTORATE  
WRIGHT LABORATORY  
AIR FORCE MATERIEL COMMAND  
WRIGHT-PATTERSON AFB OH 45433-7734

DTIC QUALITY EXCELLENCE

## NOTICE

WHEN GOVERNMENT DRAWINGS, SPECIFICATIONS, OR OTHER DATA ARE USED FOR ANY PURPOSE OTHER THAN IN CONNECTION WITH A DEFINITELY GOVERNMENT-RELATED PROCUREMENT, THE UNITED STATES GOVERNMENT INCURS NO RESPONSIBILITY OR ANY OBLIGATION WHATSOEVER. THE FACT THAT THE GOVERNMENT MAY HAVE FORMULATED OR IN ANY WAY SUPPLIED THE SAID DRAWINGS, SPECIFICATIONS, OR OTHER DATA, IS NOT TO BE REGARDED BY IMPLICATION OR OTHERWISE IN ANY MANNER CONSTRUED, AS LICENSING THE HOLDER OR ANY OTHER PERSON OR CORPORATION, OR AS CONVEYING ANY RIGHTS OR PERMISSION TO MANUFACTURE, USE, OR SELL ANY PATENTED INVENTION THAT MAY IN ANY WAY BE RELATED THERETO.

THIS REPORT IS RELEASABLE TO THE NATIONAL TECHNICAL INFORMATION SERVICE (NTIS). AT NTIS, IT WILL BE AVAILABLE TO THE GENERAL PUBLIC, INCLUDING FOREIGN NATIONS.

THIS TECHNICAL REPORT HAS BEEN REVIEWED AND IS APPROVED FOR PUBLICATION.



ROBERT L. CRANE  
Nondestructive Evaluation Branch  
Metals and Ceramics Division



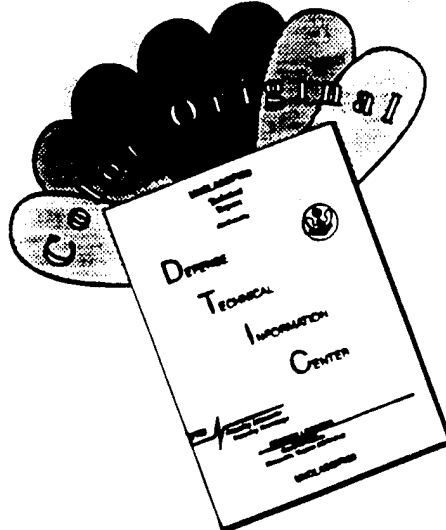
TOBEY M. CORDELL, Chief  
Nondestructive Evaluation Branch  
Metals and Ceramics Division

  
WALTER M. GRIFFITH, Asst. Chief  
Metals and Ceramics Division  
Materials Directorate

IF YOUR ADDRESS HAS CHANGED, IF YOU WISH TO BE REMOVED FROM OUR MAILING LIST, OR IF THE ADDRESSEE IS NO LONGER EMPLOYED BY YOUR ORGANIZATION, PLEASE NOTIFY, WL/MLP, WRIGHT-PATTERSON AFB OH 45433-7817 TO HELP US MAINTAIN A CURRENT MAILING LIST.

COPIES OF THIS REPORT SHOULD NOT BE RETURNED UNLESS RETURN IS REQUIRED BY SECURITY CONSIDERATIONS, CONTRACTUAL OBLIGATIONS, OR NOTICE ON A SPECIFIC DOCUMENT.

# **DISCLAIMER NOTICE**



**THIS DOCUMENT IS BEST  
QUALITY AVAILABLE. THE COPY  
FURNISHED TO DTIC CONTAINED  
A SIGNIFICANT NUMBER OF  
COLOR PAGES WHICH DO NOT  
REPRODUCE LEGIBLY ON BLACK  
AND WHITE MICROFICHE.**

REPORT DOCUMENTATION PAGE			FORM APPROVED OMB NO. 0704-0188
<p>Public reporting burden for this collection of information is estimated to average 1 hour per response, including the time for reviewing instructions, searching existing data sources, gathering and maintaining the data needed, and completing and reviewing the collection of information. Send comments regarding this burden estimate or any other aspect of this collection of information, including suggestions for reducing this burden, to Washington Headquarters Services, Directorate for Information Operations and Reports, 1215 Jefferson Davis Highway, Suite 1204, Arlington, VA 22202-4302 and to the Office of Management and Budget, Paperwork Reduction Project (0704-0188), Washington, DC 20503.</p>			
1. AGENCY USE ONLY (Leave blank)	2. REPORT DATE	3. REPORT TYPE AND DATES COVERED	
	November 1994	Final Report for 1 Sept 1989 - 31 Aug 1994	
4. TITLE AND SUBTITLE		5. FUNDING NUMBERS	
Research on Advanced NDE Methods for Aerospace Structures		C - F33615-89-C-5612 PE - 62102F PR - 2418 TA - 02 WU - 45	
6. AUTHOR(S)		8. PERFORMING ORGANIZATION REPORT NUMBER	
Brian Frock, Prasanna Karpur, Richard Martin, Theodore Matikas, and Mark Ruddell		UDR-TR-94-141	
7. PERFORMING ORGANIZATION NAMES(ES) AND ADDRESS(ES)		10. SPONSORING/MONITORING AGENCY REPORT NUMBER	
University of Dayton Research Institute 300 College Park Dayton, Ohio 45469-0128		WL-TR-95-4012	
9. SPONSORING/MONITORING AGENCY NAMES(ES) AND ADDRESS(ES)		11. SUPPLEMENTARY NOTES	
Materials Directorate Air Force Wright Laboratory Wright-Patterson AFB OH 45433-7734		N/A	
12a. DISTRIBUTION/AVAILABILITY STATEMENT		12b. DISTRIBUTION CODE	
Approved for public release; distribution is unlimited.		A	
13. ABSTRACT (Maximum 200 words)			
<p>Studies were conducted which determined the capabilities and limitations of ultrasonic NDE techniques for evaluating the interphase/interface region between the fiber and the matrix in metal matrix composites. The major developments include: a physical model of the elastic interphase region between the fiber and matrix in the fiber-reinforced materials; an ultrasonic wave propagation model; an experimental procedure for interface elastic property measurements; experimental determination of the semi-empirical relationship between the ultrasonic shear wave reflection coefficient and the magnitude of the radial residual stress at the fiber matrix interface; a method for ultrasonic imaging of fiber fracture during single-fiber fragmentation testing of metal matrix composites; and a method for in situ ultrasonic imaging of fiber fragmentation during incremental loading tests. Applicability studies resulted in: the use of software gating techniques for imaging near entry surface anomalies in kevlar polyester radome materials; use of an entry surface echo removal algorithm to improve time of flight C-scan images of near entry surface delamination damage; modification of an entry surface echo removal algorithm for application to sparsely samples, depot collected ultrasonic B scan data; and development and use of two dimensional Fourier domain zero padding for producing high quality enlargements of small, sparsely sampled depot type C-scan data sets. Many of the applicability studies were conducted in cooperation with Air Force ALCs.</p>			
14. SUBJECT TERMS		15. NUMBER OF PAGES	
NDE, ultrasonics, metal matrix composites, ceramic matrix composites, nondestructive characterization of advanced composite fiber matrix interface characterization, matrix consolidation characterization, image expansion, digital processing of ultrasonic signals		122	
16. PRICE CODE			
17. SECURITY CLASSIFICATION OF REPORT	18. SECURITY CLASSIFICATION OF THIS PAGE	19. SECURITY CLASSIFICATION OF ABSTRACT	20. LIMITATION OF ABSTRACT
Unclassified	Unclassified	Unclassified	Unlimited

## ***Table of Contents***

---

<u>Section</u>	<u>Page</u>
1 Introduction .....	1-1
2 Executive Summary .....	2-1
3 Development of NDE Techniques for Characterization of Fiber-Reinforced Composites.....	3-1
3.1. A Nondestructive Methodology for Measuring the Shear-Stiffness Coefficient of the Fiber-Matrix Interface.....	3-2
3.1.1 Concepts: Modeling the Interface/Interphase Between Fiber and Matrix.....	3-3
3.1.2 Ultrasonic Wave Propagation Model.....	3-6
3.1.2.1 Analysis.....	3-6
3.1.2.2 Numerical Results - Discussion .....	3-11
3.1.3 Experimental Procedure for Interface Elastic Property Measurement.....	3-17
3.1.4 Effect of Residual Stresses on the Measurement of Interfacial Stiffness .....	3-20
3.1.4.1 Finite Difference Analysis and the Experimental Approach.....	3-21
3.1.4.2 Experimental Determination of the Semiempirical Relationship Between the Ultrasonic Reflection Coefficient and the Magnitude of Radial Residual Stress .....	3-23
3.1.5 Influence of Fiber Volume Fraction, Residual Stress and the Interface Elastic Properties on CMC Micro-Cracking .....	3-26
3.1.5.1 Approach.....	3-26
3.1.5.2 Results .....	3-28
3.2 Ultrasonic NDE Techniques for Improving the Results of Destructive Mechanical Tests .....	3-32
3.2.1 Single-Fiber Fragmentation Test for Metal Matrix Composites.....	3-32
3.2.1.1 Ultrasonic Visualization of Fiber Fracture .....	3-33
3.2.1.2 <i>In Situ</i> Observation of Fiber Fragmentation .....	3-39
3.2.2 Ultrasonic Imaging for Improved Fiber-Push-Out Test Results .....	3-44
3.2.3 Ultrasonic Imaging of Fiber-Matrix Interface Damage During Transverse Loading of Metal-Matrix Composites.....	3-46
3.2.3.1 Mechanism of Damage Evolution in Titanium Matrix Composites During Transverse Testing .....	3-47
3.2.3.2 Experimental Approach .....	3-49
3.2.3.3 Experimental Results and Discussion.....	3-53
3.3 Ultrasound for Post-Processing NDE of Fiber-Reinforced Metal Matrix and Ceramic Matrix Composites.....	3-61
3.3.1 Evaluation of Consolidation in Metal Matrix and Ceramic Matrix Composites .....	3-62
3.3.1.1 Processing of Advanced Composites .....	3-62

## *Table of Contents (Cont'd)*

---

<u>Section</u>	<u>Page</u>
3.3.1.2 Fabrication of Single Fiber Titanium Matrix Composites .....	3-63
3.3.1.3 Ultrasonic Experimental Approach .....	3-64
3.3.1.4 Results and Discussion - MMC.....	3-69
3.3.1.5 Results and Discussion - CMC .....	3-73
3.3.2 Characterization of Matrix Microstructure and Morphology in Titanium Matrix Composites .....	3-76
3.3.2.1 Role of the Matrix Microstructure and Morphology on the Performance of the Composite .....	3-77
3.3.2.2 Modeling the Propagation of Ultrasound in an Anisotropic Polycrystalline Matrix Material .....	3-77
3.3.2.3 Fabrication of the Samples Used in the Study .....	3-80
3.3.2.4 Ultrasonic Imaging - Results.....	3-81
4 Applicabilities Studies .....	4-1
4.1 Digital Techniques for Ultrasonic Imaging of Near-Entry-Surface Anomalies in Highly Attenuative Materials .....	4-1
4.1.1 Entry-Surface-Echo C-Scan Imaging .....	4-1
4.1.2 Digital Filtering Improves C-Scan Image Resolution .....	4-2
4.1.3 Additional Information .....	4-3
4.2 Time-of-Flight C-Scan Imaging of Near-Entry-Surface Anomalies .....	4-6
4.2.1 Preprocessing with Entry-Surface-Echo-Removal Algorithm, REFSUB .....	4-7
4.2.2 "Nontraditional" TOF C-Scan Image Generation Steps .....	4-7
4.3 High-Quality C-Scan Image Enlargements From Depot and In-Field-Collected Small Data Sets .....	4-8
4.3.1 Enlarging (Interpolation) Method.....	4-9
4.3.2 Additional Information -- Sample and Transducer .....	4-10
4.3.3 Additional Information -- Scanning and Data Acquisition.....	4-10
4.4 Hlgh Precision Scanning Acoustic Microscope System (HIPSAM) .....	4-10
4.5 Application of an Entry Surface-Echo-Removal Algorithm to Anomaly Detection in Depot-Type Data.....	4-13
4.6 Split Spectrum Processing of Ultrasonic Signals Improves Detection and Sizing of Material Anomalies .....	4-14
4.6.1 Fatigue-Microcrack Detection .....	4-14
4.6.2 Fatigue-Microcrack Sizing and Growth Monitoring .....	4-15
4.6.3 Reliable Detection of Small Hard-Alpha Inclusions in Titanium Products .....	4-16
4.6.4 Improving the Reliability of Artificial Neural Network Classifications.....	4-17
4.7 Leaky Lamb Wave Inspection Techniques for Detecting Damage in Composite Structures .....	4-18
4.7.1 Major Advantages and Disadvantages.....	4-19

## *Table of Contents (Concluded)*

---

<u>Section</u>	<u>Page</u>
4.7.2 Swept-Frequency, Tone-Burst Lamb Wave Generation.....	4-19
4.7.3 Median-Frequency Processing .....	4-20
4.8 B-Scan to C-Scan Conversion Software Upgrades .....	4-22
4.9 Collaborative Efforts with Air Force ALCs.....	4-23
5 References .....	5-1
Appendix A List of Publications.....	A-1

Accesion For	
NTIS	CRA&I <input checked="" type="checkbox"/>
DTIC	TAB <input type="checkbox"/>
Unannounced <input type="checkbox"/>	
Justification .....	
By .....	
Distribution /	
Availability Codes	
Dist	Avail and / or Special
A-1	

## *List of Illustrations*

---

<u>Figure</u>	<u>Page</u>
3-1 (a) Schematic of the interphase region between the matrix and the fiber. (b) Schematic showing the 'equivalent elastic interface' between the matrix and the fiber materials .....	3-4
3-2 Schematic of a layered interface.....	3-4
3-3 (a) Compressional spring model of the interfacial behavior for incident dilatational waves. (b) Shear spring model of the interfacial behavior for incident transversely polarized shear waves.....	3-5
3-4 Geometry of the problem .....	3-7
3-5 (a) Back-reflection coefficient amplitude as a function of interfacial shear stiffness coefficient and frequency. (b) Isolevel contour map representation of the data in Figure 3-5a. ....	3-12
3-6 Back-reflection coefficient amplitude vs. shear stiffness coefficient for a frequency which is: (a) near a resonance peak (16.0 MHz, line a-a Fig. 3-5b), (b) slightly lower than the resonance dip (24.0 MHz, line b-b in Figure 3-5b), and (c) slightly higher than the resonance dip (29.0 MHz, line c-c in Figure 3-5b). ....	3-13
3-7 (a) Back-reflection amplitude as a function of interfacial shear stiffness and for a range of frequencies 1-150 MHz. (b) Isolevel projection of the data in 3-7a.....	3-14
3-8 Back-reflection coefficient amplitude versus frequency for a fiber-matrix bond which is: (a) 'infinitely' rigid (shear stiffness coefficient=100.0 GPa/ $\mu$ m), (b) intermediate in rigidity (shear stiffness coefficient=10.0 GPa/ $\mu$ m), and (c) flexible (shear stiffness coefficient=2.0 GPa/ $\mu$ m) .....	3-15
3-9 Resonant back-reflection coefficient amplitude vs. shear stiffness coefficient for a given frequency of (a) 15.0 MHz, (b) 66.0 MHz, and (c) 141.0 MHz .....	3-16
3-10 Back-reflection coefficient amplitude as a function of frequency and angle of incidence in the case of a bond which is: (a) 'infinitely' rigid (shear stiffness coefficient=100.0 GPa/ $\mu$ m), and (b) flexible (shear-stiffness coefficient=2.0 GPa/ $\mu$ m) .....	3-17
3-11 Experimental procedure for the measurement of the shear stiffness coefficient .....	3-18
3-12 Procedure to experimentally calculate the reflection coefficient at a specific frequency selected based on the theoretical modeling .....	3-18

## List of Illustrations (Cont'd)

<u>Figure</u>	<u>Page</u>
3-13 Inversion of shear stiffness coefficient of the fiber-matrix interface from the experimentally calculated shear back-reflection coefficient.....	3-19
3-14 (a) Ultrasonic back-reflected amplitude image of an SCS-6 fiber embedded in Ti-6Al-4V matrix showing varying interfacial property compared to the image from a hole of the same diameter as that of the fiber. (b) Line plots of the reflected amplitudes along the lengths of the fiber and the hole, respectively, showing the variability of the reflected amplitude from the fiber-matrix interface. ....	3-19
3-15 Schematic of the cross-sectional metallograph of the fiber-matrix interface variability in (a) Ti-6Al-4V, and (b) Ti-24Al-11Nb matrix composites with SCS-6 fibers .....	3-20
3-16 Factors which produce two types of bonds that affect shear-stress transfer between the fiber and the matrix: (a) radial component of the residual stresses, and (b) chemical reactions between the fiber and the matrix.....	3-21
3-17 Theoretical residual stress model of Coker, Ashbaugh and Nicholas.....	3-22
3-18 Back-reflection coefficient versus shear stiffness coefficient for different composite systems made from various types of glass matrices with SCS-6 Fibers (frequency: 25.0 MHz) .....	3-25
3-19 Linearity of ultrasonic reflection as a function of radial residual stress .....	3-25
3-20 Composite cracking stress versus fiber volume fraction for (a) SIGMA fiber reinforced glasses and (b) SCS-6 fiber reinforced glasses.....	3-29
3-21 Ultrasonic images of SCS-6 fiber reinforced glass sample after tensile loading: (a) surface wave image showing surface cracks, (b) acoustic microscopy image showing surface cracks and interfacial debonding of the first layer of fibers, (c) oblique-incidence shear-wave image of upper surface of sample showing upper-surface and internal cracks, and (d) oblique-incidence shear-wave image of lower surface of sample showing lower-surface and internal cracks.....	3-30
3-22 Shear-wave back-reflectivity (SBR) images showing (a) a stiff interface in a SIGMA fiber reinforced "E" glass composite, and (b) a highly compliant interface in an SCS-6 fiber reinforced "E" glass composite .....	3-31
3-23 Shear-wave back-reflection coefficient amplitude versus shear stiffness coefficient for "E" glass matrix composites reinforced with different fibers.....	3-31

## List of Illustrations (Cont'd)

<u>Figure</u>	<u>Page</u>
3-24 (a) Shear-wave ultrasonic imaging configuration..... (b) Gated ultrasonic signal reflected from a fiber embedded in a metal matrix. The signal was obtained using the shear wave back-reflectivity technique.....	3-34 3-34
3-25 Schematic of a defocused imaging configuration .....	3-35
3-26 (a) Ultrasonic image of a SIGMA SiC fiber embedded in Ti-14Al-21Nb matrix. 25 MHz ultrasonic beam is focused on the fiber. (b) Image of the same sample with a defocus of -1 mm. (c) Image of the same sample with a defocus of -1.5 mm.....	3-36
3-27 (a) Ultrasonic image of an untested single fiber sample. (b) Fiber fragmentation image in Ti-6Al-4V sample with SCS-6 Fiber. (c) Fiber fragmentation image in Ti-14Al-21Nb (or Ti-24Al-11Nb by atomic %) sample with SCS-6 Fiber. (d) Corroboration of the ultrasonic imaging of fiber fragmentation with metallography. (e) SEM image of the fragmented fiber showing secondary fractures in addition to the primary fracture.....	3-37
3-28 (a) Ultrasonic signal from a microcrack (frequency: 50 MHz) and (b) Ultrasonic signal from a fiber (frequency: 50 MHz) .....	3-38
3-29 Output from the Neural Network when Trained with Six Examples per Class (a) Image of the Fragmented Fiber, (b) Image of Microcracks on the Fiber, and (c) Surrounded Matrix.....	3-39
3-30 The loading device in the water tank with the acoustic transducer in position <i>for in situ</i> ultrasonic imaging of the fiber fragmentation process.....	3-40
3-31 <i>In situ</i> ultrasonic images of the fiber fragmentation process. Images 1 through 9 are sequentially obtained by imaging the same fiber through the loading process with the strain increasing at a nominal rate of 0.75% from 1 through 9 .....	3-41
3-32 <i>In situ</i> ultrasonic images of the single row of chopped fibers fragmentation process. (a) Pretest image of the sample with a single row of chopped fibers (b) The sample shown in Figure 9a after the first interruption (strain = 2.7%). (c) The sample after the second interruption (strain = 7%) .....	3-43
3-33 Configuration of the push-out test .....	3-45

## List of Illustrations (Cont'd)

<u>Figure</u>	<u>Page</u>
3-34 (a) Normal incidence ultrasonic (50 MHz) image showing areas of poor bonding and improper consolidation in addition to good bonding areas. The inset shows the location of the test specimen cut-out from the plate and the corresponding peak-load for each fiber. (b) SBR image of the sample showing interfacial integrity.....	3-47
3-35 Experimental configuration showing transverse orientation of the fiber in a sample and the direction of loading .....	3-48
3-36 Schematic of microscopic-damage evolution at the fiber-matrix interface in a transversely loaded single-fiber MMC .....	3-49
3-37 Damage evolution at fiber-matrix interface (in SiC-fiber-reinforced Ti-6Al-4V MMC) due to increasing transverse load (elastic range, "a" through "d"; plastic range, "e")" (a) residual-stress change, no observable damage; (b) chemical-bond failure on sides; (c) entire chemical-bond fails; (d) physical separation between fiber and matrix; and (e) pronounced fiber-matrix separation at interface.....	3-50
3-38 Configuration of the micro-straining stage for ultrasonic <i>in situ</i> imaging arrangement .....	3-50
3-39 Schematic of ultrasonic interrogation of the interface damage evolution: (a) Bonded interface, (b) Partial interfacial debond (with no physical separation) in the direction of loading, (c) Complete interfacial debond (with no physical separation), (d) Physical separation of the interface in the direction of loading, and (e) Change of slope of the physical separation of the interface in the direction of loading .....	3-51
3-40 Schematic of the proposed relationship between microscopic damage and ultrasonic reflection coefficient using the SBR technique .....	3-52
3-41 <i>In situ</i> ultrasonic SBR imaging of an embedded SCS-6 fiber in Ti-6Al-4V matrix during various stages of transverse loading.....	3-53
3-42 Ultrasonic reflectivity from the fiber-matrix interface at various locations for selected stages of loading of the test specimen (indicated by A, F, and K in Figure 3-41) .....	3-54
3-43 <i>In situ</i> ultrasonic SBR imaging of a Ti-6Al-4V/SCS-6 single fiber composite sample during various stages of transverse loading.....	3-55
3-44 <i>In situ</i> ultrasonic SBR imaging of a Ti-6Al-4V/SCS-0 single fiber composite sample during various stages of transverse loading .....	3-56

## *List of Illustrations (Cont'd)*

---

<u>Figure</u>	<u>Page</u>
3-45 <i>In situ</i> ultrasonic SBR imaging of a SCS-0 single fiber embedded in Ti-6Al-4V matrix subjected to transverse loading .....	3-57
3-46 Experimental configuration showing transverse orientation of three fibers in a sample, and the direction of loading .....	3-57
3-47 <i>In situ</i> ultrasonic imaging of the transverse test of a Ti-6Al-4V matrix composite made with three fibers (SCS-0, SCS-6, SCS-0 with Yttria coating).....	3-58
3-48 Ultrasonic shear wave images of (a) a fiber with free edge, and (b) a completely embedded in the matrix fiber .....	3-59
3-49 Interfacial radial stress distribution near the fiber tip .....	3-59
3-50 Schematic diagram of the transverse section of a continuously reinforced composite showing shear wave interrogation of a fiber embedded in the matrix .....	3-64
3-51 Schematic diagram of the transverse section of a continuously reinforced composite showing longitudinal wave interrogation of a fiber embedded in the matrix .....	3-64
3-52 Amplitude of oblique-incidence shear waves back-reflected from fiber matrix interface with: (a) good consolidation, (b) regions of poor consolidation with $\alpha \neq \theta_s$ , (c) poor consolidation with $\alpha = \theta_s$ , and (d) complete debond around the fiber .....	3-66
3-53 Amplitude of normal-incidence longitudinal wave back-reflected from fiber-matrix interface with: (a) good consolidation, (b) poor consolidation with larger reflected amplitude than for good consolidation, and (c) poor consolidation with $\alpha \approx 0$ .....	3-68
3-54 Ultrasonic image from Ti-14Al-21Nb/SiC sample which was consolidated by vacuum hot pressing + HIPing (Panel A) - - (a) oblique-incidence ( $24^\circ$ ) shear wave, and (b) normal-incidence longitudinal wave .....	3-69
3-55 Ultrasonic images from Ti-14Al-21Nb/SiC single fiber composite (Panel B) using shear wave interrogation with different angles of wave front incidence: (a) $18^\circ$ and (b) $24^\circ$ .....	3-69
3-56 Ultrasonic image from Ti-14Al-21Nb/SiC single fiber composite (Panel B) using longitudinal wave interrogation. AA', BB', and CC' indicate sections at which metallographic samples were examined .....	3-70
3-57 Optical micrograph of Ti-14Al-21NB/SiC single fiber composite (Panel A) sample showing good consolidation.....	3-70

## ***List of Illustrations (Cont'd)***

---

<u>Figure</u>	<u>Page</u>
3-58 Optical images of fiber-matrix interface which correspond with specific regions across the C-scan image in Figure 3-56: (a) across AA', (b) across BB', and (c) across CC' .....	3-71
3-59 Shear wave interrogation of a Ti-6Al-4V/SiC single-ply composite showing areas of poor consolidation.....	3-73
3-60 Metallography of section from a uniform region showing good consolidation .....	3-73
3-61 Oblique-incidence, back-reflected shear-wave images of Glass-F composites with embedded single fibers: (a) SCS-6 fiber with good consolidation, (b) SCS-6 fiber with poor consolidation, and (c) SCS-0 fiber with poor consolidation.....	3-74
3-62 Oblique-incidence, back-reflected shear-wave images of single-ply SCS-6 fibers in borosilicate matrices: (a) glass-D, poor consolidation, $\sigma_r = 6.5$ Mpa; (b) glass-C, global lack-of-consolidation, $\sigma_r = 13.6$ Mpa; and (c) glass-E, good consolidation, $\sigma_r$ nearly zero .....	3-75
3-63 Oblique-incidence, back-reflected shear-wave images of single-ply fibers embedded in glass-E matrix: (a) SIGMA fibers with good consolidation, and (b) SCS-6 fibers with poor consolidation.....	3-75
3-64 Oblique-incidence, back-reflected shear-wave images of glass-F/SCS-6 fiber composites before and after reprocessing: (a) no reprocessing, poor consolidation and substantial matrix porosity; (b) first reprocessing, better consolidation and less matrix porosity; and (c) second reprocessing, good consolidation and absence of matrix porosity.....	3-76
3-65 Images of single fiber embedded in Ti-6Al-4V matrices with different microstructure: (a) ultrasonic image, inhomogeneous, coarse plate-like alpha plus beta microstructure; (b) homogeneous, fine, equiaxed alpha plus beta microstructure; (c) metallographic image, microstructure as in "a"; and (d) metallographic image, microstructure as in "b" .....	3-82
3-66 Images of three fibers embedded in Ti-6Al-4V matrix: (a) ultrasonic image, (b) metallographic image of section perpendicular to fiber direction, and (c) metallographic section through fibers and parallel to the fiber direction .....	3-82
4-1 Software-gated C-scan images of a kevlar-polyester radome segment: (a) data from back-surface echo; and (b) data from entry-surface-echo ring-down region .....	4-1

## *List of Illustrations (Cont'd)*

---

<u>Figure</u>	<u>Page</u>
4-2 Data from the three-dimensional data set used for this study: (a) RF A-scan; and (b) Fourier magnitude spectra of the RF A-scan in "a" .....	4-3
4-3 C-scan images generated after band-pass filtering the RF B-scans: (a) filter centered about the 3.25 MHz mode; and (b) filter centered about the 5.5 MHz mode.....	4-3
4-4 Time-of-Flight C-scan images of layer-by-layer, impact-induced damage in graphite-epoxy composites: (a) and (b) "traditional" TOF imaging; (c) and (d) C-scan image generation after preprocessing the data to remove the entry-surface-echo .....	4-6
4-5 C-scan images of the delamination damage (very dark regions): (a) from original small data set; (b) from large, over-sampled data set.....	4-8
4-6 Enlargements of the C-scan image in Fig. 4-5a by: (a) pixel replication; and (b) use of method developed in WL/MLLP branch .....	4-9
4-7 C-scan image showing a cross-sectional view of SCS-6 fibers embedded in a Ti-6Al-4V matrix. Data for the image were collected using the HIPSAM system.....	4-11
4-8 <u>Hlgh Precision Scanning Acoustic Microscope System (HIPSAM)</u> .....	4-12
4-9 Near-entry-surface-echo B-scans: (a) as-digitized data; (b) entry-surface echo removed with an earlier version of REFSUB; and (c) entry-surface echo removed with the new version of REFSUB .....	4-14
4-10 Rayleigh waves backscattered from fatigue crack; (a) original A-scan; and (b) results of processing the A-scan in "a" using the SSP technique.....	4-15
4-11 Peak-to-peak amplitude of SSP-processed, microcrack-backscattered Rayleigh wave as a function of the number of fatigue cycles .....	4-15
4-12 C-scan images of impact-induced delamination in a graphite-epoxy composite. Image generated by applying: (a) software-gates to original the RF A-scans; (b) BP-ANN to the original RF A-scans; and (c) BP-ANN to the SSP-processed RF A-scans .....	4-17
4-13 C-scan images of delamination damage using: (a) swept-frequency, tone-burst, leaky Lamb wave technique; and (b) conventional normal-incidence time-of-flight technique.....	4-18
4-14 C-scan images of impact damage at the interface between a composite face sheet and a honeycomb core using: (a) swept-frequency, tone-burst, leaky Lamb wave technique; and (b) conventional normal-incidence back-surface amplitude technique. The damaged region is shown in light gray and white near the center of each image.....	4-19

## List of Illustrations (Concluded)

<u>Figure</u>	<u>Page</u>
4-15 Schematic diagram of leaky Lamb wave generation. "LW" indicates the region of the leaky wave whereas "N" denotes a null within the leaky wave .....	4-20
4-16 Swept-frequency, tone-burst data in defect-free region: (a) pseudo RF A-scan; and (b) Fourier magnitude spectra of "a" .....	4-21
4-17 Swept-frequency, tone-burst data in delaminated region: (a) pseudo RF A-scan; and (b) Fourier magnitude spectra of "a" .....	4-21

## *List of Tables*

---

<u>Table</u>	<u>Page</u>
3-1 Theoretically Calculated Shear Stiffness Coefficient Based on Experimentally Measured Back-Reflection Coefficient .....	3-19
3-2 Elastic Properties of Various Types of Custom Glasses with Similar Elastic Properties but with Different Coefficients of Thermal Expansion Due to Small Differences in Chemical Composition .....	3-23
3-3 Properties of Various Fibers.....	3-23
3-4 Elastic Properties, Coefficients of Thermal Expansion and Residual Stresses of Some Glass Matrix Composites with SCS-6 Fibers.....	3-24
3-5 Composite Cracking Stress.....	3-28
3-6 Reflection and Shear-Stiffness Coefficients of Four CMCs .....	3-31
4-1 Software Gating .....	4-4
4-2 Storing Three-Dimensional RF Waveforms.....	4-4
4-3 Digital Filtering .....	4-4
4-4 Sample Information.....	4-5
4-5 Transducer and Scanning Information .....	4-5
4-6 Ultrasonic Beam Characteristics .....	4-5
4-7 Image-Generation Steps .....	4-7
4-8 Requirements for Removing the Entry-Surface Echo and Generating TOF C-Scan Images .....	4-7
4-9 Sample, Transducer and Data-Collection Parameters .....	4-8
4-10 Image Enlargement Methodology .....	4-9
4-11 Sample and Transducer Information .....	4-10
4-12 Ultrasonic Scanning and Acquisition Parameters.....	4-11
4-13 Data Collection Parameters for Image in Figure 4-7 .....	4-12
4-14 Major Features of the HIPSAM System .....	4-13
4-15 Reliability of Artificial Neural Network Classification.....	4-18
4-16 Major Advantages and Disadvantages of the Leaky Lamb Wave Generation and Processing Techniques .....	4-19
4-17 BTOC Additions and Modifications.....	4-22
4-18 Advantages and Disadvantages of Using BTOC.....	4-23
4-19 Collaborative Efforts with Air Force ALCs .....	4-24

## ***Foreword***

---

This final technical report describes the work accomplished during the period from 1 September 1989 through 31 August 1994 by the University of Dayton Research Institute (UDRI) under Contract Number F33615-89-C-5612 for the Wright Laboratories Materials Directorate. Dr. Thomas Moran of the Nondestructive Evaluation Branch (MLLP), Metals and Ceramics Division was the Contract Monitor.

The efforts reported here were performed by several UDRI employees. Mr. Brian G. Frock of the UDRI Structural Integrity Division was Principal Investigator for the contract. Mr. Robert Andrews, also of the UDRI Structural Integrity Division was the Program Manager. The following University employees contributed to the work: Jeffrey Fox, Prasanna Karpur, Edward Klosterman, Richard Martin, Theodoros Matikas, Mary Papp and Mark Ruddell. Dianne Benson and Orlando Canelones - - both of whom were graduate students - - worked on the project at different time periods. Marylea Barlow was responsible for typing and assembling the monthly progress reports. Marylea Barlow and LaVonna Stathes were responsible for typing and assembling this final report.

# **Section 1**

## ***Introduction***

---

The research and development efforts described in this report were conducted to:

- ***Develop new NDE techniques for characterization of fiber-reinforced composite materials, and***
- ***Apply previously developed NDE techniques to solve existing Air Force nondestructive inspection problems.***

***The NDE Technique-Development Efforts*** yielded novel ultrasonic methods for characterizing metal-matrix and ceramic-matrix composites. These efforts were concentrated in two areas: (1) nondestructive techniques which evaluate the shear-stress transfer capabilities of the fiber-matrix interface, and (2) nondestructive techniques which complement and improve existing mechanical, destructive testing methods for characterizing the properties of the fiber-matrix interface. The techniques which were developed should be of significant use to scientists and engineers working in the new-materials development and new-materials processing areas. The major techniques developed during this contract are listed in Exhibit 1-1.

SUMMARY OF MAJOR TECHNIQUES DEVELOPED
<ul style="list-style-type: none"><li>• A combined mathematical and experimental nondestructive methodology for measuring the shear stiffness of the fiber-matrix interface in MMCs and CMCs</li><li>• After loading and <i>in situ</i> nondestructive ultrasonic techniques for imaging fiber fracture resulting from mechanical, destructive loading tests</li><li>• An ultrasonic NDE technique for evaluating the consolidation of MMCs and CMCs</li><li>• An ultrasonic NDE technique for characterizing the matrix microstructure and morphology in titanium-matrix composites</li></ul>

Many of these efforts were cooperative ventures with scientists in the Nondestructive Evaluation, Materials Behavior, Materials Development and Structural Materials branches of the Wright Laboratories Materials Directorate.

SUMMARY OF NDE APPLICATION ACCOMPLISHMENTS
<ul style="list-style-type: none"><li>• Use of software gates within the entry-surface echo to generate C-scan images of near-entry-surface anomalies</li><li>• Application of an entry-surface-echo removal algorithm for improving time-of-flight C-scan images of near-entry-surface anomalies</li><li>• Modification of an entry-surface-echo removal algorithm for application to sparsely sampled, depot-collected ultrasonic B-scan data</li><li>• Digital filtering for improving lateral resolution in C-scan images</li><li>• Two-dimensional Fourier-domain zero padding for producing high-quality enlargements of small, sparsely sampled depot-type C-scan data sets</li></ul>

***The NDE Applications Efforts*** resulted in the use of Air Force developed digital signal- and image-processing techniques to fulfill in-field and depot inspection facilities' needs. The applications efforts are briefly outlined in Exhibit 1-2, "NDE Applications Efforts". Those efforts were undertaken in cooperation with SM-

ALC/TIELD, McClellan AFB; OO-ALC, Hill AFB, UT; and WL/Flight Dynamics Directorate, WPAFB, OH.

In addition to the developmental and applications efforts, a Hlgh Precision Scanning Acoustic Microscope (HIPSAM) system was designed and constructed for use with the NDE technique development efforts. This system is used for ultrasonic immersion scans with transducer frequencies up to 100 MHz.

The software algorithms, BTOC and REFSUB, were modified to improve the possibilities for their transition to Air Force ALCs. These modifications consisted of:

- *Upgrading the B-scan to C-scan (BTOC) conversion software to run on X Window terminals*
- *Upgrading the entry-surface-echo-removal algorithm, REFSUB, to run on X Window terminals*

## **Section 2**

### ***Executive Summary***

---

The **NDE technique development efforts** have produced novel ultrasonic methods, and signal- and image-processing techniques for characterizing metal-matrix and ceramic-matrix composite materials. The **NDE applications efforts** have demonstrated the applicability of previously developed ultrasonic techniques as well as previously developed signal- and image-processing techniques to existing NDE needs of Air Force ALCs. Brief summaries of the results of both efforts are provided in the following paragraphs.

#### **DEVELOPMENT OF NDE TECHNIQUES FOR CHARACTERIZATION OF FIBER-REINFORCED COMPOSITES**

New ultrasonic NDE techniques have been developed which can be used for characterization and evaluation of micro-properties of the fiber-matrix interface in metal-matrix and ceramic-matrix composites. Significant improvements in the reliability of interface-characterization results can be obtained when these NDE techniques are used in conjunction with the "more traditional" destructive tests, e.g., fiber push-in, push-out, pull-out, fiber fragmentation, etc.

##### **A Nondestructive Methodology for Measuring the Interface Shear-Stress Transfer Properties**

Research efforts in this area resulted in a novel methodology for measuring the **effective shear-stiffness coefficient** of the fiber-matrix interface in MMCs and CMCs. This is a necessary, but previously unmeasurable input parameter for composite fracture-behavior models. The methodology combines a rigorous model of the fiber-matrix interface elastic properties with the results of experimental ultrasonic measurements to determine the value of the effective shear-stiffness coefficient. This methodology accounts for shear-stress transfer at the fiber-matrix interface due to: (1) **elastic** properties (resulting from chemical bonding) of the interphase region, and (2) **dynamic** properties resulting from mechanical bonding which is caused by the existence of radial residual stresses at the interface. A preliminary method for accommodating changes in the dynamic component of the effective shear-stiffness coefficient caused by changes in radial residual stresses was developed; this method is valid for CMCs only.

##### **Ultrasonic NDE Techniques for Improving the Results of Destructive Mechanical Tests**

*Fiber-Fragmentation Testing* -- An ultrasonic, shear-wave back-reflection (SBR) technique (shear waves which were back-reflected from the fiber-matrix interface) was used to improve the reliability of mechanical fiber-fragmentation test results. SBR imaging used after

mechanical loading improved the reliability of fiber-length measurements, whereas *in situ* SBR imaging techniques improved the ability to resolve multiple breaks in the fiber. The development and use of neural-network techniques improved the detectability of secondary fractures adjacent to primary fractures. Use of these techniques improved the reliability of calculations of shear-stress transfer across the fiber-matrix interface, and improved the understanding of how loads are transferred during progressive loading of samples.

*Fiber Push-Out Testing of CMCs* -- A technique which combined the results from ultrasonic longitudinal-wave imaging and ultrasonic SBR imaging was developed and used to screen CMC samples prior to fiber push-out tests. C-scan images generated from longitudinal waves were used to assess the overall integrity of the composites and to verify the effectiveness of the consolidation and densification of the composites. SBR C-scan images of the fiber-matrix interfaces were used to verify the integrity of the interfaces. Use of this combined-imaging technique to screen the CMC samples prior to application of the fiber push-out tests significantly reduced the scatter in the push-out test results.

*Transverse-Loading Tests of MMCs* -- An *in situ* SBR technique was developed for imaging the fiber-matrix interface region during mechanical transverse-loading tests of MMCs. This technique was found to be sensitive to fracture and deformation of the interface, and to the amount and sign of the residual stresses at the interface. The technique provided information about the propagation of damage and about the role of the redistribution of residual stresses in the interface damage behavior. Results from this study demonstrated that an MMC sample having a single embedded fiber with exposed ends will have pre-existing (pre-loading) interfacial cracks which are a few microns in length at the exposed ends. During the effort it was demonstrated that the technique can provide precise information about the time of fracture initiation of the fiber-matrix interface, and thereby the applied load at the time of fracture initiation. Precise knowledge of the applied load at the time of fracture initiation of the fiber-matrix interface can significantly improve the calculation of the *minimum-stress-at-fracture* (MSF) of the interface. That MSF is an important input parameter for the composite fracture-behavior models.

#### Ultrasound for Post-Processing NDE of Fiber-Reinforced Metal Matrix and Ceramic Matrix

*Evaluation of Consolidation in Metal Matrix and Ceramic Matrix Composites* -- A methodology was developed which combined the results obtained from longitudinal ultrasonic waves and back-reflected shear waves. This methodology allows the user to nondestructively evaluate the lack-of-consolidation in MMCs and CMCs. In addition, the technique can be used to evaluate the improvements in matrix consolidation which accrue from reprocessing the material.

*Characterization of Matrix Microstructure and Morphology in Titanium Matrix Composites*

-- A nondestructive ultrasonic technique was developed for characterizing the matrix microstructure and morphology in titanium matrix composites. The technique relies on the concurrent use of back-reflected shear waves and normal-incidence, high-frequency longitudinal waves. Use of this technique can improve the reliability of nondestructive detection of coarse plate-like alpha plus beta microstructure in these composites.

## NDE APPLICATIONS EFFORTS

### Digital Techniques for Ultrasonic Imaging of Near-Entry-Surface Anomalies in Highly Attenuative Materials

Software-gating techniques were successfully applied to three-dimensional ultrasonic RF B-scan data to image near-entry-surface anomalies in a section of a kevlar-polyester radome. C-scan images generated by the software-gating techniques clearly imaged the anomalies. Digital filtering of that three-dimensional ultrasonic data set prior to use of the software gates resulted in significant lateral-resolution improvement in the C-scan images. Application of the entry-surface-echo-removal algorithm, REFSUB, to that three-dimensional ultrasonic data set significantly improved the visual detectability of near-entry-surface anomalies in the B-scan images.

### Time-of-Flight (TOF) C-Scan Imaging of Near-Entry-Surface Anomalies

The entry-surface-echo-removal algorithm, REFSUB, was used as a preprocessor for three-dimensional ultrasonic RF B-scan data prior to generating time-of-flight (TOF) C-scan images from that data. The data were acquired from graphite-epoxy composite samples with impact-induced delamination damage. The samples were provided by Mr. Gregory Czarnecki of the WL/Flight Dynamics Directorate. Use of REFSUB as a preprocessor significantly improved the ability to image near-entry-surface delamination damage in TOF C-scan data.

### High-Quality C-Scan Image Enlargements from Depot and In-Field-Collected Small Data Sets

One- and two-dimensional Fourier-domain zero-padding algorithms were developed and applied to enlarge very small data sets of the type usually collected during in-field inspections. Application of the technique resulted in very accurate and precise enlargements of ultrasonic B-scan and C-scan images.

### High-Precision Scanning Acoustic Microscope System (HIPSAM)

A high-precision, immersion scanning acoustic microscopy system was designed, developed, and tested for the MLLP (NDE) branch of the WL/Materials Directorate. The system includes a high-speed digitizer ( $\leq 2$  gigasamples/second) and can use transducers at frequencies up to 100 MHz. The minimum step size (distance between data-collection points) of the system is 0.001 mm in the X, Y, and Z directions. The system is controlled by a 486-

based PC using UDRI-developed software running under LabWindows (a Registered Trademark of National Instruments Corporation, Austin TX) development software.

#### **Application of an Entry-Surface-Echo-Removal Algorithm to Anomaly Detection in Depot-Type Data**

The entry-surface-echo-removal algorithm, REFSUB, was modified for application to depot-acquired data which is usually digitized at a very low sampling rate. This modified version of REFSUB provided excellent results when applied to depot-type (sparsely sampled) ultrasonic RF B-scan data. The results achieved with the newly modified version of REFSUB were significantly superior to those achieved with the original version of REFSUB.

#### **Split Spectrum Processing of Ultrasonic Signals Improves Detection and Sizing of Material Anomalies**

The application of Split Spectrum Processing (SSP) to ultrasonic signals has been shown to yield a considerable improvement in the signal-to-noise ratio of those signals. During the course of this contract preprocessing of ultrasonic signals via SSP was found to be of significant benefit for: (1) *in situ* early detection of fatigue microcracks during mechanical testing, (2) *in situ* fatigue-microcrack sizing and growth monitoring during mechanical testing, (3) reliable detection of hard alpha inclusions in titanium disks, and (4) improving the reliability of Artificial Neural Network classifications of ultrasonic signals from anomalous and anomaly-free regions of materials.

#### **Leaky Lamb Wave Inspection Techniques for Detecting Damage in Composite Structures**

The feasibility of using leaky Lamb waves for imaging impact-induced delamination damage in graphite-epoxy composites was demonstrated. The capabilities, limitations and applicability of the swept-frequency, tone-burst Lamb wave generation technique followed by median-frequency signal processing for encoding the delamination depth in the C-scan image data were determined during the course of this study. This study has been completed.

#### **B-Scan to C-Scan Conversion Software Upgrade**

The B-scan TO C-scan (BTOC) software algorithm which generates C-scan image data from previously-digitized-and-stored three-dimensional B-scan data was upgraded during the course of this contract. The upgrades were made to: (1) achieve portability to many types of computers and operating systems thereby improving technology transition opportunities; (2) utilize the X Window System which has emerged as the dominant graphical interface system that is supported on a broad range of the workstation-class computers; and (3) implement the BTOC software, which employs advanced software gating techniques, on fast workstation-class computers. The upgraded version is now operating on X Window terminals in the MLLP (NDE) branch of the WL/Materials Directorate.

## **Section 3**

### ***Development of NDE Techniques for Characterization of Fiber-Reinforced Composites***

---

Research efforts described in this section have resulted in the development of unique ultrasonic **nondestructive** methods for improving the characterization of metal-matrix and ceramic-matrix composites in general, and for improving the characterization of the interphase/interface region between the fiber and the matrix in particular. The high temperatures and pressures that are typically used during processing of fiber-reinforced composites causes a chemical reaction between the matrix and the fiber which produces this thin "interphase zone"; this interphase zone generally has mechanical properties which are different from those of the two original constituents [Metcalfe, 1974]. The properties of fiber-reinforced composites are dominated and determined by the properties and mechanical behavior of the fiber-matrix interphase region [Evans et al., 1991; and, Clyne and Watson, 1991], and it is through the interphase region that the load is transferred from the matrix to the fiber, and that the toughness of the composite is determined [Evans et al., 1991; and Park et al., 1989]. Therefore, accurate and precise characterization of the interphase/interface region is very important for characterization of fiber-reinforced composite properties.

The first of the nondestructive methods -- described in subsection 3.1, "A Nondestructive Methodology for Measuring the Interface Shear-Stress Transfer Properties" -- allows the user to determine the value of the **effective shear-stiffness coefficient** of the fiber-matrix interface. This is a very valuable input parameter for composite fracture-behavior modelers, but its value could not be determined prior to the development of the methodology described in subsection 3.1.

Several indirect, destructive techniques [Karpur et al., 1992; Krishnamurthy et al.; Waterburry et al., 1994; and Kerans and Parthasarathy, 1991] such as fiber push-in, fiber push-out, fiber pull-out, fiber fragmentation, and transverse loading were developed in the past to characterize the fiber-matrix interface. Methods described in subsection 3.2, "Ultrasonic NDE Techniques for Improving the Results of Destructive Mechanical Tests", complement and improve the results of those "indirect" destructive mechanical techniques. Use of those ultrasonic nondestructive methods provided: (1) more accurate and precise fiber-fragmentation test results (primarily by *in situ* ultrasonic imaging), (2) increased reliability of fiber push-out test results through pre-test screening and (3) improved detection of fiber-matrix fracture-initiation by *in situ* ultrasonic imaging during transverse loading tests of MMCs.

### 3.1 A Nondestructive Methodology for Measuring the Shear-Stiffness Coefficient of the Fiber-Matrix Interface

This subsection of the report describes the development of a nondestructive methodology for measuring the shear stiffness of the fiber-matrix interface in a fiber-reinforced composite material. The shear stiffness of the fiber-matrix interface is an important input parameter for composite fracture-behavior models, but it has been impossible, until now, to measure its value. In brief, the methodology consists of: (1) a rigorous mathematical model of the **elastic** shear-stress transfer across the fiber-matrix interface which defines the relationship between the elastic shear-stiffness coefficient and the reflection coefficient of a shear wave which is back-reflected from the fiber-matrix interface, and (2) an ultrasonic NDE technique for measuring the reflection coefficient of an ultrasonic, shear wave which is back-reflected from the fiber-matrix interface.

Although the model considers only the elastic mechanism (component) of shear-stress transfer at the interface, there is also a mechanical (dynamic) component. The ultrasonic reflection coefficient referred to above is sensitive to the dynamic component as well as the elastic component. Thus, the NDE methodology which is developed in this subsection of the report actually measures the **effective** shear-stiffness coefficient which is a combination of two coefficients, an elastic shear-stiffness coefficient and a dynamic coefficient. These coefficients are measures of the two components of shear-stress transfer at the fiber-matrix interface. The elastic shear stiffness coefficient is a static parameter and depends on the properties of the interphase (chemically bonded) region between the matrix and the fiber. It is the ratio of the *shear modulus of the fiber-matrix interface* and the *thickness of the fiber-matrix interphase region*. The **dynamic** coefficient accounts for stress transfer due to mechanical bonding at the interface. The mechanical bonding results from a combination of radial residual stresses and surface roughness at the interface. The magnitude of the stress transfer due to this dynamic component changes with temperature because the radial residual stresses at the interface change with temperature.

An experiment was designed and conducted to demonstrate the reflection coefficient's and, therefore, the NDE methodology's sensitivity to changes in the **dynamic** component of the effective shear-stiffness coefficient, i.e., to changes in the radial residual stresses. The results of the experiment, **conducted on CMCs only**, demonstrated the sensitivity of the reflection coefficient to changes in the dynamic component of the effective shear-stiffness coefficient. These results suggest a possible method for determining values of the elastic shear-stiffness coefficient from experimentally measured values of the effective shear-stiffness coefficient.

NOTES TO THE READER
Components of the
Effective Shear-Stiffness Coefficient
1. <i>Elastic</i> -- due to the chemical bond between the fiber and the matrix
2. <i>Dynamic</i> -- due to mechanical bonding at the fiber-matrix interface caused by:
- Mechanical roughness at the interface
- Normal forces from <u>radial residual stresses</u> at the interface

A guide to Subsection 3.1 is provided in Exhibit 3-1.

<b>SUMMARY OF SECTION 3.1</b>	
<b>A Nondestructive Methodology for Measuring the Interface Shear-Stress Transfer Properties</b>	
<b>OBJECTIVE:</b> Develop a nondestructive methodology for measuring the <b>effective shear-stiffness coefficient</b> of the fiber-matrix interface. The methodology must be sensitive to the <b>elastic</b> and <b>dynamic</b> components of this effective coefficient	
<b>JUSTIFICATION:</b> The effective shear-stiffness coefficient is an important, but previously unmeasurable input parameter for composite fracture-behavior models	
<b>RESULTS</b>	
3.1.1&2	Developed a mathematical model relating the elastic shear-stiffness coefficient of the fiber-matrix interface, and the reflection coefficient of an ultrasonic shear wave which is back-reflected from the fiber-matrix interface <ul style="list-style-type: none"><li>* <b>Importance</b> -- provided a theoretical basis for determining the <b>elastic</b> component of the stress transfer at the fiber-matrix interface if the <b>dynamic</b> component is zero</li></ul>
3.1.3	Developed an ultrasonic NDE technique for measuring the <u>reflection coefficient</u> of an ultrasonic shear wave which is back-reflected from the fiber-matrix interface <ul style="list-style-type: none"><li>* <b>Importance</b> -- provided experimental technique for determining the effective shear-stiffness coefficient of the fiber-matrix interface</li></ul>
3.1.4	Designed and conducted an experiment which demonstrated the sensitivity of the <u>reflection coefficient</u> of shear waves which are back-reflected from the fiber-matrix interface to changes in radial residual stresses in CMCs <ul style="list-style-type: none"><li>* <b>Importance</b> -- demonstrated the sensitivity of the reflection coefficient to changes in radial residual stresses, i.e., the <b>dynamic</b> component of the effective shear-stiffness coefficient</li></ul>

### **3.1.1 Concepts: Modeling the Interface/Interphase Between Fiber and Matrix**

In this study, a novel approach to nondestructively evaluate the elastic load transfer behavior between the matrix and the fiber is provided by defining a quantifiable parameter to describe the 'elastic behavior' of the interface. The interphase region is modeled here by an 'equivalent elastic interface' which has a specific 'elastic behavior'. The 'equivalent elastic interface' is a boundary between the matrix and the fiber that takes into account the elastic properties of the interphase region and has a precise elastic behavior which is pictorially represented in Figures 3-1a and 3-1b. Figure 3-1a shows the interphase region between the matrix and the fiber. The gradation of gray scale in the interphase region has been drawn to represent the possibilities of either multiple interphase layers or an interphase region of variable properties through thickness. In Figure 3-1b, the interphase region has been condensed to represent the 'equivalent elastic interface' which, because of its elastic properties (shear modulus and the local thickness) can elastically deform without fracture. The replacement of the interphase region by an equivalent elastic interface eliminates the need for the treatment of the interphase region as a third layer sandwiched between the matrix and the fiber. As a result,

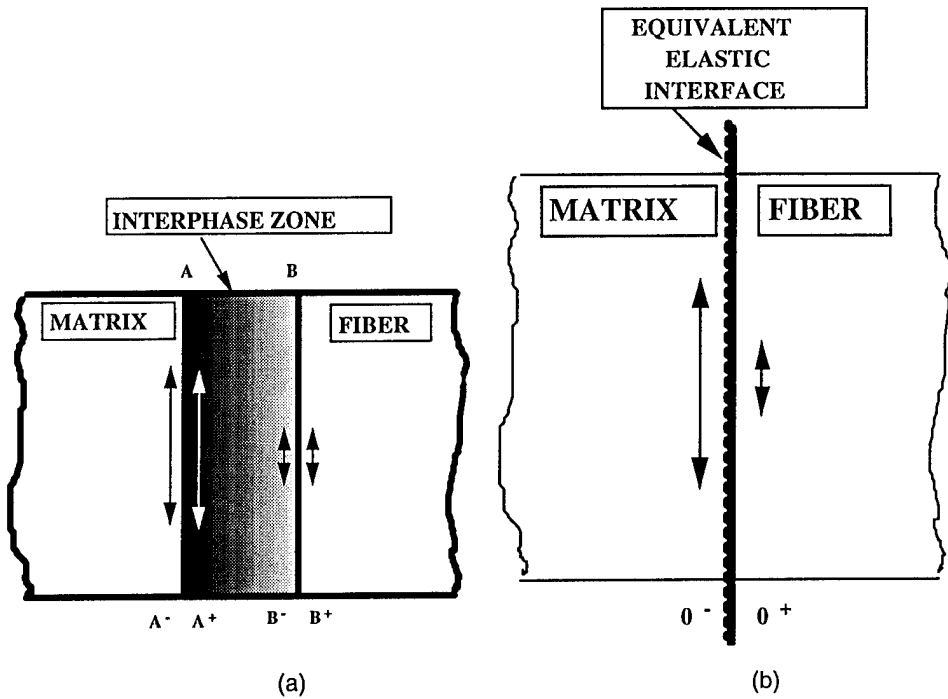


Figure 3-1. (a) Schematic of the interphase region between the matrix and the fiber. (b) Schematic showing the 'equivalent elastic interface' between the matrix and the fiber materials.

the properties such as the density, modulus and the thickness of the interphase zone need not be known for the analysis. The preceding discussion assumes that the interphase region is homogeneous and made from a single material. However, in reality, the interphase region is likely to be either made-up of several sublayers of different compositions or comprised of a layer with gradually varying properties [Baumann et al., 1990; Rhodes, 1992 and Cooper & Chyung, 1987] as represented in Figure 3-2 wherein the absence of clear boundaries

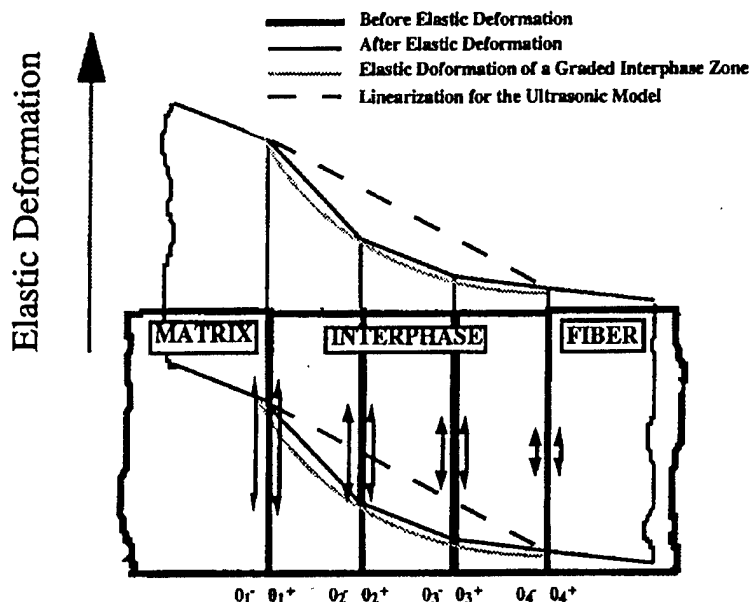


Figure 3-2. Schematic of a layered interface.

(interfaces) for the matrix-interphase and interphase-fiber combinations is represented. Such an interphase region is evident in both metal matrix composites and ceramic matrix composites [Luh & Evans, 1987]. In this study, the case of an intermittent interface [Margetan et al., 1992] is not considered. However, good consolidation is assumed which is a realistic approach for a functional composite. Also, it is feasible to assure proper consolidation by using a novel ultrasonic nondestructive technique [Krishnamurthy et al., 1993 and Matikas et al., 1992], developed for the evaluation of the degree of consolidation in composites.

Ultrasonic stress waves as used in nondestructive evaluation produce extremely small elastic displacement amplitudes of a fraction of an Angstrom (for example, in steel using 25 MHz shear waves, 0.01 nm of displacement corresponds to a strain of about  $10^{-7}$ ). Since ultrasonic waves produce strains within the elastic range of materials, it is feasible to study the properties of the fiber-matrix interphase region (that is modeled by the equivalent elastic interface) using elastic ultrasonic waves. This methodology does not provide a measurement of the strength of the interfacial bonding. The proposed approach would complement, while deviating from, the present methodology of indirect evaluation of the interface behavior and deterioration [Wright et al., 1990; Karpur et al., 1993; Blatt et al., 1993 and Russ et al., 1991], through experimental procedures such as monitoring of crack initiation and propagation [Marshall & Evans, 1985 and McCartney, 1987] and analysis of micro-mechanical stresses [Pagano, 1991 and McCartney, 1990].

The interphase zone, by virtue of its elastic behavior in response to the small amplitude ultrasonic waves, acts as a coupling between the matrix and the fiber. The ultrasonic stresses incident on the interphase can be generally of two modalities: compressive waves and shear waves. The interphase behaves differently to the two incident modes of ultrasonic waves. When the compressional waves are incident from the matrix to the fiber through the interphase, the stresses and displacements are transmitted as if a compressional spring exists (Figure 3-3a) in place of the interphase. On the other hand, when elastic (ultrasonic) shear waves are incident from the matrix to the fiber through the interphase region, the interphase acts like a shear spring as shown in Figure 3-3b.

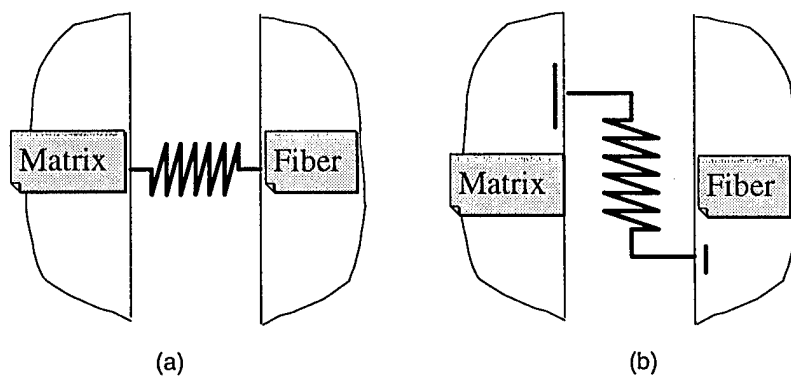


Figure 3-3. (a) Compressional spring model of the interfacial behavior for incident longitudinal waves. (b) Shear spring model of the interfacial behavior for incident transversely polarized shear waves.

### **3.1.2 Ultrasonic Wave Propagation Model**

In this section a newly developed analytical model is presented for the microscopic evaluation of the elastic properties of the fiber-matrix interface. This model is necessary for the selection of various experimental parameters such as the frequency of ultrasound and angle of incidence and provides the relationship which is necessary to interpret the future experimental results. The theoretical model considers the reflection of an ultrasonic wave front from a single fiber embedded in a homogeneous isotropic matrix. Although the analysis of the ultrasonic technique is developed for a monofilament composite, the method is equally applicable to study the fiber-matrix interface in the outermost layers of a real, multifiber composite system. The ultrasonic characterization of the interface is achieved by the analysis of the back-reflected signal [Karpur et al., 1992] from the fiber-matrix interface.

#### **3.1.2.1 Analysis**

Let us consider a plane elastic wave  $\exp[i(\omega t + k_1 z_i)]$  propagating in the positive direction  $z_i$ , and obliquely incident at an angle  $\theta$  on a model composite immersed in water, made with a cylindrical isotropic and homogeneous fiber embedded in a ceramic matrix. Here  $k_1$  is the wave number in the fluid, where  $\omega$  is the angular frequency and  $c_1$  is the sound speed in the fluid medium.

For the development of the theoretical model, the composite is simulated by an infinitely extended plate consisting of an isotropic matrix with an embedded cylindrical isotropic and homogeneous fiber (which is justified at the wavelength of interest - frequency < 50MHz). Further, since the ultrasonic beam is assumed to be incident on the composite such that the refracted wave is always normal to the fiber circumference (shear wave back-reflection technique - SBR [Matikas & Karpur, 1993 (25)]), without the loss of the generality, the cylindrical fiber can be replaced with an infinitely extended homogeneous isotropic layer of thickness equal to the diameter of the fiber (shown in dotted lines in Figure 3-4). Although it is relatively easy to model the fiber as a cylinder [Matikas & Karpur] and use the Bessel function response of the cylinder, the present formulation of a plate will not deviate substantially from the reflected amplitude at the center of the main lobe of the Bessel function (the center of the main lobe of the Bessel function is the only point of interest for this study because the ultrasonic beam is normally incident to the circumference of the cylindrical fiber). Effects of attenuation and diffraction [Matikas & Karpur] can also be considered in the model if the matrix propagation path and the fiber thickness are significant. However, since the matrix path is relatively thin (approximately five times the wavelength) for this application, the effect of attenuation and diffraction are omitted.

As the acoustic wave is incident on the composite, a part of the energy will be reflected into the fluid and another part of the energy will be transmitted into the matrix. Two types of

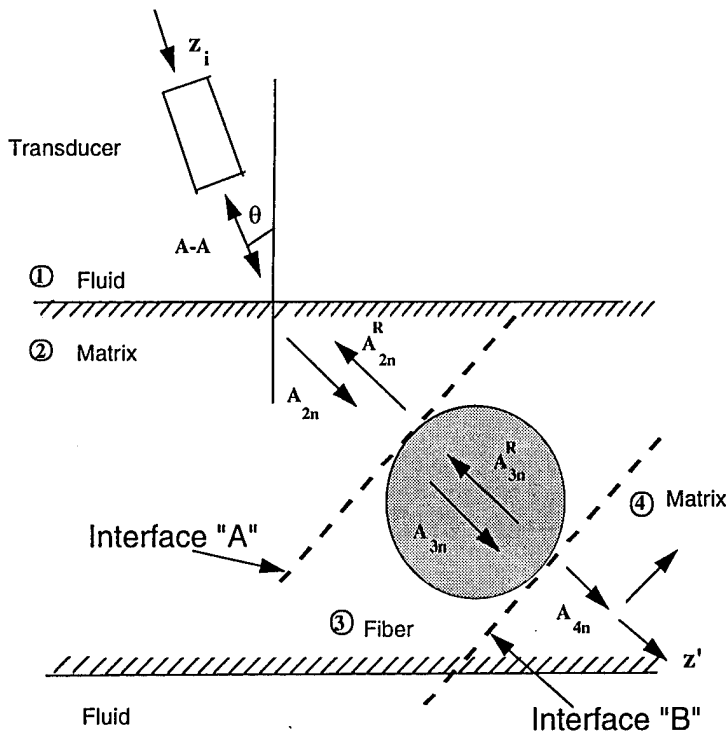


Figure 3-4. Geometry of the problem.

waves can be propagated in the matrix material: (i) a refracted longitudinal wave with transmission coefficient,  $T_L$ , given by Equation 3-3, and propagation angle,  $\theta_{2L}$ , defined by the Snell's law; and (ii) a mode-converted shear wave with transmission coefficient,  $T_S$ , given by Equation 3-4, and propagation angle,  $\theta_{2S}$ , from Snell's law. Now consider an acoustic wave (either longitudinal or shear) of displacement amplitude  $A_{2n}$  propagating in the positive direction of the  $z'$  axis and normally incident on the matrix-fiber interface (see Figure 3-4). The fiber is denoted by medium 3, and the upper and lower regions of the matrix are denoted by medium 2 and medium 4, respectively. The two interfaces between the matrix and the plate representing the fiber are normal to the  $z'$  axis with the 'upper' interface located on the plane  $z'=d_n$  (interface A) and the 'lower' interface on the plane  $z'=d_n+d'$  (interface B). In medium 2, for a given mode of wave propagation, two wave fronts are propagating: one incident ( $A_{2n}$ ) on the interface A and one reflected ( $A_{2n}^R$ ) from that interface. Also, in medium 3 two wave fronts are propagating: one incident ( $A_{3n}$ ) on the interface B and one reflected ( $A_{3n}^R$ ) from that interface. In medium 4, only one wave (the transmitted wave of amplitude  $A_{4n}$ ) is considered because of the configuration shown in Figure 3-4 (i.e., no back-reflection due to the angle of incidence at the lower interface between the matrix and the fluid). Therefore, medium 4 is equivalent to a semi-infinite medium.

#### *The interfacial conditions between the matrix and the fiber.*

The interface between the matrix and the fiber is modeled by: (a) assuming continuity of normal and shear stresses and normal displacements at the interface, and (b) by allowing

the discontinuity of shear displacements at the interface. It is assumed that the vibration is transmitted instantaneously from one medium to the other by weightless springs with an equivalent rigidity of  $N_n$  [GPa/ $\mu\text{m}$ ]. The interfacial stiffness coefficient,  $N_n$ , of the matrix-fiber boundaries (upper and lower) can be generally different around the circumference, due to the fabrication conditions or due to the use of different material for each matrix plate. Thus, consider two different coefficients  $N_n$  and  $\tilde{N}_n$ , one for each interface. Accordingly, the interface conditions are:

$$\begin{aligned} \{\sigma^P\} &= 0 & \{\sigma^T\} &= 0 & \{u^P\} &= 0 \\ \sigma^T &= N_n[u^T] \quad (\text{interface A}) & \text{or } \sigma^T &= \tilde{N}_n[u^T] \quad (\text{interface B}) \end{aligned} \quad (3-1)$$

where the superscripts P and T denote the normal and tangential displacements/stresses respectively; the square brackets denote the jump of a function across the interface, and the curly brackets denote the vectorial resultant of stresses at the interface. The linearity of Equation 3-1 is based on the assumption of small amplitudes of vibrations which is justified for ultrasonic applications wherein the amplitudes of displacements are around a few Angstroms. Although somewhat similar boundary conditions can be found in literature [Jones & Whittier, 1967], the boundary conditions introduced here are significant for the ultrasonic analysis because of the explicit treatment of the compressive and shear stresses as well as the slip condition of the shear spring even when contact exists.

#### *Final Expression*

The back-reflection from the fiber, represented by A-A in Figure 3-4, is the wave front of interest for this study. The back-reflection coefficients are given by Equation 3-2

$$R_n = T_n W_n T F_n \quad (3-2)$$

with n to be an index (subscript n is L in the case of a longitudinal refracted wave, and S in the case of a shear refracted wave).

where,

$$T_L = \frac{2}{M} \cos 2\theta_{2S} \quad (3-3)$$

$$T_S = -\frac{2}{M} \left( \frac{c_{2S}}{c_{2L}} \right)^2 \sin 2\theta_{2L} \quad (3-4)$$

with the abbreviation:

$$M = \left( \frac{c_{2S}}{c_{2L}} \right)^2 \sin 2\theta_{2L} \sin 2\theta_{2S} + \cos^2 2\theta_{2S} + \frac{\rho_1 c_1}{\rho_2 c_{2L}} \frac{\cos \theta_{2L}}{\cos \theta} \quad (3-5)$$

and the coefficient  $W_n$  is given by the simplified expression:

$$W_n = \frac{A_{2n}^R}{A_{2n}} = \frac{(X_n^2 - Y_n^2)(1 - e')}{(X_n^2 + Y_n^2)(1 - e') + 2X_n Y_n (1 + e')} \quad (3-6)$$

for the case infinitely rigid springs ( $N_n, \tilde{N}_n \rightarrow \infty$ ) that corresponds to perfect continuity of displacements across the interface (implies a mere contact for longitudinal waves and infinitely rigid interfaces for shear waves),

with

$$\begin{aligned} X_n &= Z_{2n} c_{2n} k_{2n} = 2\pi \rho_2 c_{2n} f \\ Y_n &= Z_{3n} c_{3n} k_{3n} = 2\pi \rho_3 c_{3n} f \\ e'_n &= \exp[i k_{3n} 2d'] \\ e_n &= \exp[i k_{2n} 2d_n] \\ d_n &= \frac{1}{2} \left( \frac{\tilde{d}}{\cos 2\theta_{2n}} - d' \right) \end{aligned} \quad (3-7)$$

where  $d_n$  is the distance through which the refracted waves travel in the matrix before incidence on the fiber,  $d_L \neq d_S$  for a given  $\theta$  because of the assumption that the reflection coefficient is always measured when the refracted wave is normal to the circumference of the fiber, and the numbers in the subscripts denote the medium with which the quantity is associated.

Finally, the transmission coefficients for a longitudinal or a shear ultrasonic wave of amplitude  $A_{2n}^R$  incident at the interface between media 2 and 1 are given by:

$$TF_L = \frac{2}{M} \frac{\rho_1 c_1}{\rho_2 c_{2L}} \frac{\cos \theta_{2L} \cos 2\theta_{2S}}{\cos \theta} \quad (3-8)$$

$$TF_S = \frac{2}{M} \frac{\rho_1 c_1}{\rho_2 c_{2L}} \frac{\cos \theta_{2L} \sin 2\theta_{2S}}{\cos \theta} \quad (3-9)$$

From Equation 3-2, the back-reflection coefficients are dependent on:

- the properties of the matrix (density,  $\rho_2$ , longitudinal,  $c_{2L}$ , and shear,  $c_{2S}$ , velocities)
- the properties of the fiber (density,  $\rho_3$ , longitudinal,  $c_{3L}$ , and shear,  $c_{3S}$ , velocities)
- the diameter of the fiber ( $d'$ )
- the angle of incidence ( $\theta$ )
- the frequency (f) of interrogation, and
- the interfacial stiffness coefficients ( $N_n, \tilde{N}_n$ )

The stiffness coefficient depends on the wave type because of the different mechanism of stress transfer for compressional or shear displacement waves as discussed in the following sections.

#### *Longitudinal wave back-reflection coefficient*

In this case, the direction of oscillation of the material particles is normal to the fiber surface. As a result, a mere contact can transmit the displacement and the normal stresses across the interface. Hence, this type of wave is not sensitive to various bonding conditions. As a result, the stiffness coefficient,  $N_L$ , can take only two values:  $N_L = 0$  (for longitudinal waves, complete unbond which implies physical separation of the matrix and the fiber with no contact) or  $N_L = \infty$  (for longitudinal waves, this implies all possibilities from a mere contact to a completely rigid bond).

#### *Shear wave back-reflection coefficient*

In this case, a mode converted shear wave propagating in the matrix will be incident normally to the fiber. Therefore, the direction of oscillation of the material particles will be tangential to the fiber surface. As a result, the interface is exposed to shear stresses which are sensitive to the interfacial bonding. Hence, in the case of a mere contact, no part of the tangential displacement will be transferred to the fiber from the matrix at the interface. On the other hand, when the matrix and the fiber are bonded at the interface, a part of the tangential displacement will be transferred to the fiber from the matrix. The magnitude of the transferred displacement will be proportional to the rigidity of bonding. As a result, there will be a tangential 'elastic' relative displacement at the interface which is proportional to the shear traction, and is characterized by the newly proposed positive coefficient  $N_S$ . The underlying assumptions and modeling in the final equation of the back-reflection coefficient for shear waves allow for intermediate bonding between  $N_S = 0$  and  $N_S = \infty$  representing different degrees of chemical/mechanical bonding. The existence of such a 'degree of chemical/mechanical bonding' has been shown in the literature [Karpur et al., 1992; Karpur et al., 1992; Karpur et al., 1992 and Matikas & Karpur, 1992]. The shear stress behavior of the interfaces is also affected by the existence of residual stresses due to the mismatch of the coefficient of thermal expansion [Karpur et al., 1992; Karpur et al., 1992 and Coker et al., 1991]. The compressive radial component of the residual stresses at the interface [Coker et al., 1991] facilitates the transfer of shear stresses across the interface at room temperature even in the absence of chemical bonding thereby providing a lower limit to the experimentally measured interfacial shear stiffness coefficient  $N_{Smin}$ . However, for this model, the existence of the residual stresses are ignored. The methodology for the estimation of the residual stresses and the related necessary modifications of the experimentally measured shear stiffness coefficient [Karpur et al., 1992; Karpur et al., 1992 and Karpur et al., 1994] are presented in detail in a following section. The properties and the reactivity of the two materials in contact provide an

upper limit to the interface stiffness coefficient  $N_{S\max}$ . Again, since the residual stresses are ignored for this theoretical modeling,  $N_{S\max}$  will be taken to be completely due to the existence of a perfect interface. However, the achieved interfacial shear stiffness coefficient,  $N_S$ , will be generally between  $N_{S\min}$  and  $N_{S\max}$  depending on the processing parameters and conditions such as temperature, pressure, surface preparation, etc.

Since the interphase might generally have variable properties along its thickness ( $h$ ), the shear modulus of the interphase zone ( $G$ ) and the shear stiffness coefficient ( $N_S$ ) are integrals over the thickness and represent statistical average values. The shear stiffness coefficient of the interface is a measure of the shear stress transmitted across the equivalent elastic interface per unit of elastic differential displacement. Elasticity analysis can easily show that the shear stiffness coefficient can also be defined as the ratio of shear modulus of the interphase material over the thickness of the interphase zone. This approach is valid if small values of interphase thickness and small interphase shear modulus compared to the matrix and the fiber are assumed. For appropriate ultrasonic frequencies of interrogation, a relationship between  $N_S$  and back-reflection coefficient can be established using the theoretical model.

### 3.1.2.2 Numerical Results - Discussion

The longitudinal waves are insensitive to the interfacial conditions as discussed above. Hence, all the results and discussions in the remaining part of this study will be for the shear wave interrogation of the interface. The back-reflection coefficient amplitude as a function of interfacial stiffness and frequency for a Ti-6Al-4V/SCS-6 composite (fiber diameter of 142  $\mu\text{m}$ ) is shown in Figure 3-5a. In the range of frequencies of 10-50 MHz two resonance peaks occur, one at 15 MHz and the other at 40 MHz. In between the two resonances, a dip is also evident. Figure 3-5b (isolevel contour map representation of Figure 3-5a) shows that the frequency at which the dip occurs, for a given stiffness coefficient, shifts up followed by a downshift as the stiffness increases from 0 (complete unbond) to 20 GPa/ $\mu\text{m}$  (almost a rigid bond). This shift is analogous to a behavior that would be produced by an apparent nonlinear variation in the effective diameter of the fiber. Additional discussions of this behavior are provided in a later section and also can be found in the literature [Evans et al., 1991 and Clyne & Watson, 1991]. Figures 3-5a and 3-5b also aid in the selection of an appropriate frequency for the experimental evaluation [Rhodes, 1992] of the matrix-fiber interfacial properties.

An appropriate ultrasonic frequency for the experimental interrogation is an important parameter necessary to improve the sensitivity of the technique. An estimation of the appropriate frequency of interrogation can be obtained from Figures 3-6a, 3-6b and 3-6c which are derived from Figures 3-5a and 3-5b. The curves shown in Figures 3-6a, 3-6b and 3-6c are cross sections of the back reflection coefficient surface (shown in Figure 3-5b by lines a-a, b-b and c-c, respectively) for frequencies of 16 MHz, 24 MHz and 29 MHz. If a near resonance frequency such as 16 MHz (Figure 3-6a) is selected for the experiments, the reflection

coefficient changes from 0.252 for a complete disbond to 0.105 for a completely rigid interface (7.6 dB). However, if the frequency of interrogation is such as 24 MHz (Figure 3-6b), the range of the reflection coefficient is 0.252-0.026 (19.7 dB). The increase in the sensitivity in Figure 3-6b compared to that of Figure 3-6a is obtained because the frequency of interrogation in Figure 3-6b is close to a resonance dip thereby exploiting the slope of the surface as it approaches the resonance dip. It is imperative that the frequency of interrogation should only approach the resonance dip from below because, otherwise, the reflection coefficient behavior at 29 MHz (Figure 3-6c) is not monotonic with respect to the interfacial stiffness coefficient, the same back reflected amplitude may correspond to various interfacial stiffness (as in line x-x in Figure 3-6c).

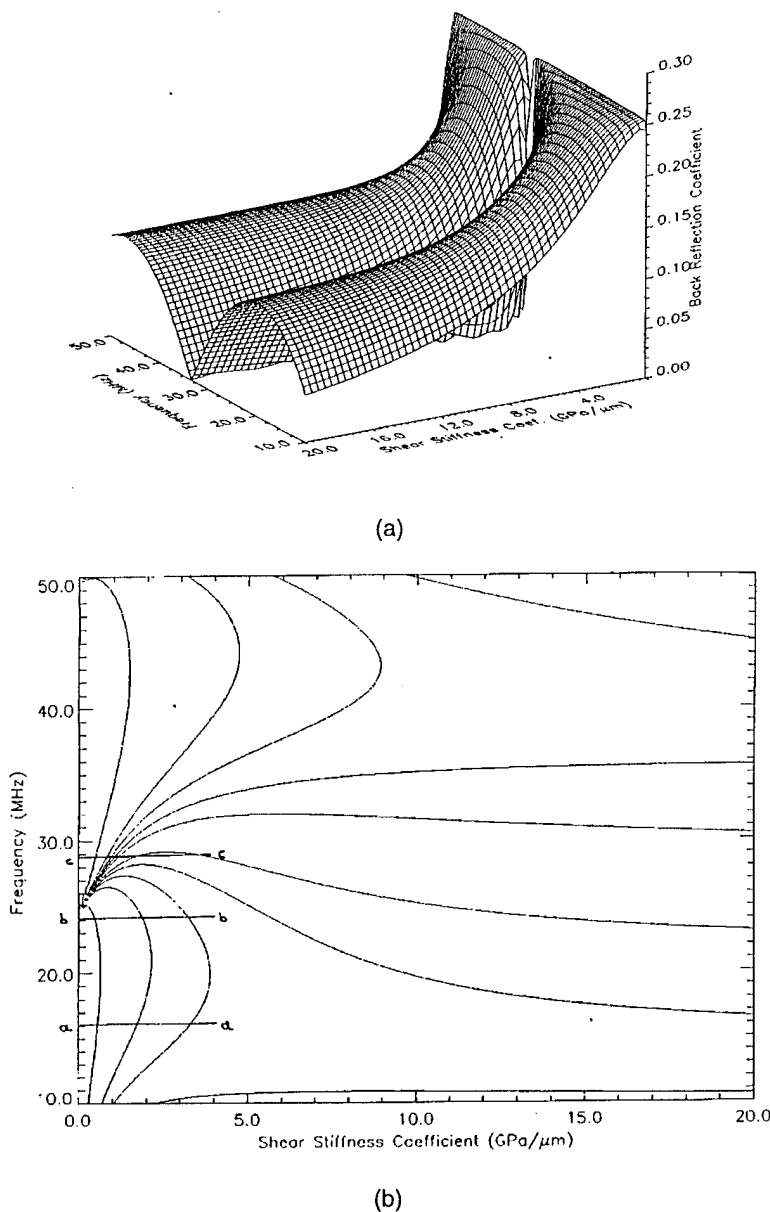


Figure 3-5. (a) Back-reflection coefficient amplitude as a function of interfacial shear stiffness coefficient and frequency. (b) Isolevel contour map representation of the data in Figure 3-5a.

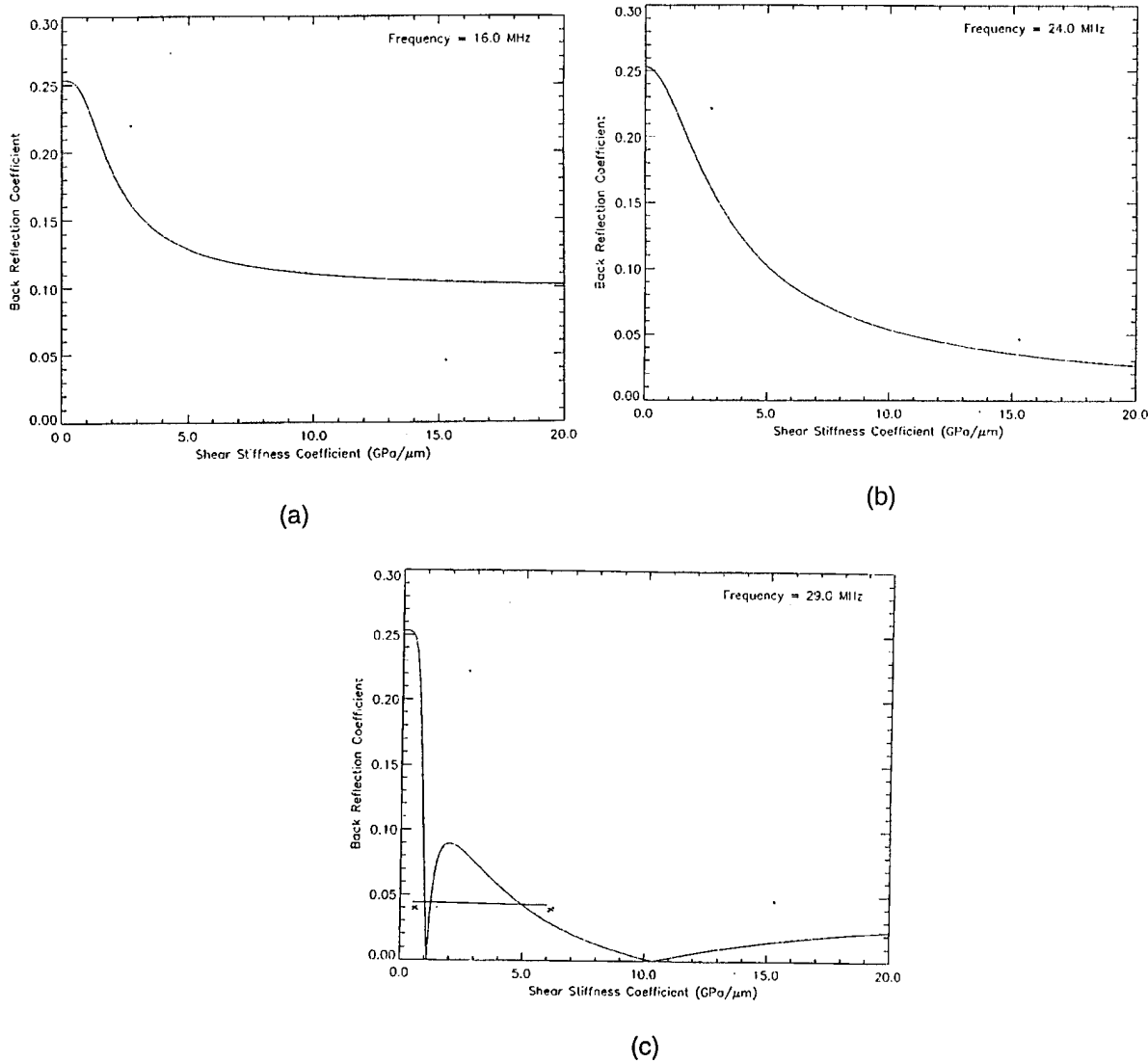


Figure 3-6. Back-reflection coefficient amplitude versus shear stiffness coefficient for a frequency which is: (a) near a resonance peak (16.0 MHz, line a-a in Fig. 3-5b), (b) slightly lower than the resonance dip (24.0 MHz, line b-b in Fig. 3-5b), and (c) slightly higher than the resonance dip (29.0 MHz, line c-c in Fig. 3-5b).

A further understanding of the behavior of the reflection coefficient as a function of the frequency of interrogation and the interfacial stiffness coefficient can be obtained by generating the back-reflection coefficient surface for a wider range of frequencies (1 - 150 MHz). Figure 3-7 shows the surface of the back reflection coefficient. Figures 3-8a-c are cross sections of the surface at three different interfacial stiffness coefficients (Figure 3-8a is from a completely rigid interfacial bond of 100.0 GPa/μm, Figure 3-8b is from an intermediate level of bonding of 10.0 GPa/μm, and Figure 3-8c is from a nearly disbonded interface of 2.0 GPa/μm). Figures 3-9a-c are derived by taking cross sections of the surface at three different resonant peak frequencies, 15 MHz, 66 MHz, 141 MHz, respectively.

Figure 3-7 demonstrates the overall nonlinear behavior of the reflection coefficient as a function of the frequency and stiffness coefficient. Figure 3-7a clearly indicates the position of the resonance dips. From Figure 3-7a, it is evident that the resonant dips run parallel to each other at higher stiffness coefficients. However, from Figure 3-7b it is evident that at lower ranges of the stiffness coefficient, the nonlinear shift of the resonance dips (such as discussed earlier for Figures 3-5a and 3-5b) shows a decreased sensitivity to the stiffness coefficient as the frequency of interrogation increases. This decreased sensitivity is evidenced due to the fact that the resonance dips at progressively higher frequencies show progressively less nonlinearity.

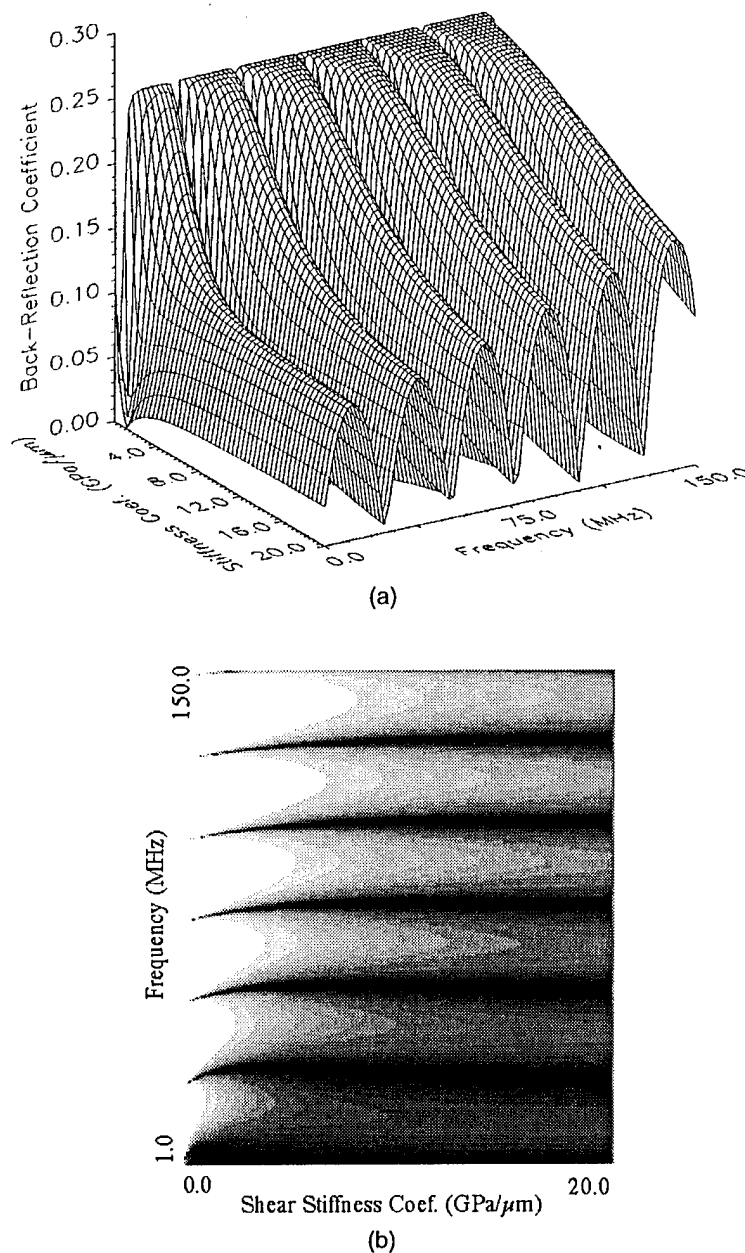


Figure 3-7 (a) Back-reflection amplitude as a function of interfacial shear stiffness and for a range of frequencies 1-150 MHz. (b) Isolevel projection of the data in 3-7a.

Figures 3-8a-c show the response of the interfaces with different stiffness coefficients when excited with different frequencies. When the bond has an almost infinite stiffness coefficient (for all practical purposes, 100 GPa/ $\mu$ m), the resonance curves (Figure 3-8a) obtained are the well known symmetric lobes with the resonance peaks of same amplitudes. However, as the stiffness coefficient of the bond progressively decreases, the obtained resonance lobes become progressively non-symmetric as shown Figures 3-8b and 3-8c wherein the amplitudes of resonance peaks are higher and higher as the frequency increases. Also, for a flexible bond, the resonance peaks at high frequencies are not any more sensitive to relatively small changes in frequency, thereby becoming plateaus (as shown in Figure 3-8c).

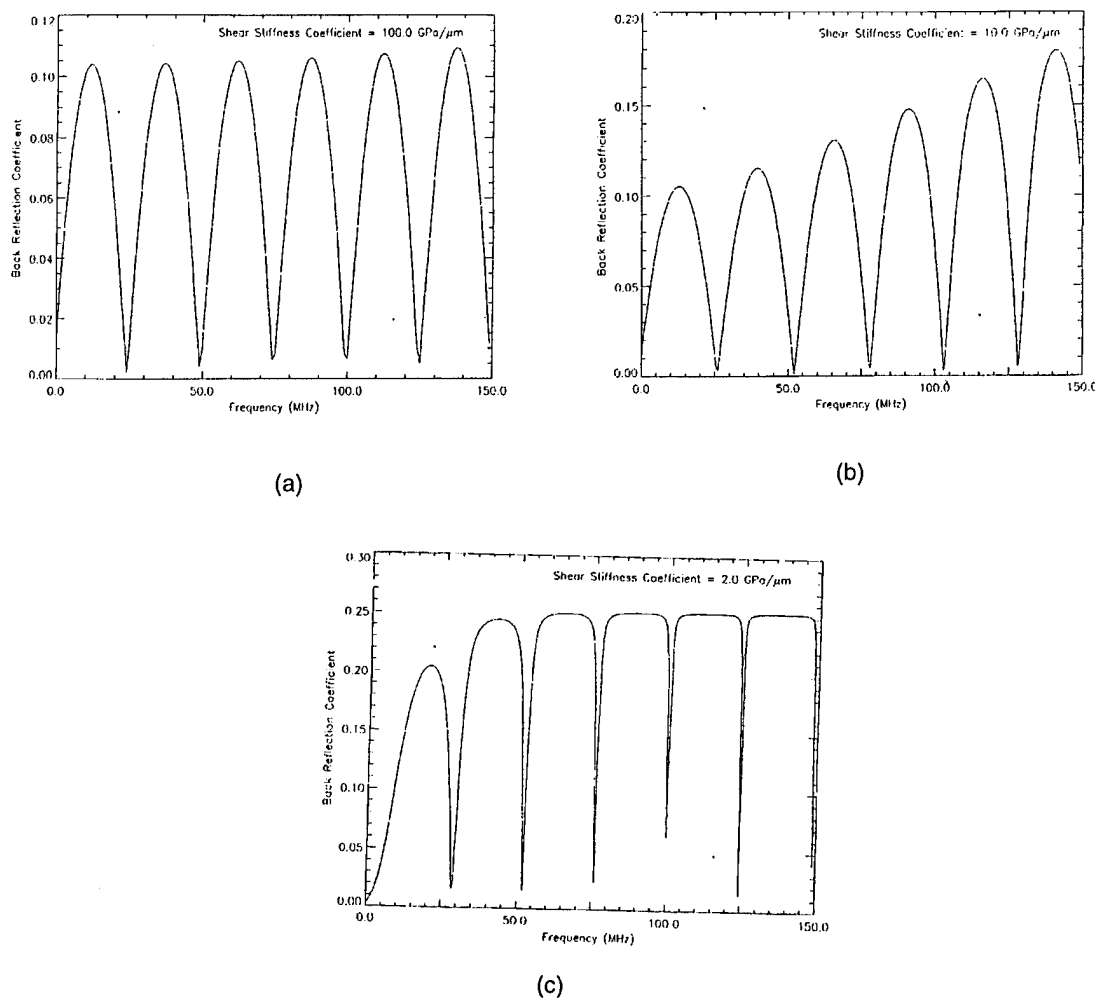


Figure 3-8. Back-reflection coefficient amplitude versus frequency for a fiber-matrix bond which is: (a) "infinitely" rigid (shear-stiffness coefficient=100.0 GPa/ $\mu$ m), (b) intermediate in rigidity (shear-stiffness coefficient=10.0 GPa/ $\mu$ m), and (c) flexible (shear-stiffness coefficient=2.0 GPa/ $\mu$ m).

The procedure demonstrated in Figures 3-6a-c is used to select the appropriate frequency of interrogation around a given resonant frequency. However, the appropriate resonant frequency around which experimental ultrasonic frequency should be selected can be determined from Figures 3-9a-c which show that longer wavelengths are effective for evaluating

the interfacial bonding due to their sensitivity to the changes in the stiffness of a relatively flexible bond (as indicated by the slope of the curve in Figure 3-9a). On the other hand, shorter wavelengths are ineffective for evaluating the interfacial stiffness due to their inability to sense small changes in the stiffness coefficient of a relatively flexible bond (as indicated by the slope of the curve in Figure 3-9c). Similar conclusions have been reported by Jones & Whittier (1967), wherein they used dispersion-determinant analysis for evaluating adhesive joints between two solid half-spaces.

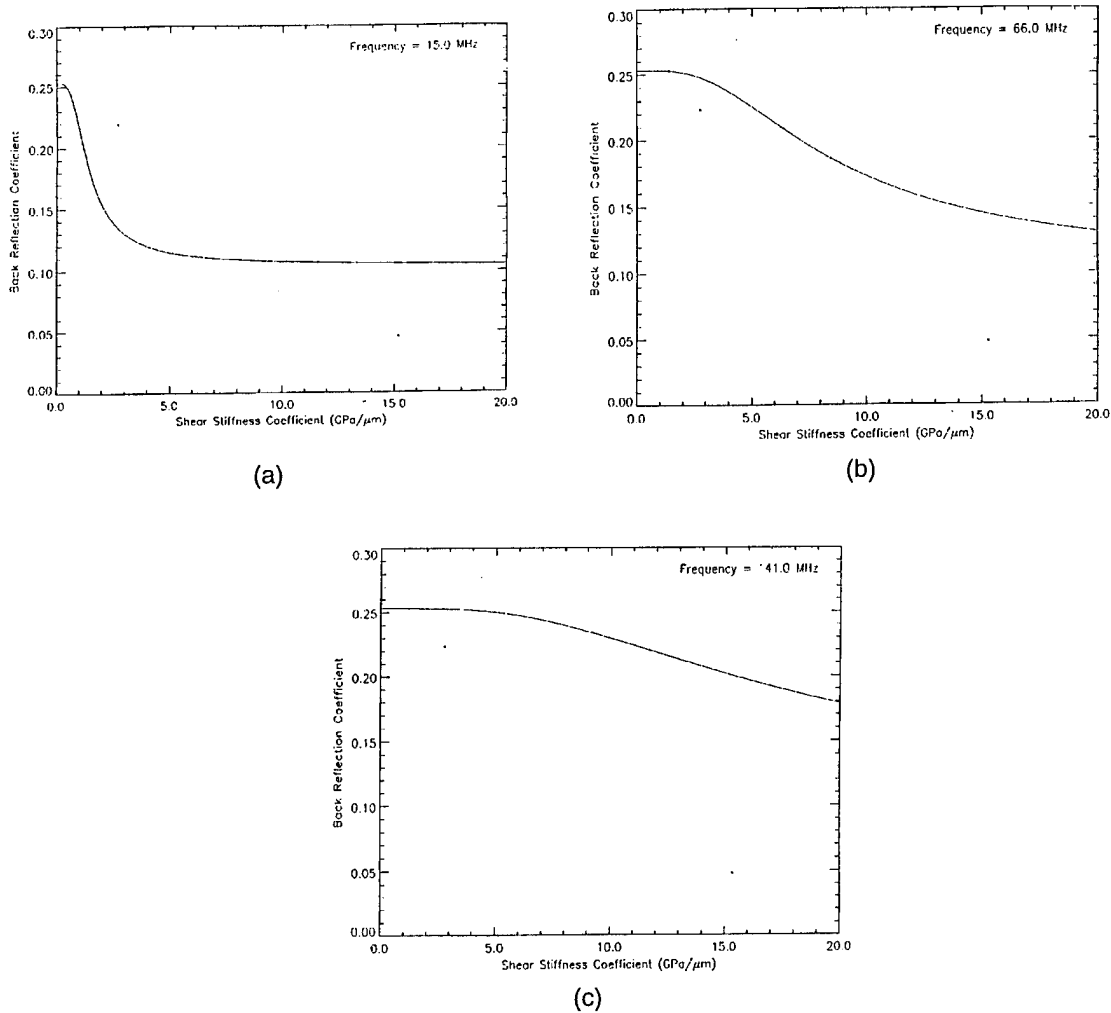


Figure 3-9. Resonant back-reflection coefficient amplitude vs. shear stiffness coefficient for a given frequency of (a) 15.0 MHz, (b) 66.0 MHz, (c) 141.0 MHz.

Figures 3-10a and 3-10b show the dependence of the back-reflection coefficient on the frequency and the angle of incidence for a given stiffness coefficient. Figure 3-10a is obtained for an infinitely rigid bond and shows symmetric resonance peaks for all angles of incidence. However, in Figure 3-10b, for a flexible bond, the resonance peak amplitudes are strongly dependent on the angle of incidence. Further, in Figure 3-10b, the resonance peaks show a plateau at higher frequencies compared to the smooth, rounded resonance lobes with a unique maximum amplitude at lower frequencies. Also, while the resonance dips (defined by

the ratio of the diameter of the fiber and the wavelength) remain equally spaced, the corners of the plateau progressively become sharper with the increase in the incident frequency. This means that higher frequencies begin to see this flexible bond as equivalent to a disbond implying that shorter wavelengths are less sensitive to the changes in stiffness coefficient of the bonding. Although the asymmetric behavior is enhanced at lower angles of incidence, it is evident at all angles of incidence. The important implication of Figures 3-10a and 3-10b is that, by using swept frequency the interface can be easily characterized as completely rigid or compliant by observing the symmetry of the profile (as shown in Figure 3-10a) or the asymmetry of the profile (as shown in Figure 3-10b).

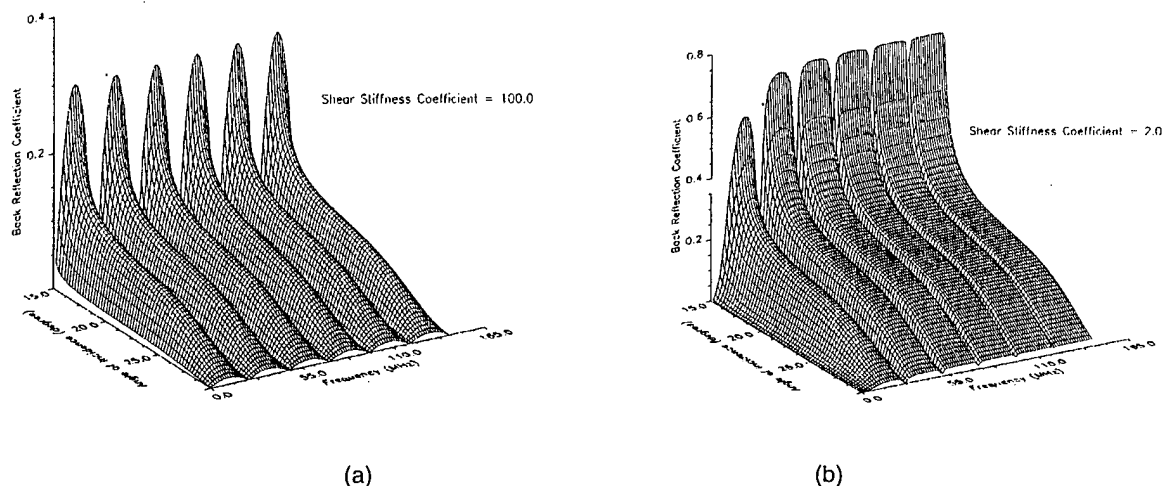


Figure 3-10. Back-reflection coefficient amplitude as a function of frequency and angle of incidence in the case of a bond which is: (a) "infinitely" rigid (shear-stiffness coefficient=100.0 GPa/ $\mu$ m), and (b) flexible (shear-stiffness coefficient=2.0 GPa/ $\mu$ m).

### 3.1.3 Experimental Procedure for Interface Elastic Property Measurement

The experimental procedure for the determination of the shear stiffness coefficient of the fiber/matrix interface consists of (a) measuring the shear wave back reflection coefficient of the interface and, (b) inverting the calculation of the shear stiffness coefficient by using the relationship between  $N_S$  and back-reflection coefficient established by using the theoretical model for an appropriate ultrasonic frequency of interrogation.

An experimental sample block was fabricated for the measurement of the reflection coefficient because the calculation of the reflection coefficient requires the measurement of the wave amplitude incident on the interface and is shown in Figure 3-11 wherein the machined angle is the same as the refracted shear wave angle. Air was sealed in behind the angle surface as shown. The sample also had a drilled hole with the same diameter as that of the fiber (142 microns). The drilled hole was sealed to keep out the coupling fluid (water) and was used as a target to simulate an unbonded interface. Finally, the sample also had an SCS-6 fiber embedded in the matrix material (either Ti-6Al-4V or Ti-24Al-11Nb).

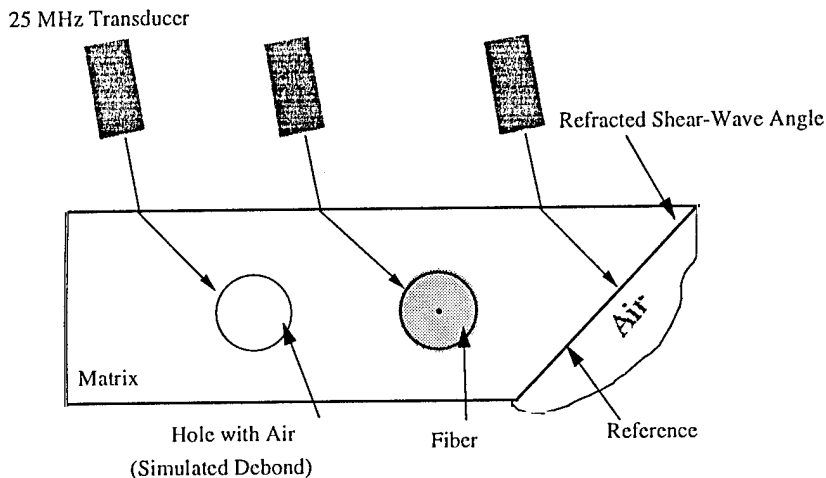


Figure 3-11. Experimental procedure for the measurement of the shear stiffness coefficient.

The experimental procedure for the measurement of the interfacial shear stiffness coefficient was carried out in several steps. First, a reference A-scan was obtained from the angled surface as shown. A Fourier transformation of that reference A-scan provided the incident magnitude at 25 MHz. Similarly, A-scans were obtained from the hole and the fiber and the corresponding reflected magnitudes at 25 MHz were measured using Fourier transformation and the reflection coefficient was calculated as shown in Figure 3-12. The

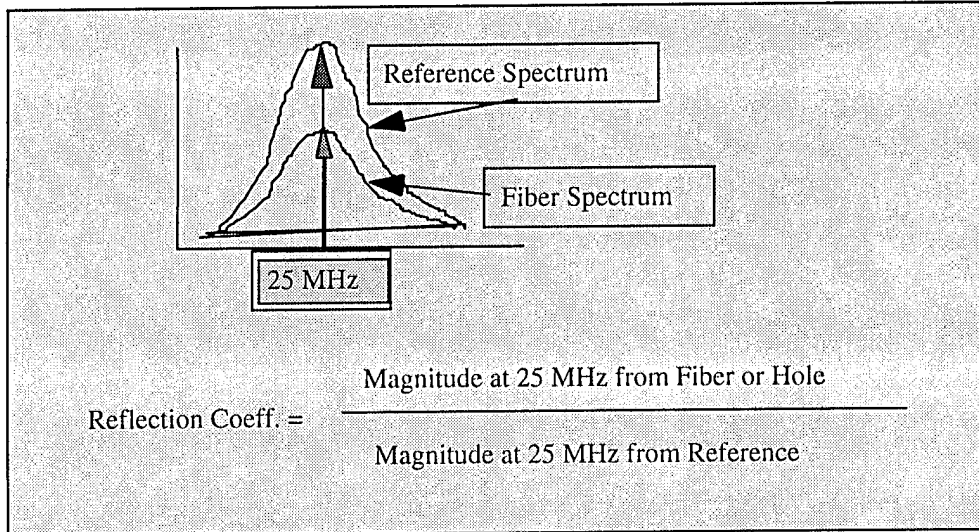


Figure 3-12. Procedure to experimentally calculate the reflection coefficient at a specific frequency selected based on the theoretical modeling.

calculated reflection coefficient was used to inverse calculate the shear stiffness coefficient of the equivalent elastic interface using the theoretical curve shown in Figure 3-13. The values are listed in Table 3-1. It should be noted that the shear stiffness coefficient for the hole was zero (Table 3-1) as expected (because the hole simulates a debond). The fiber-matrix interface and the hole in the matrix were imaged (Figure 3-14a) to show the sensitivity of the reflected

ultrasonic amplitude to the variability of the interface properties. The line plots in Figure 3-14b clearly demonstrate the sensitivity of the technique to the variability of the interfacial property.

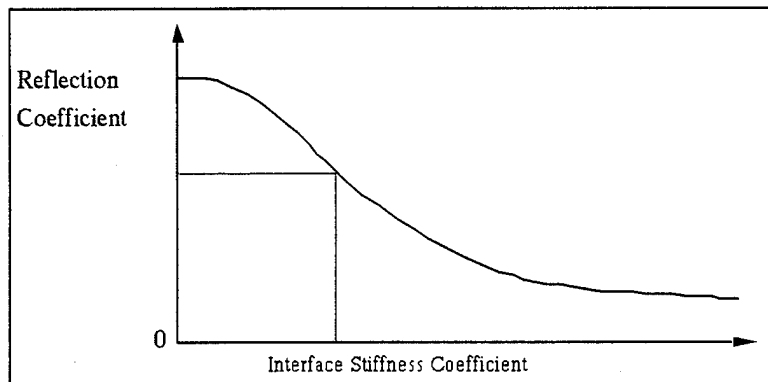


Figure 3-13. Inversion of shear stiffness coefficient of the fiber-matrix interface from the experimentally calculated shear back-reflection coefficient.

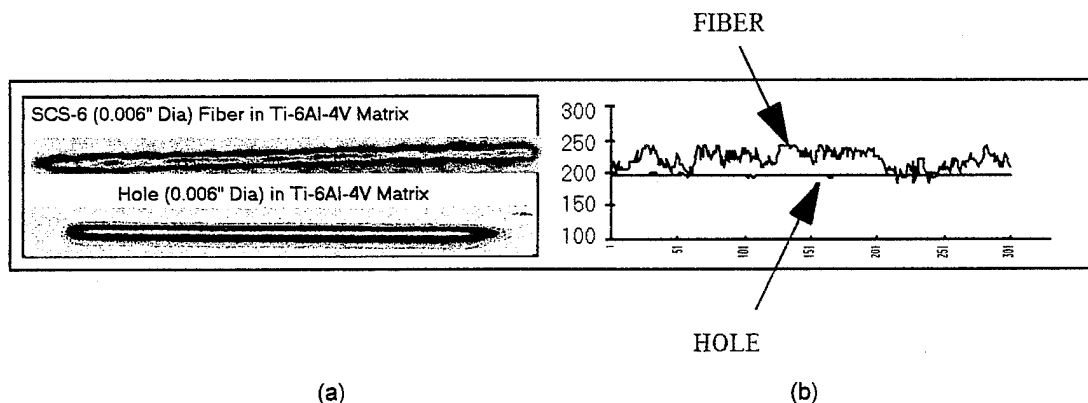


Figure 3-14. (a) Ultrasonic back-reflected amplitude image of an SCS-6 fiber embedded in Ti-6Al-4V matrix showing varying interfacial property compared to the image from a hole of the same diameter as that of the fiber. (b) Line plots of the reflected amplitudes along the lengths of the fiber and the hole, respectively, showing the variability of the reflected amplitude from the fiber-matrix interface.

**Table 3-1**  
**Theoretically Calculated Shear Stiffness Coefficient Based on Experimentally Measured Back-Reflection Coefficient**

Material	Reflection Coefficient	Shear Stiffness Coefficient (GPa/ $\mu$ m)
Hole	0.246	0.0
Ti-24Al-11Nb	0.096	7.3
Ti-6Al-4V	0.082	9.4

Cross-sectional photomicrographs of the composite systems have shown corroborating interface structure and are schematically shown in Figures 3-15a and 3-15b. From Figure 3-15, it is apparent that Ti-6Al-4V shows a greater degree of chemical bonding (and the resulting mechanical bonding due to the interface roughness) compared to that of Ti-24Al-11Nb which shows a smooth interface. The fiber fragmentation of these two composite

systems also showed [Karpur et al., 1992; Krishnamurthy et al.; Waterburry et al., 1994 and Karpur et al., 1992] a corresponding shorter fragmentation size in Ti-6Al-4V compared to Ti-24Al-11Nb, which indicates, based on Kelly's model [Kelly & Tyson, 1965], that the Ti-6Al-4V/SCS-6 interface had a better load transferability than Ti-24Al-11Nb/SCS-6 interface.

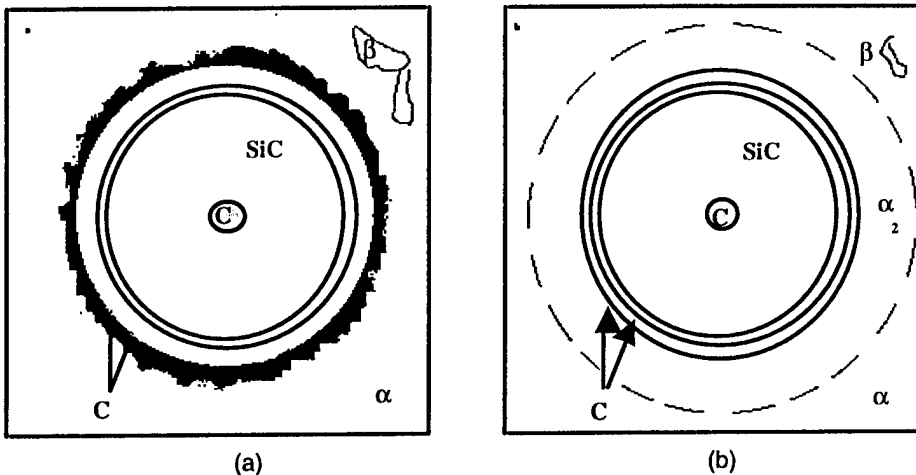


Figure 3-15. Schematic of the cross-sectional metallograph of the fiber-matrix interface variability in (a) Ti-6Al-4V, and (b) Ti-24Al-11Nb matrix composites with SCS-6 fibers.

### 3.1.4 Effect of Residual Stresses on the Measurement of Interfacial Stiffness

The objective of this section is to discuss the physical significance of the experimentally measured interfacial stiffness. It has been shown already that the interfacial stiffness largely depends on the interface elastic properties and more specifically on the shear modulus of the interphase material. However, the mismatch of the thermal expansion coefficients between the fiber and the matrix will induce radial residual stresses which can be either compressive (of significant amount in MMCs) or tensile (in some cases in CMCs). In the case of compressive radial residual stresses, the crystalline structure of the elastic interphase material will be compressed thereby providing an apparent increase in the shear stiffness of the material. Thus, the presence of compressive residual stresses either will facilitate load transfer between the matrix and the fiber in addition to that due to the elastic behavior of the equivalent elastic interface, or allow some load transfer even in the case of mere physical contact. Figure 3-16 shows both mechanisms of stress transfer at the interface. The effect of this compressive residual stress facilitated load transfer would be to modulate  $N_{e-min}$  to a higher (compared to no residual stresses) non zero, positive value. Similarly, when the residual stresses are tensile, the crystalline lattice of the interphase material is stretched (implies that the interphase region is perfectly bonded to the matrix and the fiber). As a result, the presence of tensile residual stresses impede the load transfer from the matrix to the fiber, thereby providing an apparent reduction of the shear stiffness of the interphase material. The consequence of this apparent reduction in the stiffness of the interphase is the modulation of  $N_{e-min}$  to a lower positive value compared to both no-residual stresses and compressive residual stresses.

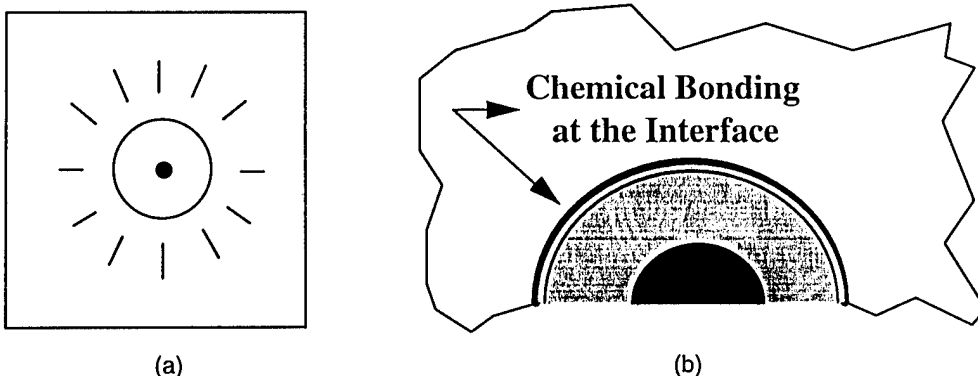


Figure 3-16. Factors which produce two types of bonds that affect shear-stress transfer between the fiber and the matrix: (a) radial component of the residual stresses, and (b) chemical reactions between the fiber and the matrix.

The effective stiffness coefficient, which is the experimentally measured parameter, represents the degree of interface bonding and depends on the chemical reaction, the mechanical interlocking due to the interface roughness, and the amount of residual stresses. It is impossible to isolate these effects and nondestructively measure the contribution of the one or the other aspect of the interface bonding alone. However, since advanced composites are designed as 'high temperature' materials, it is important to estimate the overall strength of the composite at elevated temperatures. This strength of the composite is dependent on the shear stress behavior of the interface at those temperatures.

### 3.1.4.1 Finite Difference Analysis and the Experimental Approach

A recent study [Coker et al., 1991] based on a finite difference model (FDM) was implemented to determine the three-dimensional stress state in a unidirectional composite subjected to axial loading and changes in temperature. Results from that model suggest that the residual stresses at the interface (due to the mismatch of the coefficients of thermal expansion) are reduced/altered at elevated temperatures. This implies that, at elevated temperatures, the residual stresses are no longer the predominant mechanism of shear stress transfer from the matrix to the fiber through the interface. Hence, most of the stress transfer at elevated temperature might be accomplished by the 'bonding' between the matrix and the fiber. The 'bonding' will be comprised of the chemical bonding due to the reaction between the matrix and the fiber as well as the mechanical bonding due to the surface roughness. Evaluation of the transferability of stresses across the interface is achieved using the fiber fragmentation testing [Roman and Aharonov, 1992 and Roman et al., 1992]. Ultrasonic imaging is then performed [Matikas et al., 1992] to nondestructively determine the number and sizing of the fiber fragments. Metallographic analysis corroborated the ultrasonic methods.

Figure 3-17 shows a schematic of the fiber-matrix concentric ring model used in the analysis [Coker et al.], wherein it was assumed that the temperature distribution was uniform and quasi-static, and that there was a perfect bonding between the matrix and the fiber with no

slippage or separation of the constituents. Further, axisymmetric loading and a linearly elastic fiber were assumed. A von Mises yield surface of the matrix whose plastic deformation is governed by Prandtl-Reuss flow rate was used. Further details of this analysis can be found in the literature [Coker, et al.]. The finite difference model provided the predictions of the residual stresses at different temperatures which was useful for understanding the fiber fragmentation behavior of the samples loaded at elevated temperatures.

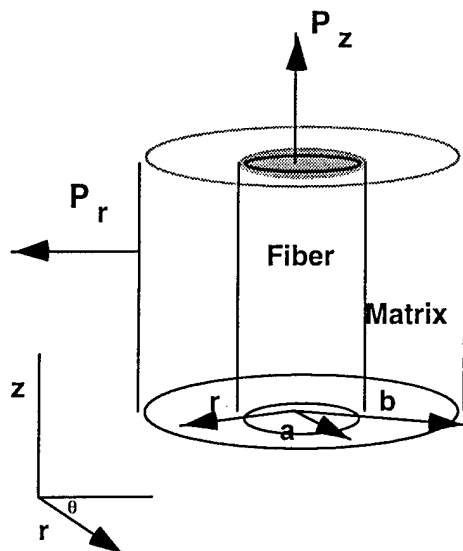


Figure 3-17. Theoretical residual stress model of Coker, Ashbaugh and Nicholas

Experimental work was conducted to understand the elevated temperature load transfer behavior of the fiber-matrix interface as well as to validate the model [Coker, et al.]. The Ti-6Al-4V/SCS-6 composite samples used for the experiments were fabricated by diffusion bonding two matrix alloy sheets with a single fiber between them. The processing method consisted of vacuum hot pressing at 925°C/5.5 MPa/30 min. followed by hot isostatic pressing at 1010°C/100 MPa/2 hr. The consolidated samples were machined into 1.5 mm thick sheet tensile specimens with 19.05 mm x 6.35 mm gage sections. All samples were examined by microfocus x-ray radiography to ascertain proper alignment of fibers parallel to the tensile specimen axis. Tensile tests were conducted on a servohydraulic machine in laboratory air at ambient temperature using a nominal strain rate of  $2 \times 10^{-4} \text{ s}^{-1}$  for Ti-6Al-4V/SCS-6. Similar tests were also conducted at elevated temperature of 650°C.

Originally, the residual stress model by Coker, et al. [Coker, et al.], was used to calculate the interfacial residual stresses at both the room temperature and elevated temperature to explain the differences in the experimentally observed fiber fragmentation behavior. Elevated temperature experiments supported by finite difference modeling and ultrasonic imaging indicate the possibility of shear stress transfer at the interface due to several mechanisms including residual stresses and chemical bonding. Further, experiments have

been conducted on various glass matrix composites to study the effect of residual stress on the ultrasonic interface characterization process which are outlined in the next session.

### 3.1.4.2 Experimental Determination of the Semiempirical Relationship Between the Ultrasonic Reflection Coefficient and the Magnitude of Radial Residual Stress

The effect of the existence of residual stresses at the fiber-matrix interface on the amplitude of the back-reflected ultrasonic shear wave from the interface is clearly demonstrated in the following results from experiments performed on different types of glass matrix composites. Six types of glasses with virtually identical elastic properties (Table 3-2) but with

**Table 3-2**

**Elastic Properties of Various Types of Custom Glasses with Similar Elastic Properties but with Different Coefficients of Thermal Expansion Due to Small Differences in Chemical Composition**

GLASS TYPE	Density* (Kg/m <sup>3</sup> )	Longitudinal Velocity (m/s)	Shear Velocity (ms)	Young's Modulus** (GPa)	Shear Modulus** (GPa)	Bulk Modulus** (GPa)	Poisson's Ratio**	Coefficient of Thermal Expansion (1E-6/°C)
Glass B	2142	5315.7	3194.3	53.21	21.85	31.40	0.218	3.00
Glass C	2220	5367.2	3270.5	57.22	23.75	32.29	0.205	3.33
Glass D	2171	5391.2	3237.4	55.44	22.76	32.77	0.218	3.66
Glass E	2211	5411.8	3294.7	57.88	24.00	32.76	0.205	3.95
Glass F	2259	5406.8	3303.5	59.27	24.65	33.17	0.202	4.25
Glass G	2260	5479.3	3346.4	60.86	25.30	34.10	0.203	4.61

\* Experimentally measured using Archimedes' Principal

\*\* Dynamic modulii obtained using ultrasonic velocities

different coefficients of thermal expansion were used, thereby producing varying degrees of radial residual stress. Various types of fibers were used for the experiment (measured properties are shown in Table 3-3). Results from the composites with different matrices and SCS-6 fibers will be illustrated in the following paragraphs.

**Table 3-3**  
**Properties of Various Fibers**

Fiber Name	Weight** (g)	Length (mm)	Diameter*** (mm)	Density (g/cm <sup>3</sup> )	Bar Velocity (m/s)	Young's Modulus (GPa)
SCS-6	0.00220	43.78	0.142	3.173	11376.33	410.66
SCS-0	0.00167	36.38	0.134	3.255	11508.00	431.08
BP SIGMA	0.00114	45.23	0.094	3.655	10390.67	394.64
AMERCOM	0.00188	44.69	0.123	3.540	11566.33	473.63
SAPPHIRE ACP	0.00347	43.21	0.151*	4.484	10281.00	473.95

\* Diameter varied significantly along the fiber length; ranged between 0.121 mm and 0.170 mm

\*\* Weights were obtained using a highly accurate electronic balance

\*\*\* The diameters and lengths were obtained using Scanning Electron Microscope

The theoretical process of calculation [Jero et al., 1991] of the residual stresses is shown in Equation 10 and the corresponding calculated values are shown in Table 3-4.

$$\sigma_N = \gamma(\Delta\alpha)(\Delta T)$$

where,

(3-10)

$$\gamma = \frac{E_m E_f}{E_f(1 + v_m) + E_m(1 - v_f)}$$

with  $E_m$  and  $E_f$  as the Young's moduli of the matrix and the fiber, respectively,  $v_m$  and  $v_f$  as the Poisson's ratios of the matrix and the fiber, respectively.

Table 3-4

**Elastic Properties, Coefficients of Thermal Expansion and Residual Stresses of Some Glass Matrix Composites with SCS-6 Fibers**

GLASS TYPE	Young's Modulus (GPa)	Poisson's Ratio	Coefficient of Thermal Expansion (1E-6/°C)	Residual Stress at the Interface (MPa)
Glass B	53.21	0.218	3.00	* -18.917
Glass C	57.22	0.205	3.33	* -13.61
Glass D	55.44	0.218	3.66	* -6.547
Glass E	57.88	0.205	3.95	** -0.833
Glass F	59.27	0.202	4.25	*** 5.548
Glass G	60.86	0.203	4.61	*** 13.541
SCS-6 Fiber	410.66	0.150	3.99	

\* Tensile residual stress

\*\* Almost zero residual stress

\*\*\* Compressive residual stress

The elastic properties in the Tables 3-2, 3-3, and 3-4 were ultrasonically obtained [Matikas et al., 1994]. The shear back reflection coefficient model described in a previous section of this report was used to predict the reflection coefficients for these glass composites with SCS-6 fibers. The theoretical curves for a selected frequency of 25 MHz is shown in Figure 3-18 demonstrating that, when the residual stresses are ignored, the reflection coefficient relationships with the shear stiffness coefficient are very similar in all the types of glasses because of the fact that the elastic properties of these glasses are similar to each other. However, substantial differences in back reflected amplitudes of incident shear waves from the fiber-matrix interface were recorded from these samples.

Figure 3-19 shows the experimentally measured back-reflected shear wave amplitudes from the interface as a function of the residual stress for each type of matrix material. It has to be emphasized again here that the theoretically calculated reflection coefficients based only on the elastic properties are very similar to each other when residual stresses are ignored (see Figure 3-18). The measured reflected amplitudes from the fiber-matrix interfaces are plotted in Figure 3-19 as a function of the radial interfacial residual

stresses calculated using Equation 10. Figure 3-19 and Table 3-4 clearly demonstrate that the assumption of linear dependency of the reflected shear amplitude on the residual stresses is acceptable except when the residual stress is tensile enough (glasses B and C in Figure 3-19) to perhaps produce interfacial fracture and loss of contact.

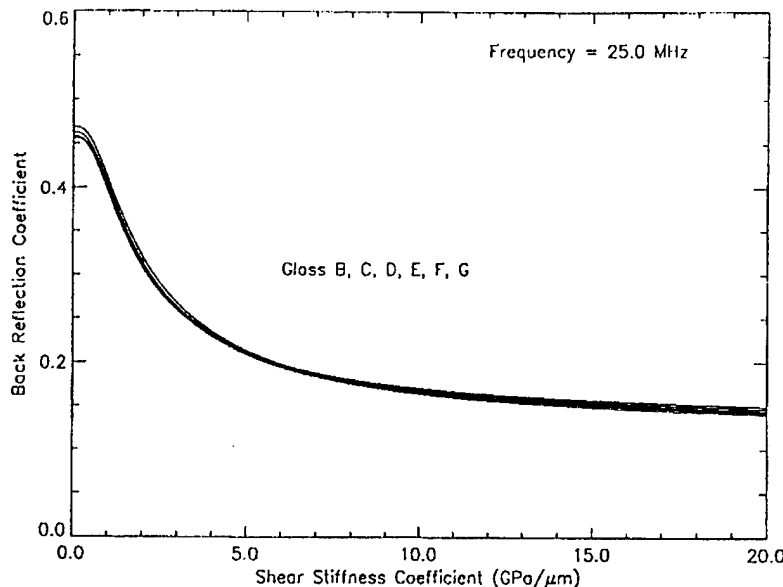


Figure 3-18. Back-reflection coefficient versus shear stiffness coefficient for different composite systems made from various types of glass matrices with SCS-6 fibers (frequency: 25.0 MHz).

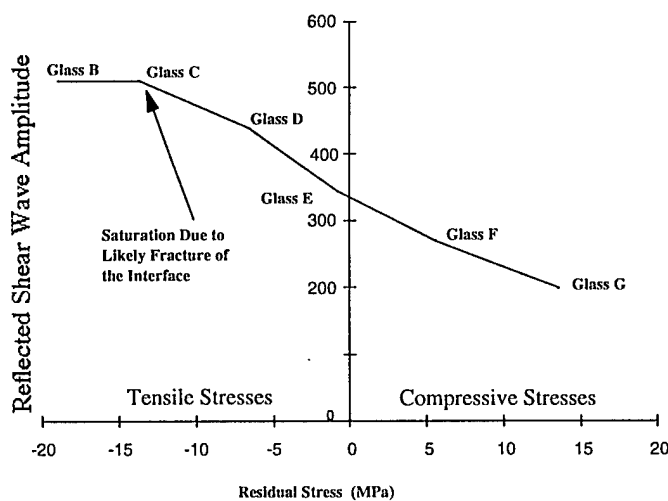


Figure 3-19. Linearity of ultrasonic reflection as a function of radial residual stress.

In summary, it has been shown here that the ultrasonic reflected amplitude, and thereby the ultrasonically measured interfacial stiffness coefficient, is not only a function of the interface shear modulus but, is also linearly dependent on the radial residual stress at the interface. Rigorous theoretical modeling does not exist to quantify the effect of the residual stresses on the measured interfacial stiffness. Therefore, the elastic shear stiffness coefficient

of the fiber-matrix interface cannot be precisely calculated from the back-reflected ultrasonic shear wave coefficient data.

### 3.1.5 Influence of Fiber Volume Fraction, Residual Stress and Interface Elastic Properties on CMC Micro-Cracking

There have been several recent analytical and experimental studies [Pagano & Kim, 1993; Pagano & Brown, 1993; Kaw & Pagano, 1993 and Pagano & Kim, 1991] with glass-ceramic composites containing Nicalon fibers in a Calcium-Aluminosilicate (CAS) matrix. These studies have provided evidence linking the increase in crack-growth resistance which have been noted in regions of high fiber-volume-fraction to higher microcrack-initiation stress levels for composites in which the fibers are uniformly and closely spaced.

Research efforts were conducted by UDRI to improve the understanding of this phenomenon. The objective of those research efforts was twofold: (1) determine the effects of three factors on the *initiation of microcracking under tensile loading* in unidirectional SiC-fiber-reinforced **borosilicate**-glass-matrix composites, and (2) investigate the effects of variations in fiber-matrix-interface stiffness on the composite cracking stress, i.e., the stress in the composite when matrix cracking first occurs. The three factors investigated to accomplish the first part of the objective were: (1) variations in fiber spacing, (2) variations in fiber-matrix interface bonding properties, and (3) variations in radial residual stress at the fiber-matrix interface. The results are briefly outlined in the summary displayed at the right.

SUMMARY OF RESULTS CMC Cracking Stress
<ol style="list-style-type: none"><li>1. Fiber Volume Fraction -- composite cracking stress increased with increasing fiber volume fraction</li><li>2. Interface Bond Quality -- composite cracking stress was higher for CMCs in which the fibers were strongly wet by the matrix than for CMCs in which the fibers were weakly wet by the matrix</li><li>3. Residual Stress -- composite cracking stress was lower for CMCs with significant <u>compressive</u> residual stress at the interface than for CMCs with no significant residual stress at the interface</li><li>4. Interface Elastic Properties -- composite cracking stress increased as interface shear stiffness decreased</li><li>5. There is good agreement between preliminary experimental results and <i>full-cell-model</i> predictions of composite cracking stress</li><li>6. Ultrasonic techniques were able to discriminate between internal and external cracks, thus improving the reliability of determination <u>internal</u> crack initiation</li><li>7. SBR techniques were able to determine the interface stiffness</li></ol>

#### 3.1.5.1 Approach

**Controlled variations in fiber spacing** were achieved by using a tape-casting fabrication process in which green tapes (with a relative glass density of 50%) were cut to size and laminated with fiber mats of the desired fiber spacing (68 or 120 fibers per 2.5 cm). The volume fraction of fibers in the composites was varied by altering the thicknesses of the green tapes and by using the two different fiber spacings within the tapes.

**Two different "qualities" of interface bonding** were achieved by using two different fibers in each type of glass. In some of the composites SIGMA fibers (102 micron diameter) coated with TiB<sub>2</sub> (strongly wet by borosilicate glasses) were used. Strong wetting should have

produced good bond quality between the fiber and the matrix in the processed composite. In other composites, SCS-6 fibers (142 micron diameter) were used. Those fibers were weakly wet by the borosilicate glasses and, therefore, should have produced poor bond quality between the fiber and the matrix in the processed composites.

**Differences in radial residual stresses** at the fiber-matrix interfaces were created by varying the composition of the borosilicate glass which was supplied by Corning as an eight-micron powder. The compositions were varied such that the coefficients of thermal expansion of the glasses were different, while the elastic properties of the glasses were very similar. The TiB<sub>2</sub>-coated SIGMA fibers and the SCS-6 fibers had identical coefficients of thermal expansion. The differences in the thermal expansion coefficients of the glass matrices combined with the identical thermal expansion coefficients for the fibers produced differences in the radial residual stresses at the fiber-matrix interfaces in the different composites after thermal processing. Three different compositions of borosilicate glass were used in this study: (1) 7040 glass, (2) a custom glass named "E", and (3) a custom glass named "F".

**The composite-fabrication process** (after initial lay-up and lamination) consisted of inserting the composites into a tube furnace and vacuum sintering at 710°C for one hour. The samples were then hot isostatically pressed at 650°C for 30 minutes with an applied pressure of 35 MPa to remove the residual porosity (about 2%). The resulting samples were approximately 10 cm long by 2 cm wide with a thickness of 0.2 cm.

**The theoretical values** of the matrix axial stresses for which cracking initiated in the matrices were calculated by using the full-cell crack model [Kaw & Pagano, 1993]. That model will not be presented here: rather, the interested reader should refer to the literature [Kaw & Pagano, 1993].

**The experimental evaluation** of the composite cracking stress of the samples was conducted using a procedure outlined in the literature [Pagano & Kim, 1993]. The composite cracking stress was determined from the tensile load at which an internal crack (full-cell crack mode) initiated. The samples were mechanically loaded in tension and *in situ* acoustic emission techniques were used to detect the supposed initiation of a crack. Axial and transverse strains were measured during loading using strain gages. The mechanical loading test was interrupted when a significant acoustic-emission event occurred and the samples were physically examined to verify the initiation of an internal crack; it was those internal cracks (consistent with the full-cell crack mode) rather than surface cracks which were of interest for assessing the composite cracking stress. Dye-penetrant-aided photomicrographic methods were initially used to determine whether a surface crack rather than an internal crack had been initiated. Free edges and flat surfaces of the specimens were polished with diamond past to enhance microscopic imaging for crack detection. Ultrasonic techniques -- surface waves, acoustic microscopy, and oblique-incidence shear waves -- were used to detect surface and

internal cracks, and thereby improve the reliability of determining whether a crack had actually initiated, and if so, whether that crack was an internal or a surface crack. In later tests, the upper and lower surfaces were coated with a thin layer of epoxy to reduce the dominance of surface cracks. The shear-wave back-reflection (SBR) technique was used to evaluate the shear stiffnesses of the fiber-matrix interfaces.

### 3.1.5.2 Results

**Fiber-volume-fraction-study results** are presented in Table 3-5 and in Figure 3-20. The data in Table 3-5 and in Figure 3-20a indicate that for the SIGMA-fiber-reinforced glasses (both 7040 and "F") the composite cracking stress increased as the volume fraction of fibers increased. The data in Table 3-5 also illustrates that good agreement was obtained between theory and experiment.

**Table 3-5**  
**Composite Cracking Stress**

Glass Type	Fiber Type	Volume Fraction (%)	Thermal Expansion Coefficient of Glass (per $^{\circ}\text{C}$ )	Composite Cracking Stress	
				From Experiment (MPa)	Calculated From Model (MPa)
7040	SIGMA	30	$5.40 \times 10^{-6}$	98	91
7040	SIGMA	35	$5.40 \times 10^{-6}$	107	105
7040	SIGMA	36	$5.40 \times 10^{-6}$	105	108
F	SIGMA	20	$4.25 \times 10^{-6}$	97	98
F	SIGMA	22	$4.25 \times 10^{-6}$	112	106
F	SIGMA	28	$4.25 \times 10^{-6}$	128	130
				No Bond	Perfect Bond
7040	SCS-6	25	$5.40 \times 10^{-6}$	32	35
7040	SCS-6	27	$5.40 \times 10^{-6}$	65	35
F	SCS-6	29	$4.25 \times 10^{-6}$	54	36
F	SCS-6	29	$4.25 \times 10^{-6}$	36	159

Notes:

1. The thermal expansion coefficients of SIGMA and SCS-6 fibers are identical ( $4.23 \times 10^{-6}/^{\circ}\text{C}$ ). The thermal expansion coefficient for 7040 glass is  $5.40 \times 10^{-6}$  and the thermal expansion coefficient of the F glass is  $4.25 \times 10^{-6}$ . Thus, in 7040 glass there are compressive residual stresses at the interface due to a mismatch in the thermal expansion coefficients of the matrix and the fiber, whereas for the F glass there are virtually zero residual stresses at the interface because there is virtually zero mismatch in the thermal expansion coefficients.
2. The toughness of both glasses are the same, i.e.,  $K_{IC} = 0.77 \text{ MPa}^{\sqrt{m}}$

**Interface bond "quality" results** are illustrated in Figure 3-20 and in the data of Table 3-5. The data and the theoretical curves in Figure 3-20b, and the data in the bottom four rows of Table 3-5 show that the experimentally determined composite cracking stress values for the SCS-6 fiber-reinforced glasses match the calculated composite cracking stress values for the "no-bond" case (with the possible exception of the SCS-6 fiber-reinforced 7040 glass). This agreement with the "no-bond" calculated values was expected because of the poor wetting of

the SCS-6 fibers by the borosilicate glass matrices. There were no significant differences in the volume fractions of fibers in the SCS-6 fiber-reinforced glasses (7040 and "F") used for this study. Therefore, no conclusions can be reached regarding the relationship between composite cracking stress and volume fraction of fibers for the SCS-6 fiber-reinforced 7040 and "F" glasses.

**Significant amounts of compressive residual stress** at the fiber-matrix interface result in lower values of composite cracking stress. Data in Table 3-5 shows that specific values of composite cracking stresses are reached at lower fiber volume fractions for the SIGMA-fiber-reinforced "F" glass than for the SIGMA-fiber-reinforced 7040 glass. This is better illustrated in Figure 3-20a. The theoretical curve in Figure 3-20a for "F" glass (virtually zero residual stress) is shifted upward (higher composite cracking stress) relative to the curve for 7040 glass which had a significant amount of compressive residual stress. It can be seen in Figure 3-20a that the experimental data that were available for the "F" glass and the 7040 glass agree very well with the theoretical curves. The "E" glass had a thermal expansion coefficient slightly lower than the SiC fibers; this resulted in a slightly tensile stress at the fiber-matrix interface. That the composite-cracking-stress values of the "E" glass (Figure 3-20a) are lower than those predicted by theory is most likely due to the existence of tensile-stress-induced partial debonds at the fiber-matrix interface.

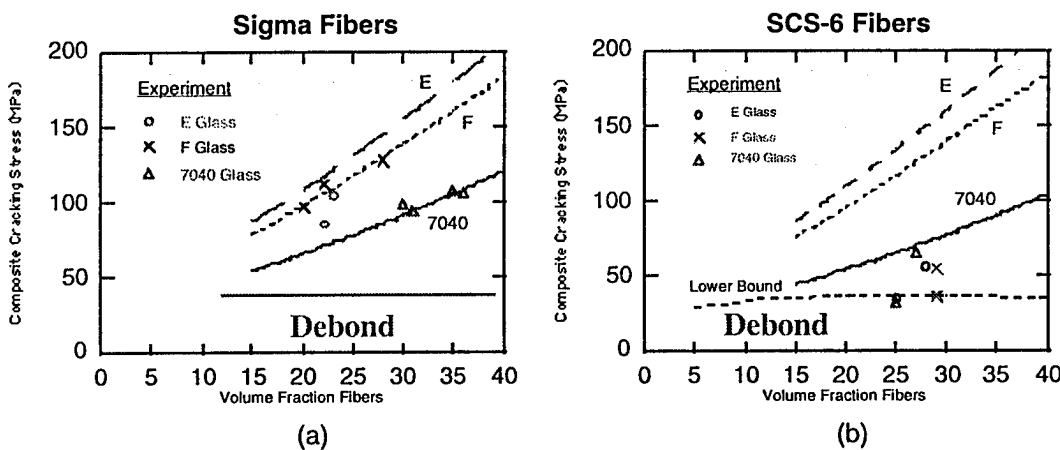


Figure 3-20. Composite cracking stress versus fiber volume fraction for (a) SIGMA fiber reinforced glasses and (b) SCS-6 fiber reinforced glasses.

**Ultrasonic evaluation** of the strongly wet SIGMA-fiber-reinforced glasses did no show dramatic debonding or cracking behavior as a result of the mechanical loading. However, ultrasonic evaluation of the weakly wet SCS-6 fiber-reinforced glasses revealed poor interfacial bond integrity as shown in images "a", "b" and "c" of Figure 3-21. Figure 3-21a shows the surface-breaking cracks as imaged using ultrasonic surface waves, and Figure 3-21b shows both the surface-breaking and the internal cracks as imaged using oblique-incidence shear waves. Acoustic microscopy of the SCS-6 fiber-reinforced glasses imaged large areas of fiber-

matrix debonding as shown in Figure 3-21c. This debonding behavior indicates weak interfacial bonding of the SCS-6 fiber-reinforced glasses relative to the SIGMA-fiber-reinforced glasses.

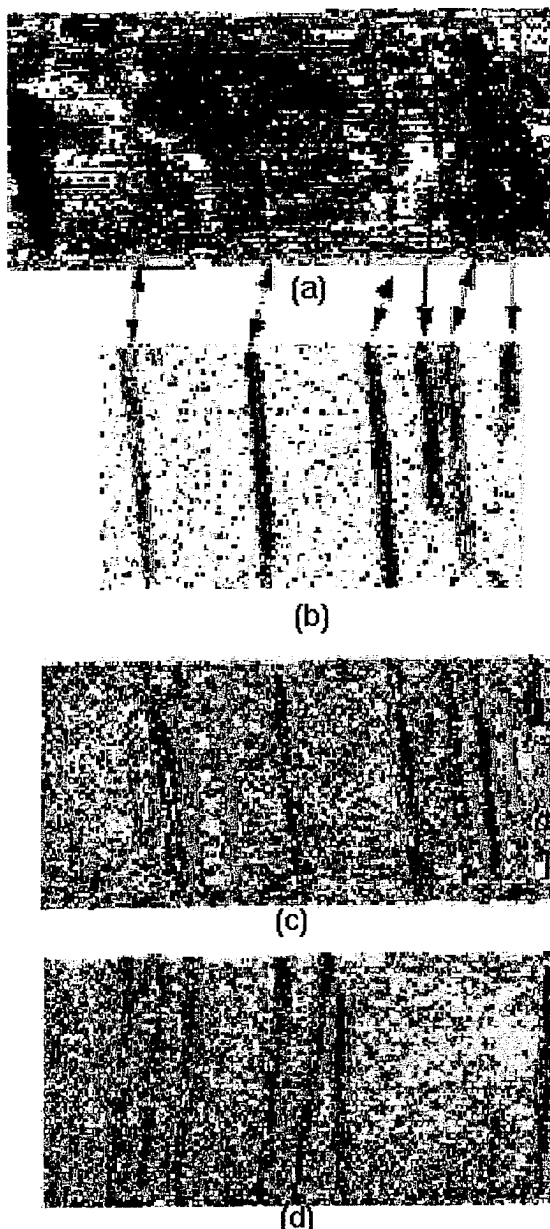


Figure 3-21. Ultrasonic images of SCS-6 fiber reinforced glass sample after tensile loading: (a) surface-wave image showing surface cracks, (b) acoustic microscopy image showing surface cracks and interfacial debonding of the first layer of fibers, (c) oblique-incidence shear-wave image of upper surface of sample showing upper-surface and internal cracks, and (d) oblique-incidence shear-wave image of lower surface of sample showing lower-surface and internal cracks.

Additional experiments were conducted to confirm this observation. The shear-wave back-reflectivity (SBR) technique was used [Matikas & Karpur, 1993] to image ("a" and "b" in Figure 3-22) and to quantify the stiffness coefficients of the fiber-matrix interfaces for both SIGMA and SCS-6 fibers embedded in 7040 glass and the custom "E" glass. The results

(Table 3-6) were obtained using theoretical curves of the type shown in Figure 3-23. The interface quantification process indicates that the interface for the 7040-SIGMA glass is relatively stiff compared to the other interfaces, with the E-SCS-6 glass interface being the most compliant.

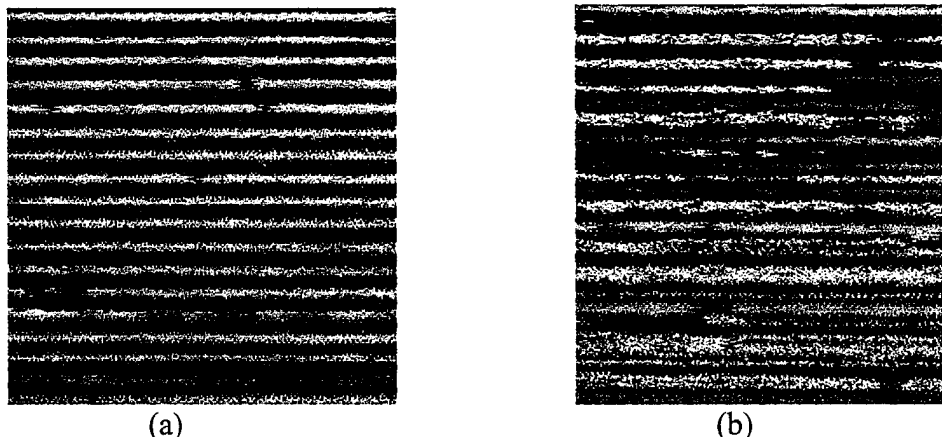


Figure 3-22. Shear-wave back-reflectivity (SBR) images showing: (a) a stiff interface in a SIGMA fiber reinforced "E" glass composite, and (b) a highly compliant interface in an SCS-6 fiber reinforced "E" glass composite.

**Table 3-6**  
**Reflection and Shear-Stiffness Coefficients of Four CMCs**

Matrix/Fiber	Reflection Coefficient (Unitless)	Shear-Stiffness Coefficient (MPa/ $\mu$ m)
7040/SIGMA	0.242	700
"E"/SIGMA	0.231	600
7040/SCS-6	0.318	700
"E"/SCS-6	0.208	400

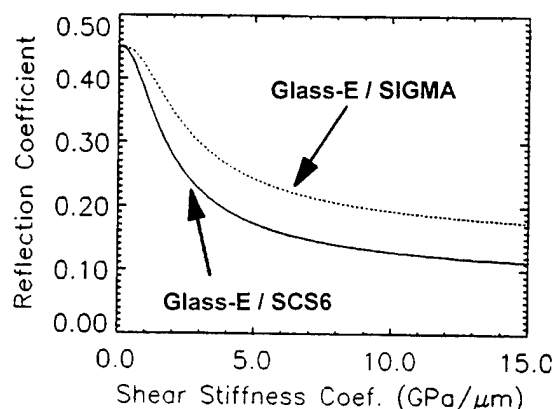


Figure 3-23. Shear-wave back-reflection coefficient amplitude versus shear stiffness coefficient for "E" glass matrix composites reinforced with different fibers.

### **3.2 Ultrasonic NDE Techniques for Improving the Results of Destructive Mechanical Tests**

Model single-fiber composites having interfaces with specifically tailored properties are often used to determine the properties of fiber-reinforced composites. Many investigators have employed a number of destructive experimental techniques including fiber pull-out, fiber push-out, fiber fragmentation, transverse loading tests, etc. to characterize the interface in model composites. This subsection presents results which illustrate the benefits of the concurrent use of the above mentioned techniques and NDE techniques which were developed during the course of this contract. A brief outline of this subsection is provided in Exhibit 3-2.

<b>SUMMARY OF SECTION 3.2</b>	
<b>Ultrasonic NDE Techniques for Improving the Results of Destructive Mechanical Tests</b>	
<b>OBJECTIVE:</b> Develop NDE techniques which complement and improve existing mechanically destructive techniques that are used to characterize MMCs and CMCs	
<b>JUSTIFICATION:</b> Existing mechanical testing techniques can be very time consuming and there is often considerable scatter in the results obtained from their application	
<b>RESULTS</b>	
3.2.1 Developed ultrasonic imaging techniques which improved the reliability of mechanical fiber-fragmentation test results <ul style="list-style-type: none"><li>* Improved reliability of fiber-fragment-length measurements</li><li>* <i>In situ</i> technique allowed resolution of multiple breaks</li><li>* neural-network techniques improved detectability of secondary fractures adjacent to primary fractures</li><li>* <b>Importance --</b><ul style="list-style-type: none"><li>--improved reliability of calculations of shear-stress transfer across the fiber-matrix interface</li><li>--improved understanding of how loads are transferred during progressive loading of samples</li></ul></li></ul>	
3.2.2 Developed ultrasonic imaging technique to screen samples prior to fiber push-out testing <ul style="list-style-type: none"><li>* <b>Importance --</b><ul style="list-style-type: none"><li>--correlated scatter in results with matrix consolidation at the fiber-matrix interface</li><li>--reduced scatter in the push-out test results, thereby improving reliability of test results</li></ul></li></ul>	
3.2.3 Developed an <i>in situ</i> ultrasonic imaging technique to improve detection of fiber-matrix fracture-initiation during transverse loading tests of MMCs <ul style="list-style-type: none"><li>* <b>Importance --</b> allowed more reliable calculation of the <u>minimum stress at fracture</u>; this is an important input parameter for composite fracture-behavior models</li></ul>	

#### **3.2.1 Single-Fiber Fragmentation Test for Metal Matrix Composites**

In the fiber-fragmentation test, a composite sample made of a single fiber embedded in a ductile matrix is subjected to tensile loading along the fiber axis [Kelly and Tyson, 1965; Ochiai and Osamura, 1986; Roman and Aharonov, 1992; Vassel et al., 1988; LePetitcorps et al., 1989; Waterburry and Drzal, 1991; and Curtin, 1991]. When the tensile stress, which is transferred from the matrix to the fiber by shear, exceeds the local fiber strength, the single fiber breaks successively into smaller fragments until the fragments become too short to enable

further increases in stress level. Using arguments based on shear lag analysis, Kelly and Tyson (1965) showed that the critical length of fiber for load transfer,  $L_c$ , is a function of the interfacial shear stress according to the equation

#### NOTES TO THE READER

1. Results of nondestructive imaging of fiber fragments **after** mechanical loading will be found in the subsection titled "*Application of Ultrasonic Imaging to Fiber Fragmentation Tests*," page 3-36.
2. Results of *in situ* imaging of fiber fragments will be found in the subsection titled "*In situ Observation of Fiber Fragmentation*," page 3-39.

$$\tau_i = \sigma_f \frac{d}{2L_c} \quad (3-11)$$

where  $\tau_i$  is the shear stress,  $\sigma_f$  is the tensile strength of the fiber of critical length,  $L_c$ , and  $d$  is the fiber diameter. As a result, the measurement of fiber fragment size is critical to the understanding of the load transfer behavior of the fiber-matrix interface. However, the metallographic approach to measure the fiber fragmentation size might induce further fragmentation. Also, even after a laborious and meticulous sample preparation for metallography, parts of the fiber can still retain remnants of the matrix and/or interphase materials thereby masking any fiber fracture present at that location. Therefore, a nondestructive method of imaging fiber breaks would improve the reliability of the measurement of the lengths of the fragments of the embedded fiber. In the next several sections, we present a revolutionary nondestructive ultrasonic approach developed [Karpur et al., 1992 and Karpur et al., 1992] to image the fragmented fiber which remains embedded in the matrix. This is the first time that fiber fragmentation has been nondestructively imaged in opaque matrices.

#### 3.2.1.1 Ultrasonic Visualization of Fiber Fracture

A 25 MHz focused transducer (6.35 mm dia, 12.7 mm focus) has been used in the pulse-echo mode for the imaging of the embedded fiber in a sample which had already undergone the fragmentation test. The ultrasonic wave front was incident on the composite at an angle of 24° (which is between the first and the second critical angles). As a result, vertically polarized shear waves were incident on the interface between the fiber and the matrix. Figure 3-24a shows a schematic of the shear-wave interrogation approach. The transducer was positioned such that the wave front was defocused (-1.5 mm) from the surface of the sample, so that the focal plane of the incident beam (as shown in Figure 3-24a) was at the back-surface of the fiber. The reason for the defocus of the ultrasonic beam will be explained in details later in this section. Back-reflected ultrasound was gated for imaging as shown in Figure 3-24b. Since the wave front was incident at an angle, the received signal was either low amplitude due to back-scattering from the material texture or a very strong amplitude due to the back-reflection from the cylindrical fiber (when the wave front was perpendicular to the fiber

circumference). As a result, the dynamic range of the image of the fiber was excellent ( $> 17$  dB).

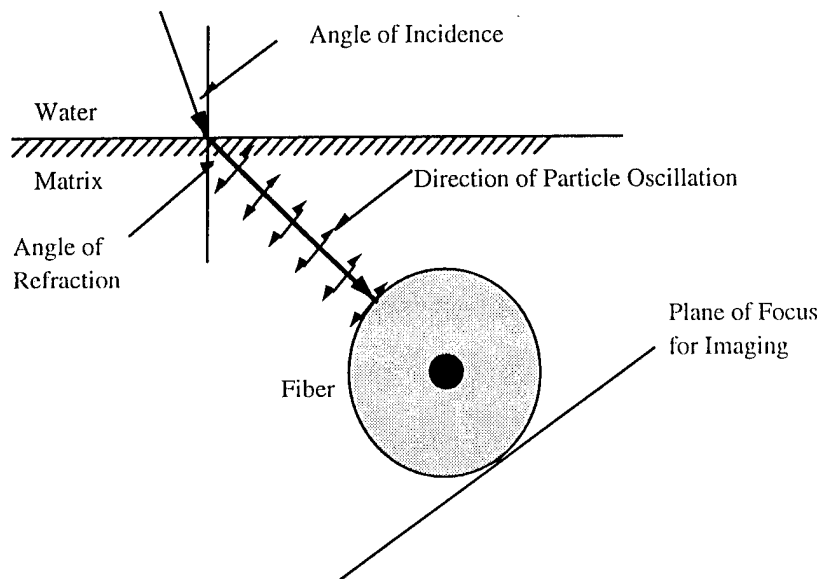


Figure 3-24a. Shear-wave ultrasonic imaging configuration.

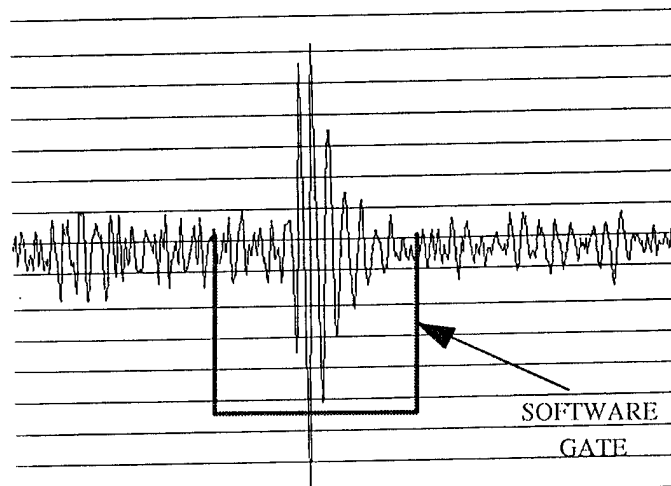


Figure 3-24b. Gated ultrasonic signal reflected from a fiber embedded in a metal matrix. The signal was obtained using the shear wave back-reflectivity technique.

#### *Physical Principle of Ultrasonic Imaging of Fiber Fracture*

Figure 3-25 is a schematic representation of a magnified region of the interface showing the matrix, fiber and a crack. The schematic also shows a defocused beam incident on the region. The ultrasonic beam is not incident normal to the sample surface but is always normal to the fiber-matrix interface as shown in Figure 3-24. From Figure 3-25, it is clear that the beam diameter, due to defocus, is incident such that it covers a portion of the fiber as well as the crack at the same time. However, since the acoustic impedance of the fiber is higher than that of the matrix while the impedance of the crack is less than that of the matrix, the

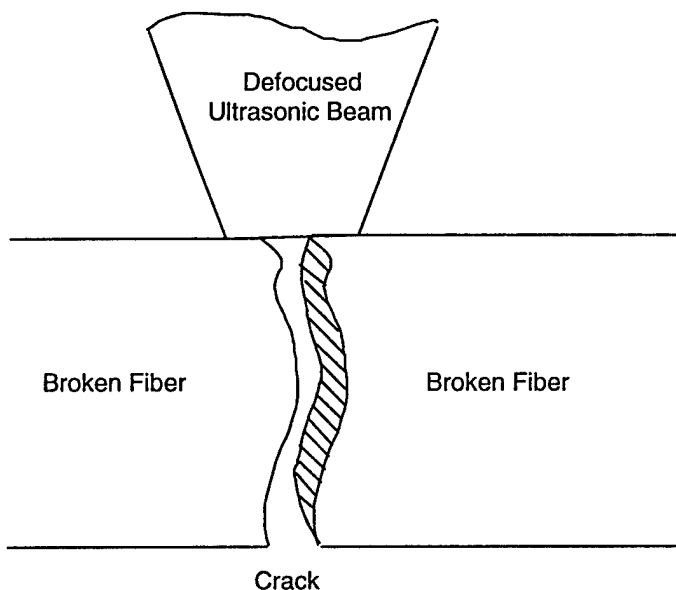


Figure 3-25. Schematic of a defocused imaging configuration.

reflections of the regions of the beam overlapping the fiber and the crack are out of phase with respect to one another. On the fiber, since the wave is propagating from a medium of lower impedance to a medium of higher impedance, the reflection coefficient has a positive phase and hence no stress reversal takes place. However, when the wave front impinges from the matrix on to the crack (which is a void with virtually negligible impedance), the reflection coefficient has a negative phase and hence a stress reversal occurs. Due to the fact that the two different reflection behaviors exist in different parts of the same beam, the transducer senses an amplitude which is the algebraic sum of the two reflections with opposite signs. As a result, by changing the extent of defocus which changes the relative areas of the fiber and the crack exposed to the incoming beam, the ultrasonic energy flux (defined as area times the intensity of ultrasound where intensity is the energy per unit area) reflected from the fiber remains constant with the defocus (because larger area reflects lower intensity). However, the energy flux from the crack diminishes with the defocus, because, the area of the crack exposed to the incoming ultrasound remains unaltered while the intensity of ultrasound diminishes. Therefore, by suitable defocusing, it is possible to balance the positive and negative energy fluxes from the fiber and the crack regions thereby canceling the received ultrasonic amplitude. Hence, the appearance of the crack can be substantially enhanced resulting in a phase sensitive 'microscope'. The size of the crack seen in the image will perhaps be exaggerated and might map the beam diameter. However, with the knowledge of the possible inaccuracy in the crack size measurement, a correction factor can be used to estimate the size of the fiber fragments. Experimental proof of this physical phenomenon is provided in Figure 3-26.

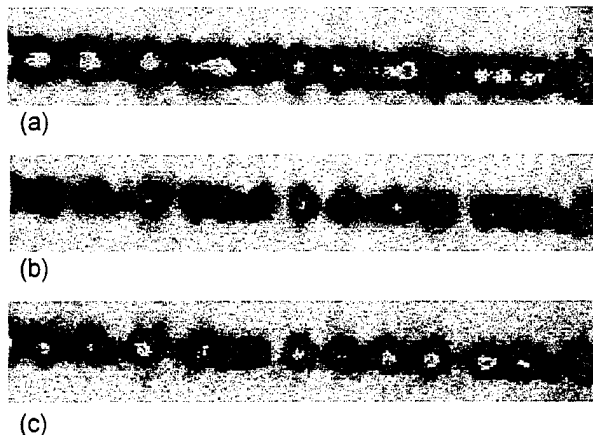


Figure 3-26. (a) Ultrasonic image of a SIGMA SiC fiber embedded in Ti-14Al-21Nb matrix. 25 MHz ultrasonic beam is focused on the fiber. (b) Image of the same sample with a defocus of -1 mm. (c) Image of the same sample with a defocus of -1.5 mm.

Figure 3-26a was obtained with the ultrasonic beam focused on the surface of a tested sample containing a single SIGMA fiber embedded in a Ti-14Al-21Nb matrix. The breaks in the fiber, although apparent in the image in Figure 3-26a, are not very clear. As a result, accurate estimation of the fiber fragmentation size is not feasible. Figures 3-26b and 3-26c show the same sample with a defocus of -1 mm and -1.5 mm, respectively, where the fiber fragmentation becomes more and more clearly visible. If the defocus is even more, the destructive interference between reflected signals from the fiber region and the crack region progressively disappears and an image similar to Figure 3-26a is obtained.

#### *Application of Ultrasonic Imaging to Fiber Fragmentation Tests*

The fiber fragmentation behavior of SIGMA SiC or SCS-6 fiber-reinforced Ti-6Al-4V and Ti-14Al-21Nb (both compositions in wt. %) was studied to determine the role of fiber-matrix interface characteristics in load transfer. Ultrasonic back-reflected shear-wave techniques (SBR) were applied to the specimens to image the fiber fragments. As an aid to the reader, an abbreviated summary of the results of the ultrasonic imaging after mechanical loading is provided in the block at the right.

The composite samples were fabricated by diffusion bonding -- vacuum hot pressing 15 925°C for 5.5 minutes followed by hot isostatic pressing at 101°C at 100 Mpa for 2 hours -- two matrix alloy sheets with a single fiber between them. The consolidated samples were machined into 1.5 mm thick sheet tensile specimens with 19.05 mm

SUMMARY OF RESULTS
<b>After-Loading Imaging of Fiber Fragmentation in MMCs</b>

1. Used ultrasonic shear-wave back-reflection (SBR) technique to image breaks in single-fiber MMCs
  - a. fiber-fragment length measurements made from SBR images were more reliable than length measurements made after conventional mechanical sectioning and polishing
  - b. technique could not resolve closely spaced multiple breaks in fibers
  - c. technique could not resolve interface debonding
2. Applied neural-network technique to high-frequency (50 MHz) SBR signals
  - a. technique resolved secondary fractures adjacent to primary fractures in the fibers
  - b. technique helped verify the theory of fiber-break detection

ultrasonically imaged, sectioned and polished parallel to the fiber axis. Metallographic examination of the fiber fragments was conducted by using optical microscopy and SEM.

Figure 3-27a shows the before-loading image of an SCS-6 fiber embedded in a Titanium Aluminide matrix (Ti-6Al-4V). Figure 3-27b shows the fiber after loading. Since the average fragment size is about the same as the diameter of the fiber, the interface has successfully transferred the load to the fiber. Figure 3-27c shows another sample with an SCS-6 fiber embedded in a Ti-14Al-21Nb matrix after loading. Since the average fragment size is more than three times the diameter of the fiber, the interface has less efficiently transferred the load to the fiber compared to the sample shown in Figure 3-27b. In both the 'after-test' images, in addition to the main breaks, smaller pieces due to secondary breaks are also observed in both Figures 3-27b and 3-27c. The presence of such secondary pieces have been corroborated by metallography (Figure 3-27d and 3-27e).

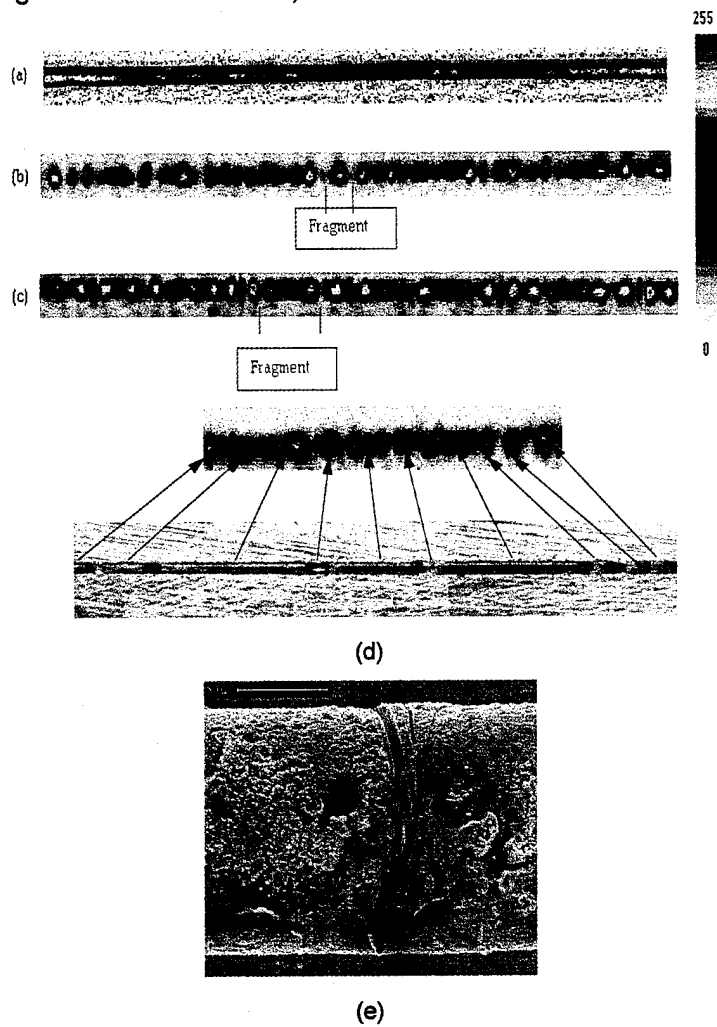


Figure 3-27. (a) Ultrasonic Image of an untested single fiber sample. (b) Fiber fragmentation image in Ti-6Al-4V sample with SCS-6 fiber. (c) Fiber fragmentation image in Ti-14Al-21Nb (or Ti-24Al-11Nb by atomic %) sample with SCS-6 fiber. (d) Corroboration of the ultrasonic imaging of fiber fragmentation with metallography. (e) SEM image of the fragmented fiber showing secondary fractures in addition to the primary fracture.

### *Neural Networks Approach for the Mapping of Fiber Microcracking in Composites*

It has been shown in the previous paragraphs (refer to Figure 3-26) that the presence of a fiber crack can be imaged by taking advantage of the 'defocus interference phenomenon'. The phenomenon produces cancellation of the reflected ultrasonic signal when the beam overlaps both the fiber and the crack regions so that the ultrasonic energy flux from the two areas is equal but with opposite signs. An independent method of verifying that phenomenon was attempted. The approach of verification was to use a transducer of high enough frequency (50 MHz) to produce a sharper focus than that possible using a 25 MHz transducer thereby making it feasible to reduce the effect of the interference between the reflections from the fiber and the cracks due to a relative imbalance between the energy fluxes from the fiber and the crack. Therefore, no signal cancellation - which is necessary to reveal the presence of a crack during the ultrasonic mapping of a fragmented fiber - was observed when the beam was focused on the surface of the fiber and also when it was slightly defocused. However, distortion of the signal was observed (see Figure 3-28). The signal from the crack (Figure 3-28a) as well as its spectrum were different from those from the fiber (Figure 3-28b). Next, a supervised backpropagation neural network [Lippman, 1987; Wasserman, 1989; Baker & Windsor, 1990; Damarla et al., 1991 and Damarla et al., 1992] was used for the classification of the obtained ultrasonic signals in the frequency domain to reveal the presence of the fiber breaks (Figure 3-29). Three classes of signals have been used: (a) signals corresponding to the fiber, (b) signals corresponding to the micro-cracks on the fiber, and (c) signals from the matrix. The locations of the fiber cracks, shown in Figures 3-29a and 3-29b, correspond to the indication obtained ultrasonically using the 25 MHz transducer operating in a defocus mode. More details about this work can be found in literature [Mann et al., 1992].

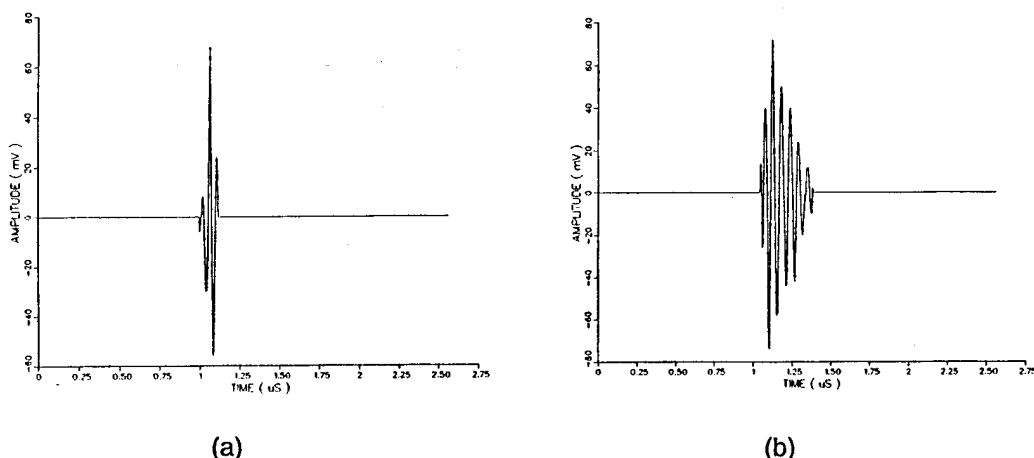


Figure 3-28. (a) Ultrasonic signal from a microcrack (frequency: 50 MHz) and (b) Ultrasonic signal from a fiber (frequency: 50 MHz).

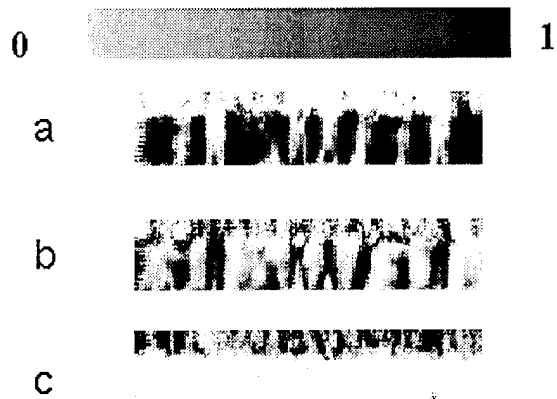


Figure 3-29. Output from the neural network when trained with six examples per class (a) Image of the fragmented fiber, (b) Image of microcracks on the fiber, and (c) Surrounded matrix.

### 3.2.1.2 *In Situ* Observation of Fiber Fragmentation

An innovative *in situ* methodology for monitoring the fiber-fragmentation process during mechanical loading is described in this section. This method combines acoustic emission techniques with the newly developed fiber-fragmentation ultrasonic imaging technique. The new methodology was developed and used to better understand the process of single-fiber fragmentation in titanium-matrix composites. The major results obtained with the *in situ* application of ultrasonic imaging is provided at the right. Post test scanning electron microscopy has been used also to corroborate the results.

The interpretation of fragmentation tests in ceramic fiber-reinforced metal and intermetallic matrices is particularly difficult because of the presence of multiple interfaces between the fiber, its coatings, and the matrix. The presence of several potential failure initiation sites and secondary fiber failure events further complicates the analysis, as does damage induced by specimen preparation. *In situ* nondestructive imaging of single-fiber composites after each of several small strain increments can aid interpretation by providing more complete information than a single destructive observation after fiber fragmentation. High frequency (25 MHz) ultrasonics can produce such images [Waterburry et al., 1994 and Waterburry et al., 1993] for systems with

SUMMARY OF RESULTS <i>In Situ</i> Imaging of Fiber Fragmentation	
<b>1. Single fiber embedded in a metal matrix</b>	<ul style="list-style-type: none"> <li>a. fiber-break images at prior coupon strain levels could be used to resolve multiple breaks which were too closely spaced for resolution in the final image</li> <li>b. fiber breaks observed by shear-wave back-reflection (SBR) imaging correlated well with number of breaks indicated by acoustic emission</li> <li>c. fiber breaks observed by SBR imaging correlated well with numbers of breaks observed by scanning electron microscopy</li> </ul>
<b>2. Single row of chopped fibers embedded in a metal matrix</b>	<ul style="list-style-type: none"> <li>a. the interface debonding which results from fiber fracture could be detected</li> <li>b. the fiber-fragmentation history helped determine how loads are transferred during progressive loading</li> <li>c. the global strain of the sample was measured by using the ultrasonically determined elongation of the distance between the chopped fibers</li> <li>d. fiber breaks do not generally consist of single fracture surfaces; rather, they comprise a fracture zone which contains one or two primary fractures followed by multiple secondary fractures</li> </ul>

sufficiently large fiber diameters, such as the 142 micron silicon carbide fibers used in this study. In addition to information about fiber-break locations, the technique may provide useful data about the interfacial debonding that occurs adjacent to the breaks.

*In Situ Observation of Fiber Fragmentation of a Single Fiber Embedded in a Metal Matrix.*

Single fiber fragmentation tests with continuous silicon carbide fibers in a Ti-6Al-4V alloy matrix were conducted with *in situ* ultrasonic imaging to monitor the fragmentation process. Straining proceeded incrementally on a specially designed load frame with acoustic emission (AE) detection performed during each increment and shear-wave back reflectivity (SBR) ultrasound images acquired following each increment. Metallographic examination of the fragmented fiber was performed following the straining sequence by electropolishing and scanning electron microscopy.

Sheets of Ti-6Al-4V 1.27 mm thick were used as the matrix material. Textron SCS-6 silicon carbide fibers 142 microns in diameter were used for the reinforcements. Fibers were aligned by placing them in a fiber retention groove that was machined with a specially-constructed shaping apparatus in one titanium preform plate. Specimens were fabricated by hot pressing at 954°C/10 MPa for 75 minutes followed by cooling at 10°C/minute [Waterburry et al., 1994].

Specimens were strained with a specially-constructed *in situ* straining stage [Karpur et al., 1992] which was designed for low frame compliance and low background noise for acoustic emission work. A simple, compact design was used so that ultrasound imaging could be performed without removing the specimen from the straining stage and releasing the specimen strain. The straining stage with the loaded sample was then placed in a water tank (shown in Figure 3-30), and ultrasonic imaging was performed after each strain increment. Straining proceeded in nominal increments of 0.75%, with the acoustic emissions recorded during each strain increment.

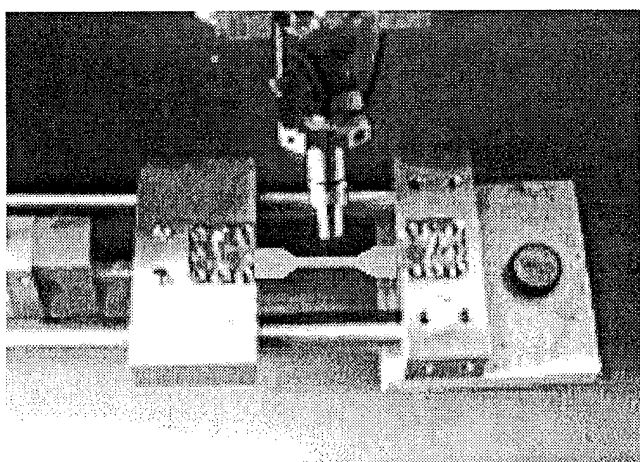


Figure 3-30. The loading device in the water tank with the acoustic transducer in position for *in situ* ultrasonic imaging of the fiber fragmentation process.

A 25 MHz focused transducer (6.4 mm dia. 12.7 mm focus) was used in the pulse-echo mode for the imaging of the embedded fiber. The shear-wave back reflectivity technique was used wherein the ultrasonic wave front was incident on the composite at an angle of 24° (which is between the first and the second critical angles).

Acoustic emission data were collected with a Physical Acoustics Locan AT acoustic emission data acquisition system with 8 mm diameter broadband transducers and 40 dB preamplifiers which had 100-400 KHz bandpass filters.

Previous work [Krishnamurthy & Roman, 1992] had shown that fiber damage is introduced during metallographic sectioning by mechanical means, and the smallest fiber pieces, associated with secondary fiber fractures generated during the fragmentation test, are typically lost. Therefore, following straining, specimens were electropolished to expose the fiber fragments for observation. Acid resistant lacquer was then applied to exposed areas followed by subsequent electropolishing until the fiber was exposed along the entire specimen gage section. Scanning electron microscopy (SEM) of the electropolished samples was performed with a field emission scanning electron microscope. Digital images produced with this system were downloaded to a computer and assembled with a graphics program into a single, contiguous, high-resolution image of the entire fragmented fiber, some 23,000 pixels in length. Fiber breaks were identified in this image and in other higher magnification images, and compared with the images obtained by ultrasonic imaging.

A single fiber fragmentation specimen imaged by reflected ultrasound is shown in Figure 3-31, with increasing coupon strain levels moving from top to bottom in nominal strain

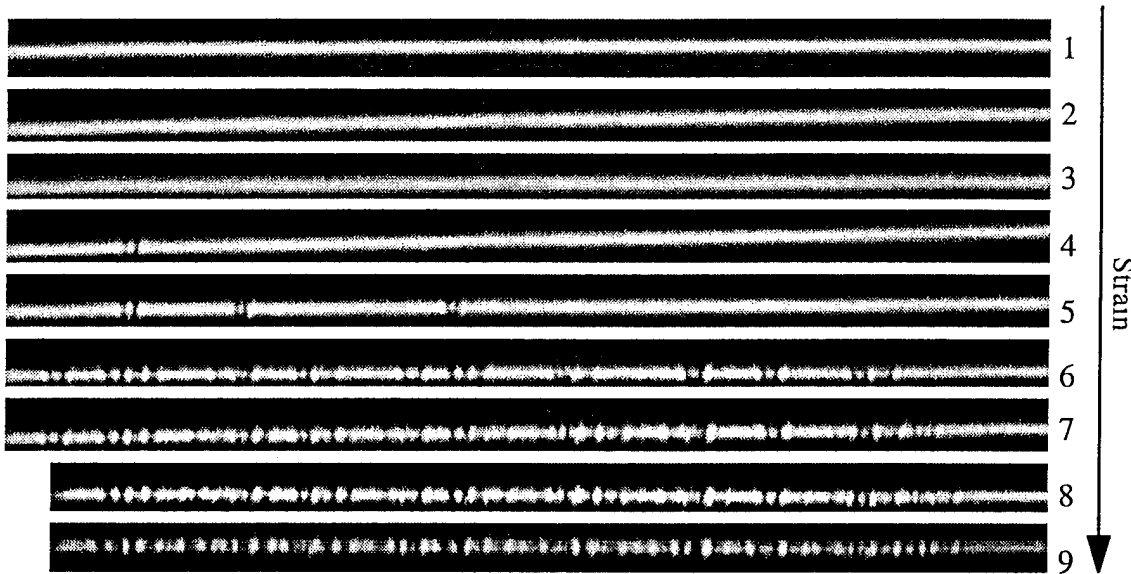


Figure 3-31. *In situ* ultrasonic images of the fiber fragmentation process. Images 1 through 9 are sequentially obtained by imaging the same fiber through the loading process with the strain increasing at a nominal rate of 0.75% from 1 through 9.

increments of 0.75%. Ultrasonically detected breaks using SBR technique were compared by SEM performed after the final loading of the sample. It was found that the SBR ultrasound image indicated the presence of a fiber break that was not visible under the SEM, but was apparently concealed by the reaction zone, which is not removed by electropolishing and was masking these regions of the fiber. This interpretation was supported by the identification of other previously concealed fiber breaks by additional polishing. Changes in the polishing solution to allow it to attack the reaction zone and completely expose the fiber are under investigation.

Before fragmentation begins, the fiber/matrix interface uniformly reflects the ultrasound, producing the homogeneous band in the topmost image. The first fiber breaks produce clear patterns consisting of pairs of dark regions where the sound waves reflecting from the new surfaces created by the fiber fracture destructively interfere with a central bright region where constructive interference occurs [Karpur et al., 1992]. When the spacing between fiber breaks is large the pattern of constructive and destructive interference is unambiguous and easy to interpret in terms of break locations. With smaller break-to-break spacing at the end of the test, however, the observed ultrasound interference patterns may be the result of more than one possible fiber break arrangement and interpretation becomes more difficult. The images of fiber breaks at prior coupon strain levels may be consulted in this case to determine the actual fiber break pattern.

*In Situ Observation of Fiber Fragmentation of a Single Row of Chopped Fibers Embedded in a Metal Matrix.*

A different experimental study for *in situ* monitoring of the fiber fragmentation process in metal matrix composites was performed using the SBR technique. This time, a composite made by a single row of chopped fibers was tested. Figure 3-32a shows a row of four chopped fibers embedded in the matrix before any load was applied to the sample. In Figures 3-32b and 3-32c, the same row of fibers is shown after the first loading and after the second loading, respectively. It can be seen from Figure 3-32, that the fiber numbered 1 had two breaks at the first loading and no additional breaks at the second loading. The fiber numbered 2 had only one break at the first loading and no additional breaks at the second loading. The fiber numbered 3 (which was the longer one) had one break at the first loading and a second break at the second loading. The fiber numbered 4 (which was the shorter one) had no breaks in the first interruption and one break in the second interruption. From Figure 3-32, it is feasible to calculate the strain of the sample at a particular load. For that reason, the images of the first chopped fiber in the row, before and after testing, are aligned. The distance between the ends of the first fiber and of the other three fibers is denoted by  $d_i$  where the subscript 'i' indicates the number of the fiber in the row, with  $i = 1$  to  $4$  (where by definition  $d_1 = 0$ ) as shown in Figure 3-32. The imaging of the fibers embedded in the sample was used to measure the elongation of the sample for a particular applied load. Therefore, the elongation of the sample is defined

the distance between the before and after testing positions of each fiber and is denoted by  $\Delta d_i$  (where by definition  $\Delta d_1=0$ ) as shown in Figure 3-32. Hence, the strain,  $\varepsilon$ , of the sample at the given load is given by  $\varepsilon = \Delta d_i/d_i$ , with  $i$  to take the values 2, 3, or 4. Using this approach, ultrasonically measured strains in Figures 3-32b and 3-32c are 2.7% and 7%, respectively.

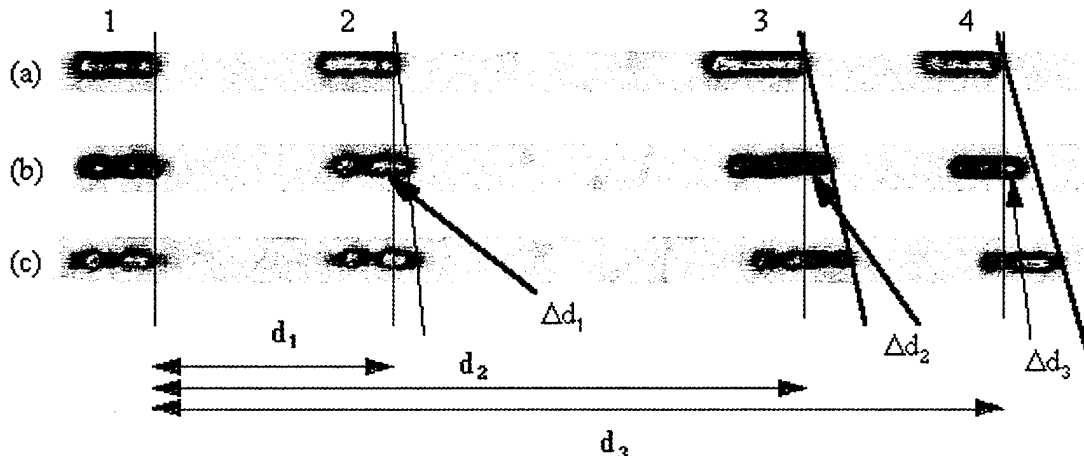


Figure 3-32. *In situ* ultrasonic images of the single row of chopped fibers fragmentation process. (a) Pretest image of the sample with a single row of chopped fibers (b) The sample shown in Figure 9a after the first interruption (strain = 2.7 %). (c) The sample after the second interruption (strain = 7 %).

It can be seen from the past paragraphs that ultrasonic back-reflectivity imaging provided a new insight into the fiber fragmentation process. It was observed that upon each fiber failure in a fragmentation specimen, elastic strain in the adjacent fiber fragments is relaxed by the retraction of the broken fiber ends, opening one or more cracks in the fiber. Simultaneously, the load formerly borne by the fiber is rapidly transferred through the fiber-matrix interfaces on either side of the fiber-break to the adjacent matrix material. The shock wave produced by the failing fiber and the subsequent load redistribution may initiate mode II interfacial cracks, mode I matrix cracks, or additional fiber fractures. No evidence of relaxation by mode I matrix cracks has been observed in the current study, although a shattered fiber morphology associated with fiber fragmentation is typically observed. As the strain in the fragmentation specimen is increased during subsequent strain increments, the interfacial cracks may propagate, and fretting damage and changes in acoustic reflectivity will occur indicating that a mode II interfacial crack has initiated and propagated between the fiber and matrix near the break. The ability to observe fiber debonding by this method would provide a tool that is analogous to the use of optical birefringence patterns to assess failure modes in transparent polymer matrix fragmentation testing [Fraser et al., 1983; Drzal et al., 1980; Netravali et al., 1989 and Waterbury, 1991].

It was observed in this study that fiber breaks do not generally consist of single fracture surfaces, but comprised a fractured zone, with two to five closely spaced fractures. These fractures appeared along a length of fiber 1/4 to 1/2 fiber diameters. It is believed that this morphology is generated by an initial tensile fiber failure, followed by additional damage produced by the fiber ends being driven back together in compression by a combination of the

reflected elastic shock wave and the CTE mismatch forces. Exposure of the fiber by electropolishing was found to reveal the fracture morphology without the disruption of the fiber fragments that occurred during mechanical polishing. The process of single fiber fragmentation in silicon carbide fiber reinforced Ti-6Al-4V matrix composites has been observed *in situ* by both shear wave back reflectivity ultrasound imaging and acoustic emission monitoring techniques and post-test by SEM observation of fibers exposed by electropolishing. Fiber breaks observed by SBR ultrasound imaging correlated well with the numbers of breaks indicated by acoustic emission data and the positions and numbers observed by scanning electron microscopy. Well-separated fiber fractures may be clearly distinguished by SBR ultrasound imaging, while more closely spaced fractures produce interference between breaks which makes interpretation more difficult. It has been clearly demonstrated in this section that ultrasonic NDE monitoring of fiber fragmentation provides more complete information about the fiber fragmentation process and final specimen state than does either technique in isolation. The results presented in this section are also supported by numerical simulation based on lattice approach [Hrennikoff, 1941; Herrmann & Roux, 1990; Charmet et al., 1990; Schlangen & Van Mier, 1992; Murat et al., 1992; Monette et al., 1992; Dai & Frantziskonis, 1993; Roman et al., 1983; Ochiai & Osamura, 1986 and Ochiai & Osamura, 1986]. The method is a computer assisted simulation of actual experiments of the fiber fragmentation process, including fiber breakage, matrix yield and/or cracking, and interface failure. Details on this work can be found in literature [Frantziskonis et al., 1993 and Frantziskonis et al., 1994].

### 3.2.2 Ultrasonic Imaging for Improved Fiber-Push-Out Test Results

Some of the ultrasonic techniques which were discussed in previous sections of this report were used to nondestructively evaluate samples prior to application of destructive mechanical fiber push-out tests. A summary of the results is provided to the right.

The fiber push-out test is one of the most commonly used techniques for examining interfacial phenomena in ceramic matrix composites. The fiber push-out test consists of measuring the force necessary to slip a fiber along its length by pushing fibers embedded in a thin (less than 3 mm) test specimen (see Figure 3-33). The procedure of the test is to apply the load on the fibers via a 10-100  $\mu\text{m}$  diamond-tipped indenter until the entire interface is debonded and the fiber is displaced in the matrix. The resulting load-deflection curves recorded during the push process yield information related to useful interface properties such as friction coefficient, toughness [Evans & Marshall, 1989, Marshall, 1984; Marshall & Oliver, 1987 and

SUMMARY OF RESULTS	
Application of Ultrasonic Imaging to Fiber Push-Out Tests	
1.	Peak loads required to push out the fibers correlated with ultrasonic evaluations of the interfacial consolidations
2.	Use of ultrasonic imaging techniques to screen out all samples with improper consolidation: <ol style="list-style-type: none"><li>reduced the scatter in the data</li><li>improved the accuracy and reliability of the test results</li></ol>

Mandell et al., 1987], interfacial topography or roughness [Jero & Kerans, 1991; Mero et al., 1991; Kerans et al. and Kerans & Parthasarathy, 1991], etc. However, fiber push results tend to exhibit a wide scatter of data for a given material system [Jurewicz et al., 1989]. One of the main reasons for this scatter is the fact that the interface integrity might be affected by incomplete consolidation or improper processing. As a result, there is a need to nondestructively ensure the homogeneity and complete consolidation of the composite plate before the push tests are performed. Therefore, ultrasonic nondestructive characterization methods have been developed to enhance the understanding of the interfacial debond process due to fiber push testing and to accurately assess the state of the interfacial bond characteristics. In this section, the newly developed ultrasonic capabilities which permit the monitoring of elastic stress wave transfer from the matrix to the fiber are described and the correlation with fiber-push-testing results is outlined.

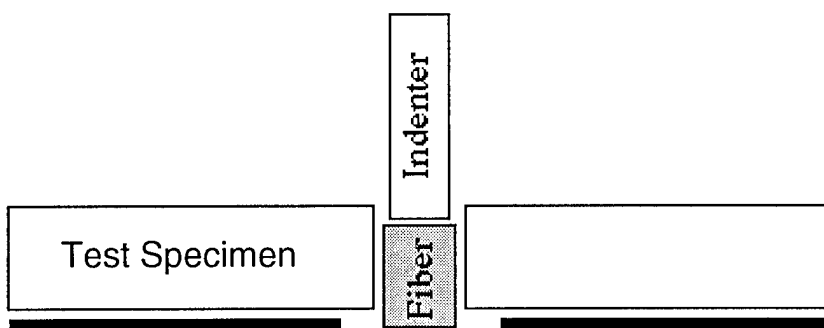


Figure 3-33. Configuration of the push-out test.

#### *Ultrasonic Experimental Approach*

Analysis of the interfacial debond characteristics of CMC test specimens is performed using two different ultrasonic techniques: normal incidence C-scan and shear-wave back reflection (SBR). Normal incidence C-scanning was performed to assess the overall integrity of the composite and to verify the effectiveness of the consolidation and densification [Krishnamurthy et al., 1993]. The ultrasonic response of the back reflected ultrasonic shear wave from the fiber-matrix interface was used to image the interface and verify its integrity [Waterburry et al., 1994; Matikas & Karpur, 1993 and Matikas & Karpur, 1993]. These approaches have been implemented extensively for the characterization of selected metal matrix composites [Waterburry et al., 1994 and Krishnamurthy et al., 1993].

A model test specimen of a single ply SCS-6/7740 glass (borosilicate glass) was investigated for its interfacial bond characteristics using destructive fiber push-out technique and the novel ultrasonic nondestructive approach. The SCS-6/7740 glass composite specimen was processed by hot pressing a lay-up of SCS-6 fibers between two glass plates at 3.447 MPa and 800°C for 20 minutes. The as-made composite was ultrasonically scanned for gross defects and delaminations using normal incidence longitudinal waves at 50 MHz (6.35 mm dia.,

25.4 mm focused transducer). A 25 MHz transducer (6.35 mm dia., 50.8 mm focus), incident at an angle of 19° was used for the SBR technique, in order to image the integrity of the fiber-matrix interface. The back reflected ultrasonic response from the resulting vertically polarized shear waves incident on the fiber-matrix interface was software gated for imaging [Buynak et al., 1989]. The experimental ultrasonic parameters (frequency and angle of incidence) were selected using methodology described in the literature [Matikas & Karpur, 1993] to provide the optimal dynamic range for the specific properties of the fiber and matrix. Subsequently, the as-made composite specimen was cut into test specimens for push-out testing. The test specimens were intentionally selected to contain both areas of poor bonding and/or delamination and areas of good bonding (shown by the ultrasonic pre-test scans in Figure 3-34).

#### *Results and Discussion*

The normal incidence and SBR imaging of the as-made SCS-6/7740 glass composite are shown in Figures 3-34a and 3-34b, respectively. The scans indicate good interfacial bonding regions as well as regions of delamination and/or poor consolidation at the interface between the plates and the fiber-matrix interface. The ultrasonic image (Figure 3-34a) shows that the consolidation is good from fiber 1 to 5 while it is progressively poor going from fiber 6 to 12. The peak loads that were required to push-out the fibers in the sample clearly show a correlation with the ultrasonic evaluation of the interfacial consolidation. Thus, if the ultrasonic scan is properly used to sort out the samples with improper consolidation, the validity of tests such as fiber push-out can be enhanced by reducing the scatter in the data. The push-out data will then reflect only the interfacial property rather than the scatter due to processing problems. The initiation and progression of damage due to fiber-push tests were further studied using a computer assisted simulation based on the lattice approach [Frantziskonis et al., 1993 and Frantziskonis et al., 1994].

#### **3.2.3 Ultrasonic Imaging of Fiber-Matrix Interface Damage During Transverse Loading of Metal-Matrix Composites**

The improvement of the transverse properties of titanium matrix composites (TMC) reinforced with continuous silicon carbide (SiC) fibers requires a basic understanding of the dependence of the fiber-matrix interface deformation and debonding on the residual stresses, on the fiber-matrix bond strength, and on the matrix properties, under transverse loading conditions of the composite. This section presents a new methodology to assess the interfacial stress at fracture. The newly developed method is based on an ultrasonic NDE technique which is used *in situ* to monitor the deformation and failure of the fiber-matrix interface under transverse loading. In this section, the damage evolution mechanism of a transversely loaded sample will be provided first based on the photomicrographic observations. Next, ultrasonic interaction with the evolving fiber-matrix interface damage will be modeled at various stages of

damage. Finally, experimental results will be provided to nondestructively evaluate the interface damage evolution based on the modeling.

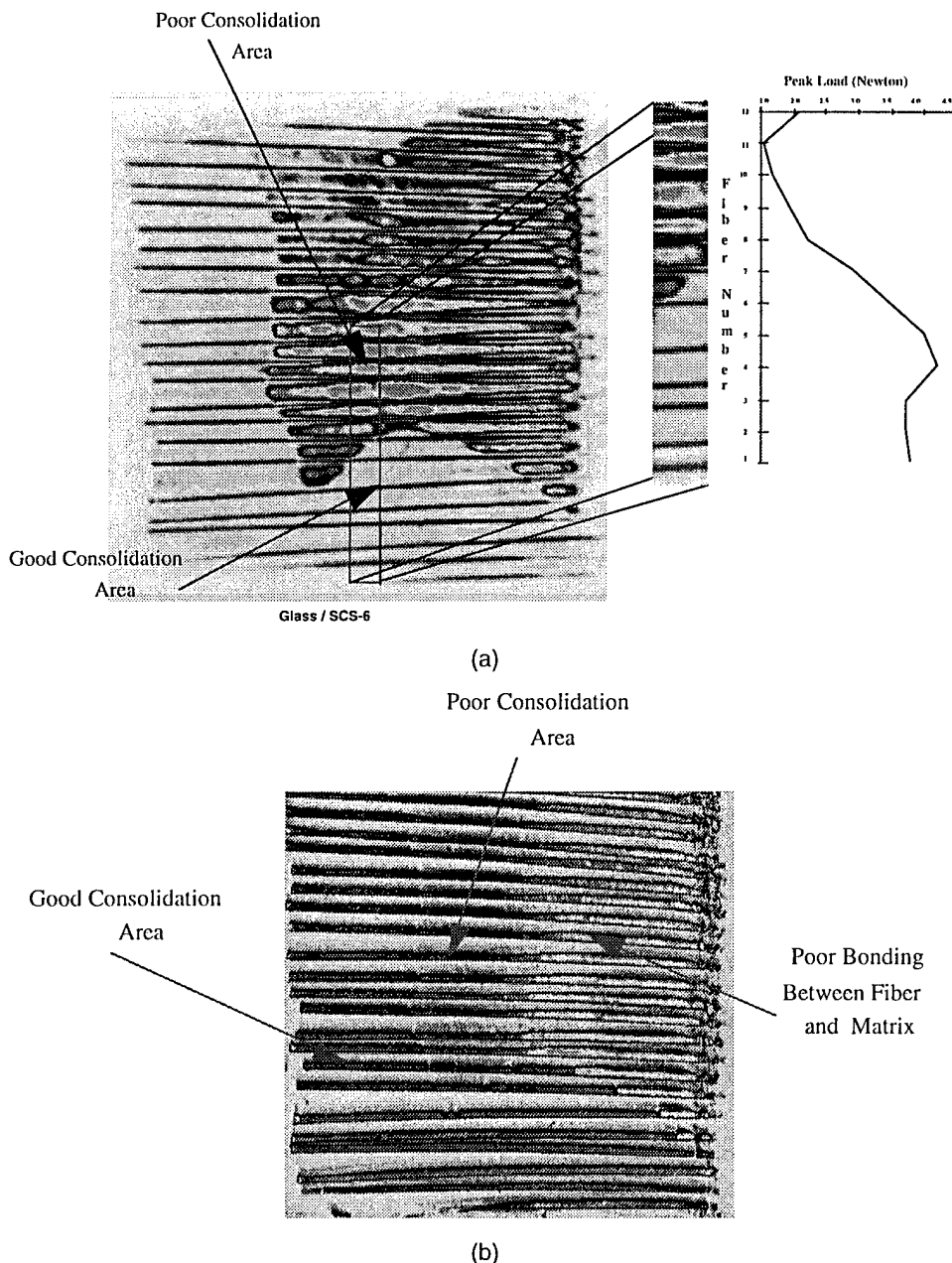


Figure 3-34. (a) Normal incidence ultrasonic (50 MHz) image showing areas of poor bonding and improper consolidation in addition to good bonding areas. The inset shows the location of the test specimen cut-out from the plate and the corresponding peak-load for each fiber. (b) SBR image of the sample showing interfacial integrity.

### 3.2.3.1 Mechanism of Damage Evolution in Titanium Matrix Composites During Transverse Testing

Ultrasonic NDE techniques were developed to image the fiber-matrix interface during transverse loading tests. As an aid to the readers of this subsection, the major results obtained with these techniques are listed.

The transverse tests for which these methods were developed were used for the most part to study the fracture behavior of single-fiber, model composites. Single-fiber (monofilament) specimens are well suited for interface evaluation because, (1) the interface chemical bonding, which depends on the chemical bonding, which depends on the chemical reaction between the matrix and the fiber materials during processing, remains the same in a single-fiber sample as in a multi-ply composite panel; and (2) the residual stresses at the interface are relatively easy to calculate in the single-fiber sample, thereby making it feasible to account for the residual stresses in the modeling of the test to derive more accurate conclusions about the stress when the fiber-matrix interface fractures.

Monofilament composite samples for these experiments were processed by the foil-fiber-foil technique. After processing of the single fiber composite samples, the samples were cut into dog-bone-shaped specimens with the fiber axis perpendicular to the loading axis of the samples as shown in Figure 3-35.

### SUMMARY OF RESULTS

#### Ultrasonic Imaging of Fiber Matrix Interface Damage During Transverse Loading of MMCs

1. The shear-wave back-reflectivity (SBR) technique is sensitive to:
  - a. fracture and deformation of the interface
  - b. amount and sign of the residual stresses at the interface.
2. The SBR technique provides information about:
  - a. propagation of damage
  - b. role of the redistribution of residual stresses in the interface damage behavior
3. A sample having a single embedded fiber with exposed ends will have pre-existing (pretest) interfacial cracks which are a few microns in length at the exposed ends
  - a. the cracks are caused by the existence of large tensile stresses at the free ends of the fiber
  - b. this produces dumbbell-shaped features in the SBR images of the fiber ends
4. The SBR technique can provide precise information about the time of fiber-matrix-interface fracture-initiation, and thereby the applied load at the time of fracture initiation
  - a. the stress at the fiber-matrix interface at the time of fracture initiation can be calculated from the applied load
  - b. the calculated stress at the fiber-matrix interface together with the local residual stresses can be used to determine the minimum-stress-at-fracture (MSF) of the fiber-matrix interface
  - c. the MSF is an important input parameter for the composite fracture-behavior models

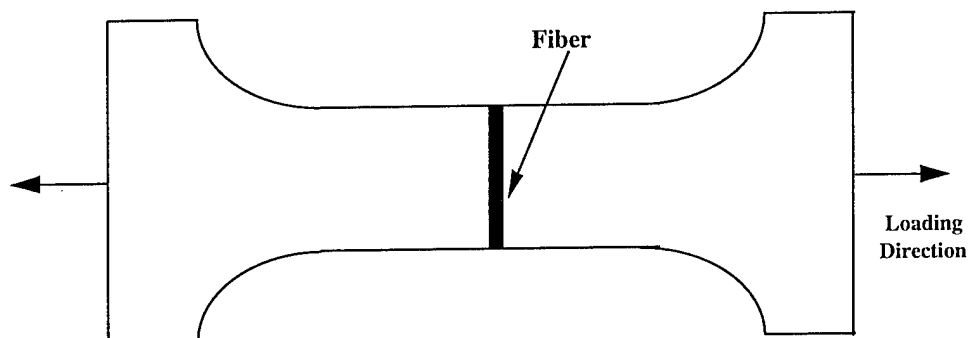


Figure 3-35. Experimental configuration showing transverse orientation of the fiber in a sample and the direction of loading.

The evolution of interface damage during the transverse test is illustrated schematically in Figure 3-36. During the initial stages of loading, the radial compressive residual stresses at the interface are decreasing while the interface remains intact. As the load increases further (in the elastic range) progressive failure of the chemical bond occurs, starting from the two sides in the direction of loading and progressing to the entire interfacial debond.

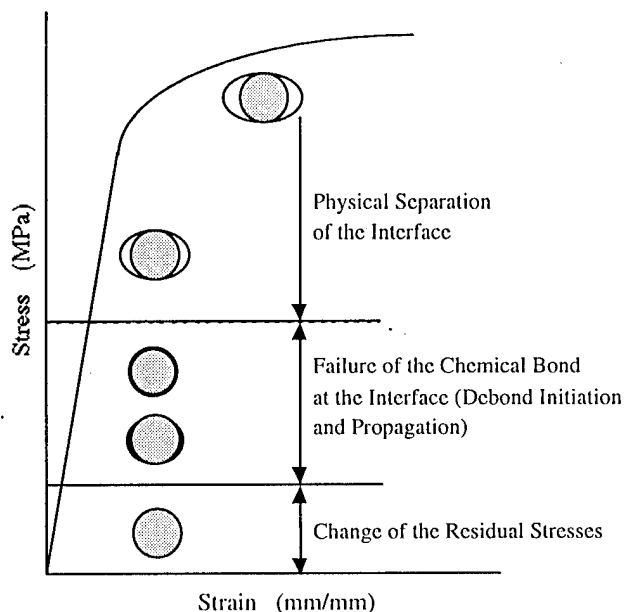


Figure 3-36. Schematic of microscopic-damage evolution at the fiber-matrix interface in a transversely loaded single-fiber MMC.

During this stage, there is no observable physical separation between the matrix and the fiber. As the load continues to increase (still in the elastic range) physical separation between matrix and fiber occurs and progressively increases with increase of load into the plastic range, as can be seen in Figure 3-36. Metallographic evidence of the evolution of damage as described above can be seen in Figure 3-37.

### 3.2.3.2 Experimental Approach

Two distinct sample configurations were used for this study. In one configuration, a single SiC fiber (SCS-6 or SCS-0) was hot pressed between two sheets of Ti-6Al-4V. In the other configuration, three different fibers (a "normal, noncoated" SCS-0 fiber, a yttria-coated SCS-0 fiber, and an SCS-6 fiber) were hot pressed between two Ti-6Al-4V sheets. Samples made from both configurations were processed at 960°C with 17 MPa pressure for 1.5 hours. Several single-fiber-configuration samples were fabricated and tested; only one triple-fiber-configuration sample was fabricated and tested. The interfacial microstructure obtained with this processing condition clearly indicates that some chemical reaction between the graded carbon coating and the matrix has taken place during the consolidation process. Furthermore, this reaction is nonuniform. Transverse tensile tests were carried out using a micro-straining stage (Figure 3-38) built in the WL/Materials Directorate [Waterburry et al., 1994]. The loading

was applied stepwise so that the ultrasonic scanning could be done *in situ* under the loaded condition at different stress levels. An *in situ* ultrasonic nondestructive technique was used for this purpose.

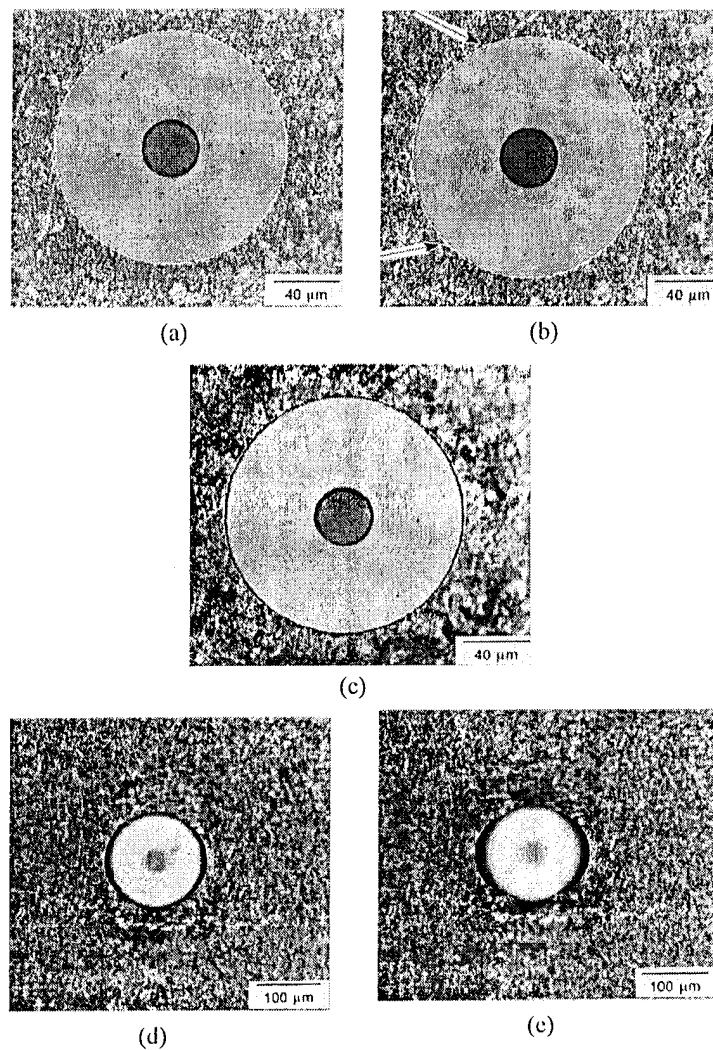


Figure 3-37. Damage evolution at fiber-matrix interface (in SiC-fiber-reinforced Ti-6Al-4V MMC) due to increasing transverse load (elastic range, "a" through "d"; plastic range, "e"): (a) residual-stress change, no observable damage; (b) chemical-bond failure on sides; (c) entire chemical-bond fails; (d) physical separation between fiber and matrix; and (e) pronounced fiber-matrix separation at interface.

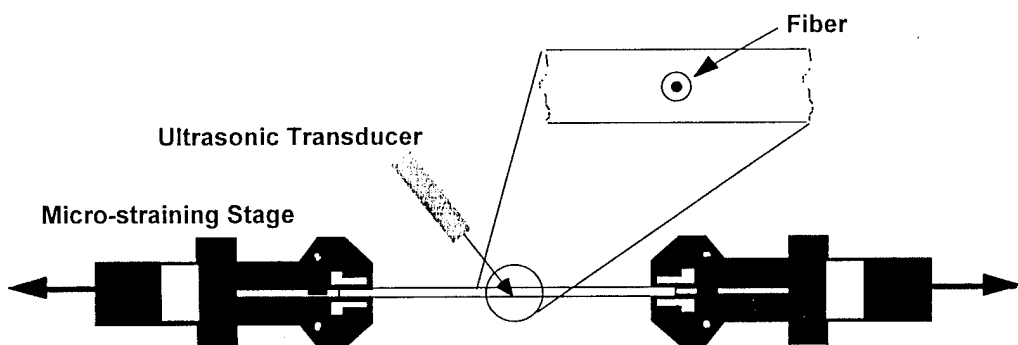


Figure 3-38. Configuration of the micro-straining stage for ultrasonic *in situ* imaging arrangement.

### *Mechanism of Ultrasonic Visualization of Interface Damage under Transverse Loading*

The damage of the fiber-matrix interface during the transverse test was evaluated using the shear-wave back reflectivity technique (SBR) [Matikas & Karpur, 1993 and Matikas & Karpur, 1993]. The loading of the samples was done in incremental steps. At each step of loading the fiber-matrix interface was imaged (while holding the sample under that load) in a pulse-echo mode using a focused ultrasonic beam which was incident on the surface of the samples at an angle of 24°. That angle was between the first and the second critical angles of the matrix material. Hence, mode-converted vertically polarized shear waves were incident on the fiber-matrix interface. The shear waves were back-reflected to the transducer and the reflection coefficient from the interface was evaluated and used to characterize the interface fracture. The model which was presented in a previous section (Section x.x.x.x) and in the literature [Matikas & Karpur, 1993] was used for the modeling of the reflection coefficient. The interface fracture was modeled based on theoretical predictions and experimental data. The reflected amplitude from a hole, which represents a complete debond (see previous section), was used to define the maximum reflected signal from the fiber. This would correspond to a signal from a fractured interface.

Figure 3-39 shows the ultrasonic beam used for the SBR imaging of interface damage evolution focused on the fiber-matrix interface and incident perpendicular to the axis of the fiber. Figure 3-39a shows the beam incident on an intact interface (zone I in Figure 3-40). The embedded reflector in the matrix is a perfect cylinder (well consolidated cylindrical fiber) in this case, and the reflected signal has an amplitude as predicted from the theoretical model [Matikas & Karpur, 1993] for the specific composite system. As the fracture of the chemical

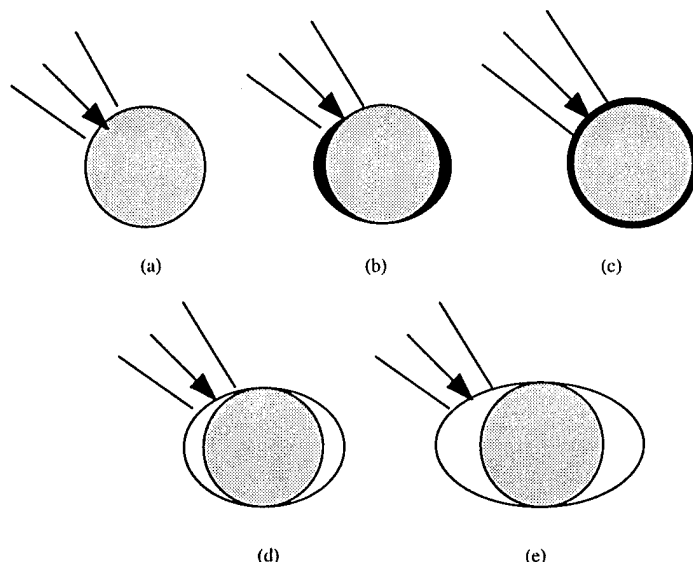


Figure 3-39. Schematic of ultrasonic interrogation of the interface damage evolution: (a) Bonded interface, (b) Partial interfacial debond (with no physical separation) in the direction of loading, (c) Complete interfacial debond (with no physical separation), (d) Physical separation of the interface in the direction of loading, and (e) Change of slope of the physical separation of the interface in the direction of loading.

bond begins (see Figure 3-39b), part of the ultrasonic beam will be incident on the bonded fiber and the other part of the beam will be incident on the fractured interface causing destructive interference between the reflections (positive and negative reflections) of the two parts of the beam which causes a reduction in the total reflected amplitude (zone II in Figure 3-40). This drop in amplitude may not always be observed because it depends on the load increment interruption chosen for the ultrasonic imaging. As the fracture of the interfacial chemical bonding progresses to final complete interface fracture (as shown in Figure 3-39c), the reflected amplitude will reach a maximum (zone III in Figure 3-40) as per the theoretical modeling [Matikas & Karpur, 1993] and experimental calibration done using a simulated debond as reported in Chapter 1 as well as in the literature [Matikas & Karpur, 1993]. Finally, as the load increases further and physical separation occurs and progresses (as shown in Figures 3-39d and 3-39e), the reflected amplitude of the signal will drop slightly because the embedded reflector is no longer cylindrical, and so, part of the incident wave will be reflected away from the receiver causing the amplitude of the reflection coefficient to drop (zone IV in Figure 3-40). While the physical separation between the matrix and the fiber continues to grow it is possible that the slope of the opening crack surface is perpendicular to the axis of the incident ultrasonic beam. In this case the ultrasonic amplitude will further increase and then will continue to decrease when the slope changes further. The experimental observation of this increase of the amplitude of the signal depends on the load at which ultrasonic imaging is performed. Figure 3-40 summarizes the above proposed ultrasonic amplitude and the corresponding microscopic interfacial damage during the transverse test. The possible drop of the ultrasonic amplitude in zone II, and the possible increase of the amplitude in zone IV, as explained above, are shown by the dashed lines in Figure 3-40.

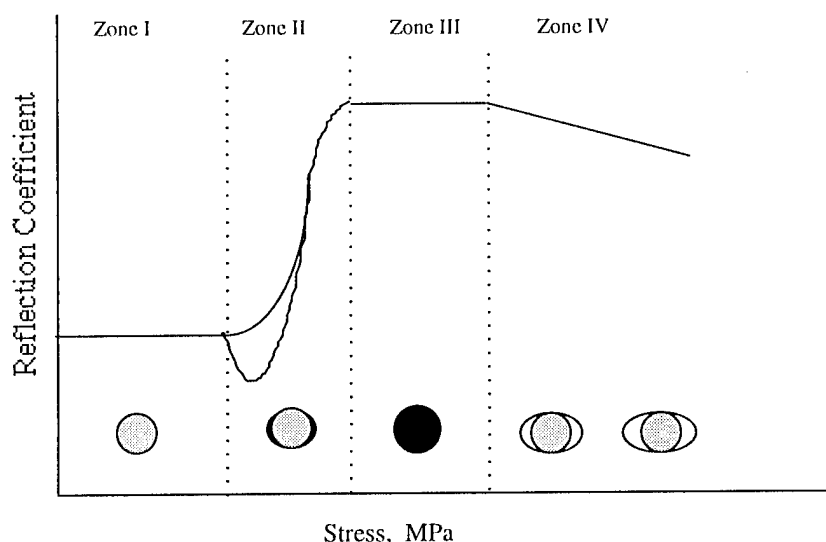


Figure 3-40. Schematic of the proposed relationship between microscopic damage and ultrasonic reflection coefficient using the SBR technique.

### 3.2.3.3 Experimental Results and Discussion

Figure 3-41 shows the stress-strain diagram for the tensile test of a Ti-6Al-4V/SCS-6 single fiber composite sample under transverse loading. Ultrasonic shear-wave C-scan images made at various stress levels of the sample labeled "A" through "K" are shown above the stress-strain diagram. The image labeled 'A' in Figure 3-41 corresponds to the fiber-matrix interface before the commencement of the mechanical loading of the sample. Image 'B' indicates the first few points of interface that fracture at about 350 MPa (shown with the maximum amplitude calibrated to red in the color scale). These points of interface fracture are located near the two ends of the fiber and in several places at the center of the fiber. The reflectivity images 'C' through 'J' show the progression of interfacial damage as the load increases. The image 'K' shows that the entire interface has been fractured at about 700 MPa. An important conclusion drawn from using *in situ* SBR imaging of the transverse test contradicts a commonly accepted assumption that the entire interface is likely to fracture almost instantaneously once a sufficiently high stress level is reached because of the existence of a weak diffusion bond [Wright et al., 1989] (as contrasted to mechanical bonding). The work reported here suggests that the debonding progresses from a small number of isolated points at a low load, to the entire interface over a finite range of applied stress (almost 350 MPa as shown in Figure 3-41). This range is dependent mainly on the redistribution of stress along the

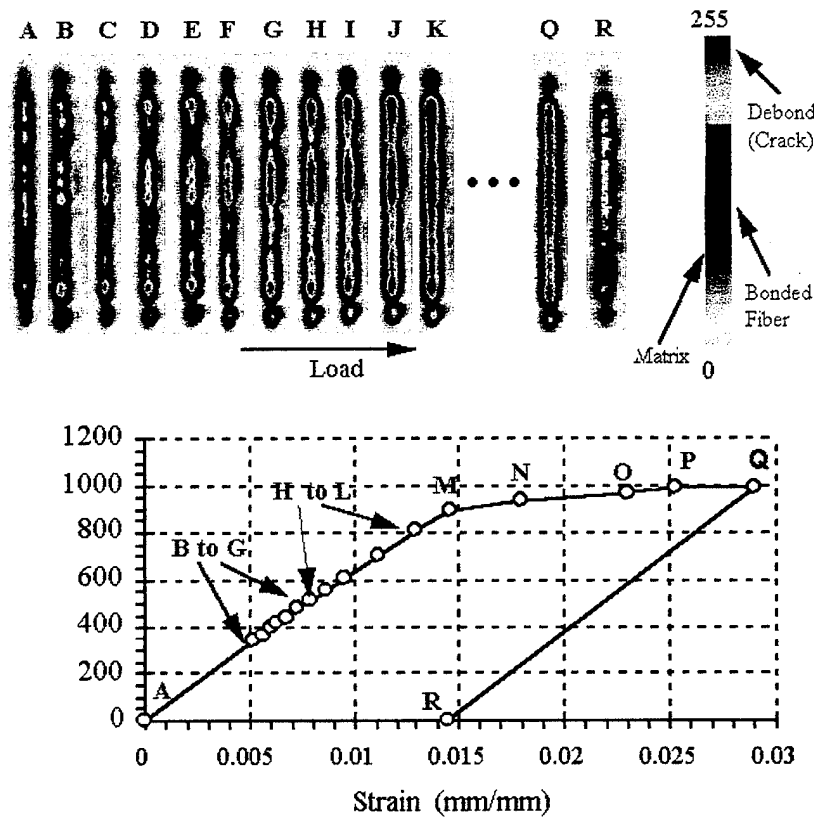


Figure 3-41 *In situ* ultrasonic SBR imaging of an embedded SCS-6 fiber in Ti-6Al-4V matrix during various stages of transverse loading.

interface which occurs due to the propagation of the interfacial crack as well as on the homogeneity of the fiber-matrix interface. It may also be noticed that the decrease of ultrasonic amplitude of the reflected signal that was predicted to be seen when the configuration of the defect is as described in Figure 3-40 (zone II), was not observed in this experiment. The reason for this is that the first point of loading at which an ultrasonic image was obtained was relatively high (at 350 MPa - see Figure 3-41) thereby a possible decrease of the reflected signal was simply missed. Next, the applied stress increased further to the plastic range of the specimen and the ultrasonic reflected amplitude started to drop as can be seen in the Figure 3-41 (image labeled 'Q' at almost 1 GPa (as predicted in Figure 3-40). Finally, the applied load completely released and the image of the fiber significantly reduced as the open interface cracks closed.

Figure 3-42 shows that the reflected amplitude along the fiber axis varies with position, suggesting a nonuniform interfacial "shear stiffness coefficient" (see section A.1.2 in this report). This variation in shear stiffness coefficient is the reason for the existence of a few points of weak interface properties at which the interface first fractured. A point of weak interface properties has lower shear stiffness coefficient, thereby higher reflected amplitude (as reported in the section A.1.1 and A.1.2 in this report). On comparison of the regions of higher reflected amplitude in the image of the interface before any applied load (labeled 'A') with the first few points of interface fracture in the image labeled 'B', it can be concluded that in fact compliant interface regions are likely to possess lower strength.

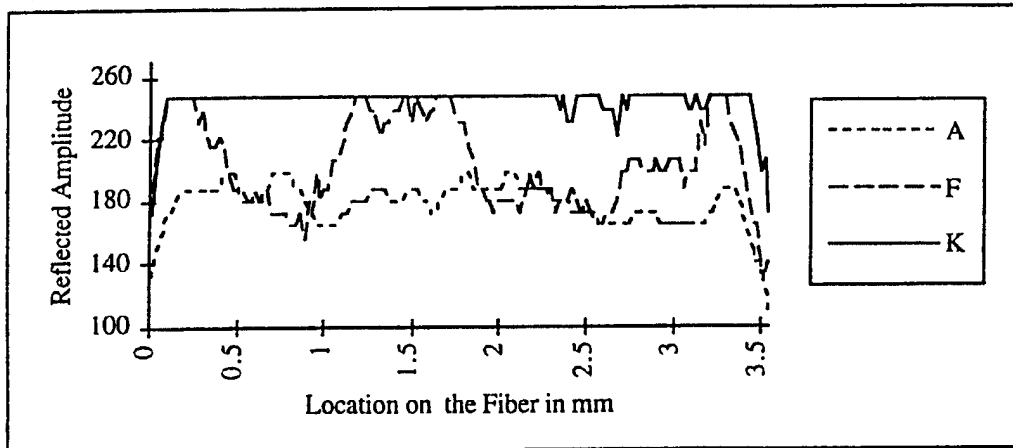


Figure 3-42. Ultrasonic reflectivity from the fiber-matrix interface at various locations for selected stages of loading of the test specimen (indicated by A, F, and K in Figure 3-41).

Another transverse test of a Ti-6Al-4V/SCS-6 single fiber composite is shown in Figure 3-43. Image 'A' shows the fiber before any applied load. Images 'B' to 'E' show the fiber from 50 MPa to 250 MPa while no interface fracture was observed. There is a drop in the signal amplitude (as predicted in zone II of Figure 3-40) in image "F" (at about 450 MPa) indicating that the interface fracture configuration is similar to that shown in Figure 3-39b. It is evident

from the image that the interface damage configuration as shown in Figure 3-39c (uniform fracture of cylindrical form around the fiber) did not occur in this case. The embedded reflector had no cylindrical form when the entire interface was fractured, and so, the reflected signal from the fractured interface did not reach the maximum value. Images 'G' through 'J' show the physical separation between matrix and fiber. The physical separation does not have the same slope along the length of the fiber. Therefore the image shows variation in the reflected amplitude along the length of the fiber. Image 'K' shows significant drop of the reflected signal from when all the applied load was released.

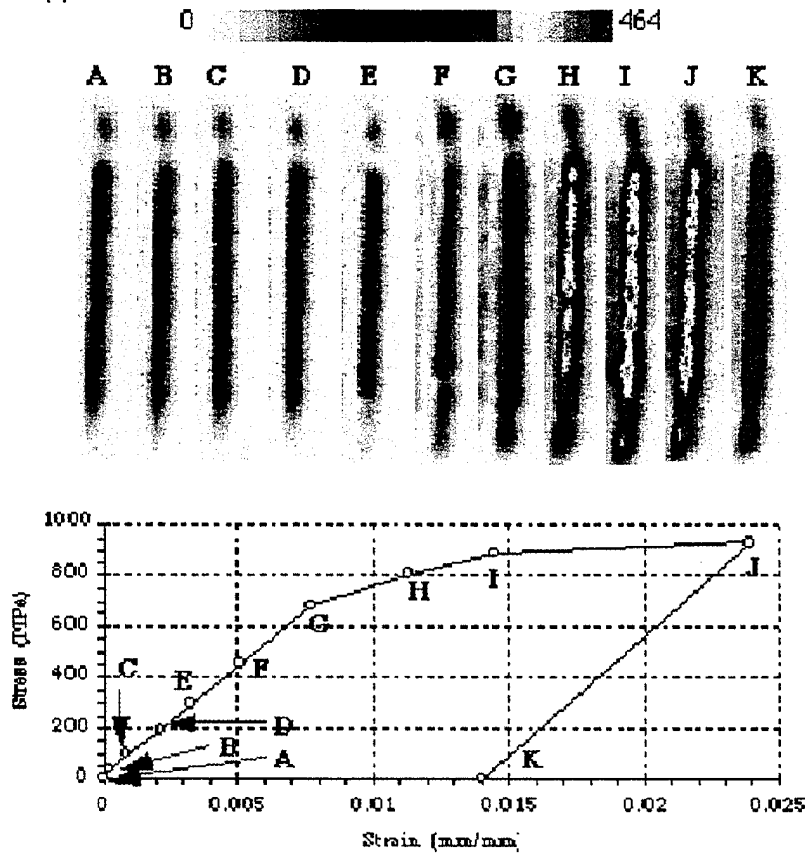


Figure 3-43 *In situ* ultrasonic SBR imaging of a Ti-6Al-4V/SCS-6 single fiber composite sample during various stages of transverse loading.

Figure 3-44 shows the transverse test of another composite system (Ti-6Al-4V/SCS-0). This specimen was tested in the elastic range only. Image 'A' shows the fiber before testing. The local variation in reflected amplitude together with the variation in apparent diameter of the fiber along its length indicate localized poor consolidation along the length of the fiber. The ultrasonic evaluation of poor consolidation is discussed in details in a later section of this report. Image 'B' shows no change of the interface at 100 MPa. Images 'C' through 'F' indicate a slight change in reflected amplitude mainly because of the combination of regions of poor consolidation and the change in residual stresses as the load increases. Images 'D' through 'F' (300-400 MPa) show decreases of the reflected amplitudes at the two ends of the fiber indicating local fracture of the interface and propagation of interfacial cracks.

Finally, it can be seen in Figure 'G' (at 450 MPa) that a drop of reflected amplitude along the entire interface occurs. This is an indication of fracture of the entire interface.

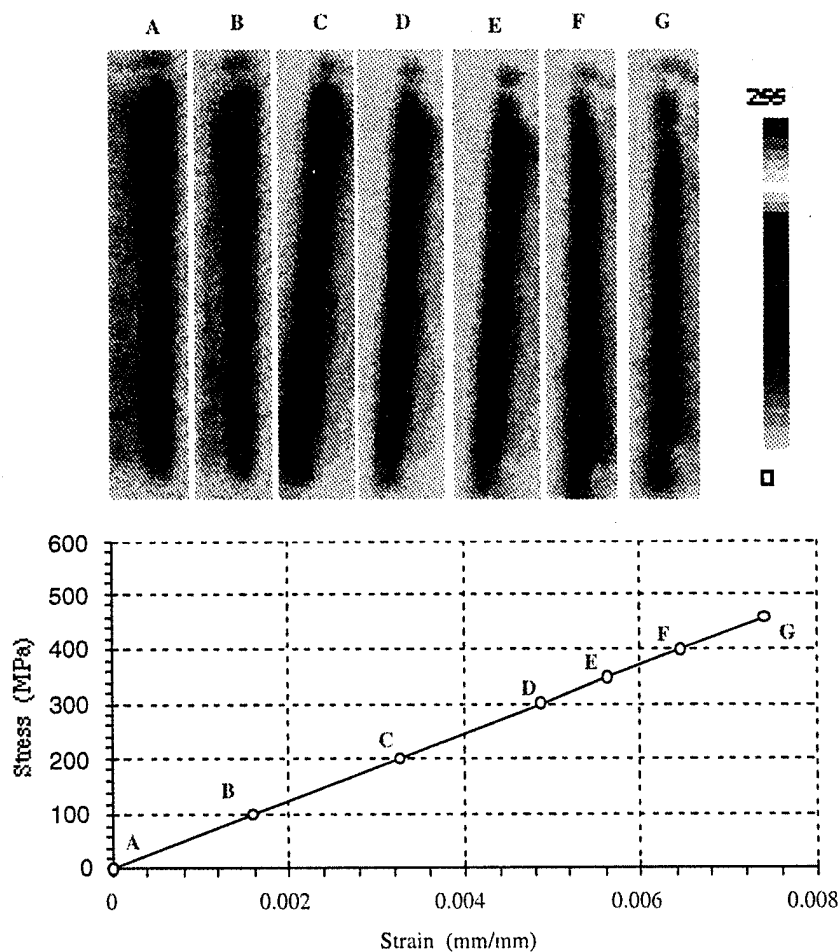


Figure 3-44. *In situ* ultrasonic SBR imaging of a Ti-6Al-4V/SCS-0 single fiber composite sample during various stages of transverse loading.

Figure 3-45 shows again the SBR image of a Ti-6Al-4V/SCS-0 composite sample tested under transverse loading. Image 'A' shows the fiber before testing. Images 'B' and 'C' do not show any change in the interface. Images 'D' (about 350 MPa) and 'E' show interface fracture (drop in reflected amplitude) at the one end (upper) of the fiber. Images 'F' through 'H' show another fracture of the interface at the other end of the fiber. The two cracks are propagating along the interface. Image 'I' (at 600 MPa) shows a drop in signal amplitude indicating that the interface has been entirely fractured. Images 'J' through 'L' show the physical separation between the matrix and the fiber and that the slope of the interface is not the same along the length of the fiber. At about 870 MPa (image 'L') the slope of the interface at some places is perpendicular to the axis of the incident ultrasonic beam.

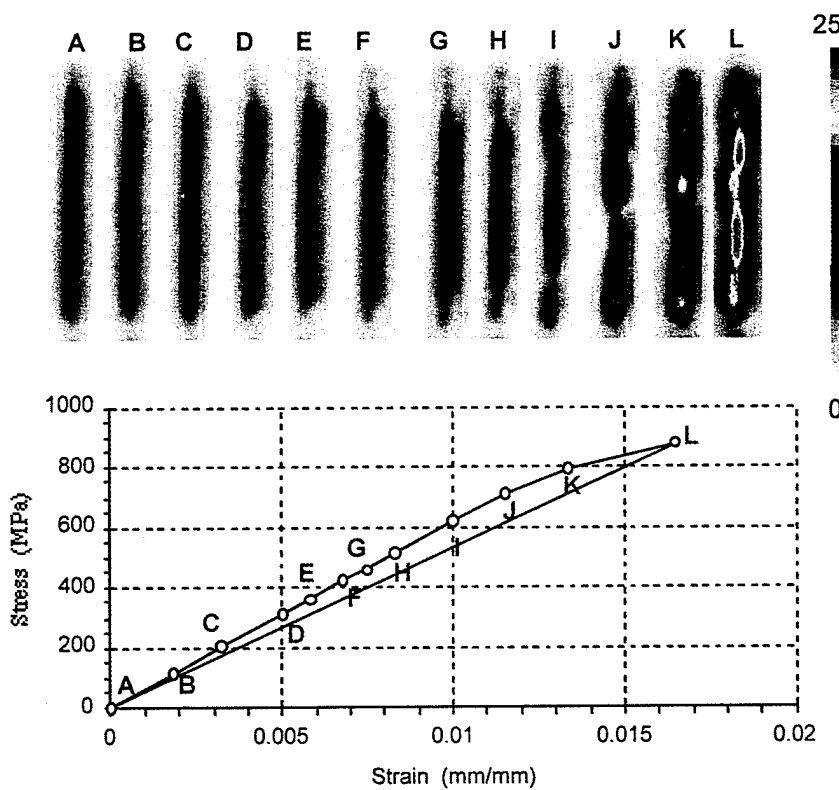


Figure 3-45. *In situ* ultrasonic SBR imaging of a SCS-0 single fiber embedded in Ti-6Al-4V matrix subjected to transverse loading.

Finally a composite with three fibers (SCS-0, SCS-6, SCS-0 with yttria coating) embedded in Ti-6Al-4V matrix is shown in the schematic (Figure 3-46). This sample was subjected to transverse loading.

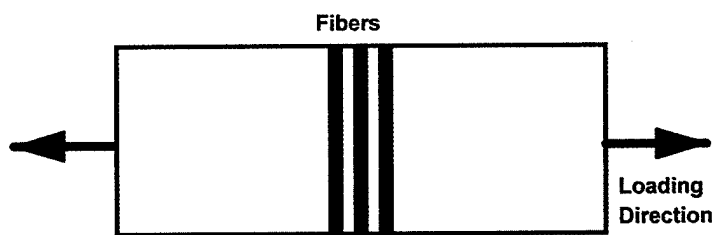
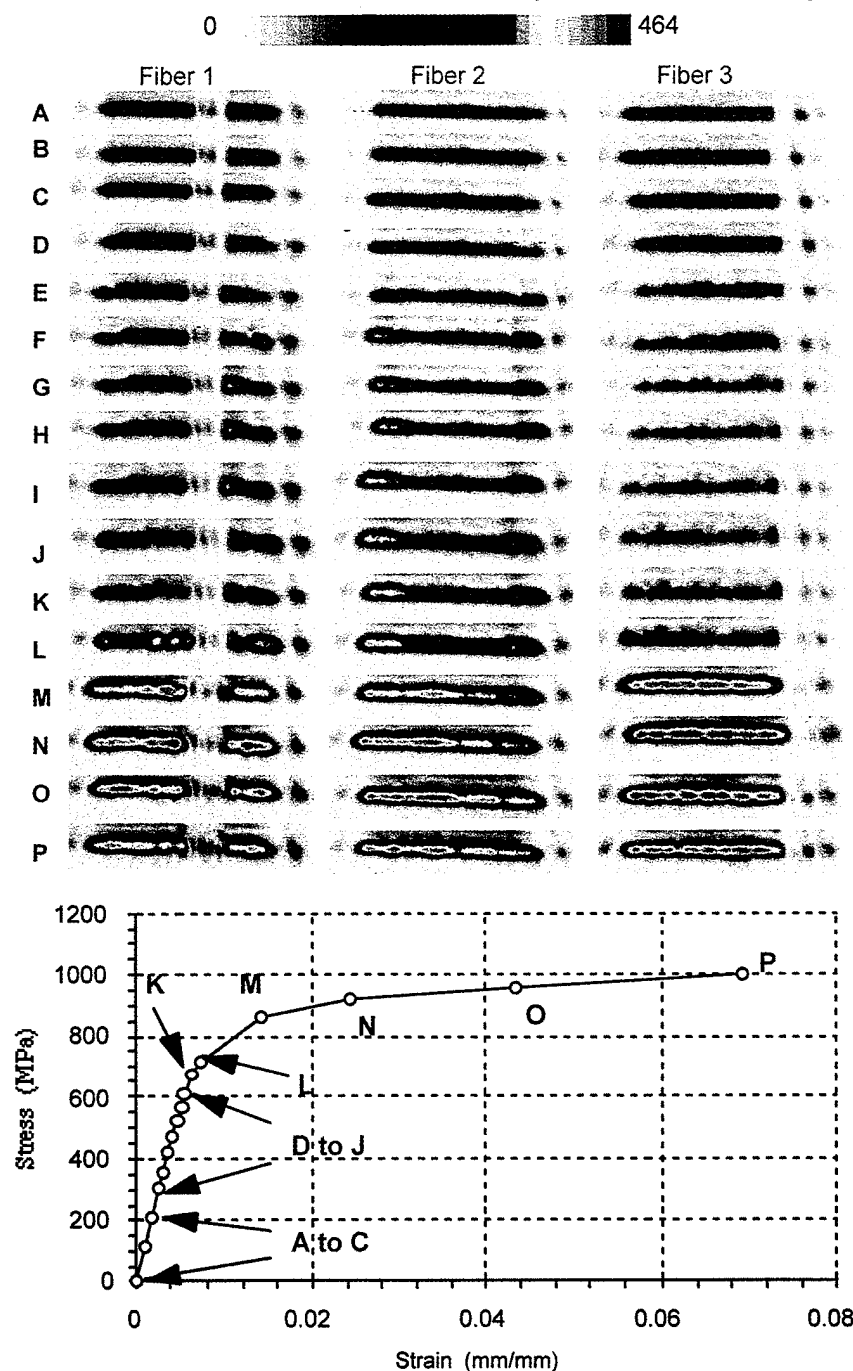


Figure 3-46 Experimental configuration showing transverse orientation of three fibers in a sample, and the direction of loading

Figure 3-47 shows the SBR monitoring of this specimen. Image 'A' is the image of the fibers before loading. The fiber numbered 1 was broken during processing. It can be seen from Figure 3-47 that interface fracture occurred first at one end of the fibers at about 300 MPa (image 'D') and then propagated. The entire interface for fiber 3 was fractured at about 480 MPa (image 'E') as indicated by a drop of reflected amplitude along the entire interface. For fiber 2 fracture of the entire interface is not certain but only estimated at about 420 MPa (image 'F') and for fiber 1 at about 480 MPa (image 'G') because of big change in amplitude in these load stages. Finally, images 'L' through 'P' for the fiber 1, and 'M' through 'P' for the fibers 2 and 3 show the physical separation between the matrix and the fiber. The reason difficulty in

determining the stress at fracture for the entire interface for two of the three fibers is that in the case of a sample with three fibers, the redistribution of stresses is extremely complicated. When the interface fractures at some point along a fiber and an interfacial crack propagates, the next interface region to be fractured can not be predicted because of the stress redistribution. Also, after fracture of the entire interface for all the fibers, the redistributed residual stresses at the interface of the fibers will influence the reflected amplitude on the SBR signal.



**Figure 3-47.** *In situ* ultrasonic imaging of the transverse test of a Ti-6Al-4V matrix composite made with three fibers (SCS-0, SCS-6, SCS-0 with Yttria coating).

The model monofilament composite used for the transverse loading experiment was made with an embedded fiber with exposed ends as shown in Figure 3-35. Ultrasonic imaging of such a fiber always showed dumbbell shaped ends [Hu et al., 1994] as seen in Figure 3-48a. However, when a completely embedded fiber was imaged, such a dumbbell appearance was not seen as in Figure 3-48b. This behavior is due to the presence of tensile residual stress at the exposed end of the fiber-matrix interface, as it is explained in the next paragraphs.



Figure 3-48. Ultrasonic shear wave images of (a) a fiber with free edge, and (b) a completely embedded in the matrix fiber.

The free edge model by Pagano and Pipes [Pagano, 1991 and Pipes & Pagano, 1970] was used to calculate the radial residual stresses at the fiber-matrix interface of the test sample being evaluated. The model [Pagano, 1991] is based on elasticity theory for the free edge effect in a single fiber composite and predicted a reversal in sign of the radial stress in the edge region. For composites of titanium matrix reinforced with silicon carbide fibers, the matrix coefficient of thermal expansion (CTE) is much larger than the fiber CTE, resulting in a large and negative (compressive) thermally-induced residual radial stress in the interior of the body. However, in the neighborhood of the singular point (within less than a fiber radius from the edge) the analysis predicted a very steep gradient in radial stress causing the stress to vary from negative to positive (tensile) as shows Figure 3-49.

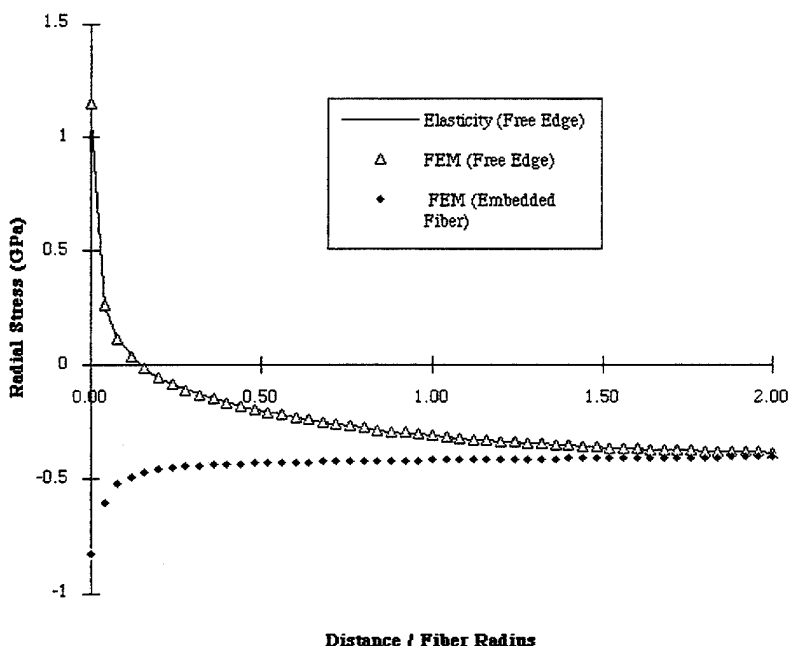


Figure 3-49. Interfacial radial stress distribution near the fiber tip.

### *The Role of Residual Stress in the Ultrasonic Imaging of Fiber-Matrix Interface*

In addition to the Pagano and Pipes [Pagano, 1991 and Pipes & Pagano, 1970] model, a two-dimensional axisymmetric finite element analysis was used to predict the state of stresses. The commercially available finite element package ANSYS was used for this analysis. The mesh in the region of interest was very fine so that the shear stress and longitudinal normal stress was very close to zero at the free edge. This satisfied the free surface boundary conditions. The stress results in the neighborhood of the singular point show excellent agreement with the elasticity model [Pagano, 1991] as shown in Figure 3-49.

The existence of large tensile stresses of about 1 GPa (Figure 3-49) at the free end of the fiber (higher than the stress at fracture of the interface) leads to the existence of an interfacial crack growing a few microns along the interface. Therefore, finite element analysis was performed to simulate the cracking behavior using bi-linear contact elements at the possible fracture area. The contact element incorporates a bi-linear stress/strain relationship under loading. When in tension, the element does not function. This allows the separation of fiber and matrix. When in compression, the element functions like a stiff spring and satisfies displacement continuity. By performing a similar finite element analysis for a single fiber completely embedded in the matrix, it has been found that the radial stress remains negative throughout entire interface (Figure 3-49) thereby no pretest interface crack was predicted. This confirms the observation in Figure 3-48a and 3-48b suggesting that the reason for the appearance of the dumbbell shape is phase alteration of the reflected wave caused by the existence of the pretest interfacial cracks in the case of a fiber with exposed ends. If the focal zone of the ultrasonic beam covers part of the bonded interface area with compressional residual stress, and part of the crack area initiated because of the large tensile residual stress, the signal can be canceled due to the phase reversal of the wave reflected from the two regions. This is described in the section on fiber fragmentation and can be found in the literature [Karpur et al., 1992 and Karpur et al., 1992]. Using the SBR technique together with the phenomenon of signal phase alteration, it is feasible to detect an interfacial crack which is much smaller than the ultrasonic wavelength. This provides a nondestructive technique for detecting defects which usually are too small to detect using conventional ultrasound.

In conclusion, the above results indicate that the SBR technique is sensitive to the fracture and deformation of the interface in metal matrix composites as well as the amount and sign of the residual stresses at the interface. The information provided by the SBR technique is complementary [Shaw et al., 1994] to the information obtained by other experimental techniques and analyses including the replica method, metallography, electro-etching of the matrix, acoustic emission, elasticity modeling, and Finite Element Analysis. Moreover the SBR technique is extremely useful for providing unique information not only about the stress at

fracture of the interface but also about the propagation of damage and the role of the redistribution of residual stresses in the interface damage behavior.

Another important benefit of ultrasonic nondestructive evaluation of interface damage under transverse loading conditions is the possibility to determine the initiation of fracture of the fiber-matrix interface and the corresponding applied load. The value of the measured applied load can be used to calculate the stress at the fiber-matrix interface (taking into account the stress concentration). The calculated applied stress as well as the local residual stresses can be used together to determine the stress at fracture of the weakest portion of the fiber-matrix interface, thereby defining a '**minimum stress at fracture (MSF)**' of the fiber-matrix interface. The MSF could be used as an important parameter to assess and compare the overall performance of different composite systems.

### **3.3 Ultrasound for Post-Processing NDE of Fiber-Reinforced Metal Matrix and Ceramic Matrix Composites**

An ultrasonic nondestructive evaluation methodology has been developed for characterization of the consolidation and microstructure of advanced composites. This NDE methodology will optimization of processing parameters so that the desired microstructure can be achieved in metallic matrices and complete densification around the fibers can be achieved in MMCs and CMCs. The methodology can be used to ensure that the composite panels are devoid of any global problems such as fiber swimming, ply delamination, embedded manufacturing anomalies, etc. A guide to subsection 3.3 is provided in Exhibit 3-3 below.

<b>SUMMARY OF SECTION 3-3</b> <b>Ultrasound for Post-Processing NDE of Fiber-Reinforced Metal Matrix and Ceramic Matrix Composites</b>	
<b>3.3.1 Evaluation of Consolidation in Metal Matrix and Ceramic Matrix Composites</b> <b>OBJECTIVE:</b> Develop an ultrasonic NDE method to assess the consolidation of MMCs and CMCs <b>JUSTIFICATION:</b> Good consolidation is important for achieving the required performance parameters for these materials. No reliable nondestructive means for evaluating consolidation currently exists. <b>RESULTS:</b> Developed a combined approach using longitudinal and shear waves ( <b>SBR</b> ) for evaluating the degree of lack-of-consolidation in MMCs and CMCs. Demonstrated the feasibility of using that combined approach for evaluating the improvements in matrix consolidation which accrue from reprocessing * <b>Importance</b> -- this methodology, when fully developed should be very useful for improving the fabrication processes of MMCs and CMCs and for controlling the fabrication processes once they are established	
<b>3.3.2 Characterization of Matrix Microstructure and Morphology in Titanium Matrix Composites</b> <b>OBJECTIVE:</b> Develop an ultrasonic nondestructive method fro evaluating matrix microstructure and morphology of titanium matrix composites <b>JUSTIFICATION:</b> Proper microstructure is essential for achieving the required performance parameters of this material. No reliable nondestructive means for evaluating this microstructure exists. <b>Results:</b> Developed an approach for characterizing microstructure and morphology by the concurrent use of shear waves ( <b>SBR</b> ) and normal-incidence, high-frequency longitudinal waves Improved the reliability of nondestructive detection of coarse plate-like alpha plus beta microstructure * <b>Importance</b> -- evaluation of internal microstructure is important because undesirable microstructure, especially at the fiber-matrix interface can result in inferior mechanical properties	

### **3.3.1 Evaluation of Consolidation in Metal Matrix and Ceramic Matrix Composites**

Ultrasonic NDE techniques have been used in the past for global inspection of composites to determine the distribution of reinforcements and to detect defects present in composite panels [Johnson, 1989]. In the case of fiber-reinforced metal matrix composites, ultrasonic methods have been employed to screen for macroscopic defects such as ply delaminations and nonuniform fiber spacing arising from either missing fibers or displacement of fibers during fabrication [Johnson, 1989 and Liaw, et al., 1992]. The ultrasonic approach outlined in this section describes a methodology for evaluating consolidation on a "microscopic" localized level. The development of this methodology is in response to a need for a quick and reliable tool for post-processing evaluation of the consolidation of advanced composites. An outline of the results obtained from this study are provided above.

SUMMARY OF RESULTS Matrix Consolidation Study	
<b>1. Longitudinal Waves</b>	a. are <i>not</i> sensitive to fiber-matrix interface conditions when the interface is well consolidated b. are sensitive to lack-of-consolidation or delamination between the matrix-alloy foils or sheets and can be used to image such zones c. are useful for detecting macroscopic defects in composites with a high volume fraction of fibers
<b>2. Back-Reflected Shear Waves (SBR)</b>	a. can be used to determine the extent of an interface void (due to lack-of-consolidation) by varying the incidence angle b. are sensitive to fiber-matrix interface conditions even when the interface is well consolidated c. are useful for studying the outermost layer of fibers in a composite with a high volume fraction of fibers d. can be used to evaluate matrix porosity in CMC matrices e. can be used during CMC-reprocessing efforts to evaluate improvements in matrix consolidation at the interface and to evaluate reductions in matrix porosity

#### **3.3.1.1 Processing of Advanced Composites**

Composites based on reactive matrices with high melting temperatures such as titanium alloys are usually processed by solid state diffusion bonding of matrix foils, powders, or sprayed deposits with reinforcements [Bampton, et al., 1993]. For example, the processing of continuously reinforced titanium matrix composites by the foil-fiber-foil method typically involves diffusion bonding of rolled matrix alloy foils with reinforcing fibers in the form of woven mats with a cross-weave to hold the fibers in place [Larson, et al., 1992]. The foils and the fiber mats are stacked alternately and consolidated by vacuum hot pressing or hot isostatic pressing. The processing conditions are carefully selected to achieve complete consolidation and produce acceptable composite material. While higher temperatures and longer processing times may enable consolidation, they can promote undesirable reactions at the fiber/matrix interface and also cause high residual stresses after the composite is cooled to ambient temperature. On the other hand, lower processing temperatures can lead to fiber damage as well as incomplete consolidation. In practice, optimum processing conditions are determined through preliminary diffusion bonding experiments using small samples. The initial processing temperatures are chosen on the basis of known flow characteristics of the matrix alloy at different temperatures

and strain rates, and the consolidation of these samples is checked by metallographic examination of polished sections. However, the use of metallography alone is generally inadequate since consolidation often occurs nonuniformly within the composite panels.

Densification problems can also be seen in the fabrication process of continuously reinforced ceramic matrix composites made by tape casting to obtain uniform fiber spacing [Gustafson and Dutton, 1994]. Photo-micrographic analysis to detect poor consolidation in CMC is again inadequate to provide reliable results.

In this section, it will be demonstrated that ultrasonic NDE is a valuable tool for post-processing detection of microscopic consolidation defects arising during the fabrication of composites and that ultrasonic NDE can be reliably used to minimize the number of iterations required for optimization of the consolidation process. The application of two different ultrasonic techniques involving shear wave and longitudinal wave interrogations for evaluating the consolidation of advanced composites will be discussed. The examples provided here consist of ultrasonic evaluation of consolidation in various material systems including both metal matrix and ceramic matrix composites having various configurations (single fiber/ply etc.). Finally, in the case of ceramic matrix composites, the influence of residual stress, degree of wetting of the fiber coating by the matrix, and re-processing, on the degree of consolidation will be discussed.

### **3.3.1.2 Fabrication of Single Fiber Titanium Matrix Composites**

These model composites consisting of an SCS-6 SiC fiber in a Ti-14Al-21Nb (wt. %) alloy matrix were fabricated in the form of 2 mm thick panels by diffusion bonding two matrix alloy sheets with a single fiber between them using two different processing conditions: (1) vacuum hot pressing at 925°C with 5.5 MPa pressure for 30 minutes followed by hot isostatic pressing (HIP'ing) at 1010°C with 100 MPa pressure for 2 hours (Panel A), and (2) vacuum hot pressing at 982°C with a pressure of 9.2 MPa for 30 minutes (Panel B).

#### *Fabrication of Single Ply Titanium Matrix Composites*

The single ply composites consisted of a layer of SCS-6 SiC fibers in a Ti-6Al-4V (wt. %) alloy matrix. These were also fabricated in the form of 2 mm thick panels by vacuum hot pressing at 954°C under a pressure of 9.2 MPa for 2 hours (Panel B).

#### *Fabrication of Fiber Reinforced Ceramic Matrix Composites*

The composites were processed by tape casting the glass powder into a green tape with a relative density of 50%. The green tapes were cut to size and laminated with fiber mats of the desired SiC fiber spacing (68 or 120 fibers per inch). The volume fraction of fibers in the composites was varied by altering the thickness of the green tape and using the two different fiber spacings. After lamination the composites were inserted into a tube furnace and vacuum sintered at 710°C for one hour. The samples were then hot isostatically pressed at 650°C for

30 minutes with an applied pressure of 35 MPa to remove the residual porosity (~2%). The resulting samples were approximately 100 mm long by 2 cm wide with a thickness of 2 mm.

### 3.3.1.3 Ultrasonic Experimental Approach

The samples made as described above were ultrasonically imaged using two different techniques: (1) shear wave interrogation and (2) longitudinal wave interrogation. Figures 3-50 and 3-51 show schematics of these two techniques, respectively. In the shear wave technique, a 25 MHz focused transducer (6.3 mm diameter, 12.7 mm focal length) was used in the pulse-echo mode. The ultrasonic wave front was incident on the specimen surface inclined to the vertical plane at an angle between the first and the second critical angles. As a result, only vertically polarized shear waves propagated in the matrix with a refraction angle ' $\theta_s$ ' (given by the Snell's law). These shear waves were incident on the fiber/matrix interface (Figure 3-50).

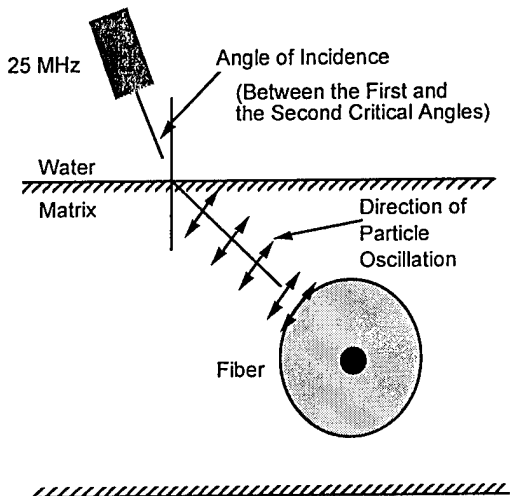


Figure 3-50. Schematic diagram of the transverse section of a continuously reinforced composite showing shear wave interrogation of a fiber embedded in the matrix.

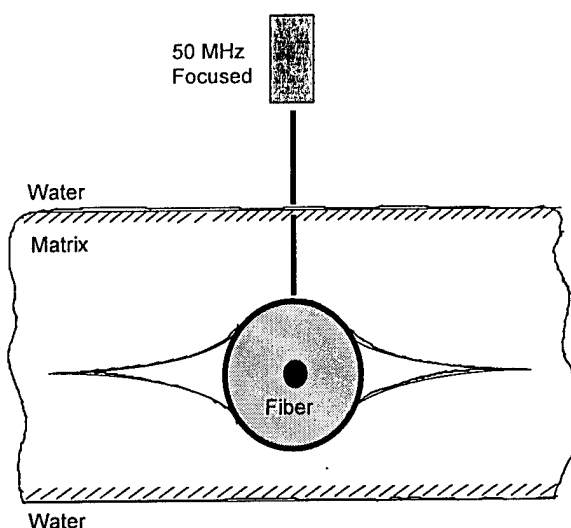
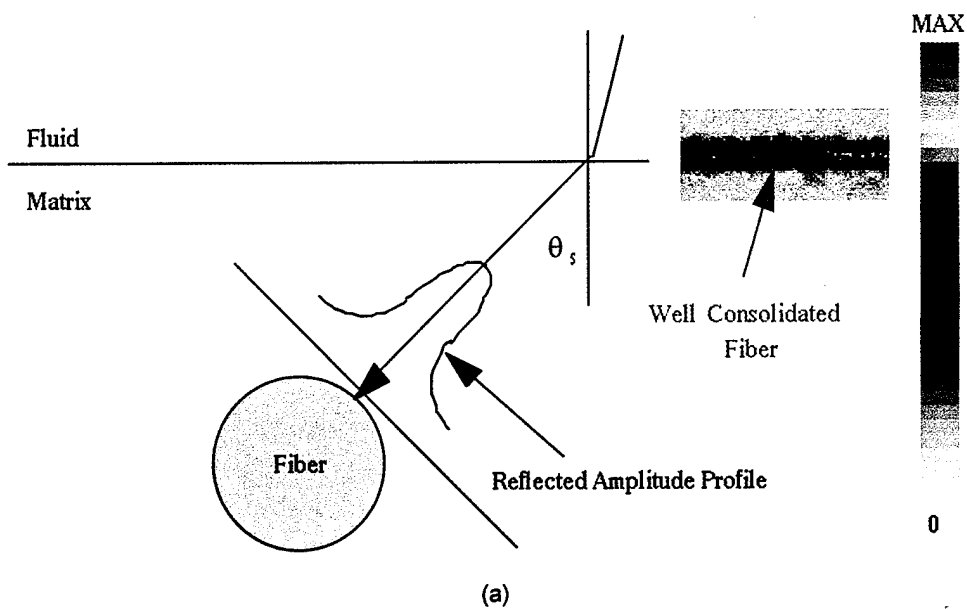
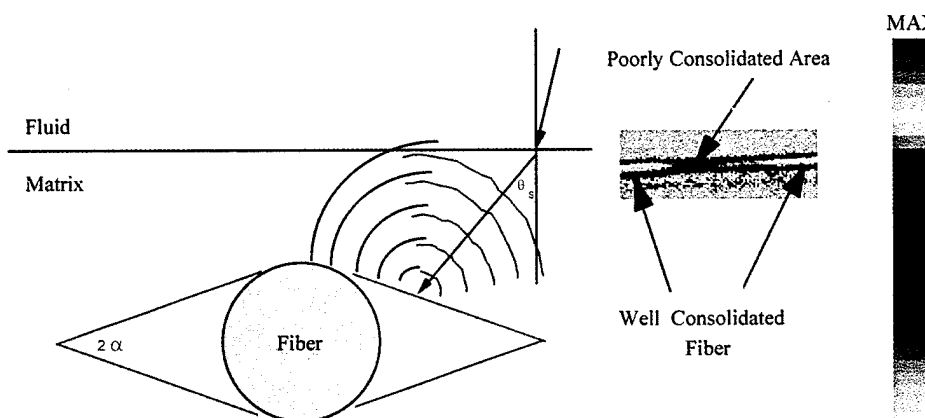


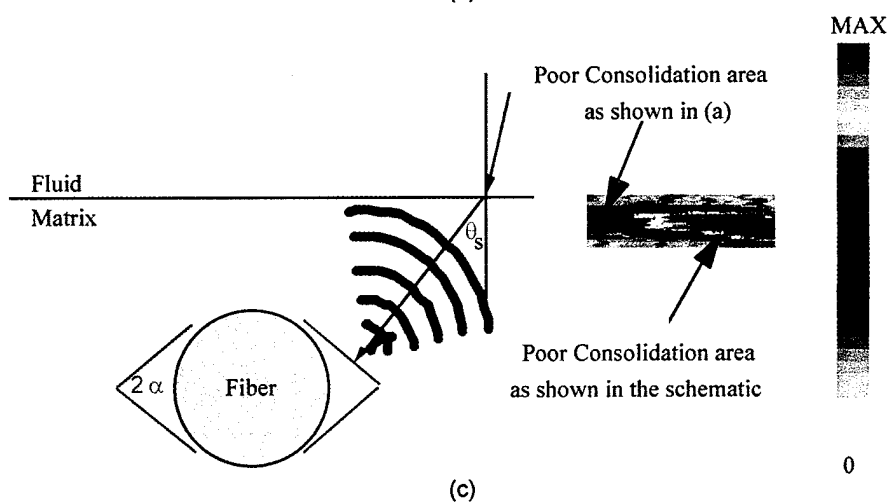
Figure 3-51. Schematic diagram of the transverse section of a continuously reinforced composite showing longitudinal wave interrogation of a fiber embedded in the matrix.

The ultrasonic image of fibers with different degrees of consolidation depends on the angle of incidence of the beam and the shape of the cross-section of the poor consolidation area. Figure 3-52a shows the reflected shear wave amplitude from a fiber in a fully densified composite. The reflected amplitude is maximum at the center of the fiber (which is a cylindrical reflector) and is gradually reduced as the transducer is scanning away from the center of the fiber. Figure 3-52b shows a general case of reflection of ultrasound from a fiber with poor consolidation where ' $\alpha$ ' is the half angle of poor consolidation and is related to the shape of the defect. Here, the embedded reflector in the matrix is non cylindrical in shape as shown in Figure 3-52b. Therefore, the wave will be reflected away from the receiver and only a small part of the energy (which is incident on the region close to the top of the fiber) will come back to the transducer, thereby distorting the ultrasonic image of the fiber. Consequently, the image of the fiber will appear with a smaller diameter compared to a well consolidated fiber, and also the reflected ultrasonic amplitude will be lower (see color scale in Figure 3-52b). In Figure 3-52c, the half angle of poor consolidation is equal or close to the refraction angle of shear waves. In this case, a strong reflection is expected from the defect. The image of the fiber will appear much larger in diameter compared to a well consolidated fiber, and also the reflected ultrasonic amplitude will be maximum (total reflection). Figure 3-52d shows another type of defect which is a complete debond around the fiber. In this case the reflected ultrasonic amplitude will be maximum in the center of the fiber and will be reduced as the transducer is moving away from the center of the fiber. The image of the fiber will appear in this case with a diameter slightly larger than the well consolidated fiber and with maximum reflected amplitude.

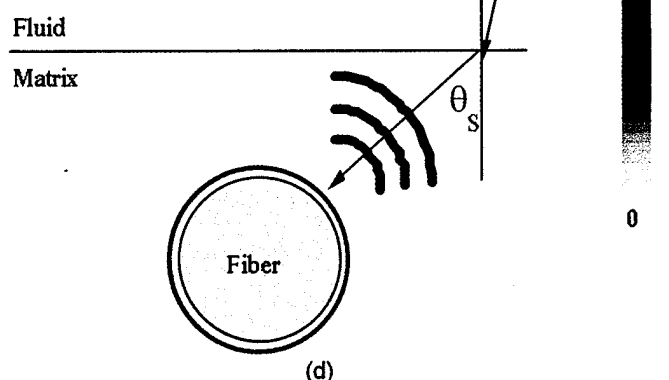
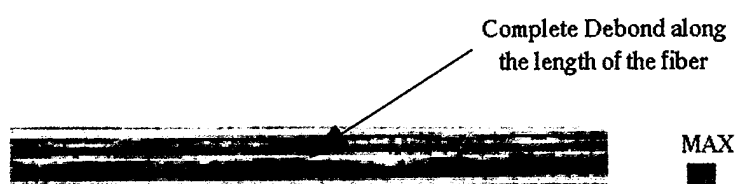




(b)



(c)

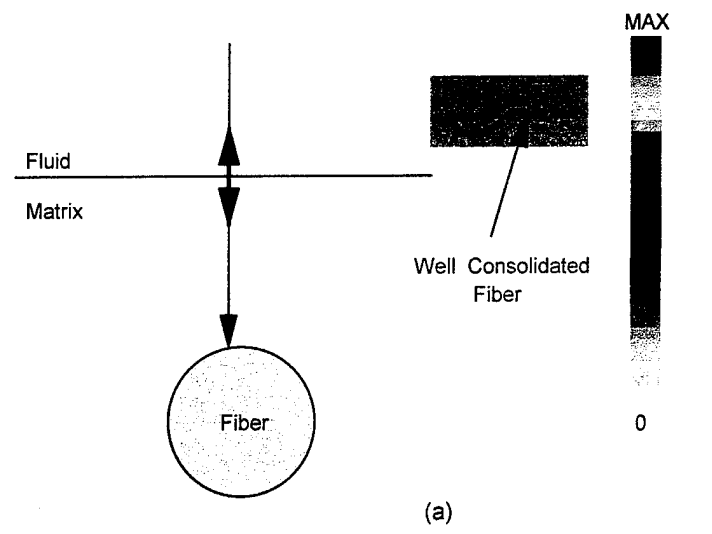


(d)

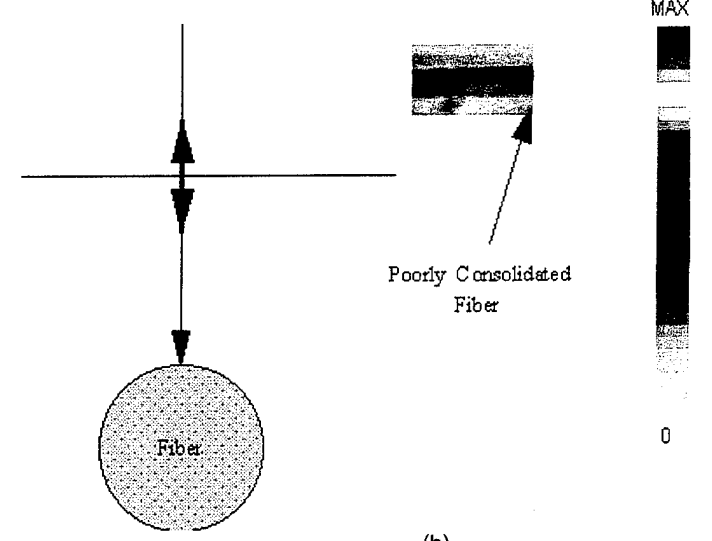
Figure 3-52. Amplitude of oblique-incidence shear waves back-reflected from fiber matrix interface with: (a) good consolidation, (b) regions of poor consolidation with  $\alpha \neq \theta_s$ , (c) poor consolidation with  $\alpha = \theta_s$ , and (d) complete debond around the fiber.

In the longitudinal wave technique, a 50 MHz focused transducer (6.3 mm diameter, 25.4 mm focal length) was used in the pulse-echo mode and the wave front was incident normal to the specimen surface. Under this condition, a compressional wave propagates in the matrix and is reflected from the fiber back to the transducer. The reason for using a transducer of a different frequency for the longitudinal wave technique is as follows. The wavelength of the wave propagating in the matrix is calculated by the simple expression,  $\lambda = c_i / f$ , where  $c_i$  is the velocity of the ultrasonic stress wave ( $c_i = c_S$  or  $c_L$  for a shear or a longitudinal wave, respectively) and  $f$  is the frequency of interrogation. In the case of the Ti-14Al-21Nb matrix alloy, the velocity of the shear wave generated by the 25 MHz transducer was measured to be  $c_S = 3209$  m/sec and, therefore, the wavelength was about 130  $\mu\text{m}$ . The velocity of the longitudinal wave propagating in the same matrix was measured to be  $c_L = 6489$  m/sec, which is approximately twice the shear wave velocity. Since the frequency of longitudinal wave interrogation was twice that of shear wave interrogation, the wavelength remained the same (about 130 microns). Consequently, the two interrogation techniques can be directly compared based on the same resolution in terms of wavelength. In the case of normal incidence longitudinal wave interrogation, and when a well consolidated fiber is imaged (Figure 3-53a), the amplitude of the signal which is reflected back to the transducer will be small and the fiber will be barely visible. However, when a situation similar to the configuration in Figure 3-53b is present, a higher amplitude signal will be reflected back to the transducer and the image of the fiber will be as shown in the Figure 3-53b. Finally, when  $\alpha$  is equal or close to  $0^\circ$  (implying delamination between plies), total reflection from the defect will be observed as shown in Figure 3-53c. A maximum reflected signal will also be observed in the case of a complete debonding around the fiber.

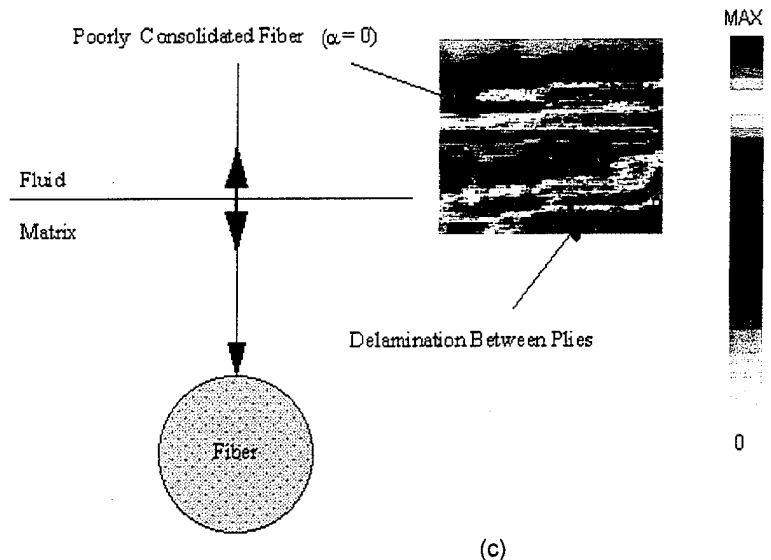
In both shear wave and longitudinal wave interrogation techniques, the image of the fiber was obtained by scanning the ultrasonic transducer along and across the fiber with an increment of 25  $\mu\text{m}$  between signal acquisition points. At each point, the back-reflected ultrasound was software-gated for imaging [Buynak, et al., 1989]. The ultrasonic techniques had been used to evaluate the Ti-14Al-21Nb/SiC single fiber composite samples and the Ti-6Al-4V/SiC single-ply composite specimens. The same ultrasonic techniques had also been used for evaluating the SiC glass matrix composites. In the case of a single-ply composite, because of the small spacing between fibers, a smaller angle of incidence was used ( $19^\circ$ ) to image the fibers without overlapping. The elastic properties of the matrix material (Ti-6Al-4V) used for the single-ply composites are close to the properties of the matrix material (Ti-14Al-21Nb) used for the single fiber composites, so the ultrasonic velocities in the matrix are practically the same and the wave-length of ultrasound remains the same (about 130  $\mu\text{m}$ ). The ultrasonic wave-length in the case of the ceramic matrix was also close (about 132  $\mu\text{m}$ ) to that in titanium composites.



(a)



(b)



(c)

Figure 3-53. Amplitude of normal-incidence longitudinal wave back-reflected from fiber-matrix interface with: (a) good consolidation, (b) poor consolidation with larger reflected amplitude than for good consolidation, and (c) poor consolidation with  $\alpha \approx 0$ .

In the case of metal matrix composites, the correlation between the ultrasonic image and the local microstructure was also studied. Therefore, the composite specimens were sectioned normal to the fiber axis at several locations along the fiber. These sections were metallographically polished and examined by optical microscopy.

### 3.3.1.4 Results and Discussion - MMC

The ultrasonic images of the Ti-14Al-21Nb/SiC single fiber composite sample which was processed by vacuum hot pressing followed by HIP'ing (Panel A) are shown in Figure 3-54. Figure 3-54a corresponds to shear wave interrogation and shows uniform reflection along the fiber. Figure 3-54b shows the image resulting from longitudinal wave interrogation of this material and indicates that the reflected signal is uniformly weak along the length of the fiber.

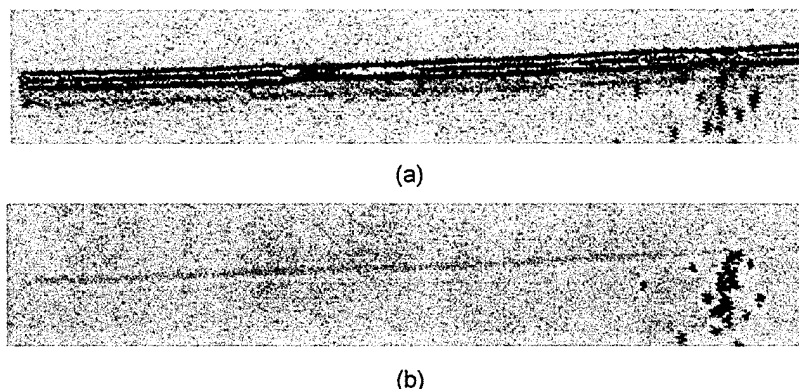


Figure 3-54. Ultrasonic image from Ti-14Al-21Nb/SiC sample which was consolidated by vacuum hot pressing + HIP'ing (Panel A) -- (a) oblique-incidence ( $24^\circ$ ) shear wave, and (b) normal-incidence longitudinal wave.

Figure 3-55 shows two ultrasonic images of the composite sample consolidated by vacuum hot pressing alone (Panel B). The images were obtained by shear waves interrogation at two different angles of incidence. The use of different angles of incidence helps to determine the

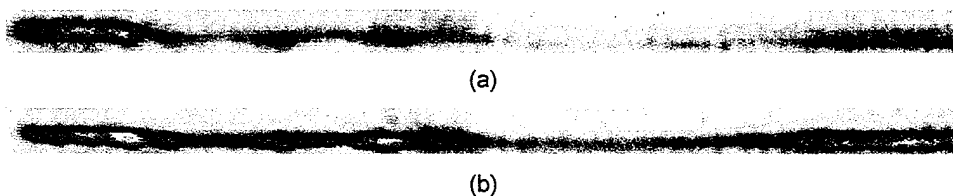


Figure 3-55. Ultrasonic images from Ti-14Al-21Nb/SiC single fiber composite (Panel B) using shear wave interrogation with different angles of wave front incidence: (a)  $18^\circ$  and (b)  $24^\circ$ .

value of  $\alpha$  and to map the shape of the consolidation defect. In the example shown in Figure 3-55, the two images of the fiber indicate significant variations in the reflected intensity along its length. The variation in amplitude of the images is because, by varying the angle of incidence thereby varying the refracted angle of shear waves,  $\theta_S$ , the difference between the angle of poor consolidation,  $\alpha$  and  $\theta_S$ , also varies. As seen from Figure 3-55, this difference becomes smaller for an angle of incidence of  $24^\circ$  (Figure 3-55b) than for  $18^\circ$  (Figure 3-55a). Hence, for this

particular case,  $\alpha$  is closer to  $\theta_S$  for an incidence of  $24^\circ$  than of  $18^\circ$ . Figure 3-55 also shows a nonuniformity of the defect in this panel. The nonuniformity in this panel is also evident from the image obtained by longitudinal wave interrogation (Figure 3-56).

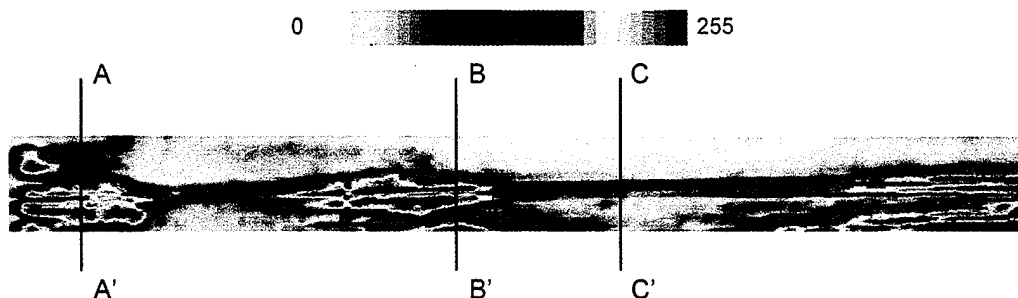


Figure 3-56. Ultrasonic image from Ti-14Al-21Nb/SiC single fiber composite (Panel B) using longitudinal wave interrogation. AA', BB', and CC' indicate sections at which metallographic samples were examined.

An optical micrograph from a cross section of the composite panel A is shown in Figure 3-57. This micrograph shows that the consolidation of the matrix around the fiber is complete in this composite. This result was typical of the various cross sections examined,

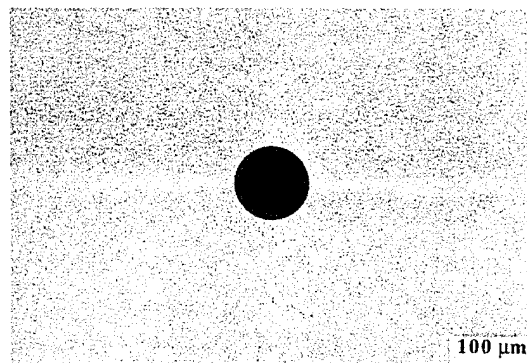


Figure 3-57. Optical micrograph of Ti-14Al-21NB/SiC single fiber composite (Panel A) sample showing good consolidation.

suggesting that the consolidation occurred uniformly within the panel A. Figure 3-58 shows optical micrographs taken from the composite panel B corresponding to the sections AA', BB' and CC' which are indicated in Figure 3-56. It is clear from these micrographs that the bonding of the matrix alloy sheets is incomplete around the fiber. Further, there is a considerable variation in the degree of bonding of the matrix along the length of the fiber (Figure 3-58).

A good correlation is found between the microstructure of the composite panels and the observed ultrasonic images. These results show that the diffusion-bonding conditions used for processing of panel B did not lead to complete consolidation, whereas panel A was fully consolidated. These results are in general agreement with previous observations dealing with the sequence of events during the consolidation of such composites by the foil-fiber-foil method [Guo & Derby, 1992 and Nicolaou, et al., 1992]. When the foil-fiber-foil preform is subjected to

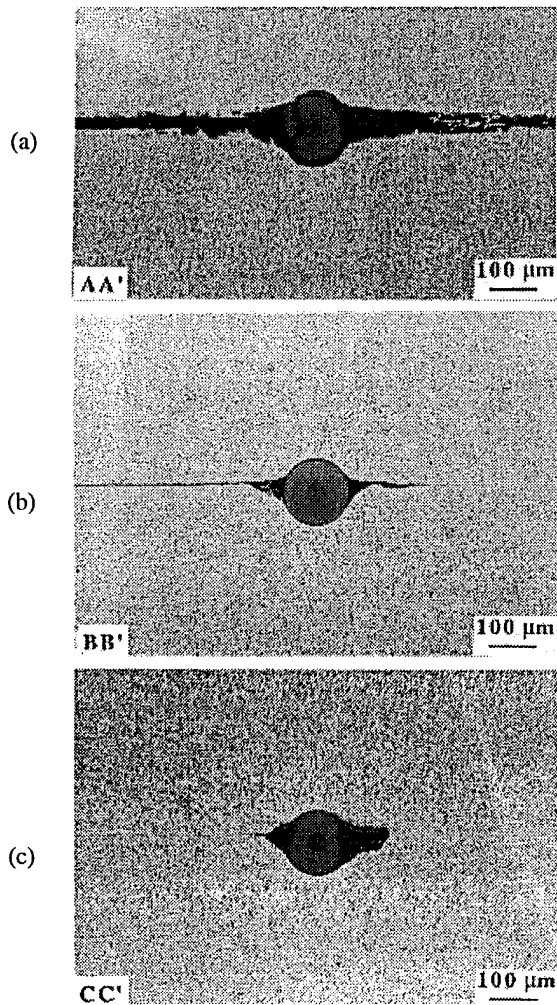


Figure 3-58. Optical images of fiber-matrix interface which correspond with specific regions across the C-scan image in Figure 3-56: (a) across AA', (b) across BB', and (c) across CC'.

elevated temperature under pressure, the process begins with the indentation of matrix alloy foils by the fibers and is followed by matrix creep, leading to diffusion-bonding between the foils. At the end of this stage, two large pores remain on opposite sides of each fiber along the bond plane of the foils due to lower local stresses [Guo & Derby, 1992; Nicolaou, Piehler & Saigal, 1992; Nicolaou, Piehler & Saigal, 1995; Nicolaou, Piehler & Kahni, 1991; and Nicolaou, Piehler & Saigal, to be published] as observed in Figure 3-58. The composite is fully consolidated when these remnant voids near the fibers are eliminated (Figure 3-57). The present results also indicate that consolidation can occur nonuniformly along the length of the fiber (Figure 3-58). Clearly, metallographic characterization alone is tedious under such conditions and other techniques such as ultrasonic NDE will be very useful.

The ultrasonic images are formed when ultrasonic energy is reflected from the scattering cross-section of a reflector (cylindrical fiber) present in the path of wave propagation through a homogeneous medium (matrix). In the present application, the matrix may be

assumed to be homogeneous since the wavelength of interrogation ( $130\text{ }\mu\text{m}$ ) is large compared to the average grain size of the matrix ( $<10\text{ }\mu\text{m}$ ).

In the case of shear wave interrogation, mode-converted shear waves propagate through the matrix and are back-scattered from the fiber (Figure 3-50). When the matrix is completely consolidated around the fiber, the maximum of the reflected signal occurs when the polarized shear waves propagating in the matrix are incident perpendicular to the ruled surface of the cylindrical fiber as indicated in Figure 3-52a. It should be noted that the maximum of the received energy corresponds to the main lobe of the Bessel function which is the theoretical response of a cylindrical reflector embedded in a medium [Schultz & Neubauer, 1977]. Thus, a well-consolidated sample will provide an image as shown in Figure 3-54a. On the other hand, when the composite is poorly consolidated, the reflector is defined by the envelope that includes both the fiber and the void regions. In other words, the reflector boundaries are the matrix-fiber boundaries together with the matrix-void boundaries and, therefore, the reflector has a non-cylindrical shape (Figure 3-50b). In this case, the reflected signal can have either low or high amplitudes due to shear wave scattering from matrix-void regions which usually have variable curvatures as explained before. For a given angle of incidence of ultrasonic waves on the surface of the composite panel, the angle of refraction of the shear waves propagating in the matrix is defined according to Snell's law [Krautkrämer & Krautkrämer, 1990]. By changing the angle of incidence, the effect of the slope of the matrix-void boundary can be evaluated and the optimum angle of incidence corresponding to the maximum ultrasonic signal from that boundary may be determined. The use of different angles of incidence as shown in Figure 3-55 is thus necessary in order to determine the extent of the void. Furthermore, because of the variable slope and hence different 'effective scattering cross-section' of the reflector, the image of the fiber appears to possess a variable diameter along its length. This implies that the void shape varies along the length of the fiber due to nonuniform consolidation.

In the case of longitudinal wave interrogation, compressional waves are incident normal to the surface of the panel specimen as well as the foil-foil interface as shown in Figure 3-51. When the composite is fully consolidated, longitudinal waves are much less sensitive to various fiber-matrix interfacial conditions as compared to shear waves [Matikas & Karpur, 1993] and the reflected amplitude does not show any wide fluctuations (Figure 3-54b). However, the normal incidence longitudinal waves are sensitive to any lack of consolidation or delamination between the matrix alloy foils or sheets and will produce high reflected ultrasonic amplitudes which can be mapped to outline these zones as observed in Figure 3-56.

Although these results were obtained from a model composite containing a single fiber, these ultrasonic techniques are equally applicable for studying the consolidation of real composites containing a high volume fraction of fibers. Figure 3-59 shows an image obtained by shear wave interrogation of a Ti-6Al-4V/SiC single-ply composite specimen. The non

uniform reflection along a number of fibers is evident, implying global poor consolidation. Metallographic examination of sections from the uniform region of a sample confirmed good consolidation as shown in Figure 3-60. Metallographic sections corresponding to the regions of nonuniform reflection revealed incomplete consolidation similar to the results shown in Figure 3-58. With regard to the evaluation of composites containing a high volume fraction of fibers, it should be noted that the shear wave technique is useful for studying the outermost layer of fibers while the longitudinal wave interrogation is more suited for detecting macroscopic defects.

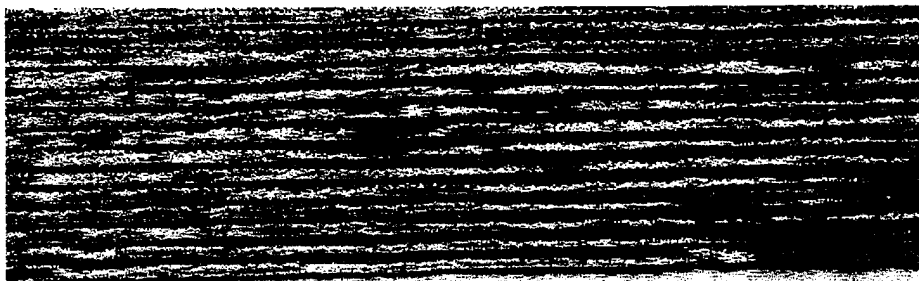


Figure 3-59. Shear wave interrogation of a Ti-6Al-4V/SiC single-ply composite showing areas of poor consolidation

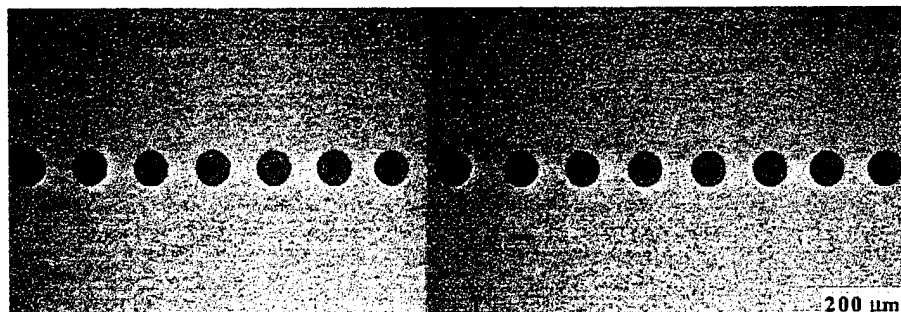


Figure 3-60. Metallography of section from a uniform region showing good consolidation

In addition to the studies of composite consolidation, these NDE methods are very useful for the detection of fiber fractures and fiber-matrix interfacial debonding in continuously reinforced metal matrix composites [Karpur & Matikas, 1992]. Further details on the ultrasonic evaluation of consolidation in MMC can be found in literature [Krishnamurthy, et al., 1993 and Matikas & Karpur, 1993].

### 3.3.1.5 Results and Discussion - CMC

The ultrasonic images of three single fiber ceramic matrix composites made with glass-F matrix, are shown in Figure 3-61. The fibers were imaged using the shear wave interrogation technique. Figure 3-61a shows the glass-F/SCS-6 single fiber composite with relatively uniform reflection along the fiber, implying a good consolidation along the length of the fiber. Figure 3-61b shows another sample (glass-F/SCS-6), but with poor consolidation along the length of the fiber. Figure 3-61c shows a glass-F/SCS-0 single fiber composite with poor consolidation along the length of the fiber. Here (Figure 3-61c) there is a variation in the degree

and orientation of consolidation of the matrix along the length of the fiber. In this case, contrary to Figure 3-61b, there are large poorly consolidated regions.

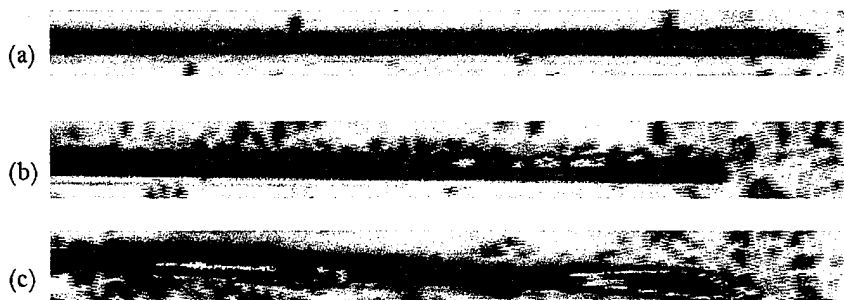


Figure 3-61. Oblique-incidence, back-reflected shear-wave images of Glass-F composites with embedded single fibers: (a) SCS-6 fiber with good consolidation, (b) SCS-6 fiber with poor consolidation, and (c) SCS-0 fiber with poor consolidation.

Figure 3-62 shows three single-ply samples made with SCS-6 fibers and three different borosilicate glass matrices having slightly different chemical composition so that their thermal expansion coefficients vary while their elastic properties remain similar [Matikas & Karpur, 1993]. The fibers were imaged using the shear wave interrogation technique. Figure 3-62a shows a glass-D/SCS-6 single-ply composite with some tensile radial residual stress ( $\sigma_r$ ), because of the thermal expansion coefficient mismatch between fiber and matrix. Therefore, regions of local lack of consolidation are seen. Figure 3-62b shows a glass-C/SCS-6 single-ply composite with a substantial tensile radial residual stress. Global lack of consolidation was seen in this case. Figure 3-62c shows a glass-E/SCS-6 single-ply composite with almost zero radial residual stress. Here, a good consolidation was seen along the length of the fibers.

Figure 3-63 shows two single-ply samples made with glass-E matrix and two different types of fibers. Figure 3-63a shows a glass-E/Sigma single-ply composite imaged using the shear wave interrogation technique. The borosilicate glass strongly wets the  $TiB_2$  coating of the SIGMA fiber, therefore, the consolidation along the fiber was good [Matikas & Karpur, 1993]. Figure 3-63b shows a glass-E/SCS-6 single-ply composite. The glass weakly wets the carbon coating of the SCS-6 fiber [Matikas & Karpur, 1993], hence, global lack of consolidation was seen in this case.

An application of the capability developed in the Materials Directorate to nondestructively evaluate the extent of consolidation in advanced composites will be discussed in the next few paragraphs. A glass F/SCS-6 single fiber composite was used for that study. The composite was processed using the burnout and sinter cycle. The sample was first processed in oxygen at  $200^\circ C$  to  $450^\circ C$  with temperature gradient of  $2^\circ C/min$ , then, hold at  $450^\circ C$  for one hour, next, processed in vacuum/argon at  $450^\circ C$  to  $730^\circ C$  with temperature gradient of  $4^\circ C/min$ , then hold at  $730^\circ C$  for one hour, next, hold in argon at  $730^\circ C$  for 20

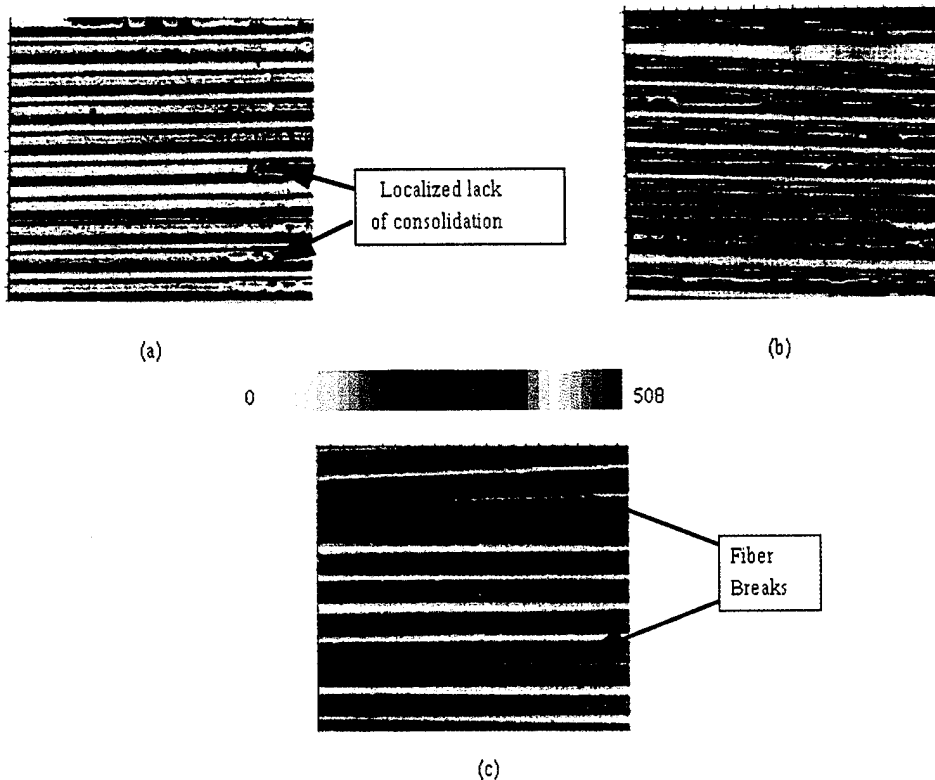


Figure 3-62. Oblique-incidence, back-reflected shear-wave images of single-ply SCS-6 fibers in borosilicate matrices: (a) glass-D, poor consolidation,  $\sigma_r = 6.5$  MPa; (b) glass-C, global lack-of-consolidation,  $\sigma_r = 13.6$  MPa; and (c) glass-E, good consolidation,  $\sigma_r$  nearly zero.

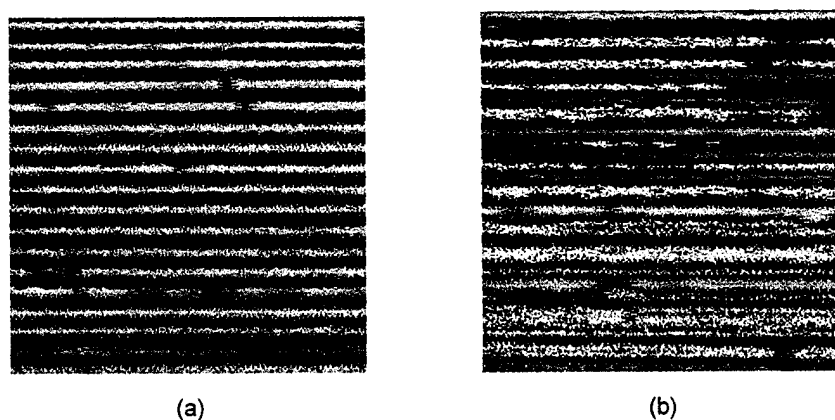


Figure 3-63. Oblique-incidence, back-reflected shear-wave images of single-ply fibers embedded in glass-E matrix: (a) SIGMA fibers with good consolidation, and (b) SCS-6 fibers with poor consolidation.

minutes and, finally, cooled down in argon from 730°C to 200°C with temperature gradient of 5°C/min. Next the sample was hipped at 650°C for 30 minutes with an applied pressure of 34.5 MPa to remove the residual porosity. Figure 3-64a shows an ultrasonic SBR image of the sample after processing. From Figure 3-64a it can be seen that the sample had poor consolidation along the fiber and also had a lot of porosity in the matrix. Taking advantage of the use of a nondestructive technique to evaluate the consolidation of the composite, it was decided to reprocess the specimen and evaluate it again with the SBR technique. Therefore,

the sample was rehipped at 700°C for 30 minutes with the same applied pressure of 34.5 MPa. The ultrasonic image of the rehipped sample, Figure 3-64b, shows improvement in the consolidation around the fiber as well as significant reduction of porosity in the matrix. Finally, the sample was hipped for a third time at 730°C for 30 minutes with the same applied pressure of 34.5 MPa. The ultrasonic image this time showed a good consolidation along the fiber (Figure 3-64c). No porosity was detected in the matrix



Figure 3-64. Oblique-incidence, back-reflected shear-wave images of glass-F/SCS-6 fiber composites before and after reprocessing: (a) no reprocessing, poor consolidation and substantial matrix porosity; (b) first reprocessing, better consolidation and less matrix porosity; and (c) second reprocessing, good consolidation and absence of matrix porosity.

The reason for the improvement in consolidation and reduction of porosity shown in Figure 3-64 is that, by increasing the processing temperature while keeping the applied pressure the same during the reprocess, the viscosity of the glass decreases significantly. For example, if the temperature increases by 50°C, the viscosity of the glass will drop, approximately, by a factor of 10. By decreasing the viscosity it is easier for the glass to densify around the fiber forming a well consolidated composite with a porosity-free matrix. Small changes in temperature may result in big changes of the viscosity of the glass, because of the logarithmic relationship between temperature and viscosity. Therefore, it is difficult in many cases to predict a processing temperature for which the composite will be well consolidated. It is shown in this section that ultrasonic NDE is important for the evaluation of post-processed composites and can feed back important information to the processing groups thereby helping the improvement of the fabrication process of composite materials.

### 3.3.2 Characterization of Matrix Microstructure and Morphology in Titanium Matrix Composites

Current needs for higher performance systems have led to extensive research on fiber reinforced titanium matrix composites (TMC) due to their low density and attractive mechanical properties. Composites based on a number of titanium matrix alloys are being evaluated on the basis of fiber/matrix compatibility, environmental resistance and mechanical properties. Conventional nondestructive testing is routinely used for detecting macro-scale defects such as

ply delamination in those composites. However, as was demonstrated in the previous sections of this document, the newly developed NDE capabilities based on back-reflectivity ultrasonic methods, provide valuable micro-level information for the characterization of both localized properties and defects. Therefore, ultrasonic methodologies can serve as a powerful diagnostic tool for assuring the integrity of TMCs before undertaking detailed mechanical testing and evaluation. The characterization of matrix microstructure and morphology in metal matrix composites using innovative ultrasonic techniques will be discussed in this subsection.

### **3.3.2.1 Role of the Matrix Microstructure and Morphology on the Performance of the Composite**

Conventional titanium alloys can be classified as near alpha, alpha + beta, or metastable beta compositions. A variety of microstructures with different phase morphologies can be obtained depending on the alloy composition and processing conditions. All these alloy classes have been investigated to develop matrices for the fiber reinforced metallic composites. For example, published work [Larsen, et al., 1989] includes composites based on the two-phase alloy (Ti-6Al-4V), the near alpha alloy (Ti-1100), and the metastable beta alloys such as Ti-15-3 and Timetal 21S. More recently, there has been considerable interest in compositions based on Ti alloys containing much higher levels of aluminum and niobium. These higher levels lead to the formation of ordered intermetallic compounds based on alpha-2 and orthorhombic phases which appear to provide improved mechanical properties and oxidation resistance.

While different types of matrix microstructures have been examined for the TMCs, the existence of multiple types of grain structure in the composite, especially near the fiber-matrix interface region, might be undesirable for certain types of TMCs. Also, changes in the microstructure of the matrix from region to region of the sample might introduce zones of stress concentration resulting in reduced overall strength of the composite system. Thus detection, monitoring and control of the microstructure of the composite matrix is essential to obtain the desired mechanical behavior of the composite.

### **3.3.2.2 Modeling the Propagation of Ultrasound in an Anisotropic Polycrystalline Matrix Material**

Most engineering materials are polycrystalline in nature and are constituted by a large number of grains compactly packed within the boundaries of the material. Such materials are usually amenable to be treated as homogeneous and isotropic in many applications involving ultrasonic nondestructive evaluation because the ultrasonic wavelengths are generally orders of magnitude larger than the grain size and the grains are generally equiaxed, single phase and with no preferred orientation. However, it is not uncommon to encounter non-equiaxed grains or material with preferred orientation which affect ultrasonic wave propagation thereby changing the direction of the ultrasonic wave group velocity.

An ultrasonic pulse being transmitted by a transducer can be considered as a superposition of many sinusoids and can be represented by the Fourier integral:

$$u(x, t) = \int_{-\infty}^{+\infty} A(\kappa) e^{-i(\kappa x - \omega(\kappa)t + \phi)} d\kappa \quad (3-12)$$

It should be noted that although the integration is from  $-\infty$  to  $+\infty$ , only some of the amplitudes,  $A(\kappa)$ , will be nonzero subject to the bandwidth of the transducer.

When a wave pulse defined by Equation 3-12 propagates through a distance  $X_0$ , the effect of the propagation is equivalent to the pulse passing through a linear, time invariant filter with a frequency response given by,

$$H(\omega) = e^{-ikx_0} \quad (3-13)$$

Hence, when a pulse defined by Equation 3-12 is reflected by a plane reflector (located perpendicular to the direction of propagation and in an ideal noiseless and nonattenuative medium at a distance  $X_0/2$  and further propagates back to the receiver, the received signal is given by,

$$r(x, t) = \int_{-\infty}^{+\infty} A(\kappa) e^{-i(\kappa x - \omega(\kappa)t + \phi)} e^{i(\kappa x_0)} d\kappa \quad (3-14)$$

The right hand side of Equation 3-14 is the same as the transmitted signal except for a phase lag introduced due to the wave propagation (diffraction and attenuation effects are ignored). However, when strong scatterers are present in the material in which the wave pulse is propagating, the scatterers contribute to a portion of the amplitude being sensed by the receiver. Thus, the received wave pulse, in the presence of scatterers, is defined by [Robinson & Silvia, 1981 and Karpur & Canelones, 1992] the following equation:

$$\bar{r}(x, t) = \int_{-\infty}^{+\infty} A(\kappa) e^{-i(\kappa x - \omega(\kappa)t + \phi)} e^{-i(\kappa x_0)} d\kappa + \int_{-\infty}^{+\infty} A(\kappa) e^{-i(\kappa x - \omega(\kappa)t + \phi)} e^{-i(\kappa x_0)} s(\kappa) d\kappa \quad (3-15)$$

where  $s(\kappa) = \oint e^{-i\phi_{\kappa,n}} dn$  represents the integration over all the scatters present in the resolution volume of the pulse.

It is clear from Equation 3-15 above that the first term on the right hand side is the transmitted signal itself except for a change in the phase delay which is a direct function of the ratio of the distance of propagation and wavelength - or the product of the propagation distance and the wavenumber. However, the second term on the right hand side of the equation has a random phase ( $\phi_{\kappa,n}$ ) component. The randomness in the phase is introduced because the phase of the scatterer within the resolution volume. Although Equation 3-15 shows only the ultrasonic attenuation due to grain scattering, there is an additional phenomenon of wave attenuation caused by absorption. Therefore, when absorption effects are also considered,

Equations 3-12 through 3-15 can be modified to represent the amplitude of the elastic stress wave traveling in the material to a general form as shown below:

$$A = A_{att} \cdot A_{prop} \quad (3-16)$$

where  $A_{att}$  is the attenuated amplitude due to scattering and  $A_{prop}$  is the propagation term

$$A_{att} = A_0 e^{-\alpha(f)x} \quad (3-17)$$

$$A_{prop} = \sin(\beta x - \omega t) \quad (3-18)$$

where  $A_0$  is the initial amplitude, 'x' is the distance over which the wave front has traveled,  $\alpha(f)$  is the attenuation coefficient that is a function of the frequency  $f = \omega / 2\pi$  of ultrasound,  $\beta = 2\pi f / v$  is a propagation constant, and 'v' is the phase velocity. The attenuation coefficient of a polycrystalline material is defined by [Papadakis, 1965; Papadakis, 1968; and Papadakis et al., 1973]

$$\alpha(f) = \alpha_a(f) + \alpha_s(f) \quad (3-19)$$

where  $\alpha_a$  is the absorption coefficient and  $\alpha_s$  is the grain scattering coefficient due to energy dispersion of the traveling waves. The velocity of wave propagation is determined by the elastic moduli and the preferred orientation of the grains. Because of the preferred orientation, the medium becomes as a whole elastically anisotropic medium, so that the velocity is a function of the direction of the propagation.

The scattering is dependent on the type, size, orientation of the grains, the mode of incident waves, etc. The grain scattering problem has been solved by Lifshitz et al. [Lifshitz & Parkhomovskii, 1950] for an isotropic, equiaxed, homogeneous grain material. Three distinct cases of attenuation caused by grain scattering exist: (a) Rayleigh zone ( $\lambda > 2\pi D_g$ ), (b) stochastic zone ( $\lambda \approx 2\pi D_g$ ), and (c) diffusion zone ( $\lambda < 2\pi D_g$ ), where  $D_g$  is the average grain diameter with an approximation of spherical grains. In the literature may be found analytical solutions of scattering coefficients for different cases. For example, Merkulov [Merkulov, 1956] specialized the general solutions of both Rayleigh and diffusion scattering to the cases of cubic and hexagonal metals. An equivalent theoretical analysis was performed by Bhatia and Moore [Bhatia & Moore, 1959], for Rayleigh scattering for the case of orthorhombic materials. In general, the attenuation due to grain scattering for all the different cases can be written in the form,

$$\alpha(f) = a_1 f + a_2 D_g^3 f^4, \quad \text{when } \lambda > 2\pi D_g, \quad (3-20a)$$

$$\alpha(f) = b_1 f + b_2 D_g f^2, \quad \text{when } \lambda \approx 2\pi D_g, \quad (3-20b)$$

$$\alpha(f) = c_1 f + c_2 f^2 + c_3 / D_g, \quad \text{when } \lambda < 2\pi D_g, \quad (3-20c)$$

where  $a_1, b_1, c_1, c_2$  are absorption coefficients and  $a_2, b_2, c_3$  are scattering coefficients. Thus, from Equations 3-20a, 3-20b, and 3-20c, it is clear that

$$\alpha_s(f) \text{ proportional to } D_g^3 f^4, \quad \text{when } \lambda > 2\pi D_g, \quad (3-21a)$$

$$\alpha_s(f) \text{ proportional to } D_g f^2, \quad \text{when } \lambda \approx 2\pi D_g, \quad (3-21b)$$

$$\alpha_s(f) \text{ proportional to } 1/D_g, \quad \text{when } \lambda < 2\pi D_g, \quad (3-21c)$$

Hence, the degree of scattering is a function of both the incident frequency and the average grain dimension. It should be remembered that Equations 3-21a through 3-21c are valid only if the grain shape could be approximated as spherical (equiaxed).

Since columnar grains do not conform to the model of spherical grains assumed for equiaxial grains, Equations 3-21a through 3-21c are no longer valid because the equations assume a mean spherical diameter,  $D_g$ , for the grains. Columnar grains, because of the wave guide phenomenon, might cause different modes of 'guided waves' to propagate in the test material. Propagation of higher modes is dependent on the frequency and the cross sectional dimension of the columnar grains. When the frequency is varied over a range, new modes of wave propagation are induced in the columnar material depending on the ratio of the cross sectional dimension and the wavelength. However, since the columnar grains generally have irregular cross sectional shape, the analytical expressions are only approximations of the relationship between the wavelength and the average cross sectional dimension of the grains.

The effect of columnar grains on the wave propagation, especially when the elongation direction of the grains does not coincide with the direction of wave transmission, the direction of propagation of the wave front (group velocity vector) will be modulated resulting in the skewing of the acoustic beam. As a result, the transmitted ultrasonic energy might not reach the intended target in the material thereby producing a distorted image. One form of distortion is the production of a patchy image wherein the acoustic beam reaches the intended target at times and misses the target at other times due to inhomogeneities in the grain formation. Similar effect will be evident in the case of textured materials wherein the preferred orientation of grains may change the scattering of elastic waves traveling in the material. The basic mechanism of change in scattering is due to the reduced impedance to the acoustic wave front offered by preferred orientation of the grains, when the direction of propagation coincides with the direction of orientation. When both columnar grains and preferred orientation are present, the effect of beam distortion is further accentuated.

### 3.3.2.3 Fabrication of the Samples Used in the Study

The samples used in this study were composites made with either a single SCS-6, SiC fiber or three SCS-6, SiC fibers embedded in Ti-6Al-4V alloy matrix. The composite samples were fabricated by diffusion bonding two matrix alloy sheets with the fibers between them. A small amount of an organic binder was applied to the two ends of the fibers and the fibers were glued to the sheets prior to consolidation. Diffusion bonding was accomplished by hot pressing at 1010°C which is about 15°C higher than the beta-transus temperature of the Ti-6Al-4V alloy.

The samples were cooled very slowly following the hot pressing. Under this thermal excursion, the resulting matrix was expected to be a two phase mixture of somewhat coarse plate-like alpha titanium phase and finer beta phase at alpha plate boundaries. It should be pointed out, however, that the beta-transus temperature varies with the amounts of interstitial impurities such as carbon and oxygen that are generally present in the matrix and, therefore, the resulting microstructure will also be dependent on the local composition of the alloy.

### 3.3.2.4 Ultrasonic Imaging - Results

The SBR (back-reflected shear wave) technique was used to interrogate all samples. A 25 MHz, 6.35 mm diameter, 12.7 mm focal length transducer was operated in the pulse-echo mode to generate the ultrasonic waves, and the back-reflected shear waves were gated [Buynak, et al., 1989] to produce the ultrasonic images.

Two distinct types of matrices were formed during processing. These were:

- (1) An inhomogeneous and anisotropic matrix with oriented plate-like alpha grains of average size on the order of the wavelength of the shear waves. This matrix produced a wave-guide phenomenon and beam skewing due to the anisotropy, i.e., the phase velocity and the group velocity vectors were not in the same direction. As a result, the ultrasonic image (Figure 3-65a) shows areas where the wave energy reached the fiber producing a good dynamic range, and areas where the fiber image is either distorted or completely lost.
- (2) A mostly homogeneous and isotropic matrix consisting of equiaxed alpha plus beta structure with average alpha-grain sizes much less than the wavelength of the ultrasonic waves used for the experiment. In this case, since the ultrasound was incident at an angle, the received signal was either low amplitude due to the back-scattering from the material texture or very high amplitude due to the back-reflection from the cylindrical fiber (when the wave front was perpendicular to the fiber circumference). As a result, the dynamic range of the image of the fiber was excellent (Figure 3-65b).



(a)



(b)

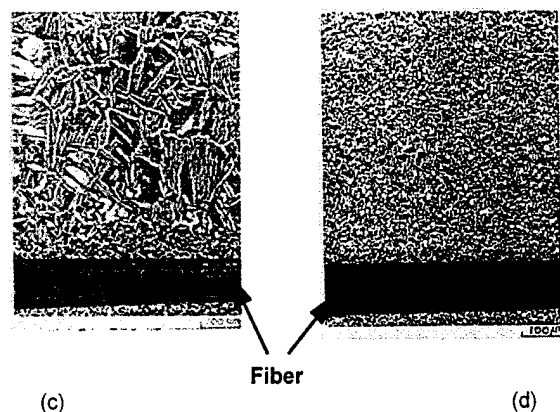


Figure 3-65. Images of single fiber embedded in Ti-6Al-4V matrices with different microstructure: (a) ultrasonic image, inhomogeneous, coarse plate-like alpha plus beta microstructure; (b) homogeneous, fine, equiaxed alpha plus beta microstructure; (c) metallographic image, microstructure as in "a"; and (d) metallographic image, microstructure as in "b".

The ultrasonic images ("a" and "b" in Figure 3-65) correlate very well with the results obtained from metallography for a single fiber embedded in the inhomogeneous and homogeneous matrices ("c" and "d" respectively in Figure 3-65). The ultrasonic image of three fibers embedded in a Ti-6Al-4V matrix is shown in Figure 3-66a. In this case, the matrix was consolidated at a temperature slightly above beta-transus. Metallographic images ("b" and "c" in Figure 3-66) reveal that the matrix regions away from the fibers consisted of coarse alpha plates and elongated beta phase, whereas the matrix regions adjacent to the fibers consisted of equiaxed alpha plus beta structure which had been stabilized by carbon diffusion from the fiber.

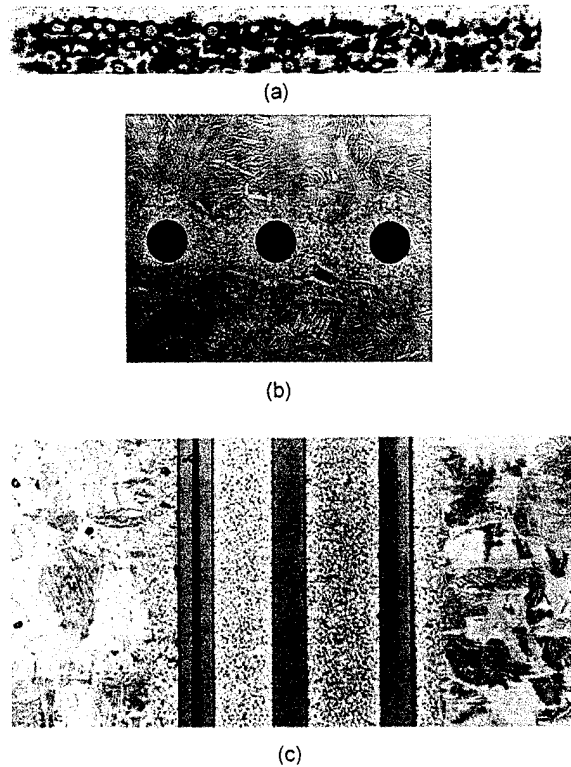


Figure 3-66. Images of three fibers embedded in Ti-6Al-4V matrix: (a) ultrasonic image, (b) metallographic image of section perpendicular to fiber direction, and (c) metallographic section through fibers and parallel to the fiber direction.

# **Section 4**

## ***Applicabilities Studies***

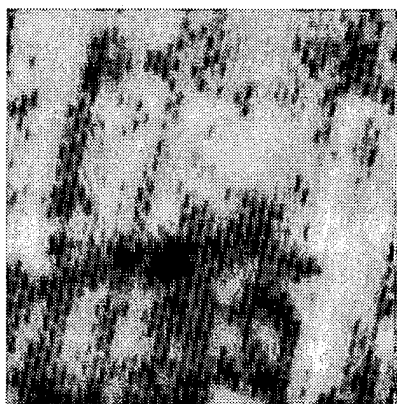
---

### **4.1 Digital Techniques for Ultrasonic Imaging of Near-Entry-Surface Anomalies in Highly Attenuative Materials**

Ultrasonic back-surface-echo C-scan images such as the one in Figure 4-1a are often used to locate anomalous regions in materials and structures. In that image of a kevlar-polyester radome section, the darker shades of gray denote regions of high ultrasonic energy transmission (normal regions), whereas the light shades of gray denote regions of low energy transmission (anomalous regions). Such images can be obtained relatively quickly, and provide information regarding the existence of anomalous regions. They do not, however, provide precise information about the shapes of the anomalies nor the depth-wise location of the anomalies.



(a)



(b)

Figure 4-1. Software-gated C-scan images of a kevlar-polyester radome segment: (a) data from back-surface echo; and (b) data from entry-surface-echo ring-down region.

Obtaining precise information about the shapes and depths of anomalies can be very difficult, especially if the attenuation of ultrasound in the material increases rapidly with frequency and the anomalies lie close to the ultrasonic entry surface of the material. In such cases, low frequencies must be used to obtain usable echo amplitudes from the back-surface of the sample. Unfortunately, low-frequency A-scans have long ring times which tend to obscure echoes from near-entry-surface anomalies.

#### **4.1.1 Entry-Surface-Echo C-Scan Imaging**

A near-entry-surface C-scan image (Figure 4-1b) was generated by processing data from a software gate positioned within the entry-surface echo (Figure 4-2a). The lighter shades of gray in Figure 4-1b denote regions of high ultrasonic energy transmission (normal regions) whereas the darker shades of gray denote regions of high ultrasonic reflectivity (anomalous regions) near the entry surface of the sample. Note in particular the relatively precise definition

of the shape of the anomalous reflectors. Note also how well the general outlines of the anomalous (dark) regions in the near-entry-surface-echo C-scan image of Figure 4-1b match the anomalous (light) regions in the back-surface-echo C-scan image of Figure 4-1a. This matching lends credence to the hypothesis that the near-entry-surface anomalies are the source of the major variations in back-surface-echo amplitude which was observed in the back-surface-echo-amplitude C-scan image (Figure 4-1a). The texture is visible in the near-entry-surface image (Figure 4-1b), but not in the back-surface image (Figure 4-1a), because the ultrasonic beam had a relatively short depth of field and was focused on the entry-surface of the sample.

Depth information is not directly encoded in either of the C-scan images in Figure 4-1. However, since the gate for the image in Figure 4-1b is actually located in the "dead zone" or "echo ring-down" region of the A-scan, it can be inferred that many of the anomalies lie very close to the entry surface of the sample. A better approximation of depth could be obtained using a series of contiguous very narrow gates with the first starting at the surface-tracking threshold of the A-scan. The gate in which the anomaly echoes first appear could then be used in conjunction with A-scan length and sample thickness information (Table 4-5) to calculate a better approximation of the anomaly depth.

#### **4.1.2 Digital Filtering Improves C-Scan Image Resolution**

The Fourier magnitude spectra of the RF A-scan in Figure 4-2a is shown in the plot of Figure 4-2b. This plot shows that the ultrasonic energy is grouped into distinct modes with the maximum magnitude at the transducer nominal center frequency of 1 MHz. It is well known that the beam diameter and the depth of field of a focused ultrasonic beam decrease as the interrogating frequency increases [Saglio and Prot, 1985]. The interested reader should refer to Tables 4-5 and 4-6 for relevant information about the transducer used for data collection together with the relationships between frequency, focal spot size and depth of field. Because the beam diameter decreases with increasing frequency, the lateral resolution in B-scan images and C-scan images increases with increasing frequency. Therefore, a digital filtering computer algorithm was used to band-pass filter the original three-dimensional RF B-scan data set. The upper and lower cut-off frequencies were set so that only the frequency components in the mode centered at approximately 3.25 MHz would remain in the signals. A second band-pass filtering operation was conducted on the original data set; this time the filter was set to pass frequencies about the mode centered at 5.5 MHz.

The software-gating algorithm, BTOC, was applied to the three-dimensional B-scan data set that had been band-pass filtered about the 3.25 MHz mode. The resultant near-entry-surface C-scan image is shown in Figure 4-3a. Note that there is a considerable improvement in resolution of the near-entry-surface anomaly features. No back-surface C-scan image could

be generated from the band-pass filtered data because of the material's high attenuation at that frequency.

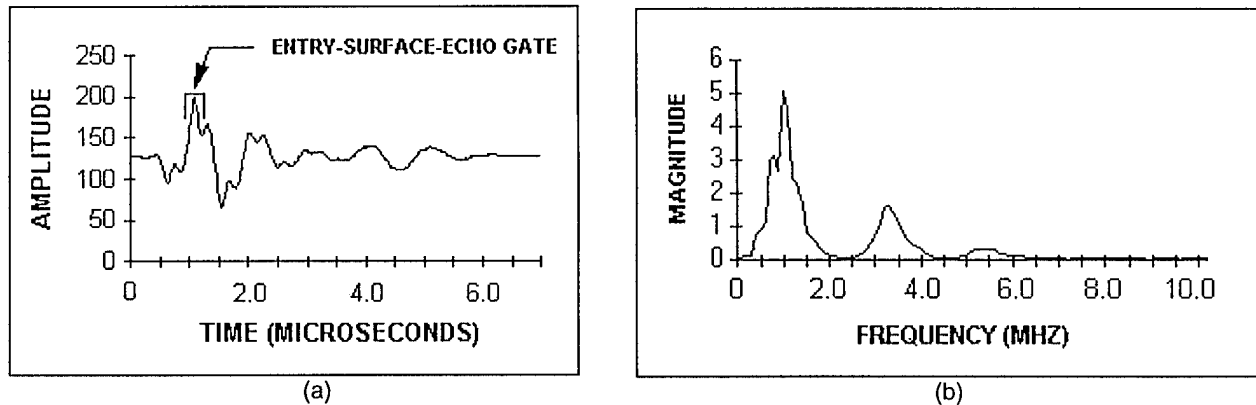


Figure 4-2. Data from the three-dimensional data set used for this study: (a) RF A-scan; and (b) Fourier magnitude spectra of the RF A-scan in "a".

The results of applying the software-gating algorithm, BTOC, to the B-scan data set which had been band-pass filtered to include only the frequencies centered at 5.5 MHz are shown in Figure 4-3b. That figure shows the further improvements in spatial resolution that were obtained relative to Figure 4-3a by using only the higher frequency components in each A-scan of the three-dimensional B-scan data set.

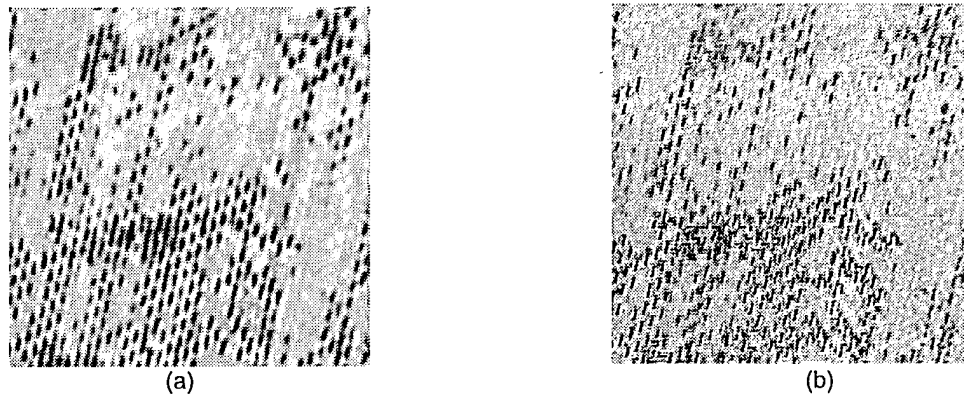


Figure 4-3. C-scan images generated after band-pass filtering the RF B-scans: (a) filter centered about the 3.25 MHz mode; and (b) filter centered about the 5.5 MHz mode.

#### 4.1.3 Additional Information

Tables 4-1 through 4-6 list some of the advantages and disadvantages of the various digital techniques which were described in this section of the final report as well as sample and transducer information, and ultrasonic beam-width characteristics.

**Table 4-1**  
**Software Gating**

- |   |
|---|
| <p>1. Advantages</p> <ul style="list-style-type: none"><li>a. Many gates can be set at once</li><li>b. Gates can be set anywhere on the waveform and can be extremely narrow</li><li>c. Information can be processed in a variety of ways to generate values for C-scan images</li></ul> <p>2. Disadvantages</p> <ul style="list-style-type: none"><li>a. Data must be digitized at a relatively high rate to<ul style="list-style-type: none"><li>i. Satisfy the Nyquist criterion</li><li>ii. Provide stable surface tracking</li><li>iii. Maximize the signal-to-noise ratio of the value being extracted from the gate</li></ul></li><li>b. Computer storage must be available for<ul style="list-style-type: none"><li>i. All C-scan data values for each C-scan which is generated</li><li>ii. All RF A-scans if the three-dimensional waveform is digitized and stored prior to C-scan data generation</li></ul></li></ul> |
|---|

**Table 4-2**  
**Storing Three-Dimensional RF Waveforms**

- |  |
|--|
| <p>1. Advantages</p> <ul style="list-style-type: none"><li>a. B-scan and C-scan images can be generated when convenient and as often as is necessary without repeating the scanning process</li><li>b. The data can be analyzed in a variety of different ways</li><li>c. Signal and image processing techniques can be applied to the RF A-scans prior to B-scan and C-scan image generation</li></ul> <p>2. Disadvantages</p> <ul style="list-style-type: none"><li>a. Considerable data storage space is required during data acquisition</li><li>b. High-speed digitizers are required to digitize the data</li><li>c. Computer algorithms must be available to convert the acquisition instrument's data storage format to a data format which is recognized by the analysis algorithms</li></ul> |
|--|

**Table 4-3**  
**Digital Filtering**

- |   |
|---|
| <p>1. Advantages</p> <ul style="list-style-type: none"><li>a. Allows the user to improve lateral resolution by decreasing the focal spot size of focused, broad-band transducers</li></ul> <p>2. Disadvantages</p> <ul style="list-style-type: none"><li>a. Requires that the signals be digitized and stored</li><li>b. Requires time for processing</li><li>c. Requires additional space for storing the filtered three-dimensional waveforms</li></ul> |
|---|

**Table 4-4**  
**Sample Information**

	(mm)	(in)
1. Sample Dimensions		
a. Length	254	10
b. Width	254	10
c. Thickness	0.5	0.2
2. Material	Kevlar-polyester	

**Table 4-5**  
**Transducer and Scanning Information**

1. Transducer Information	1 MHz
a. Center frequency (nominal)	19 mm (.75 in)
b. Element diameter	36.7 mm (1.5 in)
c. Focal length in water	Entry surface of sample
d. Location of focal point	
2. Scanning Information	
a. Number of B-scans	251
b. Distance between successive B-scans	0.254 mm (0.01 in)
c. Total scan width	63.5 mm (2.5 in)
d. Number of A-scans per B-scan	251
e. Distance between successive A-scans	0.254 mm (0.01 in)
f. Total length of scan	63.5 mm (2.5 in)
g. Number of points per A-scan	350
h. Time between successive points in A-scan	20 nSec

**Table 4-6**  
**Ultrasonic Beam Characteristics**

	Center Frequency					
	1 MHz		3.25 MHz		5.5 MHz	
	(mm)	(in)	(mm)	(in)	(mm)	(in)
Beam Diameter	3.9	0.16	1.2	0.047	0.68	0.027
Depth of Field	31.3	1.23	9.6	0.38	5.4	0.21

## 4.2 Time-of-Flight C-Scan Imaging of Near-Entry-Surface Anomalies

Two views of a "traditional" Time-Of-Flight (TOF) C-scan image of impact-induced damage in a graphite-epoxy composite are shown in Figures 4-4a and 4-4b. The "traditional" TOF C-scan image data were acquired by starting the data-acquisition gate after the entry-surface echo had decayed to a near-zero value. The three-dimensional appearance was produced by using a "shade-surface" graphics display routine.

Two views of a "nontraditional" TOF C-scan image of the same sample are shown in Figures 4-4c and 4-4d. The C-scan data for these images were generated by preprocessing the digitized-and-stored three-dimensional B-scan data to remove the entry-surface echo. Then, the software-gating algorithm, BTOC, was applied with the TOF gate starting in the region where the entry-surface echo had been removed.

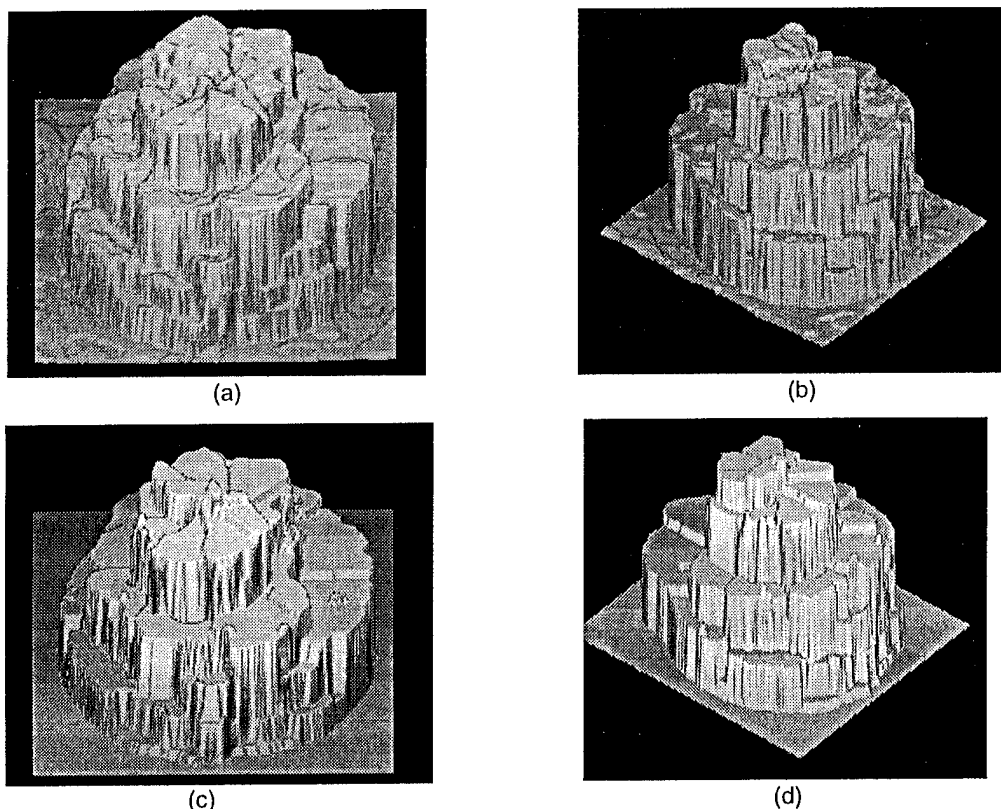


Figure 4-4. Time-of-Flight C-scan images of layer-by-layer, impact-induced damage in graphite-epoxy composites: (a) and (b) "traditional" TOF imaging; (c) and (d) C-scan image generation after preprocessing the data to remove the entry-surface-echo.

It is clear from the images in Figures 4-4c and 4-4d that at least two layers of damage were missed by the "traditional" TOF C-scan imaging technique (results in Figures 4-4a and 4-4b). It is also clear that both techniques (with and without entry-surface-echo removal) provide essentially the same layer-by-layer damage information at depths beyond the entry-surface-echo ring-down region.

#### **4.2.1 Preprocessing with the Entry-Surface-Echo-Removal Algorithm, REFSUB**

The major disadvantage of the TOF gate is that it can not be used to image near-entry-surface impact damage. The TOF gate can not be started before the entry-surface-echo has decayed to a subjectively low amplitude; otherwise, the peak-detector algorithm will often “lock onto” the entry-surface echo, and impact damage would remain undetected. To overcome that problem, the entry-surface-echo-removal algorithm, REFSUB (see Section 4.5) was used as a preprocessor to remove the unacceptably large entry-surface echo from all A-scans in the original three-dimensional RF B-scan data set. After preprocessing with REFSUB, only a “small” residual of the original entry-surface echo remained. This “small” residual did not perturb the operation of the C-scan data generation algorithm, BTOC.

#### **4.2.2 “Nontraditional” TOF C-Scan Image Generation Steps**

The steps followed to generate the three-dimensional images in Figures 4-4c and 4-4d are outlined in Table 4-7. The software requirements for using this technique for imaging near-entry-surface anomalies as well as anomalies deep within the sample are outlined in Table 4-8. Sample, transducer and scanning information are provided in Table 4-9.

**Table 4-7**  
**Image-Generation Steps**

1. Digitize and store three-dimensional RF B-scan data
2. Remove entry-surface echo from all A-scans using REFSUB
3. Generate Time-Of-Flight (TOF) C-scan data using BTOC
4. Apply median filter to TOF C-scan data
5. Generate three-dimensional shaded surface image at the desired orientation using PV-WAVE  
(PV-WAVE is a registered trademark of Precision Visuals Incorporated, Boulder, CO.)
6. Store shaded surface image as a C-scan formatted image
7. Convert C-scan image format to TIF format

**Table 4-8**  
**Requirements for Removing the Entry-Surface Echo and Generating TOF C- Scan Images**

1. Capability for digitizing and storing three-dimensional RF B-scans.
2. The entry-surface-echo-removal algorithm, REFSUB.
3. A software-gating algorithm (such as BTOC) for generating TOF C-scan data from digitized and stored three-dimensional RF B-scan data.
4. A median-filtering algorithm for application to the TOF C-scan data set.

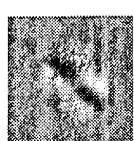
**NOTE:** Generation, storage, and redisplay of the pseudo three-dimensional images from the TOF C-scan data requires additional special software such as:  
a. PV-WAVE for generating and storing the pseudo three-dimensional images, and  
b. A conversion algorithm for converting to a file format which is compatible with existing image display systems.

**Table 4-9**  
**Sample, Transducer and Data-Collection Parameters**

PARAMETER	VALUE/LOCATION
A. Sample	
1. Length	127 mm (5 in.)
2. Width	127 mm (5 in.)
3. Thickness	4.8 mm (32 plies)
4. Composition	graphite-epoxy
B. Transducer	
1. Center frequency	10 MHz
2. Element diameter	12.7 mm (0.5 in.)
3. Focal length in water	76 mm (3 in.)
4. Location of focal point	near center of sample
C. Scanning Parameters	
1. Spatial (X,Y)	
a. Number of A-scans per line (scan width)	139 pts
b. Distance between A-scans	0.5 mm (0.02 in.)
c. Total width of scan	69 mm (2.7 in.)
d. Number of B-scan lines (scan length)	188 pts
e. Distance between B-scan lines	0.5 mm (0.02 in.)
f. Total length of scans	94 mm (3.7 in.)
2. Temporal (Time -- A-scans)	
a. Number of points per A-scan	450 pts
b. Time increment between points	10 nS

### 4.3 High-Quality C-Scan Image Enlargements From Depot and In-Field Collected Small Data Sets

Features in C-scan images generated from in-field or depot-collected data are often small and "noisy" in appearance such as the one shown in Figure 4-5a. One would prefer an image like that in Figure 4-5b which was generated by significantly "*over-sampling*", that is, collecting far more data in all three dimensions than is required to minimally define features in the image. Unfortunately, collecting enough data to produce images such as that in Figure 4-5b requires more time and data storage space than are usually available during in-field and depot inspection efforts.



(a)



(b)

Figure 4-5. C-scan images of the delamination damage (very dark regions): (a) from original small data set; (b) from large, over-sampled data set.

Enlargement of the small image in Figure 4-5a by the typical pixel replication method results in images with visually disturbing "noise" and "blockiness" such as the one shown in Figure 4-6a. The enlarging (actually interpolation) method which is outlined in this section was developed for application to in-field collected ultrasonic data with the goal of improving the visual detection and quantification of image features. When applied to the raw three-dimensional data from which the C-scan image in Figure 4-5a was generated, this method produces the results shown in Figure 4-6b. The image in Figure 4-6b is quite comparable to the over-sampled image in Figure 4-5b. This enlargement method has been applied successfully to data collected in the laboratory at WPAFB and to data collected by SM-ALC personnel.

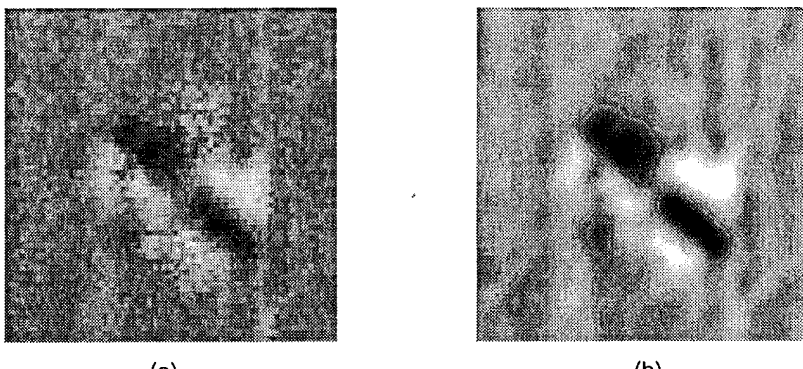


Figure 4-6. Enlargements of the C-scan image in Fig. 4-5a by: (a) pixel replication; and (b) use of method developed in WL/MLP branch.

#### 4.3.1 Enlarging (Interpolation) Method

The procedure for producing the more accurate and visually appealing C-scan image enlargements is shown in Table 4-10. A one-dimensional Fourier-domain zero-padding

**Table 4-10**  
**Image Enlargement Methodology**

1. Use the one-dimensional interpolation algorithm, INTERP\_ASCANS, to interpolate all A-scans in all B-scans from 40nS/pt to 10nS/pt.
2. Use the software-gating algorithm, BTOC, to generate C-scan image data from interpolated A-scans at the interface between the 2<sup>nd</sup> and 3<sup>rd</sup> plies.
3. Apply a two-dimensional smoothing filter to reduce noise and suppress effects of pixel offset in the C-scan image.
4. Use the two-dimensional enlargement (interpolation) algorithm, INTERP\_2D, to interpolate the C-scan image.
5. Apply a two-dimensional high-frequency emphasis filter to enhance the enlarged C-scan image.

technique was used to interpolate the time-domain (A-scan) signals and a two-dimensional Fourier-domain zero-padding technique was used to enlarge the C-scan image data after the data had been blurred with a low-pass filter. The blurring step was necessary to remove noise and "pixel offset" which was produced by the bidirectional scanning process. If noise and pixel offset are not removed, the resultant image will usually be visually unacceptable. High-

frequency enhancement filtering was applied after the C-scan image enlargement to remove some of the blur caused by the filtering and enlarging operations.

The Fourier-domain zero-padding technique [Bellanger, et al.; Schafer & Rabiner; Crochiere & Rabiner] has been used successfully for many years by engineers and scientists working in the field of electronic signal-processing. The technique yields accurate and precise interpolations (and, therefore, enlargements) of data acquired at sampling rates which are low, but which exceed the Nyquist criterion.

The one- and two-dimensional Fourier-domain zero-padding algorithms (INTERP\_ASCANS and INTERP\_2D) were developed during the course of this contract for enlargement of A-, B-, and C-scan data acquired both in the laboratory, and at depot and in-field inspection sites. The blurring filter and the high-frequency-enhancement filter used for this work were also developed during the course of this contract. Many equally effective blurring and high-frequency-enhancement filters are now available in commercial software packages.

#### 4.3.2 Additional Information -- Sample and Transducer

The data for this effort were obtained by using a focused, immersion, ultrasonic transducer to scan an impact-damaged graphite-epoxy composite sample. Pertinent information about the sample and the transducer are listed in Table 4-11.

Table 4-11

##### Sample and Transducer Information

PARAMETER	COMPOSITION/VALUE
SAMPLE	
1. Material -----	Graphite-Epoxy
2. Dimensions	
a. Length -----	149 mm (5.9 in.)
b. Width -----	120 mm (4.7 in.)
c. Thickness (32 plies) -----	5 mm (0.2 in.)
TRANSDUCER	
1. Center frequency -----	3.5 MHz
2. Element diameter -----	2.7 mm (0.5 in.)
3. Focal length in water -----	51 mm (2 in.)
4. Location of focal point -----	Entry surface

#### 4.3.3 Additional Information -- Scanning and Data Acquisition

The "comparison standard" for the enlargements is based on analyses of the data which were over-sampled in three dimensions. The data collection parameters for the standard (over-sampled) and the small (sparsely sampled) data sets are presented in Table 4-12.

#### 4.4 High Precision Scanning Acoustic Microscope System (HIPSAM)

HIPSAM is a digital, software-gated, ultrasonic C-scan data acquisition system with high mechanical precision (0.001 mm resolution) and high frequency (up to 100 MHz) interrogation capabilities. The spatial resolution which is achievable with this system is illustrated by the

**Table 4-12**  
**Ultrasonic Scanning and Acquisition Parameters**

PARAMETER	"STANDARD"	"SMALL C-SCAN"
Spatial		
1. A-scans per line	376 pts	60 pts
2. Distance between A-scans	0.10 mm (0.004 in.)	0.40 mm (0.015 in.)
3. Total width of scan	37.6 mm (1.5 in.)	23.9 mm (0.94 in.)
4. B-scan lines (scan length)	301 lines	60 lines
5. Distance between B-scans	0.10 mm (0.004 in.)	0.40 mm (0.015 in.)
6. Total length of scan	30 mm (1.2 in.)	23.9 mm (0.94 in.)
Temporal (Time or A-scans)		
1. Sampling rate	100 mega-samples/sec	25 mega-samples/sec
2. Total number of points	400 pts	64 pts
3. Total A-scan length	4 microseconds	2.52 microseconds

image in Figure 4-7. That image is a high-frequency (100 MHz) ultrasonic C-scan of a metal-matrix composite with SCS-6 fibers embedded in a Ti-6Al-4V matrix. The dimensions of the image are 0.5 mm X 0.5 mm (0.02 in X 0.02 in) or roughly the diameter of the shank of a safety pin; the step size (distance between adjacent data points in the image) is 0.001 mm.

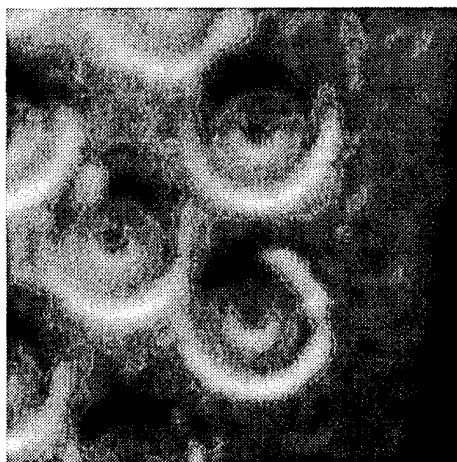


Figure 4-7. C-scan image showing a cross-sectional view of SCS-6 fibers embedded in a Ti-6Al-4V matrix. Data for the image were collected using the HIPSAM system.

The image in Figure 4-7 was processed by removing "speckle" and by adjusting the brightness and contrast. No other image processing techniques were used. The two most obvious components in this image are the dark central core (0.04 mm diameter) of the fiber, and the bright outer ring around the fiber; that bright ring defines the fiber-matrix interface at the outside diameter (.14 mm) of the fiber. The difference in gray levels between the top of each fiber (black) and the bottom of each fiber (white) is probably due to a slight tilt in the fibers relative to the acoustic beam. The small, light-colored patches toward the right side of the image are grain boundaries in the matrix material. The identification of those light-colored patches as grain boundaries was verified by optical microscopy. The data collection parameters for this C-scan image are provided in Table 4-13.

**Table 4-13**  
**Data Collection Parameters for Image in Figure 4-7**

A. Transducer	100 MHz 6.35 mm (0.25 in.) 5.08 mm (0.20 in.)
B. Data Acquisition	1 gigasample/second 8 nanoseconds (8 points) Peak amplitude
C. Image	0.5 mm X 0.5 mm (0.02 x 0.02 in.) 0.001 mm (0.00004 in.)

The major components of the HIPSAM scanning system are shown in Figure 4-8. The system components are: left -- large high-resolution image display unit, operator's keyboard and monitor; center -- rack containing ultrasonic instrumentation equipment and motor controller; right -- water-filled scan tank with three motorized axes.

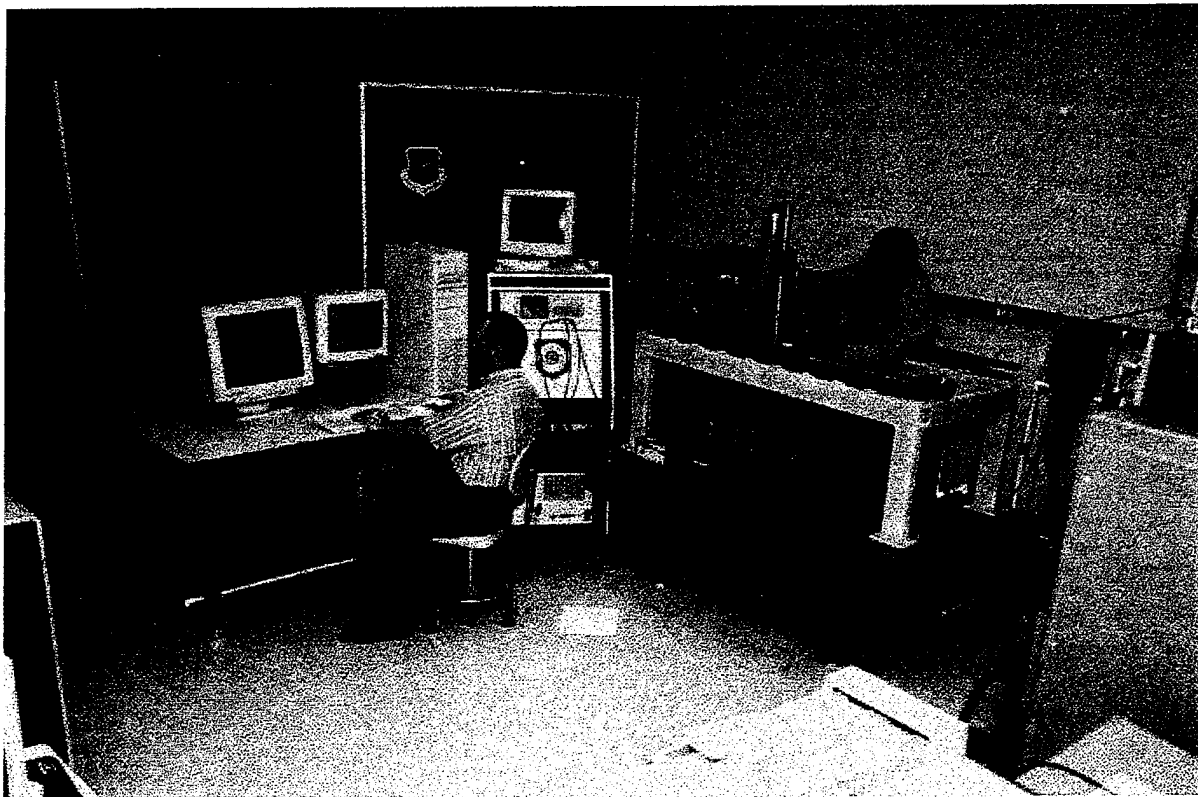


Figure 4-8. Hlgh Precision Scanning Acoustic Microscope System (HIPSAM).

The major specifications, capabilities and features of the HIPSAM system are listed in Table 4-14.

**Table 4-14**  
**Major Features of the HIPSAM System**

<b>A. Data Acquisition Specifications</b>	
1. Maximum transducer frequency -----	100 MHz
2. Maximum A-scan digitizing rate -----	2 gigasamples/second
3. Maximum number of points per A-scan -----	16384 points
4. Maximum B-scan storage size -----	4 megabytes
5. Maximum image display dimensions -----	1024 by 1024 pixels
6. Time-Of-Flight (TOF) resolution-----	16 bits
7. Amplitude resolution -----	8 bits
8. Maximum dimensions of C-scan-----	1024 points by 16384 lines
9. Number of simultaneous software gates-----	5
10. Maximum scanning resolution-----	0.001 mm (0.00004 in.)
11. Maximum scan length -----	50.8 mm (2 in.)
12. Maximum scan width -----	50.8 mm (2 in.)
13. Scan and index axes-----	Any paired combination of X, Y, Z
<b>B. Operator Interface</b>	
1. Standard window style interface for scan setup	
2. Point-and-click with mouse for operator interface	
3. Menus "guide" the operator through the proper setup procedure	
4. Each window has <b>OK</b> and <b>CANCEL</b> buttons	
5. Operator is notified of and forced to correct setup errors before proceeding further	

#### **4.5 Application of an Entry Surface-Echo-Removal Algorithm to Anomaly Detection in Depot-Type Data**

The entry-surface-echo-removal algorithm, REFSUB [Frock, et al., 1990], was originally developed to improve visual detection of near-entry-surface anomaly echoes in ultrasonic RF B-scans. The algorithm functioned well with laboratory data which was digitized at a very high rate, but did not function well with in-field-digitized data which was (and usually is) digitized at a much lower rate. The problems associated with the application of the original REFSUB algorithm to in-field digitized data are illustrated by the images "a" and "b" in Figure 4-9. The image in Figure 4-9a is an RF B-scan of a kevlar-polyester radome with near-entry-surface anomalies.

The data were acquired at a sampling rate equivalent to that which is commonly used during in-field acquisition efforts. The only echo present in the image is from the entry surface, since the material is too attenuative at the interrogating frequency to produce a back-surface echo. There is little visible evidence of near-entry-surface anomalies in the image of Figure 4-9a.

Figure 4-9b shows the results of applying the original REFSUB algorithm to the B-scan data of Figure 4-9a. Some near-entry-surface anomaly echoes are now visible, but residual echoes from the entry-surface-echo subtraction are visually disturbing, thereby making it difficult to distinguish between anomaly echoes and residual subtraction echoes. Figure 4-9c shows the results of applying the upgraded version of REFSUB to the B-scan data of Figure 4-

9a. The residual subtraction echoes are much smaller and are far less visually disturbing. Thus, it is much easier to locate the near-entry-surface anomaly echoes.

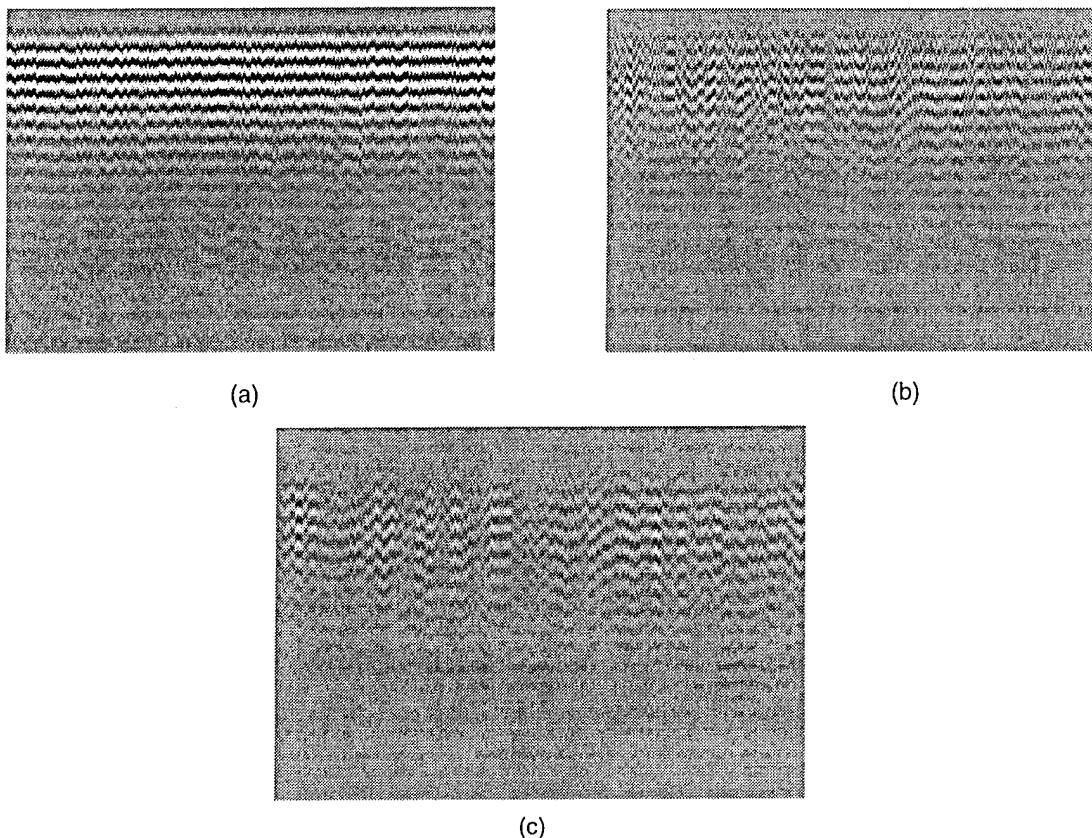


Figure 4-9. Near-entry-surface-echo B-scans: (a) as-digitized data; (b) entry-surface echo removed with an earlier version of REFSUB; and (c) entry-surface echo removed with the new version of REFSUB.

## 4.6 Split Spectrum Processing of Ultrasonic Signals Improves Detection and Sizing of Material Anomalies

Split Spectrum Processing (SSP) has been used primarily to improve the signal-to-noise ratio (SNR) of ultrasonic signals by reducing the "scattering noise" from insignificant or desirable material property variations [Chirrup, 1987; Chirrup, et al., 1987; Newhouse, et al., 1979; Newhouse, et al., 1982; Chirrup, 1990]. This improvement in signal-to-noise ratio can significantly improve the detectability of undesirable material anomalies such as cracks, voids and inclusions. During the course of this contract preprocessing of ultrasonic signals via SSP was found to be of significant benefit for:

- Early detection of fatigue microcracks,
- Fatigue-microcrack sizing and growth monitoring,
- Reliable detection of hard alpha inclusions in titanium disks, and
- Improving the reliability of Artificial Neural Network classifications.

### 4.6.1 Fatigue-Microcrack Detection

An example of the improvement in the SNR which can result from the application of SSP to RF ultrasonic signals is shown in Figure 4-10. The plot in Figure 4-10a is an

unprocessed RF ultrasonic Rayleigh-wave A-scan which was backscattered from a fatigue crack in an aluminum sample after that sample had been subjected to 80,000 fatigue cycles. The signal in Figure 4-10a has so much superimposed material noise that it is difficult to identify a crack signal. Application of an SSP algorithm to the signal in Figure 4-10a yielded the signal shown in Figure 4-10b. This very dramatic improvement makes it easy to identify the crack signal.

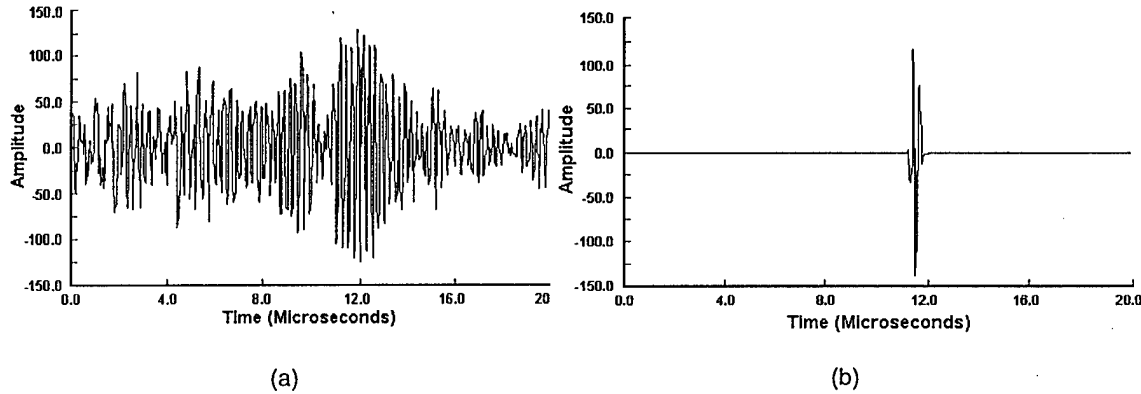


Figure 4-10. Rayleigh waves backscattered from fatigue crack: (a) original A-scan; and (b) results of processing the A-scan in "a" using the SSP technique.

#### 4.6.2 Fatigue-Microcrack Sizing and Growth Monitoring

It was not possible to obtain size information from early implementations of the SSP technique [Newhouse, et al., 1982] because phase information was not retained. However, recent modifications of the SSP algorithms do retain phase information [Chirrup, 1987 & Chirrup, et al., 1987], thereby making it possible to estimate the size of anomalies from the amplitude characteristics of reflected ultrasonic waves [Chirrup & Resch, 1991]. Application of the modified SSP algorithm to ultrasonic Rayleigh waves which were backscattered by a small but growing crack in a fatigue sample yielded the curve shown in Figure 4-11. This plot shows

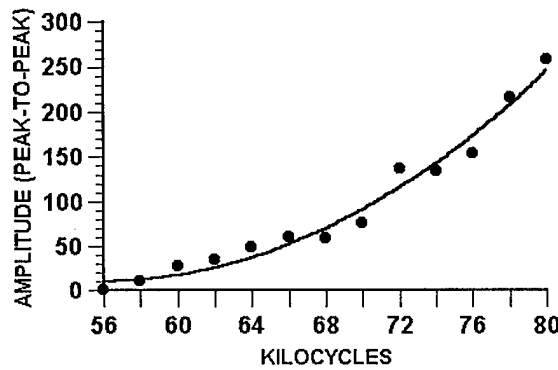


Figure 4-11. Peak-to-peak amplitude of SSP-processed, microcrack-backscattered Rayleigh wave as a function of the number of fatigue cycles.

that the peak-to-peak amplitudes of the backscattered Rayleigh waves increased with increasing number of fatigue cycles (lower horizontal axis). Before application of the SSP

algorithm, the Rayleigh-wave signals were so corrupted with material noise from the high-stress region of the sample that accurate amplitude measurements were impossible (Figure 4-10a). The size of the crack can be estimated by using a theoretical model which is available in the literature [Resch, et al., 1985].

#### **4.6.3 Reliable Detection of Small Hard-Alpha Inclusions in Titanium Products**

Split Spectrum Processing was used as an ultrasonic-signal preprocessor to improve the detection of small hard-alpha inclusions in titanium-based aerospace products. Prior to the development of this technique the detection of small-sized hard-alpha inclusions by visual observation of ultrasonic C-scan images was unreliable. Application of the SSP technique allowed reliable detection of hard-alpha inclusions equivalent to a number 3 flat-bottom hole by visual observation of C-scan images.

The five basic steps which are required for successful application of the technique are:

1. Careful selection of transducer's focal length and frequency.
  - a. Focal length is selected to ensure that the focal point will be near the center of the sample's thickness
  - b. Frequency is selected to ensure that very small inclusions will be detectable -- higher frequencies are required for detection of small inclusions, but result in more material noise.
2. Careful calibration of the ultrasonic system for determining the ultrasonic attenuation as a function of frequency. This is extremely important for synthesizing (tuning) the SSP filters to:
  - a. Detect inclusions which are greater than or equal to a specific size, and
  - b. Determine the optimal detection depth below the ultrasonic entry surface.
3. Digitizing and storing three-dimensional ultrasonic RF B-scan data from the titanium product of interest.
4. Application of the calibrated (depth- and size-tuned) SSP filters to the three-dimensional ultrasonic RF B-scan data.
5. Generation of C-scan image data from the SSP-processed, three-dimensional ultrasonic data set.

Two major limitations of the technique are:

1. The detection reliability is highly dependent on the filter-synthesis process. Considerable care must be taken during the filter-syntheses process.
2. Filters can be tuned only for a specific combination of transducer, specimen material, flaw size and flaw depth. A new filter synthesis is essential if any one of the parameters is changed. However:
  - a. Filters tuned for a specific-sized flaw can be used to reliably detect larger flaws, and
  - b. Filters tuned for a particular depth can be used for reliable flaw detection at shallower depths.

This technique was successfully transitioned to use at GE Aircraft Engines in Evendale, Ohio by UDRI personnel during the course of this contract. Funding for the transition effort was provided by GE Aircraft Engines.

#### 4.6.4 Improving the Reliability of Artificial Neural Network Classifications

Back Propagation (BP), Artificial Neural Network (ANN) techniques were applied to ultrasonic signals to detect and classify impact-induced delamination damage in a graphite-epoxy composite sample. Two distinct test conditions were used to determine the effectiveness of preprocessing the ultrasonic signals with SSP prior to application of the ANN technique. In the first case, the BP-ANN technique was applied directly to the ultrasonic signals which had been collected from the impact-damaged sample. In the second case, the ultrasonic signals were preprocessed with the modified (phase retaining) SSP algorithm prior to application of the BP-ANN technique.

The results from the two tests are shown in Figure 4-12 and in Table 4-15. The image in Figure 4-12a shows a software-gated amplitude C-scan image of the impact-damaged sample. Black indicates damaged regions, whereas white indicates undamaged regions. The accuracy of the software-gated amplitude C-scan technique has been adequately demonstrated in literature sources [Buynak & Moran, 1987; Buynak, et al., 1988; Buynak, et al., 1989]. Thus, the image in Figure 4-12a served as the standard by which the BP-ANN results were judged. The results of applying the BP-ANN technique directly to the ultrasonic signals without SSP preprocessing are shown in Figure 4-12b. Note that some of the damaged region (as imaged by the standard in Figure 4-12a) have been falsely classified as good by the directly applied BP-ANN technique. Also some regions which were undamaged (Figure 4-12a) were falsely classified as damaged by the directly applied BP-ANN technique. Figure 4-12c shows the results of applying the BP-ANN technique *after* preprocessing with the SSP algorithm. The classification results obtained by applying the BP-ANN technique *after* preprocessing with the SSP algorithm (Figure 4-12c) were much more reliable than were the results obtained by direct application of the BP-ANN technique to the ultrasonic signals without preprocessing with the SSP algorithm.

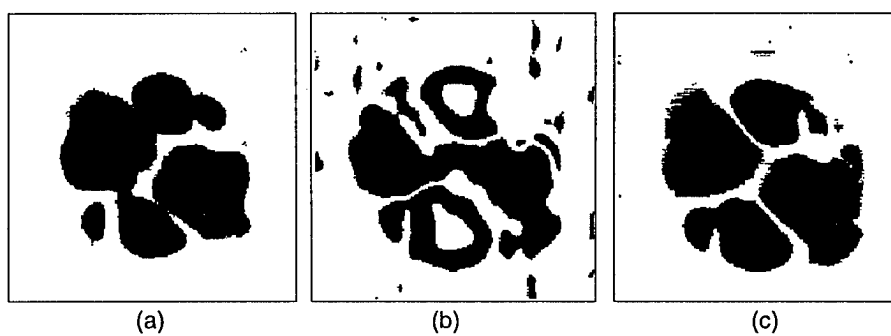


Figure 4-12. C-scan images of impact-induced delamination in a graphite-epoxy composite. Image generated by applying: (a) software-gates to original the RF A-scans; (b) BP-ANN to the original RF A-scans; and (c) BP-ANN to the SSP-processed RF A-scans.

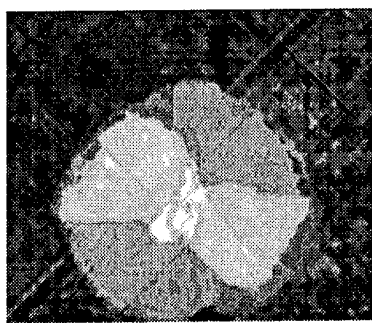
A numerical comparison of the visual results in Figure 4-12b with the standard in Figure 4-12a on a pixel-by-pixel basis is provided in the middle row of Table 4-15. Those results indicate that the application of BP-ANN *before* preprocessing with SSP yielded a 71% accuracy of detecting delamination damage when it was present (POD), and a 16% probability of falsely detecting (POFD) delamination damage when it was not present. The analogous comparison of the results in Figure 4-12c with the standard in Figure 4-12a is provided in the bottom row of Table 4-15. Those results indicate that the direct application of BP-ANN to the ultrasonic signals after SSP preprocessing yielded a 94% accuracy of detecting delamination damage when it was present, and a 9% probability of falsely detecting delamination damage when it was not present. Thus, preprocessing the ultrasonic data prior to application of the BP-ANN technique improved the reliability of delamination-damage classification.

**Table 4-15**  
**Reliability of Artificial Neural Network Classification**

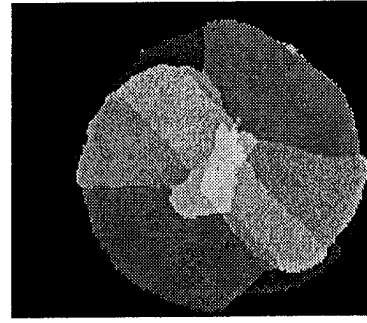
Preprocessed With SSP?	FIGURE	POD	POFD
No	3b	71%	16%
Yes	3c	94%	9%

#### 4.7 Leaky Lamb Wave Inspection Techniques for Detecting Damage in Composite Structures

Leaky Lamb Waves -- generated by a swept-frequency, tone-burst technique -- were used to make C-scan images of anomalies in advanced composite materials. Median-frequency-processing of the leaky Lamb waves generated by that technique provided excellent C-scan images of: (1) layer-by-layer spreading of delamination damage in a composite material (Figure 4-13), and (2) impact-induced delamination damage in a composite face sheet



(a)

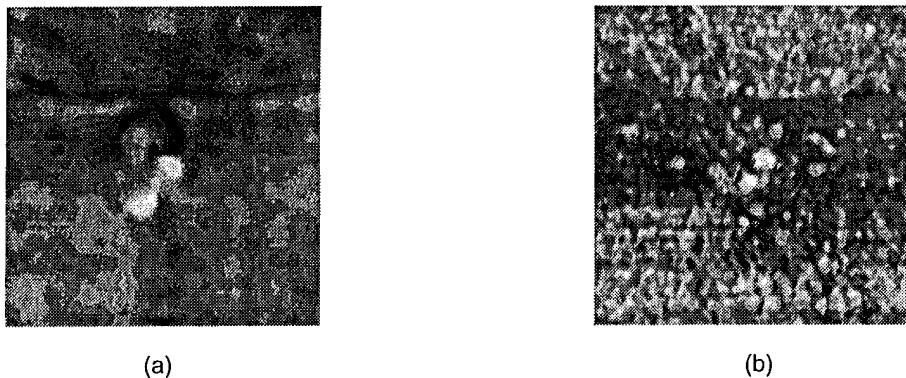


(b)

Figure 4-13. C-scan images of delamination damage using: (a) swept-frequency, tone-burst, leaky Lamb wave technique; and (b) conventional normal-incidence time-of-flight technique.

with a honeycomb backing (Figure 4-14a). The leaky Lamb wave image of layer-by-layer damage spreading (Figure 4-13a) was comparable to images that have been produced by ultrasonic time-of-flight (TOF) C-scan techniques, e.g., Figure 4-13b. The leaky Lamb wave

image of delamination damage in the face sheet of the honeycomb-backed composite (Figure 4-14a) was superior to the analogous image generated from conventional ultrasonic amplitude C-scan techniques (Figure 4-14b).



(a)

(b)

Figure 4-14. C-scan images of impact damage at the interface between a composite face sheet and a honeycomb core using: (a) swept-frequency, tone-burst, leaky Lamb wave technique; and (b) conventional normal-incidence back-surface amplitude technique. The damaged region is shown in light gray and white near the center of each image.

#### 4.7.1 Major Advantages And Disadvantages

The major advantages and disadvantages of using the swept-frequency tone-burst technique followed by median-frequency processing for C-scan image generation are listed in Table 4-16.

Table 4-16

#### Major Advantages and Disadvantages of the Leaky Lamb Wave Generation and Processing Techniques

A. Advantages
1. More acoustic energy is coupled into the sample
2. The technique is very sensitivity to small changes in reflected energy
3. Depth information is encoded into the C-scan images
4. The technique is sensitive to many types of anomalies because many Lamb wave modes are generated
5. Low-frequency (5 kilo-samples/second), low-cost digitizers can be used to acquire the data
B. Disadvantages
1. Long setup times are required to determine the proper angles, positions, and frequency for the transducers
2. The scan speed is much slower due to the time required for the frequency sweep and the median frequency processing
3. Anomalies of interest may be difficult to visually observe because Lamb waves are sensitive to so many defects and material variations

#### 4.7.2 Swept-Frequency, Tone-Burst Lamb Wave Generation

Lamb wave generation and reception generally require two transducers which are carefully positioned with respect to angle (relative to the sample surface normal), distance above the sample, and distance between transducers. Those parameters together with the ultrasonic frequency are carefully selected by referring to theoretical dispersion curves. Once

produced, the Lamb waves "leak" from the sample back into the water and form an interference pattern by overlapping with the wave which is reflected from the sample's surface. The interference creates peaks and nulls (valleys) in the waveform at the receiving transducer's location. This is depicted schematically for a single frequency in Figure 4-15 [Martin & Chimenti 1987; Chimenti & Martin, 1991].

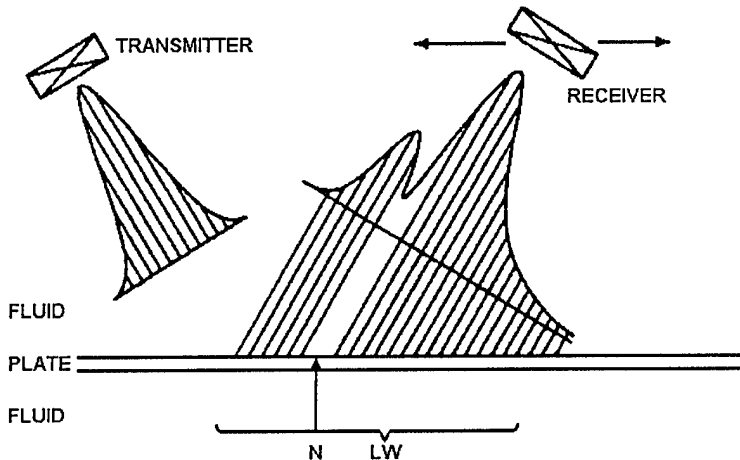


Figure 4-15. Schematic diagram of leaky Lamb wave generation. "LW" indicates the region of the leaky wave whereas "N" denotes a null within the leaky wave.

Lamb wave modes which were sensitive to anomalies at different depths were generated by exciting the transducer over a broad range of frequencies while keeping the incident angle and transducer separation distance constant. The received amplitude was then digitized at 128 discrete frequency values for each spatial position along the sample. A single value (median frequency) was extracted from that amplitude-vs-frequency data at each point, and that value was used to produce the C-scan image data for each point. The median-frequency extraction technique will be explained in the next section.

The broad-band excitation was approximated by generating a tone burst (single frequency) signal in the transmitting transducer, digitizing the peak amplitude of the received signal, and then repeating the "tone-burst excitation and digitizing procedure" over a range of frequencies from about 1 MHz through 8 MHz in 32 milliseconds. This pseudo swept-frequency technique actually consisted of a series of 128 discrete tone bursts with individual tone-burst durations of 5 to 30 microseconds. This produced the amplitude-vs-frequency data for each spatial position on the sample (Figure 4-16a). The horizontal scale at the top of Figure 4-16a is the sweep time in milliseconds whereas the horizontal scale at the bottom is the frequency range in MHz. This pseudo swept-frequency tone-burst technique was used even though it is much slower than normal broad-band excitation because much more energy could be coupled into the sample at each frequency.

#### 4.7.3 Median-Frequency Processing

Data of the type shown in Figure 4-16a were digitized at each spatial point along the sample. That data essentially show a *relatively* high frequency waveform (the null pattern for a

defect-free sample) superimposed on a very low frequency waveform (the ultrasonic system frequency response curve in the 1 MHz to 8 MHz range). This data can be treated as a single RF A-scan of 32 milliseconds length (the sweep time for the swept-frequency, tone-burst technique). The Fourier magnitude spectra of this pseudo-RF A-scan is shown in Figure 4-16b. The high-frequency null pattern is centered at about 550 Hz, whereas the transducer response curve is centered below 50 Hz. The null pattern shifts toward lower frequencies as the specimen becomes thinner. Since delaminations are ultrasonically equivalent to thinner specimens, the null-pattern frequency is lowest for delaminations which are closest to the ultrasonic entry surface. Figure 4-17 shows the pseudo-RF A-scan and its Fourier magnitude spectra in the vicinity of a delamination. The major frequency of the null pattern has shifted downward to about 260 Hz [Martin & Chimenti 1987; Chimenti & Martin, 1991; Martin & Chimenti 1989; Martin & Chimenti 1990]. Thus, the location of the major peak (after removal of the system's signature) is indicative of the depth of the delamination within the specimen.

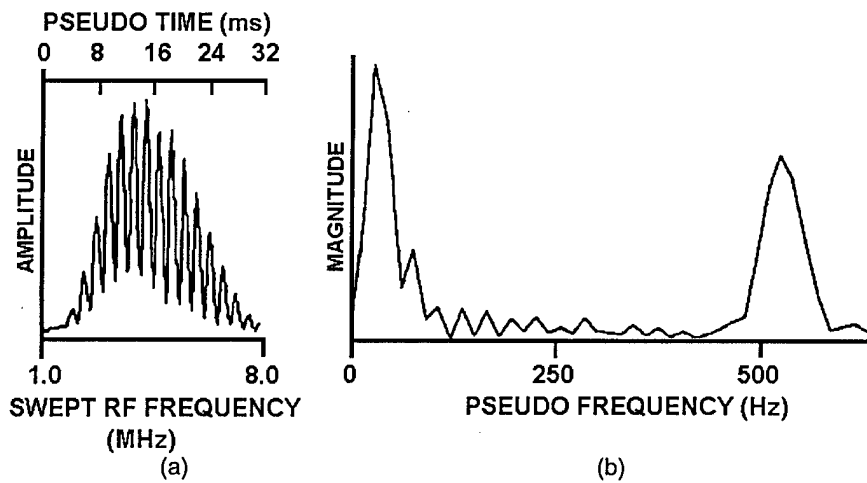


Figure 4-16. Swept-frequency, tone-burst data in defect-free region: (a) pseudo RF A-scan; and (b) Fourier magnitude spectra of "a".

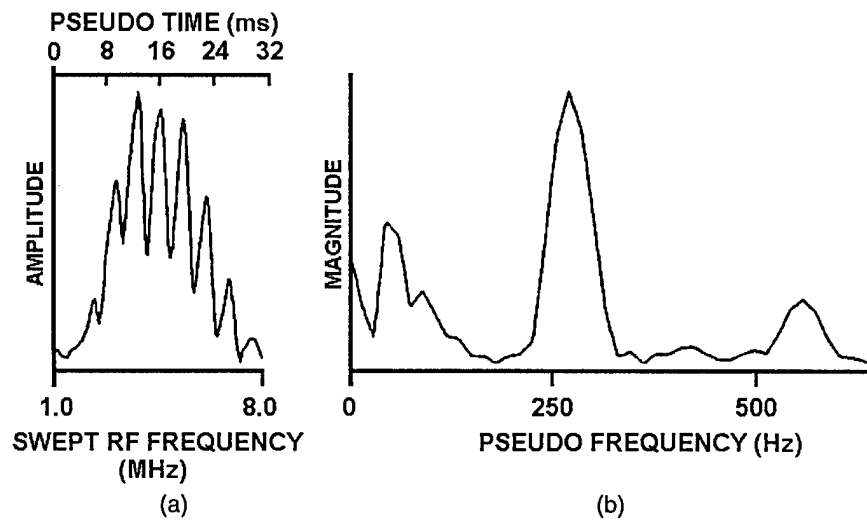


Figure 4-17. Swept-frequency, tone-burst data in delaminated region: (a) pseudo RF A-scan; and (b) Fourier magnitude spectra of "a".

C-scan image data were generated from the Fourier magnitude spectra of the pseudo-RF A-scans by first high-pass filtering to remove the system response signature, and then calculating the median frequency of the filtered magnitude spectra. Since the median value thus calculated would be proportional to the depth of any delamination, the C-scan image (Figure 4-13a) produced from such data would have the delamination depth coded into the gray levels in much the same way as an ultrasonic time-of-flight C-scan image (Figure 4-13b).

#### 4.8 B-Scan to C-Scan Conversion Software Upgrades

The B-scan-TO-C-scan (BTOC) software algorithm [Frock, et al. 1990; Frock, et al. 1988; Buynak, et al.] generates C-scan image data from ***previously-digitized-and-stored three-dimensional B-scan*** data. The original software algorithm was significantly upgraded during the course of the current contract to:

1. Achieve portability to most types of computers and operating systems thereby improving technology transition opportunities,
2. Utilize the X Window System which has emerged as the dominant graphical interface system that is supported on a broad range of the workstation class of computers,
3. Implement the BTOC software which employs advanced software gating techniques, previously developed on slower and older computers, on the faster workstation-class computers.

The major new features added and modifications made during this contract are listed in Table 4-17. The major advantages and disadvantages of using BTOC are listed in Table 4-18.

Table 4-17

##### BTOC Additions and Modifications

<b>Operator Interface</b> 1. A standard window interface is used 2. Operator interface uses a "point-and-click" method with a mouse 3. Pull-down menus and submenus "lead" the user through the proper setup procedure 4. Each window allows the operator to make desired parameter choices with a mouse and then finalize the choices by clicking on an <b>OK</b> button 5. The operator is notified of errors and is forced to correct the errors before proceeding further 6. Each window has a <b>RESET</b> button 7. <b>CANCEL</b> buttons are provided to allow the user to undo settings within a specific window 8. A summary of especially important parameters is constantly displayed, in the main BTOC window, and is updated during the setup process
<b>Processing Characteristics</b> 1. Maximum number of stored B-scan lines -- 1024 2. Maximum number of A-scans per B-scan line -- 1024 3. Maximum A-scan length -- 9999 points 4. Maximum C-scan size -- 1024 X 1024 5. Maximum number of simultaneously applied software gates -- 80
<b>Operating System and Software Code</b> 1. All software code is written in ANSI-standardized FORTRAN 77 or ANSI-standardized C to ensure maximum compatibility with other computer systems 2. OSF/MOTIF is used for the X Window System implementation 3. Currently operates on a DEC MicroVax II computer running the VMS operating system -- an X Window terminal is required

**Table 4-18**  
**Advantages and Disadvantages of Using BTOC**

<b>Advantages</b> 1. BTOC operates 20 to 40 times faster than the data acquisition system can acquire data 2. The data acquisition system can be acquiring more data while a different system generates C-scan image data from the stored three-dimensional B-scan data 3. BTOC can be applied to the stored three-dimensional B-scan data an unlimited number of times using different gate positions, settings, and processing procedures 4. The stored three-dimensional B-scan data can be preprocessed, e.g., filtered, prior to generating C-scan image data
<b>Disadvantages</b> 1. Large amounts of disk storage space are required to store the three-dimensional B-scan data sets which BTOC processes 2. Relatively high-speed digitizers ( $\geq$ 50 megasample/second) are required to digitize the data

#### **4.9 Collaborative Efforts with Air Force ALCs**

Collaborative efforts were undertaken in cooperation with two Air Force ALCs (SM-ALC and OO-ALC) during the course of this contract. These collaborative efforts are briefly outlined in Table 4-19.

The collaborative efforts which are outlined in Table 4-19 provided for the rapid transition of Air Force funded and developed techniques to depot applications. More importantly, they have provided valuable inputs to the WL/Materials Directorate regarding the current and anticipated NDE needs of the Air Force ALCs. Such inputs result in more efficient selection of which new NDE techniques to consider for additional feasibility study.

**Table 4-19**  
**Collaborative Efforts with Air Force ALCs**

ALC	Summary of Effort
SM	<p><b>Data Analysis and Consulting</b></p> <ul style="list-style-type: none"> <li>• Application of software gates to ALC-collected data for imaging near-entry-surface anomalies in kevlar-polyester radome section. Demonstrated correlation between:           <ul style="list-style-type: none"> <li>– features in near-entry-surface C-scan image, and</li> <li>– features in back-surface C-scan image.</li> </ul> </li> <li>• Application of entry-surface-removal algorithm, REFSUB, to ALC-collected RF B-scans to improve imaging of near-entry-surface anomalies:           <ul style="list-style-type: none"> <li>– integrated A-scan interpolation subroutine into REFSUB to minimize subtraction errors during application to in-field collected data.</li> </ul> </li> <li>• Application of digital Distance Amplitude Compensation (DAC) to ALC-collected RF B-scans to improve imaging of anomalies in highly attenuative materials.</li> <li>• Application of image cutting and redisplay to improve imaging of weakly reflecting anomalies in B-scan images.</li> <li>• Recommended two-step ultrasonic scanning technique for depot inspections:           <ul style="list-style-type: none"> <li>– large step-size, low resolution scans for rapid screening of large areas, followed by</li> <li>– small step-size, high resolution scans of suspect regions.</li> </ul> </li> <li>• Determined "optimal" transducer frequency for scanning of kevlar-polyester radome which allowed:           <ul style="list-style-type: none"> <li>– collection of data with unsaturated entry-surface echoes for improving imaging of near-entry-surface anomalies, and with</li> <li>– acceptably high-amplitude back-surface echo for generating back-surface-echo C-scans.</li> </ul> </li> <li>• Analyzed ultrasonic data acquired from an in-service kevlar-polyester radome before and after repairs were made.</li> <li>• Analyzed ultrasonic data acquired by SM-ALC personnel from experimental kevlar-polyester radome at WPAFB.</li> <li>• Collected and analyzed ultrasonic data to determine applicability of software gating techniques for imaging anomalies in woven kevlar-polyester structures.</li> </ul> <p><b>Software Source-Code</b></p> <ul style="list-style-type: none"> <li>• Shipped source code and documentation for the two-dimensional image-expansion algorithm, INTERP_2D, to SM-ALC. Interpolation accomplished by Fourier-domain zero-padding.</li> </ul> <p><b>Presentations and Publications</b></p> <ul style="list-style-type: none"> <li>• Joint presentation with SM-ALC personnel at Fall 1991 ASNT conference.</li> <li>• Joint publication of results in <u>International Advances in NONDESTRUCTIVE TESTING</u>, Vol. 17, W. J. McGonnagle, ed, (Gordon and Breach Science Publishers, 1994).</li> </ul>
OO	<p><b>Data Analyses</b></p> <ul style="list-style-type: none"> <li>• Analyses of ultrasonic Time-Of-Flight (TOF) data acquired by OO-ALC personnel from in-service E3A axle truck. Purpose of data collection and analyses effort was detection and quantification of thinning due to hidden corrosion.</li> </ul>

## Section 5

### References

---

- Arnold, S.M. and T.E. Wilt, Influence of Engineering Interfaces on Residual Stresses and Mechanical Response in Metal Matrix Composites, NASA Technical Memorandum 105438, (March 1992).
- Baker, A.R. and C.G. Windsor, N.D.T. International 22, 97-105 (1989).
- Bampton, C.C., J.A. Graves, K.J. Newell, and R.H. Lorenz, "Process Modeling for Titanium Aluminide Matrix Composites," in Titanium '92: Science and Technology, ed. by F.H. Froes and I.L. Caplan, (TMS, Warrendale PA, 1993).
- Baumann, S.F., P.K. Brindley, and S.D. Smith, Reaction Zone Microstructure in a Ti<sub>3</sub>Al + Nb/SiC Composite, *Metallurgical Transactions A*, **21A**, pp. 1559-1569, (1990).
- Bellanger, M.G., J.L. Daguet, and G.P. Lepagnol, "Interpolation, Extrapolation, and Reduction of Computation Speed in Digital Filters," in *IEEE Transactions on Acoustics, Speech, and Signal Processing*, Vol. ASSP-22, No. 4, pp. 231-235, (August 1975).
- Bhatia, A.B., R.A. Moore, J. Acoust. Soc. Am., Vol. 31, pp. 1140-1142, (1959).
- Blatt, D., P. Karpur, D.A. Stubbs, and T.E. Matikas, "Observations of Interfacial Damage in the Fiber Bridged Zone of a Titanium Matrix Composite," *Scripta Metallurgica et Materialia*, Vol. 29, pp. 851-856, (1993).
- Buynak, C.F., T.J. Moran, and R.W. Martin, "Delamination and Crack Imaging in Graphite-Epoxy Composites", *Mat. Eval.*, Vol. 47, (1989).
- Buynak, C.F., T.J. Moran, and R.W. Martin, "Delamination and Crack Imaging in Graphite/Epoxy Composites," *Materials Evaluation*, Vol. 47, No. 4, pp. 438-447, (1989).
- Buynak, C. F., T.J. Moran, and S.L. Donaldson, "Characterization of Impact Damage in Composites", *SAMPE Journal*, Vol. 24, No. 2, pp. 35-39, (Mar-Apr 1988).
- Buynak, C.F. and T.J. Moran, "Characterization of Impact Damage in Composites," *Review of Progress in Quantitative Nondestructive Evaluation*, eds. D. O. Thompson and D. E. Chimenti, Plenum Press, New York, Vol. 6B, pp. 1203-1211, (1987).
- Charmet, J.C., Roux S. and Guyon E., Eds., *Disorder and Fracture*, Plenum press (1990).
- Chimenti, D.E. and R.W. Martin, "Nondestructive Evaluation of Composite Laminates by Leaky Lamb Waves," *Ultrasonics*, Butterworth-Heinemann Ltd., Vol. 29, pp. 13-21, (January 1991).
- Chirrup, P., and M.T. Resch, "Improved Detectability of Fatigue Microcracks by Split Spectrum Processing of Backscattered Rayleigh Waves," *Review of Progress in Quantitative Nondestructive Testing*, eds. D.O. Thompson and D.E. Chimenti, Plenum Press, New York NY Vol. 10A, pp. 757-764, (1991).
- Chirrup, P., "Split Spectrum Processing of Ultrasonic Signals for Nondestructive Evaluation," *Journal of Non-Destructive Evaluation*, Indian Society for Non-Destructive Testing, Vol. 10, No. 1, pp. 19-28, (Jan. - Mar. 1990).

Chirrup, P., "Split Spectrum Processing: Process Modeling and the Evaluation of Polarity Thresholding Algorithm for Material Noise Reduction in Ultrasonic NDE," PhD. Thesis, Drexel University, Philadelphia PA, (1987).

Chirrup, P., P.M. Shankar, J.L. Rose, and V.L. Newhouse, "Split Spectrum Processing: Optimizing the Processing Parameters Using Minimization," *Ultrasonics*, Vol. 25, pp. 204-208, (July 1987).

Clyne, T.W. and M.C. Watson, "Interfacial Mechanics in Fibre-Reinforced Metals," Composites Science and Technology, Vol. 42, pp. 25-55, (1991).

Coker, D., N.E. Ashbaugh, and T. Nicholas, "Analysis of Thermomechanical Cyclic Behavior of Unidirectional Metal Matrix Composites," presented in the ASTM Symposium on Thermomechanical Fatigue Behavior of Materials, STP 1186, edited by H. Sehitoglu, 1991 (to be published).

Cooper, R.F. and K. Chyung, Structure and Chemistry of Fibre-Matrix Interfaces in Silicon Carbide Fibre-reinforced Glass-Ceramic Composites: an Electron Microscopy Study, *Journal of Material Science*, 22, pp. 3148-3160, (1987).

Crochier, R.E. and L.R. Rabiner, "Optimum FIR Digital Filter Implementations for Decimation, Interpolation, and Narrow-Band Filtering," in *IEEE Transactions on Acoustics, Speech, and Signal Processing*, Vol. ASSP-23, No. 5, pp. 444-456, (October 1975).

Curtin, W.A., "Exact Theory of Fibre Fragmentation in a Single-Filament Composite," *J. of Materials Science*, Vol. 26, pp. 5239-53, (1991).

Dai, H. and G. Frantziskonis, "Heterogeneity, Spatial correlations, Size Effects and Dissipated Energy in Brittle Materials," *Mechs of Matls.*, (1993), preprint.

Damarla, T.R., P. Karpur, and P.K. Bhagat, *Ultrasonics* 30, 317-324 (1992).

Damarla, T.R., S. Ghosal, and P. Karpur, Application of Neural Networks for Classification of Ultrasonic Signals. C.H. Dagli, S.R.T. Kumara, Y.C. Shin, Eds., ASME Press Series on International Advances in Design Productivity (American Society of Mechanical Engineers, 1991).

Drzal, L.T., M.J. Rich, J.P. Camping, and W.J. Park, "A Single Filement Technique for Determining Interfacial Shear Strength and Failure Mode in Composite Materials," Proceedings of 1980 Conference, Reinforced Plastics and Composites Institute, SPI, Paper 20C, 1980(B).

Evans, A.G., F.W. Zok, and J. Davis, "The Role of Interfaces in Fiber-Reinforced Brittle Matrix Composites," *Composites Science and Technology*, Vol. 42, pp. 3-24, (1991).

Evans, A.G. and D.B. Marshall, "The Mechanical Behavior of Ceramic Matrix Composites," *ActaMetall.*, 37:10, (1989).

Frantziskonis, G.N., P. Karpur, T.E. Matikas, S. Krishnamurthy, and P.D. Jero, "Fiber Matrix Interface - Information from Experiments Via Simulation," *Composite Structures Int. J.*, (1993).

Frantziskonis, G.N., T.E. Matikas, P. Karpur, and S. Krishnamurthy, "Simulation of Fiber-Matrix Interface Behavior under Various Experimental Configurations," Proceedings of the International Conference on Composites Engineering (ICCE/1), pp. 147-148, (New Orleans LA 1994).

Fraser, W.A., F.H. Ancker, A.T. DiBenedetto, and B. Elbirli, "Evaluation of Surface Treatments for Fibers in Composite Materials, Polymer Composites," Vol. 4(4), pp. 238-48, (1983).

Frock, B.G., R.W. Martin, P. Karpur, M.J. Ruddell, J.A. Fox, and E.L. Klosterman, "Research on Advanced NDE Methods for Aerospace Structures," Interim Report for 1 September 1991 through 31 August 1992, Contract No. F33615-89-C-5612, (September 1992).

Frock, B.G., R.J. Andrews, R.W. Martin, P. Karpur, J.A. Fox, E.L. Klosterman, M.J. Ruddell, and M.L. Papp, "Research on Advanced NDE Methods for Aerospace Structures," Final Technical Report, UDR-TR-89-81, also WRDC-TR-89-4134, Wright-Patterson AFB OH, (February 1990).

Frock, B.G., R.W. Martin, T.J. Moran, and K.O. Shimmin, "Imaging of Impact Damage in Composite Materials," Review Of Progress in QNDE, eds. D.O. Thompson and D.E. Chimenti, Plenum Press, New York NY, Vol. 7B, 1988, pp. 1093-1099.

Guo, Z.X. and B. Derby, in *Concurrent Engineering Approach to Materials Processing* A.J. Paul, S.N. Dwivedi, F.R. Dax, Eds. (The Minerals, Metals and Materials Society, Warrendale PA, 1992).

Gustafson, C. and R.E. Dutton, "The Effect of Fiber Coating upon the Densification of Sintered Borosilicate Glass/SiC Fiber Composites" Proceedings of the International Conference on Composites Engineering (ICCE/1), pp. 139-140, (New Orleans LA, 1994).

Herrmann H.J. and S. Roux, Eds., Statistical Models for the Fracture of Disordered Media, North-Holland (1990).

Hrennikoff A., "Solution of Problems of Elasticity by the Framework Method," *J. Appl. Mechs. ASME*, A169-A175, (1941).

Hu, S., P. Karpur, T.E. Matikas, L. Shaw, N.J. Pagano, "Free Edge Effect on Residual Stresses and Fracture of Composite Fiber/Matrix Interface," Proceedings of the International Conference on Composites Engineering (ICCE/1), pp. 221-222, (New Orleans LA, 1994).

Jero, P.D., R.J. Kerans, and T.A. Parthasarathy, "Effect of Interfacial Roughness on the Frictional Stress Measured Using Pushout Tests," *Journal of the American Ceramics Society*, Vol. 74, pp. 2793-2801, (1991).

Jero, P.D. and R.J. Kerans, *Scripta Metall. & Mater.*, Vol. 25, pp. 2457-2462 (1991).

Johnson, W.S., "Screening of Metal Matrix Composites Using Ultrasonic C-Scans", *Journal Composites Technology & Research*, pp. 31-34, (1989).

Jones, J.P. and J.S. Whittier, Waves at a Flexibly Bonded Interface, *Transactions of ASME: Jurnal of Applied Mechanics*, December, pp. 905-909, (1967).

Jurewicz, A.J.G., R.J. Kerans, and J. Wright, "The Interfacial Strengths of Coated and Uncoated SiC Monofilaments Embedded in Borosilicate Glass," *Cer. Eng Sci. Proc.* 10:7-8 (1989).

Karpur, P., T.E. Matikas, and S. Krishnamurthy, "A Novel Parameter to Characterize the Fiber-Matrix Interphase/Interface for Mechanics of Continuous Fiber Reinforced Metal Matrix and Ceramic Matrix Composites," *Acta Met*, submitted, (1994).

Karpur, P., T.E. Matikas, M.P. Blodgett, J.R. Jira, and D. Blatt, "Nondestructive Crack Size and Interfacial Degradation Evaluation in Metal Matrix Composites Using High Frequency Ultrasonic Microscopy," Symposium on Special Applications and Advanced Techniques for Crack Size Determination, (ASTM, Atlanta GA, 1993), in print.

Karpur, P. and O.J. Canelones, "Split Spectrum Processing: a new filtering approach for improved signal-to-noise ratio enhancement of ultrasonic signals," *Ultrasonics*, Vol. 30(6), pp. 351-358, (1992).

Karpur, P., T.E. Matikas, and S. Krishnamurthy, "Matrix-Fiber Interface Characterization in Metal Matrix Composites Using Ultrasonic Imaging of Fiber Fragmentation," Am. Soc. for Composites Seventh Technical Conference on Composite Materials, Mechanics and Processing, Vol. 1, pp. 420-427, (Technomic Publishing Inc., Pennsylvania State University, University Park PA, 1992).

Karpur, P., T. Matikas, S. Krishnamurthy, and N. Ashbaugh, "Ultrasound for Fiber Fragmentation Size Determination to Characterize Load Transfer Behavior of Matrix-Fiber Interface in Metal Matrix Composites," D.O. Thompson, D.E. Chimenti, Eds., 19th Annual Review of Progress in Quantitative Nondestructive Evaluation, Vol. 12B, pp. 1507-1513, (Plenum, La Jolla CA, 1992).

Karpur, P., T.E. Matikas, and S. Krishnamurthy, "Ultrasound as a Tool for the Characterization of the Matrix-Fiber Interface in Metal Matrix Composites," presented in the Mechanics of Composites Review, (1992, unpublished).

Kaw, A.K. and N.J. Pagano, "Axisymmetric Thermoelastic Response of a Composite Cylinder Containing an Annular Matrix Crack," *J. Comp. Mat.*, Vol. 27, No. 6, (1993).

Kelly, A and W.R. Tyson, "Tensile Properties of Fiber-Reinforced Metals: Copper/Tungsten and Copper/Molybdenum," *J. Mech. Phys. Solids*, Vol. 13, pp. 329-350, (1965).

Kerans, R.J. and T.A. Parthasarathy, Theoretical Analysis of the Fiber Pullout and Pushout Tests, *Journal of the American Ceramics Society*, **74**, pp. 1585-1596, (1991).

Kerans, R.J., T.A. Parthasarathy, and D.B. Marshall, *J. Am. Cer. Soc.*, submitted.

Krautkrämer, J., and Krautkrämer, H., Ultrasonic Testing of Materials (Springer-Verlag, New York), 1990.

Krishnamurthy, S., T.E. Matikas, P. Karpur, and D.B. Miracle, "Evaluation of the Processing of Fiber-Reinforced Metal Matrix Composites Using Ultrasonic Methods," *Journal of Composites Science and Technology*, (1993), to be published.

Krishnamurthy, S., T.E. Matikas, P. Karpur, and D.B. Miracle, "Metallographic and Ultrasonic Characterization of Matrix Microstructure in SCS-6 Fiber Reinforced Titanium Alloy Composites," *Journal of Materials Science Letters*, (1993), to be published.

Krishnamurthy, S. and I. Roman, Unpublished work, 1992.

Krishnamurthy, S., P. Karpur, T.E. Matikas, D.B. Miracle, and M.C. Waterburry, Nondestructive Evaluation of Fiber Fragmentation Phenomenon in Model Titanium Based Composites, submitted to *Composites Science and Technology*.

Larsen, J.M., W.C. Revelos, and M.L. Gambone, *MRS Symposium Proceedings*, Vol. 273, *Intermetallic Composites II*, D.B. Miracle, D.L. Anton, and J.A. Graves, eds., pp. 3-16, (1992).

Larsen, J.M., K.A. Williams, S.J. Balsone, and M.A. Stucke, "Titanium Aluminides for Aerospace Applications," S.H. Whang, C.T. Liu, D.P. Pope, J.O. Stiegler, Eds., *Symposium on High Temperature Aluminides & Intermetallics*, pp. 521-556, (The Minerals, Metals & Materials Society, TMS, 1989).

Le Petitcorps, Y., R. Pailler, and R. Naslain, "The Fiber/Matrix Interfacial Shear Strength in Titanium Alloy Matrix Composites Reinforced by SiC or Boron CVD Filaments," *Composites Science and Technology*, Vol. 35, pp. 207-214, (1989).

Liaw, P.K., et al., "Determining Material Properties of Metal-Matrix Composites by NDE", *Journal of Materials*, Vol. 44(10), pp. 36-40, (1992).

Lifshitz, E.M. and G.D. Parkhomovskii, *Zh. Eksperim. i Teoret. Fiz.*, Vol. 20, pp. 175-182, 1950.

Lippman, R.P., *IEEE ASSP Magazine*, 4-22, (1987).

Luh, E.Y. and A.G. Evans, High-Temperature Mechanical Properties of a Ceramic Matrix Composite, *Journal of the American Ceramics Society*, **70**, pp. 466-469, (1987).

Mandell, K.C.C. Hong, and D.H. Grande, "Interfacial Shear Strength and Sliding Resistance in Metal and Glass-ceramic Matrix Composites," *Cer. Eng. Sci. Proc.*, 8:7-8, (1987).

Mann, L.L., T.E. Matikas, P. Karpur, and S. Krishnamurthy, "Supervised Backpropagation Neural Networks for the Classification of Ultrasonic Signals from Fiber Microcracking in Metal Matrix Composites," *IEEE Ultrasonics Symposium*, Vol. 1, pp. 355-360, (Tucson AZ, 1992).

Margetan, F.J., R.B. Thompson, J.H. Rose, and T.A. Gray, The Interaction of Ultrasound with Imperfect Interfaces: Experimental Studies of Model Structures, *Journal of Nondestructive Evaluation*, **11**, pp. 109-126, (1992).

Marshall, D.B. and W.C. Oliver, "Measurement of Interfacial Mechanical Properties in Fiber Reinforced Ceramic Composites," *Am. Cer. Soc.*, 70:8, (1987).

Marshall, D.B. and A.G. Evans, Failure Mechanisms in Ceramic-Fiber/Ceramic-Matrix Composites, *Journal of the American Ceramics Society*, **68**, pp. 225-231, (1985).

Marshall, D.B., "An Indentation Method for Measuring Matrix-Fiber Frictional Stresses in Ceramic Composites," *Am. Cer. Soc.*, 67:12, (1984).

Martin, R.W. and D.E. Chimenti, "Swept Frequency Ultrasonic Imaging in Composite Plates," Review of Progress in QNDE, op. cit., Vol. 9B, pp. 1497-1504, (1990).

Martin, R.W. and D.E. Chimenti, "Leaky Plate Wave Inspection of Biaxial Composites," Review of Progress in QNDE, op. cit., Vol. 8B, pp. 1663-1670, (1989).

Martin, R.W. and D.E. Chimenti, "Signal Processing of Leaky Lamb Wave Data for Defect Imaging in Composite Laminates," Review of Progress in QNDE, eds. D.O. Thompson and D.E. Chimenti, Plenum Press, New York, Vol. 6A, pp. 815-824, (1987).

Matikas, T.E., P. Karpur, P. Jero, and S. Krishnamurthy, "Measured Elastic Properties of Various Ceramics, Titanium Alloys and Fibers Using a Novel Ultrasonic Approach," submitted to *Journal of Materials Science*, (1994).

Matikas, T.E. and P. Karpur, "Ultrasonic Reflectivity Technique for the Characterization of Fiber-Matrix Interface in Metal Matrix Composites," *Journal of Applied Physics*, Vol. 74(1), pp. 228-236, (1993).

Matikas, T.E. and P. Karpur, "Micro-mechanics Approach to Characterize Interfaces in Metal and Ceramic Matrix Composites," D.O. Thompson, D.E. Chimenti, Eds., 20th Annual Review of Progress in Quantitative Nondestructive Evaluation, Vol. 13B, pp. 1477-1484, (Plenum, Bruswick ME, 1993).

Matikas, T.E. and P. Karpur, "Ultrasonic Nondestructive Evaluation as a Tool for the Development of Aerospace Structural Ceramic Composites", NATO/AGARD 76th Meeting of the Structures and Meterials Panel, (Antalya, Turkey, 1993).

Matikas, T.E., P. Karpur, and S. Krishnamurthy, "Metal Matrix Microstructural Characterization Using Reflectivity Techniques in a Model Composite," ASNT Fall Conference, pp. 258-260, (Chicago IL, 1992).

Matikas, T.E. and P. Karpur, "Matrix-Fiber Interface Characterization in Metal Matrix Composites Using Ultrasonic Shear-Wave Back-Reflection Coefficient Technique," D.O. Thompson, D.E. Chimenti, Eds., 19th Review of Progress in Quantitative Nondestructive Evaluation, Vol. 12B, pp. 1515-1522, (Plenum, La Jolla CA, 1992).

Matikas, T.E., P. Karpur, D. Stubbs, and S. Krishnamurthy, "Metal Matrix Composite Characterization Using Nondestructive Evaluation Methods," AIAA 1992 Mini-Symposium, (Dayton OH, 1992).

Matikas, T.E. and P. Karpur, "Back-Reflection of Ultrasonic Shear Waves from Homogeneous Cylindrical Fibers Embedded in Metallic Matrix," submitted to Research in Nondestructive Evaluation.

Matikas, T.E. and P. Karpur, "Effects of Attenuation and Diffraction on the Ultrasonic Back-Reflection Technique for the Interface Characterization of Metal Matrix Composites," submitted to Ultrasonics.

McCartney, L.N., New Theoretical Model of Stress Transfer Between Fibre and Matrix in a Uniaxially Fibre-Reinforced Composite, *Proc. Roy. Soc. London*, **A425**, (1990).

McCartney, L.N., Mechanics of Matrix Cracking in Brittle-Matrix Fibre-Reinforced Composites, *Proc. R. Soc. Lond.*, **A409**, pp. 329-350, (1987).

Merkulov, L.G., Soviet Phys.-Tech. Phys. (English Transl.), Vol. 1, pp. 59-69, (1956).

Metcalfe, A.G., *Interfaces in Metal Matrix Composites*, (Academic Press, Inc., New York NY, 1974).

Monette L., M.P. Anderson, S. Ling, and G.S. Grest, "Effect of Modulus and Cohesive Energy on Critical Fibre Length in Fibre-reinforced Composites," *J. Mater. Sci.*, 27, 4393-4405, (1992).

Murat M., M. Anholt, and H.D. Wagner, "Fracture Behavior of Short-Fiber Reinforced Materials," *J. Mater. Res.*, 7, 3120-3131, (1992).

Netravali, A.N., L.T.T. Topoleski, W.H. Sachse, and S.L. Phoenix, "An Acoustic Emission Technique for Measuring Fiber Fragment Length Distributions in the Single-Fiber-Composite Test," *Composites Science and Technology*, 35, pp. 13-29, (1989).

Newhouse, V.L., W.S. Furgason, N.M. Bilgutay, and J. Saniie, "Flaw-to-Grain Echo Enhancement," Proceedings of the Ultrasonic International Symposium, Butterworth Scientific, Guildford, U.K., pp. 152-156, (1979).

Newhouse, V.L., N.M. Bilgutay, J. Saniie, and E.S. Furgason, "Flaw-to-Grain Echo Enhancement by Split Spectrum Processing," *Ultrasonics*, Vol. 20, pp. 59-68, (1982).

Nicolaou, P.D., H.R. Piehler, and S. Saigal, "Experimental and Finite Element Analytical Guidelines for Fabricating Continuous Fiber (SCS-6) Metal Matrix (Ti-6Al-4V) Composites via the Foil/Fiber/Foil Technique", to appear in *Journal of Composite Materials*, 25, 1995.

Nicolaou, P.D., H.R. Piehler, and S. Saigal, in *Concurrent Engineering Approach to Materials Processing* A.J. Paul, S.N. Dwivedi, F.R. Dax, Eds. (The Minerals, Metals and Materials Society, Warrendale PA, 1992).

Nicolaou, P.D., H.R. Piehler, and M.A. Kuhni, "Fabrication of Ti-6Al-4V Matrix, SCS-6 Fiber Composites by Hot Pressing Using the Foil/Fiber/Foil Technique", in *Developments in Ceramic and Metal-Matrix Composites*, K. Upadhyay ed., (The Minerals, Metals, and Materials Society, Warrendale PA, 1991), pp. 37-47.

Nicolaou, P.D., H.R. Piehler, and S. Saigal, "Process Parameter Selection for the Consolidation of Continuous Fiber Reinforced Composites Using Finite Element Simulations", to appear in *International Journal of Mechanical Sciences*.

Nimmer, R.P., R.J. Bankert, E.S. Russell, G.A. Smith, and P.K. Wright, Micromechanical Modeling of Fiber/Matrix Interface Effects in Transversely Loaded SiC/Ti-6-4 Metal Matrix Composites, *Journal of Composites Technology & Research*, 13, pp. 3-13, (1991).

Ochiai, S. and K.Z. Osamura, "Multiple Fracture of a Fiber in a Single Tungsten Fiber-Copper Matrix Composite," *Metallkde.*, Vol. 77, pp. 255-259, (1986).

Ochiai S. and K. Osamura, "Stress Distribution of a Segmented Fibre in Loaded Single Fibre - Metal Matrix Composites, Z. Metallkde, 77, 249-254, (1986).

Ochiai S. and K. Osamura, "Multiple Fracture of a Fibre in a Single Tungsten Fibre -Copper Matrix Composite, Z. Metallkde, 77, 249-254, (1986).

Pagano, N.J. and H.W. Brown III, "The full cell cracking mode in unidirectional brittle-matrix composites," *COMPOSITES*, Vol. 24, No. 2, pp 69-83, (1993).

Pagano, N.J. and R.Y. Kim, "Progressive Microcracking in Unidirectional Brittle Matrix Composites," presented at 1993 Winter Annual Meeting of ASME, New Orleans LA 28 Nov. to 3 Dec. 1993.

Pagano, N.J. and Ran Y. Kim, "Crack Initiation in Unidirectional Brittle-Matrix Composites," *J. Am. Ceram. Soc.*, Vol 74, No. 5, pp. 1082-1090, (1991).

Pagano, N.J., "Axisymmetric Micromechanical Stress Fields in Composites," in *Local Mechanics Concepts for Composite Material Systems* J.N. Reddy, K.L. Reifsnider, Eds., pp. 1-26, (IUTAM Symposium, Blacksburg VA, 1991).

Papadakis, E.P., K.A. Fowler, and L.C. Lynnworth, "Ultrasonic Attenuation by Spectrum Analysis of Pulses in Buffer Rods: Methods and Diffraction Corrections," *The Journal of the Acoustical Society of America*, Vol. 53(5), pp. 1336-1343, (1973).

Papadakis, E.P., in *Physical Acoustics*, W.P. Mason, Ed. (Academic Press, New York, 1968), Vol. IV - Part B, pp. 269-328

Papadakis, E.P., "Ultrasonic Attenuation Caused by Scattering in Polycrystalline Metals," *The Journal of the Acoustical Society of America*, Vol. 37, pp. 711-717, (1965).

Park, H.S., G.S. Zong, L.D. Brown, L. Rabenberg, and H.L. Marcus, "Fiber-Matrix Interface Failures in Metal Matrix Composites: Testing, Analysis, and Failure Modes," W. S. Johnson, Ed., pp. 270-279, (American Society for Testing and Materials, Philadelphia PA, 1989).

Pipes, R.B. and N.J. Pagano, "Interlaminar Stresses in Composite Laminates Under Uniform Axial Extension," *J. Compos. Mater.* Vol. 4(4), pp. 538, (1970).

Resch, M.T., D.V. Nelson, H.H. Yuce, and G.F. Ramusat, "A Surface Acoustic Wave Technique for Monitoring the Growth Behavior of Small Surface Fatigue Cracks," *Journal of Nondestructive Evaluation*, Vol. 5, No. 1, (1985).

Rhodes, C.G., Characterization of Fiber/Matrix Interfaces by Transmission Electron Microscopy in Titanium Aluminide/SiC Composites, *Materials Research Society Symposium Proceedings*, 273, pp. 17-29, (1992).

Robinson, E.A. and M.T. Silvia, Digital Foundations of Time Series Analysis: Wave Equation Space-Time Processing, Vol. 2, Holden-Day, Inc., 1981.

Roman I., S. Krishnamurthy, and D.B. Miracle, "Fiber-matrix Interfacial Behavior in SiC-Titanium Alloy Composites," (1993).

Roman, I., S. Krishnamurthy, and D.B. Miracle, in the Seventh World Conference on Titanium, San Diego CA, June 29-July 2, 1992.

Roman, I. and R. Aharonov, "Mechanical Interrogation of Interfaces in Monofilament Model Composites of Continuous SiC Fiber-Aluminum Matrix," *Acta Metall. Mater.*, Vol. 40, pp. 477-485, (1992).

Russ, S.M., T. Nicholas, M. Bates, and S. Mall, "Thermomechanical Fatigue of SCS-6/Ti-24Al-11Nb Metal Matrix Composite," in *Failure Mechanisms in High Temperature Composite Materials*, Vol. AD-Vol. 22/AMD-Vol. 122, pp. 37-43, (ASME, 1991).

Saglio, R. and A.C. Prot, "Ultrasonic Focusing Techniques" in Nondestructive Testing, Vol. 8, Academic Press Inc. (London) Ltd., (1985).

Schafer, R.W. and L.R. Rabiner, "A Digital Signal Processing Approach to Interpolation," in *Proceedings of the IEEE*, Vol. 61, No. 6, pp. 692-702, (June 1973).

Schlagent E. and J.G.M. Van Mier, "Simple Lattice Model for Numerical Simulation of Fracture of Concrete Materials and Structures," *Mater. & Struct.*, 25, 534-542, (1992).

Schuetz, L.S. and W.G. Neubauer, "Acoustic Reflection from Cylinders - Nonabsorbing and Absorbing", *J. Acoust. Soc. Am.*, Vol. 62, pp. 513-517, (1977).

Shaw, L.L., T.E. Matikas, P. Karpur, S. Hu, and D.B. Miracle, "A Novel Method of In-Situ Assessment of Fracture and Deformation of the Fiber/Matrix Interface in Metal-Matrix Composites," *Proceedings of the International Conference on Composites Engineering (ICCE/1)*, pp. 479-480, (New Orleans LA, 1994).

Vassel, A., M.C. Merienne, F. Pautonnier, L. Molliex, and J.P. Favre, "A Method to Evaluate the Bonding Between Fiber and Matrix in Ti-Base Composite," in *Sixth World Conference on Titanium*, P. Lacombe, R. Tricot, G. Beranger, eds., pp. 919-923, (Les Editions de Physique, Les Ulis Cedex, France, 1988).

Wasserman, P.D., Neural Computing Theory and Practice (Van Nostrand Reinhold, New York, NY, 1989).

Waterburry, M.C., P. Karpur, T.E. Matikas, and S. Krishnamurthy, In-situ Observation of the Single Fiber Fragmentation Process in Metal Matrix Composites by Ultrasonic Imaging, Composites Science and Technology, in print, (1994).

Waterburry, M.C., T.E. Matikas, P. Karpur, and S. Krishnamurthy, "In Situ Ultrasonic Imaging and Acoustic Emission Monitoring of Single Fiber Fragmentation in Metal Matrix Composites," TMS Fall Meeting, Symposium on Nondestructive Evaluation (NDE) and Material Properties, (Pittsburgh PA, 1993).

Waterburry, M.C. and L.T. Drzal, "On the Determination of Fiber Strengths by In Situ Fiber Strength Testing," J. of Composites Technology & Research, Vol. 13(1), pp. 22-28, (Spring 1991).

Waterburry, M.C., "Nylon 6,6 Fragmentation Testing," from dissertation, "The Influence of Processing, Chemistry, and Interphase Microstructure on the Adhesion of Carbon Fibers to Thermoset and Thermoplastic Matrices," Michigan State University, pp. 201-202, (1991).

Wright, P.K., R. Nimmer, G. Smith, M. Sensmeier, and M. Brun, The Influence of the Interface on Mechanical Behavior of Ti-6Al-4V/SCS-6 Composites, *International Conference on Interfaces in Metal-Ceramics Composites, at the TMS Annual Meeting*, Anaheim CA, pp. 559-581, (1990).

Wright, P.K., R. Nimmer, G. Smith, M. Sensmeier, and M. Brun, "The Influence of the Interface on Mechanical Behavior of Ti-6Al-4V/SCS-6 Composites," in *Interfaces in Metal-Ceramics Composites*, R.Y. Lin, R.J. Arsenault, P.G. Martins, and S.G. Fishman Eds., (1989).

## **APPENDIX A**

### ***LIST OF PUBLICATIONS***

Benson, D.M., P. Karpur, T.E. Matikas, and T. Kundu, "Experimental Generation of Lamb Wave Dispersion Using Fourier Analysis Of Leaky Modes," to be published in the Proceedings of the 21st Annual Review of Progress in Quantitative Nondestructive Evaluation, (Snowmass Village CO, 1994).

Blatt, D., P. Karpur, D. Stubbs, and T. Matikas, "Observations of Interfacial Damage in the Fiber Bridged Zone of a Titanium Matrix Composite," *Scripta METALLURGICA et MATERIALIA*, Vol. 29, pp. 851-856, (1993).

Blatt, D., P. Karpur, T.E. Matikas, M.P. Blodgett, D.A. Stubbs, "Elevated Temperature Degradation and Damage Mechanisms of Titanium Based Metal Matrix Composites with SCS-6 Fibers," American Society of Composites 8th Technical Conference on Composite Materials (Technomic Publishing Co., Cleveland OH), pp. 531-540, (October 19-21, 1993).

Blatt, D., P. Karpur, D.A. Stubbs, and T.E. Matikas, "Observations of Interfacial Damage in the Fiber Bridged Zone of a Titanium Matrix Composite," *Scripta Metallurgica et Materialia*, Vol. 29, pp. 851-856, (1993).

Blodgett, M., P. Karpur, T. Matikas, J. Jira, and D. Blatt, "Ultrasonic Evaluation of Fiber-Matrix Interfacial Degradation of Titanium Matrix Composites Due to Cyclic Temperature and Mechanical Loading," presented at the 1993 Review of Progress in Quantitative Nondestructive Evaluation, Brunswick ME, August 2-6, 1993.

Canelones, O.J. and P. Karpur, "Split Spectrum Processing with Computationally Efficient Sinusoidal FIR Filters," Submitted to Review of Progress in Quantitative Nondestructive Evaluation, Ed., D.O. Thompson, Vol. 11.

Chimenti, D.E. and R.W. Martin, "Nondestructive Evaluation of Composite Laminates by Leaky Lamb Waves," *Ultrasonics*, Butterworth-Heinemann Ltd., Vol. 29, pp. 13-21, (January 1991).

Damarla, T.R., P. Karpur, and P.K. Bhagat, "A Self-Learning Neural Net for Ultrasonic Signal Analysis," Submitted to Ultrasonics, Butterworth Publishers, Great Britain.

Damarla, T.R., S. Ghosal, and P. Karpur, "Application of Neural Networks for Classification of Ultrasonic Signals," ASME Press Series on International Advances in Design Productivity, Eds., C.H. Dagli, S.R.T. Kumara, and Y.C. Shin, pp. 377-382, (1991).

Damarla, T.R., P. Karpur, and P.K. Bhagat, "A Self-Learning Neural Net for Ultrasonic Signal Analysis," accepted for publication in Ultrasonics.

Frantziskonis, G.N., P. Karpur, T.E. Matikas, S. Krishnamurthy, and P.D. Jero, "Fiber Matrix Interface - Information from Experiments via Simulation," *accepted for publication in Composites Structures* , (1994).

Frantziskonis, G.N., T.E. Matikas, P. Karpur, and S. Krishnamurthy, "Simulation Of Fiber-Matrix Interface Behavior Under Various Experimental Configurations," Proceedings of the International Conference on Composites Engineering (ICCE/1), pp. 147-148, (New Orleans LA, 1994).

Frock, B.G., P. Karpur, and M.J. Ruddell, "Effects of Axial-Wiener Deconvolution on the Lateral Resolution in Ultrasonic C-scan Images," To be published in *Review of Progress in Quantitative Nondestructive Evaluation*, Vol. 10, (1991).

Frock, B.G., D. Bailey, D. Ballard, and D. Laufersweiler, "Digital Data Acquisition and Analyses for Improved Ultrasonic Evaluation of Materials and Structures," Presented at the ASNT 50th Anniversary Fall Conference and Quality Testing Show, September 15-18, 1991, Boston MA.

Frock, B.G. and D. Bailey, "Applications of Digital Data Acquisition and Analyses Techniques to In-Field Ultrasonic Inspections," submitted for publication in International Advances in Nondestructive Testing," Ed., Warren J. McGonnagle.

Frock, B. and D.M. Bailey, "Applications of Digital Data Acquisition and Analyses Techniques to In-field Ultrasonic Inspections," International Advances in NONDESTRUCTIVE TESTING, Ed., W.J. McGonnagle, Gordon and Breach Science Publishers, Langhorne PA, Vol. 17, pp. 157-184, (1994).

Hu, S., P. Karpur, P., T.E. Matikas, L. Shaw, and N.J. Pagano, "Free Edge Effect On Residual Stresses And Fracture Of Composite Fiber/Matrix Interface," Proceedings of the International Conference on Composites Engineering (ICCE/1), pp. 221-222, (New Orleans LA, 1994).

Hu, S., P. Karpur, and T.E. Matikas, "A Preliminary Investigation of Fiber/Matrix Interphase Oxidation in Metal Matrix Composites Using Acoustic Microscope," to be published in the Proceedings of the 21st Annual Review of Progress in Quantitative Nondestructive Evaluation, (Snowmass Village CO, 1994).

Karpur, P. and M.T. Resch, "Improved Detectability of Fatigue Microcracks by Split Spectrum Processing of Backscattered Rayleigh Waves," To be published in Review of Progress in Quantitative Nondestructive Evaluation, Vol. 10, (1991).

Karpur, P., "Split Spectrum Technique as a Preprocessor for Ultrasonic Nondestructive Evaluation," Submitted to Review of Progress in Quantitative Nondestructive Evaluation, Ed., D.O. Thompson, Vol. 11.

Karpur, P., T. Matikas, and S. Krishnamurthy, "Matrix-Fiber Interface Characterization in Metal Matrix Composites Using Ultrasonic Imaging of Fiber Fragmentation," to be presented at the 7th Technical Conference on Composite Materials, (Tucson AZ, October 13-15, 1992).

Karpur, P., T.E. Matikas, S. Krishnamurthy, and N. Ashbaugh, "Ultrasound for Fiber Fragmentation Size Determination to Characterize Load Transfer Behavior of Matrix-Fiber Interface in Metal-Matrix Composites," presented at the Review of Progress in Quantitative Nondestructive Evaluation, (La Jolla CA, July 19-24, 1992).

Karpur, P., "Split Spectrum Technique as a Signal Analysis," Materials Evaluation, Vol. 50, No. 6, pp. 793-797, (June 1992).

Karpur, P. and O.J. Canelones, "Split Spectrum Processing: A New Filtering Approach for Improved Signal-to-Noise Ratio Enhancement of Ultrasonic Signals," Ultrasonics, Vol. 30(6), pp. 351-358, (1992).

Karpur, P., T. Matikas, and S. Krishnamurthy, "A Novel Parameter to Characterize the Fiber-Matrix Interphase/Interface for Mechanics of Continuous Fiber Reinforced Metal Matrix and Ceramic Matrix Composites," submitted for publication to Composites Science and Technology.

Karpur, P., T. Matikas, M. Blodgett, J. Jira, and D. Blatt, "Nondestructive Crack Size and Interfacial Degradation Evaluation in Metal Matrix Composites Using High Frequency Ultrasonic Microscopy," presented at the ASTM Symposium on Special Applications and Advanced Techniques for Crack Size Determination, (Atlanta GA, May 19, 1993).

Karpur, P., T. Matikas, and S. Krishnamurthy, "Matrix-Fiber Interface Characterization in Metal Matrix Composites Using Ultrasonic Imaging of Fiber Fragmentation," in Proceedings of the Seventh Technical Conference for Composite Materials and Processing, American Society for Composites, (University Park PA, October 13-15, 1992).

Karpur, P., T.E. Matikas, S. Krishnamurthy, "Ultrasound as a Tool for the Development of Aerospace Structural Titanium and Ceramic Matrix Composites," in Control of Interfaces in Metal and Ceramics Composites, Eds., R.Y. Lin, S.G. Fishman, TMS Press, pp. 241-253, (1994).

Karpur, P., T.E. Matikas, M.P. Blodgett, J.R. Jira, and D. Blatt, "Nondestructive Crack Size and Interfacial Degradation Evaluation in Metal Matrix Composites Using High Frequency Acoustic Microscopy," ASTM STP 1251 on Application of Advanced Techniques for Crack Size Determination, Eds., J.J. Ruschau and J.K. Donald, in press - to be published in 1995.

Karpur, P., T.E. Matikas, M.P. Blodgett, "Acoustic Microscopy As A Tool For Fiber-Matrix Interface Evaluation," Proceedings of the International Conference on Composites Engineering (ICCE/1), pp. 253-254, (New Orleans LA, 1994).

Karpur, P. and T.E. Matikas, "Theoretical Modeling and Experimental Characterization of Fiber-Matrix Interface in Advanced Composites," to be published in the Proceedings of the 21st Annual Review of Progress in Quantitative Nondestructive Evaluation, (Snowmass Village CO, 1994).

Kent, R., P. Karpur, T. Matikas, and P. Jero, "Ultrasonic Analysis of Interfacial Debond in Ceramic Matrix Composites," presented at the 6th International Symposium on Nondestructive Characterization of Materials, (Kahuku HI, June 7-11, 1993).

Kent, R., T.E. Matikas, P. Karpur, P. Jero, "Ultrasonic Analysis of Interfacial Debond in Ceramic Matrix Composites," Sixth International Symposium on Nondestructive Characterization of Materials, (Oahu HI, 1993).

Krishnamurthy, S., T.E. Matikas, P. Karpur, and D.B. Miracle, "Ultrasonic Evaluation of the Processing of Fiber-Reinforced Metal Matrix Composites," *accepted for publication in Composite Science and Technology*, (1994).

Li, Y., V.L. Newhouse, P.M. Shankar, and P. Karpur, "Speckle Reduction in Ultrasonic Synthetic Aperture Images," Ultrasonics, Vol. 30, No. 4, pp. 233-237, (July 1992).

MacLellan, P.T., D.A. Stubbs, and P. Karpur, "In Situ Ultrasonic Surface Wave Assessment of Mechanical Fatigue Damage Accumulation in Metal Matrix Composites," Proceedings of the International Conference on Composites Engineering (ICCE/1), pp. 503-504, (New Orleans LA, 1994).

MacLellan, P.T., D.A. Stubbs, and P. Karpur, "Evaluation of Mechanical Fatigue Damage Accumulation in Metal Matrix Composites Using Ultrasonic Surface Waves," to be published in the Proceedings of the 21st Annual Review of Progress in Quantitative Nondestructive Evaluation, (Snowmass Village CO), 1994).

MacLellan, P.T., D.A. Stubbs, and P. Karpur, "Monitoring Fatigue Damage in Metal Matrix Composites, *in situ*, Using Ultrasonic Surface Waves," Proceedings of the 1994 Society for Experimental Mechanics Conference, pp: 920-928.

Mann, L., T. Matikas, P. Karpur, and S. Krishnamurthy, "Supervised Backpropagation Neural Networks for the Classification of Ultrasonic Signals from Fiber Microcracking in Metal Matrix Composites," in Proceedings of the IEEE 1992 Ultrasonics Symposium, (Tucson AZ, October 20-23, 1992).

Martin, R.W. and D.E. Chimenti, "Leaky Plate Wave Inspection of Biaxial Composites", Review of Progress in QNDE, op. cit., Vol. 8B, pp. 1663-1670, (1989).

Martin, R. W. and D.E. Chimenti, "Swept Frequency Ultrasonic Imaging in Composite Plates," Review of Progress in QNDE, op. cit., Vol. 9B, pp. 1497-1504, (1990).

Matikas, T. M. and P. Karpur, "Matrix-Fiber Interface Characterization in Metal-Matrix Composites Using Ultrasonic Shear Wave Back-Reflection Coefficient Technique," presented at the Review of Progress in Quantitative Nondestructive Evaluation, (La Jolla CA, July 19-24, 1992).

Matikas, T., P. Karpur, D. Stubbs, and P. Krishnamurthy, "Metal Matrix Composite Characterization Using Nondestructive Evaluation Methods," presented at the 18th Annual AIAA Symposium, (Dayton OH, March 26, 1992).

Matikas, T. M., P. Karpur, D.A. Stubbs, and S. Krishnamurthy, "Metal Matrix Composite Interface Characterization Using Nondestructive Evaluation Methods," presented in the NDE of Interfaces Research Symposium Program, ASNT Spring Conference, (Orlando FL, March 31-April 2, 1992).

Matikas, T. and P. Karpur, "Micro-Mechanics Approach to Characterize Interfaces in Metal Matrix and Ceramic Matrix Composites," presented at the 1993 Review of Progress in Quantitative Nondestructive Evaluation, (Brunswick ME, August 2-6, 1993).

Matikas, T. and P. Karpur, "Ultrasonic Nondestructive Evaluation as a Tool for the Development of Aerospace Structural Ceramic Composites," presented at the 76th meeting of the Structures and Materials Panel, the NATO Advisory Group for Agard, (Antalya, Turkey, April 19-22, 1993).

Matikas, T.E., P. Karpur, S. Krishnamurthy, "Modeling the Interphase as an Interface in Mechanics of Composites," American Society of Composites 8th Technical Conference on Composite Materials, pp. 3-11, (Technomic Publishing Co. Inc., Cleveland OH, October 19-21, 1993).

Matikas, T.E., P. Karpur, S. Krishnamurthy, "Study Of Elastic Behavior Of Fiber-Matrix 'interface' Using Stress Wave Mechanics Analysis," Proceedings of the International Conference on Composites Engineering (ICCE/1), pp. 331-332, (New Orleans LA, 1994).

Matikas, T.E., P. Karpur, S. Hu, L.L. Shaw, "In-situ Ultrasonic Characterization of Failure Strength of Fiber-Matrix Interface in Metal Matrix Composites Reinforced by SCS Series Fibers," to be published in the Proceedings of the 21st Annual Review of Progress in Quantitative Nondestructive Evaluation, (Snowmass Village CO, 1994).

Pagano, N.J., R.E. Dutton, R.Y. Kim, P. Karpur, and T.E. Matikas, "Influence Of The Fiber-Matrix Interface On The Micro-Cracking In Unidirectional Glass Matrix Composites," Proceedings of the International Conference on Composites Engineering (ICCE/1), pp. 387-388, (New Orleans LA, 1994).

Shaw, L.L., T.E. Matikas, P. Karpur, S. Hu, and D.B. Miracle, "A Novel Method Of In-Situ Assessment Of Fracture And Deformation Of The Fiber/Matrix Interface In Metal-Matrix Composites," Proceedings of the International Conference on Composites Engineering (ICCE/1), pp. 479-480, (New Orleans LA, 1994).

Waterbury, M.C., T.E. Matikas, P. Karpur, S. Krishnamurthy, "In Situ Ultrasonic Imaging and Acoustic Emission Monitoring of Single Fiber Fragmentation in Metal Matrix Composites," 1993 TMS Annual Fall Meeting, (Pittsburgh PA, October 17-21, 1993).

Waterburry, M.C., P. Karpur, T.E. Matikas, S. Krishnamurthy, "In Situ Observation of the Single Fiber Fragmentation Process in Metal Matrix Composites by Ultrasonic Imaging," *accepted for publication in Composite Science and Technology*, (1994).